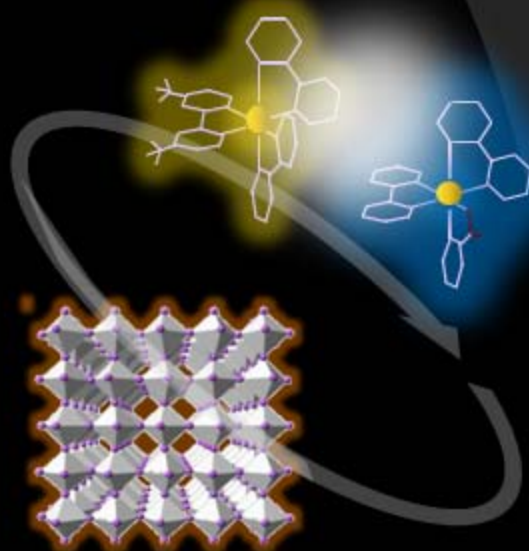
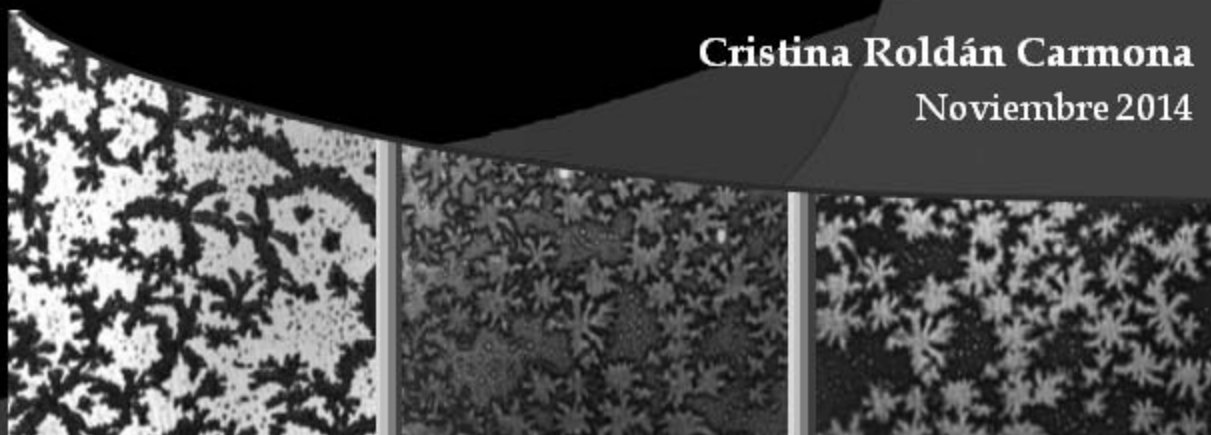


# Molecular Arrangement in ultrathin films Thin films effect in optoelectronic devices



**Cristina Roldán Carmona**  
Noviembre 2014



TITULO: *Formación de nuevas estructuras moleculares en películas ultrafinas. Preparación de dispositivos electroluminiscentes y fotovoltaicos. Molecular Arrangement in ultrathin films. Thin films in optoelectronic devices*

AUTOR: *Cristina Roldán Carmona*

---

© Edita: Servicio de Publicaciones de la Universidad de Córdoba. 2014  
Campus de Rabanales  
Ctra. Nacional IV, Km. 396 A  
14071 Córdoba

[www.uco.es/publicaciones](http://www.uco.es/publicaciones)  
[publicaciones@uco.es](mailto:publicaciones@uco.es)

---

# **Molecular arrangement in ultrathin films**

## **Thin films in optoelectronic devices**

*Formación de nuevas estructuras moleculares en películas ultrafinas. Preparación de dispositivos electroluminiscentes y fotovoltaicos.*

**PhD Thesis**

Cristina Roldán Carmona

**Córdoba, Noviembre 2014**



**Departamento de Química Física y Termodinámica Aplicada**  
**Universidad de Córdoba**



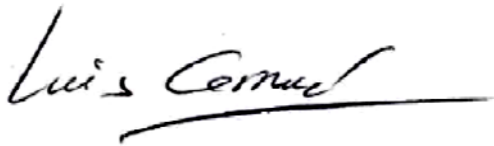
# **Molecular arrangement in ultrathin films**

## **Thin films in optoelectronic devices**

*Formación de nuevas estructuras moleculares en películas ultrafinas.*

*Preparación de dispositivos electroluminiscentes y fotovoltaicos.*

Los directores:



Prof. Dr. Luis Camacho Delgado



Dr. Hendrik Jan Bolink

Candidata a optar al grado de Doctora en Ciencias Químicas



Cristina Roldán Carmona

Licenciada en Ciencias Químicas





**TÍTULO DE LA TESIS:** Molecular arrangement in ultrathin films. Thin films effect in optoelectronic devices

**DOCTORANDO/A:** Cristina Roldán Carmona

**INFORME RAZONADO DEL/DE LOS DIRECTOR/ES DE LA TESIS**

(se hará mención a la evolución y desarrollo de la tesis, así como a trabajos y publicaciones derivados de la misma).

**D. Luis Camacho Delgado** y **D. Hendrik Jan Bolink**, Catedrático del Departamento de Química Física y Termodinámica Aplicada de la Universidad de Córdoba e Investigador de la Fundación General de la Universidad de Valencia, respectivamente, certifican que la presente Tesis Doctoral se ha desarrollado en los laboratorios del Departamento de Química Física y Termodinámica Aplicada de la Universidad de Córdoba y en el Instituto de Ciencia Molecular de Valencia (ICMoL), bajo la dirección de ambos. Esta Tesis Doctoral reúne todas las condiciones exigidas según la legislación vigente. Su evolución y desarrollo ha seguido el plan de trabajo inicialmente previsto, alcanzándose los objetivos previamente marcados. Durante la elaboración de la Tesis, el doctorando ha realizado una estancia breve de investigación en un centro internacional. Ha dado lugar a siete publicaciones, seis de ellas ya publicadas en revistas internacionales de reconocido prestigio, y una pendiente de aceptación, así como a diversas comunicaciones en congresos nacionales e internacionales.

Por todo ello, se autoriza la presentación de la tesis doctoral.

Córdoba, uno de Octubre de 2014

Firma del/de los director/es

Fdo.: Hendrik Jan Bolink

Fdo.: Luis Camacho Delgado





Mediante la defensa de esta memoria se pretende optar a la obtención de la mención de “Doctorado Internacional”, habida cuenta que la doctoranda reúne los requisitos exigidos para tal mención:

1. Se cuenta con los informes favorables de dos doctores expertos, con experiencia investigadora acreditada, pertenecientes a alguna institución de educación superior o instituto de investigación fuera de España.
2. En el Tribunal, que ha de evaluar la Tesis, existe un miembro de un instituto de educación superior o centro de investigación de un país distinto al nuestro.
3. La redacción y defensa de esta Memoria se realizará en la lengua oficial de un país europeo distinto al nuestro.
4. La doctoranda ha realizado una estancia de investigación en las instalaciones del “Centre for Molecular and Nanoscale Electronics” de la Universidad de Durham (Reino Unido). La estancia, de un trimestre de duración, se realizó gracias a la concesión de ayudas para la movilidad con objeto de obtener el Doctorado con Mención Internacional concedida por el Ministerio de Educación, Cultura y Deporte.



El trabajo que engloba la presente Memoria se ha realizado durante el periodo de disfrute de una Beca de Formación de Profesorado Universitario del Ministerio de Educación, Cultura y Deporte, asociada a los proyectos financiados por la CICYT “*Desarrollo de nuevas estrategias para la formación de estructuras moleculares Bi-Dimensionales de películas delgadas. Incorporación en dispositivos nanoestructurados*” (CTQ2010-17481), y la Junta de Andalucía “*Diseño de sistemas orgánicos nanoestructurados para su aplicación en Dispositivos Electroluminiscentes*” (P08-FQM-4011) y “*Películas ultrafinas organizadas de colorantes orgánicos como componentes de dispositivos nanoestructurados*” (P10-FQM-6703).



## *Agradecimientos*

Siempre he escuchado lo fácil que resultaba escribir esta parte de la memoria con cierto temor, pues bien sabe quien me conoce que mostrar mis sentimientos no es una de mis mejores virtudes. Mucho ha cambiado mi mundo desde que comencé este viaje y mucho he de agradecer a todas las personas que han compartido conmigo un poquito de él.

Mi más sincera gratitud por los directores de este trabajo, Dr. Luis Camacho y Dr. Hendik Jan Bolink, sin cuya dedicación y apoyo continuo no habría podido salir adelante.

Gracias de todo corazón a Rafa, por el apoyo que me dio en mis primeros pasos. Por creer en mí con tal fuerza que casi hiciera innecesaria la mía propia. Por el apoyo ante las dificultades y el cariño que nunca me faltó. Gracias por saber escuchar y darme fuerza a seguir adelante.

Quiero agradecer a todos los miembros del Departamento de Química Física y Termodinámica Aplicada por su compañía durante estos años. A quien me acogió en mis primeros pasos como aprendiz y me intentó mostrar todo su entusiasmo por la ciencia. Gracias Juanjo por esas primeras tardes de sala limpia donde el tiempo no tenía cabida. Poco duró aquél pequeño equipo de tres, pero a día de hoy creo que fui afortunada en poder disfrutarlo. Antonio, compi, nos quedábamos solos, pero el viaje seguía y contigo pude compartir el buen trabajo en equipo de lo que sería nuestra primera publicación juntos. Gracias por estar ahí. Pasó el tiempo y pronto descubrí que muy cerca había grandes personas por conocer. A mis compis de despacho, que alegraron mi día a día en esa primera etapa. Gracias Dani, por alguna que otra charla y el cariño que siempre me mostraste, y a Sara ¡qué te voy a decir a ti! Gracias por esos buenos ratos. Pensar en ti me llena

la mente de recuerdos divertidos. Gracias por dejarme adueñarme de tu taza, por hacerme esos cafelitos tan ricos... y por compartir esas historias ¡que solo te pueden pasar a ti! Gracias por ser como eres y por haberme dejado acercarme a ti. Pero el despacho era grande, y otra gran compañera me guardaba las espaldas. Gracias Guada, por todos los buenos ratos vividos, por aceptarme y tratarme desde un principio como a la mejor de tus amigas. Gracias por esas noches de risas e historietas, y por incluirme en este trío de pijamas que llegamos a formar, cuyo puzle tengo justo a mi lado mientras escribo estas líneas. A Inma, por alegrar siempre el ambiente cada mañana, y a Rafa M. por los ratillos de humor entre pasillos y visitas.

Pero años de bonanza prosiguieron y nuevas caras se sumaron al trajín diario. A mis compañeros Fernando, Rocío, R. Cano, Encarni, Alain y, muy especialmente a Carlos. Gracias por hacer del día a día un encuentro de amigos. Carlos gracias por tus conversaciones diarias y por saber escuchar en los momentos que más lo necesité. A pesar de nuestras diferencias, créeme cuando digo aquello de *ante todo admiración y respeto*, por tu perseverancia, buen trabajo y responsabilidad. Eres un ejemplo a seguir y espero que tengas la suerte que te mereces. Y no me olvido de mi compi Luisa, de quien mis idas y venidas me han tenido un poco más separada, pero a quien he tenido la suerte de conocer mejor en esta última temporada. Gracias Luisa por tu compañía en estos últimos meses, por tus conversaciones, y como no, por tu eficacia en la organización... ¡mi complemento perfecto!

También quiero mostrar mi más sincera gratitud a todos los profesores del departamento, que me han ofrecido siempre su ayuda. Quiero agradecer especialmente a Luis, por su curiosidad continua y su gusto por el trabajo bien hecho. Fuiste con diferencia uno de los mejores profesores que tuve

durante la carrera, con quien descubrí y disfruté la Química Física, razón por la que decidí continuar en esta carrera. Creo que las horas compartidas han sido insuficientes para poder aprender y expresar todos tus conocimientos de la manera que me hubiera gustado, aunque espero continuar aprovechando la oportunidad y privilegio de aquí en adelante. A Mari Tere, por sus consejos y apoyo a lo largo de estos años. Por estar siempre dispuesta a enviar un *empujoncito* o toda una *ola de calor* en el momento más apropiado. Gracias por acompañarme y escucharme cuando lo necesité. A Marta, por los momentos compartidos y, por qué no decirlo, ¡por la constante lucha y quebradero de cabeza que nos ha dado la puesta a punto de la sala limpia! Gracias a Elo, por esa frescura y alegría que me has mostrado cada día. Por escuchar y aconsejarme siempre con una sonrisa. A Teresa, por su pasión y compañía en tan diversos temas, que ponían su matiz crítico en las tertulias del almuerzo. También quiero agradecer por su disposición a Aurelio Jarque y, especialmente a Antonia Parrado, a quien en este último tiempo he tenido la suerte de conocer un poco mejor.

Pero el viaje prosiguió y el barco cambió de rumbo, con la suerte de parar en un gran puerto de tierras valencianas. Y lo que iba a ser solo unos meses... se alargó a un par de añitos. Gracias a mi otra gran familia, sin la que nada de esto habría podido ser posible. Especialmente quiero darte las gracias Henk, por tu apoyo constante, por creer en mí y convertirme en un miembro más de tu equipo. Por contar conmigo para grandes retos, y auparme en los momentos más negativos. Por esa confianza que siempre me has mostrado y por hacer sentir en mí esa gran valía.

A quien me abrió las puertas de su casa recién llegada y me hizo sentir parte de su familia. Gracias Mauri por tu acogida y tu cariño, por hacerme sentir como en casa y compartir tu tierra y tu cultura. Gracias a mis chicas

¡que tanto me han apoyado en toda mi andadura valenciana! A Alejandra, Elena, Mariam y Ana, por hacerme una más de la familia, por las comidas de los miércoles, el equipo aqua-gym y sus tejemanejes, las aventuras en avioneta... todos esos recuerdos no se pueden describir con palabras. Gracias Alejandra por ser como eres, por esa atención y cariño continuo. Por escucharme cuando necesitaba desahogarme, o aconsejarme ante las situaciones de duda. Por hacerme sentir que no estaba sola desde el instante que te conocí, y que ante cualquier problema tu ayuda no me faltaría. Gracias por mostrarte como eres y acogerme como solo tú sabes.

Me gustaría agradecer a todos mis compañeros de valencia, gracias a quienes el trabajo en el ICMol se convertía en un continuo fluir de bromas y risas. Vuestra compañía hacía posible que el tiempo en la sala limpia pasara rápido, a pesar de las largas jornadas que a veces dedicábamos. Me gustaría agradecer a Dani y a Toni, por estar siempre dispuestos a ayudarme ante cualquier necesidad, a Jorge, por todo el trabajo extra que siempre le he dado y ante el que nunca tuve ni una sola negativa. Gracias por tu disponibilidad cuando te necesité y por esas clases espontáneas donde pude aprender un poquito de todo lo que sabes. A María, por tu paciencia infinita ante todos mis papeleos y por tu amistad y compañía fuera y dentro del instituto. Agradecer también a aquellos compañeros que nos dejaron hace un tiempo, como Juanjo, Sonsoles y especialmente Takeo. Thanks Takeo for sharing with me your thoughts, your culture and what is even better... your meals! It was a pleasure to work with you in the lab and to exchange the samples for a good conversation in front of some bears in the bar. Me gustaría agradecer también al resto de mis compañeros: Michele, gran profesional con quien tuve la suerte de compartir mis últimos meses, y a Enrico, con quien pude compartir y reír en más de un almuerzo y alguna que otra cena mítica. Siempre recordaré tus risas espontáneas en los meetings de



grupo. A mis más recientes compañeras Laura, Giulia, Lidón y mi tocaya Cristina. Les deseo toda la suerte del mundo y que disfruten de esta etapa viviendo cada día al máximo. Lidón tuvo la suerte de poder formar parte de tus primeros trabajos y apreciar todo tu talento y tu manera de trabajar. Gracias por compartir tu experiencia y confiar en mí. A Giulia, ¡gracias por tu paciencia con mi organización y la constancia ante la frustrante irreproducibilidad! Cristina, solo puedo darte las gracias por el apoyo que me has dado en mis últimos días, tu continua compañía y tu confianza en mí. Gracias por ser mi compañera y amiga. También me gustaría agradecer a mis compañeros de despacho en mi última etapa. A Juanpi, Elena, Sara, Julia, Michele y Walter por animar y amenizar el ambiente y por esa energía positiva que siempre transmitisteis. Finalmente y muy especialmente, me gustaría darle las gracias a esa especie de consejero y confesor, gran profesional y gran compañero sin el que los días de trabajo realmente no habrían podido ser los mismos. Sin duda una pieza clave e invisible de todo trabajo que sale de la sala limpia. Gracias Ángel por ser como eres, por ser capaz de apoyar y animar con las más absurdas de las conversaciones, por prestar siempre tu ayuda ante cualquier complicación y compartir tu experiencia sin el más mínimo interés. Gracias por las risas diarias y por la energía que transmites día a día.

I would like to thank in a special way to Olga, who was not only a colleague but also a good friend since my arrival. You were one of my main supports in Valencia, my confident at the same time that one of the funniest person I have ever known. A mix of energy, crazyness and imagination, together with a special sense of humor and some *strange logic sense*. I can't describe all the funny situations I have lived with you, but believe me when I say that I feel really lucky on having shared all this time with you. I hope you will be plenty of success in this new stage that is starting.

Me llevo grandes recuerdos de todos vosotros. Sabed que tendréis una compañera y amiga allá donde esté.

Finalmente quiero agradecer a toda mi familia por su apoyo continuo, por quererme tal como soy y respetar todas mis decisiones. A mi padre por su complicidad, por haberme inculcado siempre el amor por el trabajo bien hecho, por su compañía y ánimo siempre que los he necesitado. Por ser él. A María José, por su apoyo constante, su cariño, su disponibilidad infinita, y como no... ¡por sus comiditas tan ricas y que tan bien me han venido en esta última temporada! gracias por tratarme siempre con tanta dedicación. A mi hermana, mi amiga de toda una vida, en quien sé que encontraré apoyo siempre que lo necesite. A José, por estar siempre dispuesto a ayudarme y comenzar alguna de nuestras tertulias continuas que siempre me enriquecen. A mi abuela, con quien tengo la suerte de vivir esta etapa de mi vida y quien me ha enseñado a ser mejor persona y valorar los pequeños placeres de la vida.

A Paolo, por tener ese don particular de saber decirme las palabras necesarias en cada momento. Gracias por levantarme cuando me he sentido vencida. Por el cariño y apoyo que me has mostrado siempre y sin el cual, este último periodo habría sido muy diferente.

*A mi familia*



## Objetivos

La presente Tesis Doctoral se enmarca en la línea de investigación *Películas Superficiales y Organización Molecular: Dispositivos Electroluminiscentes y Sensores De Gases* del grupo FQM-204 de la Junta de Andalucía. Los objetivos concretos que se persiguen son:

1. Fabricación de estructuras bi-dimensionales bien definidas en la interfase aire-agua, mediante la preparación de películas superficiales mixtas formadas por moléculas con buenas propiedades luminiscentes tales como complejos metálicos de transición, derivados de rodaminas, hemicianinas... con diferentes lípidos que actúen de matriz, en relaciones molares adecuadas, con objeto de crear monocapas estables y susceptibles de ser transferidas a soportes sólidos. Los colorantes y lípidos tendrán carga opuesta y de esta manera, mediante interacciones atractivas entre ellos, se controlará la organización lateral del sistema, así como la auto-agregación de los emisores mediante un balance adecuado entre el tamaño de los grupos hidrofóbicos y los grupos polares. La organización molecular en estas monocapas se investigará mediante técnicas espectroscópicas y microscopía.
2. Transferencia de las películas formadas en la interfase aire-agua, manteniendo su organización, a distintos tipos de soportes sólidos (vidrio, cuarzo e ITO) mediante las técnicas de deposición vertical, Langmuir-Blodgett, y horizontal, Langmuir-Schaeffer, tanto en monocapa como en multicapas de igual o diferente naturaleza, controlando en este último caso la distancia entre los grupos funcionales. La caracterización de las películas transferidas se realizará haciendo uso de técnicas espectroscópicas.
3. Análisis de la organización molecular de las estructuras bidimensionales formadas, así como de su influencia sobre las propiedades ópticas y de transferencia de carga de los emisores empleados. Se realizarán medidas de transferencia de energía entre componentes fijados en películas organizadas,

bien coexistiendo en la misma monocapa, o bien situados en diferentes monocapas (transferidas de forma alterna sobre el mismo soporte), modificando tanto la distancia de separación como la orientación y agregación de donador-aceptor. Estas medidas se llevarán a cabo mediante diversas técnicas espectroscópicas.

4. Diseño, fabricación y estudio de dispositivos optoelectrónicos tales como diodos orgánicos (OLEDs) o células electroquímicas iónicas (LECs), así como dispositivos fotovoltaicos (células solares). La preparación de las películas que conforman el dispositivo tendrá lugar mediante técnicas superficiales como Spin Coating o Meniscus Coating. Una vez conseguidos dispositivos sencillos basados en estas películas, se someterán a modificaciones en su estructura con el fin de mejorar la eficiencia del dispositivo, mediante la inserción de otras capas con funciones concretas. Con este objetivo, se estudiará la viabilidad de fabricación en tándem, el estudio de la capa generadora de carga (CGL) que interconecta las diversas unidades, así como el estudio de nuevos materiales. El funcionamiento, eficiencia y longevidad de los dispositivos fabricados se valorarán mediante espectroscopía de fluorescencia y electroluminiscencia, así como curvas  $L-I-V$  y curvas  $L-I-t$  (en dispositivos electroluminiscentes) o curvas  $(J - V)$  y conversión fotoeléctrica incidente (IPCE) (en células solares).

*Nothing in life is to be feared, it is only to be understood. Now is the  
time to understand more, so that we may fear less.*

Marie Curie

*Science is the great antidote to the poison of enthusiasm  
and superstition.*

Adam Smith





## Abstract

The evolution of technology has to meet the energetically needs of actual societies and be respectful for the environment through a sustainable and efficient use of energy. In this context organic electronic represents a promising technology. Organic semiconductors are abundant, easy to fabricate and their properties can be easily tuned. In the form of thin films, they exhibit interesting electronic and magnetic properties, which in many cases result from the specific molecular organization and interactions of their components. A low cost organic alternative to the classical lighting systems are the light-emitting electrochemical cells (LECs). They require only one ionic emitting layer, are processed at ambient conditions and are compatible with air stable electrodes, avoiding rigorous encapsulation in inert atmosphere. Recently, LECs have shown high luminance, high efficiencies and relatively high stabilities when specific emitters were used. However, their slow response, their self-limiting nature and the absence of efficient white light emission, remain the limitations preventing their application in general lighting. On the other hand, organic thin films can also be used in photovoltaics, which represents an abundant and low cost alternative to the silicon established solar cell technology. Nevertheless, their record efficiency ( $\sim 12\%$ ) is still below the requirements for a massive application. This suggests the need of new materials and configurations to achieve efficiencies close to those obtained in inorganic Si-cells (20 - 25%) but reducing the manufacturing costs.

In this Thesis, thin films are studied from two different points of view: as organized ultra-thin systems containing UV-Vis absorbing molecules, frequently used in many optoelectronic devices; and as interlayers in LECs and OPV devices. In the first case, two superficial techniques, the Brewster Angle Microscopy and the UV-Vis Reflection Spectroscopy, are studied in order to obtain useful information from such highly organized systems. A new detailed description of the theoretical treatment needed for each technique is presented, which provides, through a relatively simple

method, structural information of the molecules and their interactions in the monolayer, such as the molecular aggregation, tilt angle and position of those absorbent groups. Additionally, we have studied the influence of specific thin films in LECs and OPV as key components to overcome some of the main limitations of these devices. Hybrid organic-inorganic LECs are proposed as a possible alternative to avoid the large turn-on times usually observed in such devices, by changing the injection barrier at the electrode interfaces. The incorporation of air-stable metal oxide interlayers is shown to be useful for obtaining LECs with high luminances, high efficiencies and instantaneous switching. Additionally, such interlayers are suitable for the preparation of simple tandem structures, where a metal/metal-oxide interlayer is enough to interconnect electrically both units without the requirement of complex charge generation layers (CGL), leading to the first efficient white tandem-LEC.

Finally, organic thin layers are proposed as effective blocking components in hybrid organic-inorganic perovskite based solar cells (PSC). The use of an electron blocking polymer and a hole blocking molecular material are shown to improve substantially the performance of the cells. The combination of this new and highly efficient hybrid organic-inorganic perovskite material with a suitable organic architecture seems to present advantages from both organic and inorganic materials, enabling the preparation of very efficient flexible or semitransparent devices.

# Contents

<b>Abstract</b>	<b>21</b>
<b>Introduction</b>	<b>27</b>
1.1 Organic thin films	29
1.2 Thin film formation techniques	32
1.2.1 Physical control on the molecular organization	
1.2.2 Techniques with low control on the molecular organization	40
1.3 Thin films in optoelectronics: Light emitting and photovoltaic devices	43
1.3.1 Some fundamentals	45
Carrier injection/extraction at the organic/metal interface	46
Charge carrier transport	48
Charge blocking effect	49
1.3.2 Light emitting electrochemical cells (LECs)	50
Operation mechanism: Dynamic Interlayers	51
State-of-the-art LECs and challenges	53
1.3.3 Thin film solar cells	55
A hybrid organic-inorganic material:	
Methylammonium lead iodide perovskite ( $\text{CH}_3\text{NH}_3\text{PbI}_3$ )	57
Challenges and outlook	60
1.4 About this work	62
References	65

<b>Experimental: Methodology and characterization techniques</b>	<b>79</b>
2.1 Organized thin films	81
UV-Vis Reflection Spectroscopy	82
UV-Vis-va Reflection Spectroscopy	83
Brewster Angle Microscopy (BAM)	83
2.2 Thin films in optoelectronics	84
Light emitting electrochemical cells (LECs)	85
Photovoltaic devices	87
References	90

## **Results & Discussion**

<b>Physical control of thin films at the air-water interface</b>	<b>95</b>
3.1 Revisiting the Brewster Angle Microscopy:	
The relevance of the polar headgroup	97
3.1.1. Introduction	98
3.1.2. Theoretical model	101
3.1.3 Optical behavior at the air/water interface of octadecyl rhodamine B (C <sub>18</sub> RhB). Scenario IV	107
3.1.4 Inversion of reflectivity during a BAM experiment. Segregation of lipid in the mixed monolayers with an organometallic complex Ir-dye/DMPA. Scenarios I and II	108
3.1.5 Quantitative assessment of the molecular arrangement of the polar headgroups. Inner textures within the domains: aniso- tropy caused by the coherent organization of polar groups	112
3.1.6 Conclusions	120
3.1.7 Outlook	122
References	126

3.2 UV-Vis reflection spectroscopy under variable angle incidence at the air–liquid interface	131
3.2.1 Introduction	132
3.2.2 Experimental	134
3.2.3 Theory	135
3.2.4 Experimental results	144
3.2.5 Conclusions	153
Appendix	154
References	156
3.3 Molecular organization and effective energy transfer in iridium metallo-surfactant–porphyrin assemblies embedded in Langmuir–Schaefer films	163
3.3.1 Introduction	164
3.3.2 Experimental	165
3.3.3 Results and discussion	168
3.3.4 Conclusions	181
References	183
<b>Thin films in LECs. Dynamic and static interlayer</b>	<b>187</b>
4.1 Engineering charge injection interfaces in light-emitting electrochemical cells	189
Supporting Information	198
References	199
4.2 Dynamically Doped White Light Emitting Tandem Devices	201
Experimental Section	209

Supporting information	211
References	212
<b>Thin film high efficient solar cells</b>	<b>215</b>
5.1 Perovskite and organic blocking layers: a versatile solar cell configuration.	217
5.2 Flexible high efficiency perovskite solar cells	225
Conclusions	232
Supporting Information	232
References	236
5.3 High efficiency single-junction semitransparent perovskite solar cells <sup>239</sup>	
Conclusions	250
Supporting Information	251
References	258
<b>Overview of the main results</b>	<b>263</b>
<b>Conclusions &amp; Outlook</b>	<b>281</b>
<b>Resumen en castellano</b>	<b>289</b>
<b>Publications used for this Thesis</b>	<b>295</b>
<b>Other contributions during this Thesis</b>	<b>297</b>

# **Chapter 1**

## **Introduction**





# 1. Organic thin films

Technology involves the manipulation of the environment to meet human needs such as food, shelter, health and communication. In the last 10,000 years the development of various technologies affected societies facilitating their adaptation to the environment. Nevertheless, in the last centuries, technology has experienced one of the most impressive advances in human history. Since the Industrial Revolution and the later development of the electricity and artificial lighting, our society experienced the change to an industrialized system, where a new way of communication was emerging with the development of trading. New advances in the knowledge of basic sciences, such as physics and chemistry, laid the foundations for modern science and technologies, followed by the establishment of energetic supplies. The radio, the radar, the telephone or the magnetic storage of data were the first evidences of the modern society that was germinating in the early 20<sup>th</sup> century. Nowadays we have mobile telephones and laptops, we can move to every corner of the planet or be connected via internet in real time, we can listen to music or watch a film with very thin and light displays or take electrical energy from portable light batteries. Technology is so introduced in our lives that we do not consider it special; it is an integral part of our daily routine. However, the unsustainable increase in the use of energy, together with a very large impact of many industrial processes on the environment, is playing an important role in the present level of contamination. Additionally, some of these technologies require the use of very expensive and limited mineral resources, limiting their global accessibility. It urges a change in both the consumption and production of energy, which suggest the search for new environmental friendly alternatives.

Organic materials constitute a promising alternative to the actual limited inorganic sources as they are abundant, easier to fabricate and reasonably cheap. Specifically, organic thin films, which consist on molecularly engineered layers with a thickness between 1 nm to a few micrometers, depending on the materials and their

application,<sup>1</sup> have become increasingly important in the last decades because of their technological potential.

One of the major applications of thin films consists on the modification of the surface properties of solids in a cost effective way, finding as well applications in microelectronics and magnetic media due to their unique properties in the polarization, reflection, transmission and absorption of light. Some common examples are scratch-resistant coatings for spectacles or anti-reflection coatings for lenses. Nevertheless, organic thin films, specifically organic semiconductors, also present other inherent properties that are used in microelectronics, magnetic or optical recording media<sup>2</sup> and have led to the birth of a new technology called Organic Electronics. Compared to traditional inorganic semiconductors like silicon or gallium arsenide, organic semiconductors are lightweight, flexible and can be easily manufactured by low cost processes, enabling the fabrication of a wide range of low cost electronic devices.

One of the main discoveries that allowed the development of such a technology took place at the end of 1970's when Alan G. McDiarmid, Alan J. Heeger, and H. Shirakawa discovered the electrical behavior of organic conjugated  $\pi$  systems, enabling the rise of "conducting polymers". Although some of these materials were already known, their fabrication as thin films allowed further development and deeply research on their properties.<sup>3,4</sup> During the following years, new interpretations about the transport and doping processes in such organic systems founded the bases for organic electronics,<sup>5,6</sup> and the first organic light emitting diodes (OLEDs) were finally fabricated at the end of 1980's.<sup>7,8</sup> Alternatively, the success of OLEDs soon stimulated related technologies, such as organic photovoltaics (OPV) or organic transistors, which had already been demonstrated in 1970's.<sup>9-12</sup> Since then, a big deal of progress has been made in the understanding of the physical processes that governs the operation of these devices. Additionally, an enormous effort has been focused on the development of organic synthesis to produce materials with qualities adapted to the needs of this new area.<sup>3,13</sup> As a result, in the past two decades, the science and engineering of organic semiconducting materials have led to the optimization of a

range of organics-based solid-state devices, including organic light-emitting diodes (OLEDs),<sup>14</sup> field-effect transistors,<sup>15,16</sup> photodiodes,<sup>17</sup> and photovoltaic cells.<sup>18</sup>

One of the reasons why thin films show so promising technological potential is based on the fact that their physical properties may be very different from those of the bulk material, particularly if the thickness is very small. Thin films can exhibit peculiar properties mainly due to the nano-scale dimensions and the morphology of the layer.

Indeed, due to the high surface-to-volume ratio, thin films exhibit more “surface” dependent material properties. Thus, the physicochemical processes at the interfaces gain a huge importance in most of the organic thin films applications. Interfaces between a metal and an organic material or between two types of organic materials possess unique and useful electronic properties that are very interesting for fundamental studies and technological applications. Such electronic properties are the basis for several emerging technologies, including organic electronics or also biotechnology,<sup>19</sup> and their viability depends crucially on our ability to control and tailor those interfaces at the molecular scale. Focusing on organic electronics, the interface between thin films may give rise of new collective effects that the individual materials do not exhibit, emerging for instance, new electronic states at the interface,<sup>20</sup> interface-localized electron-hole pairs<sup>21,22</sup> or very different transport properties on adsorbed molecular ensembles respect to the isolated molecules.<sup>23,24</sup> Understanding, controlling and designing the electronic and optical properties at these interfaces is basic for the improvement of the actual and the nascent electronic technologies.

Nevertheless, not only the interface phenomena, but also the specific composition and morphology of the thin film can be responsible of unique electronic and magnetic properties, which are not present at the molecular level. These properties can emerge from collective effects among the molecules that form the system. One example of this effect is the alteration on the optical properties of thin films due to the special interaction between molecules, related with its organization in the film.<sup>25,26</sup> Another example was observed by Naaman and Vager,<sup>27</sup> who detected spin selective

electron transmission through a self-assembled monolayer (SAM) at inorganic/organic interfaces, behaving as spin filter as a consequence of the organic film organization. Morphology changes have also been related with different charge carrier mobilities in organic solar cells<sup>28,29</sup> or with different recombination rates depending on the active layer nanostructure.<sup>30-32</sup>

Thus, the developing and improvement of the current and new optoelectronic technologies should consider the nano-engineering of thin films. The ability of preparing good quality films, with a specific organization, and its controlled deposition on a specific material is crucial for the understanding of the physical processes that takes place in such basic systems. For this reason scientific and technological effort has become increasingly more intense in the set-up of new strategies, not only able to control the morphology but also enabling process scale-up for large scale production.

## **1.2 Thin film formation techniques**

There are different methods and techniques to fabricate thin layers which differ in complexity and in the resulting characteristics of the provided films: thickness, morphology, uniformity or even crystallinity.<sup>33</sup>

From a fundamental point of view, the processes that occur during the film formation will determine the morphology of the layer. Thus, the deposition techniques can be classified according to the grade of control on the molecular organization. We can find deposition techniques extensively used in the microelectronics industry that have a very few control on the film organization, such as spin-coating, sputtering or thermal vapor deposition; other techniques allow to have an intermediate control, such as chemical vapor deposition or meniscus-coating; and finally, there are techniques which allow to obtain well organized monolayers or multilayer structures such as

Langmuir-Blodgett, Chemical Self-Assembly or Electrostatic Layer-by-Layer Deposition.

Another important consideration for commercialization implies the assessment about the cost of the fabrication process or whether the method can easily be adapted to continuous coatings, such as direct printing methods and roll to roll (R2R) processing.

In the following text only those techniques for building thin films which are relevant to this Thesis will be described.

### **1.2.1 Physical control on the molecular organization**

#### **Langmuir monolayers**

A Langmuir monolayer consists on an insoluble spread monolayer of atoms or molecules (that is a single, closely packed layer) floating at the liquid-gas or at the liquid-liquid interface. In the case of organic monolayers, its formation is possible due to the forces of self-assembly existing between the insoluble molecules at the surface of a liquid, as suggested by Irwing Langmuir in the late 1910's. Nowadays these thin films are intensively studied and represent one of the most useful techniques for building new supra-molecular structures and devices with applications in very different areas such as non-linear optic sensors, molecular electronics, photochromism or even molecular biology, by modeling biological systems such as lipid membranes or immunological systems.<sup>34-43</sup>

The most common Langmuir films consist on amphiphilic monolayers prepared at the air-water interface in the so called Langmuir trough. When molecules possess both hydrophobic and hydrophilic parts and they are spread on an air-water interface, they may orientate themselves in a predictable way, forming a monolayer which extends through the entire free surface at the air-water interface.<sup>44</sup>

Due to the presence of the monolayer, the surface tension at the interface ( $\gamma$ ) decreases compared to the clean water ( $\gamma_0$ ). It is then useful to introduce a new parameter called *surface pressure* ( $\pi$ ), which is defined as:

$$\pi = \gamma_0 - \gamma \quad (1.1)$$

If the monolayer is compressed reducing the interface area by a mobile barrier, the molecular density increases, leading to a change in the surface pressure, which can be related with a change in the organization and morphology of the molecules. The graphical representation of  $\pi$  versus the molecular area ( $A_m$ ) at the air-water interface at constant temperature is called  $\pi$ - $A$  isotherm, and it contains information about the stability, organization and interactions between molecules in the monolayer.

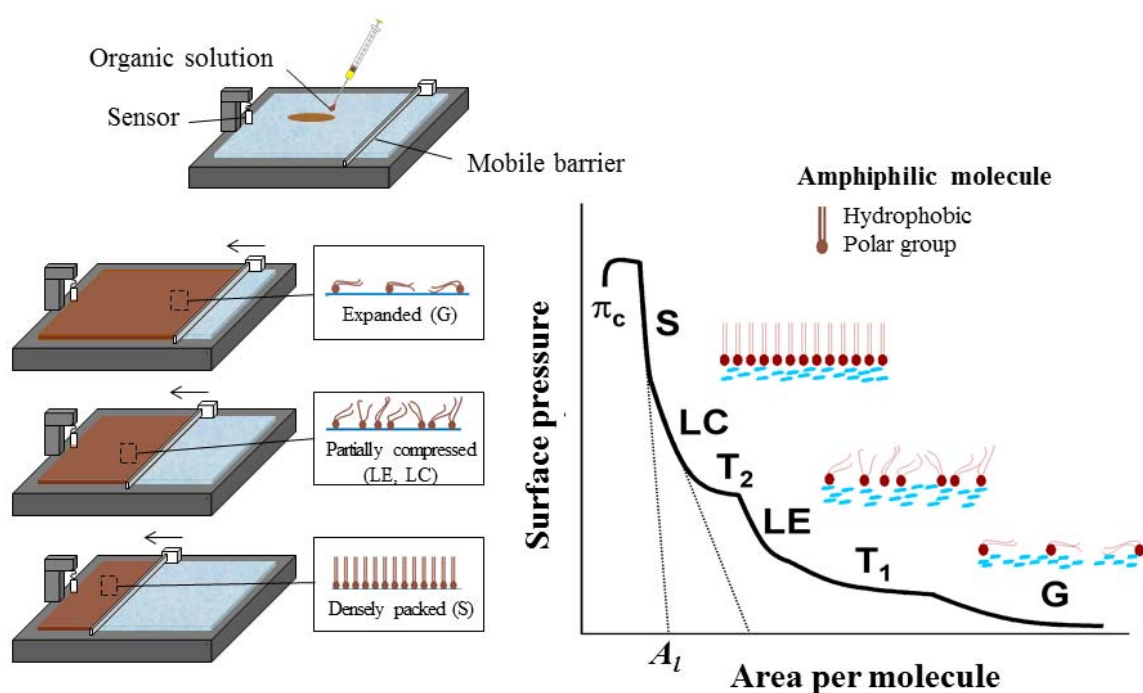


**Fig. 1.1.** Left: Langmuir trough with a spread Langmuir monolayer. Right:  $\pi$ - $A$  isotherm obtained during the compression process of the monolayer.

The  $\pi$ - $A$  isotherm contains different regions related with different phases of the monolayer (ideally they are gas (G), expanded liquid (EL), compressed liquid (CL) and solid phase (S)),<sup>44</sup> as well as transition zones (Ti) where the system changes phase.

The number and complexity of the phases depend on the intermolecular interactions and the experimental conditions used. When the system reaches the maximum compression in the monolayer it starts collapsing, experimenting more complex processes such as its breaking or the formation of multilayer regions. This process is called “collapse” and the surface pressure is called “collapse pressure” ( $\pi_c$ ). Another important parameter is the limit value of the molecular area ( $A_l$ ) which is obtained by extrapolation of the region with the highest slope in the  $\pi - A$  isotherm to  $\pi = 0 \text{ mN m}^{-1}$ . The Langmuir trough and the compression process are represented in Fig. 1.1.

Nowadays, a huge variety of molecules can be used in the preparation of these thin films, including not only amphiphilic but also semi-amphiphilic, macromolecules such as polymers or even molecules that are soluble in water, by using the specific intermolecular interaction existing in the system. All these methods open up amazing possibilities for further controlling the architecture of monolayers and creating new properties which may be tunable through controlling the packing density and the extent of neighbor-neighbor molecular interactions.

## **Characterization techniques**

There is a large variety of techniques used to characterize the Langmuir monolayers at the air-water interface. In the following subsections the most relevant techniques for the work described in this Thesis are highlighted.

### **Reflection Spectroscopy**

Reflection Spectroscopy is based on the change in reflectivity ( $\Delta R$ ) at the air-water interface when it is covered with a Langmuir monolayer, compared with the reflectivity in the absence of monolayer. Fig. 1.2 shows a schedule of the process.

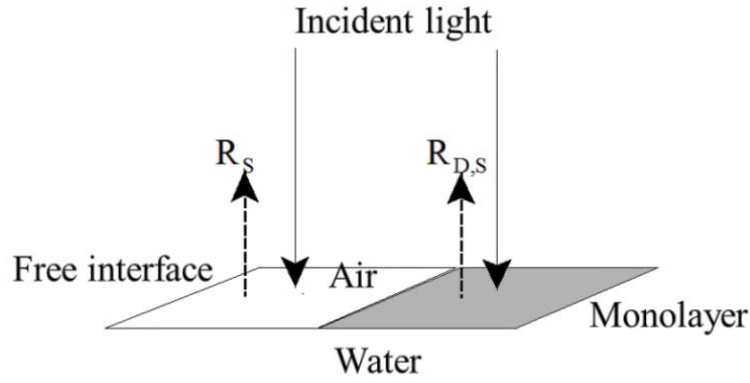


**Fig. 1.2.** Reflection process at the air-water interface.

The reflectivity ( $R$ ) at the air-water interface is defined as the ratio between the reflected light and the initial incident light.<sup>45</sup> This ratio depends on several parameters such as the polarization of the incident light or the incident angle respect to the normal of the interface. On the other hand, the reflectivity of a monolayer is also related with its capacity to absorb light. The magnitude of an electronic absorption band is determined by the so called “oscillator strength”,<sup>46</sup>  $f$ , which is a parameter that relates the total absorption of a band with the absorption of the equivalent classic oscillator:

$$f = \frac{4\varepsilon_0 2.303 m_e c_0}{N_A e^2} \int_{band} \varepsilon d\nu = 1.44 \times 10^{-19} \int_{band} \varepsilon d\nu \quad (1.2)$$

where  $\varepsilon$  is the molar absorptivity ( $\text{mol} \cdot \text{L}^{-1} \cdot \text{cm}$ ),  $\varepsilon_0$  is the vacuum permittivity ( $\text{Cul}^2 \cdot \text{s}^2 \cdot \text{Kg}^{-1} \cdot \text{m}^{-3}$ ),  $m_e$  and  $e$  are the mass (kg) and the electrical charge of an electron (Cul),  $c_0$  the speed of light in vacuum ( $\text{m} \cdot \text{s}^{-1}$ ) and  $N_A$  the Avogadro number (molec/mol). Electronic transitions allowed by the spectroscopic selection rules will lead to values of  $f \approx 1$ , while those that are not allowed will lead to values of  $f \ll 1$ .

Let us consider a non-polarized incident light, perpendicular to the interface. When the magnitude of absorption and reflection is low enough, the following approximation holds:<sup>47</sup>

$$R_{D,S} = R_S + R_D + A\sqrt{R_S} \quad (1.3)$$



$R_S$  and  $R_{D,S}$  being the reflectivities of the interface in the absence and presence of the monolayer respectively,  $R_D$  the reflection due to the monolayer by itself and  $A$  the absorption of the monolayer. As can be deduced from this expression, there is an increase in the reflectivity due to an absorption in the monolayer, which is assumed in the term  $A\sqrt{R_S}$ . Additionally,  $R_D \approx A \times A_M/4$ ,  $A_M$  being the maximum absorption of the monolayer. Thus, the difference in reflectivity ( $\Delta R$ ), which is obtained directly from the experimental measurement, can be expressed as:

$$\Delta R = R_{D,S} - R_S = A \left( \sqrt{R_S} + \frac{A_M}{4} \right) \approx A\sqrt{R_S} \quad (1.4)$$

where the term  $A_M/4$  can be neglected as the absorption of a monolayer is normally very small. Additionally, taking in consideration the relation between absorption and absorbance, we can deduce the final expression for the reflectivity to be:

$$\Delta R = 2.303 \times 10^3 \times f_0 \varepsilon \Gamma \sqrt{R_S} = \frac{2.303 \times 10^{17}}{N_A S} \times f_0 \varepsilon \sqrt{R_S} \quad (1.5)$$

where  $\Gamma = 10^{14}/(N_A \cdot S)$  is the surface concentration ( $\text{mol} \cdot \text{cm}^{-2}$ ), which depends on the area per molecule  $S$  ( $\text{nm}^2/\text{molecule}$ ), and  $f_0$  is the orientation factor, which takes into account the change in the averaged transition dipole of the molecules when they move from solution to the interface.<sup>48</sup>

By combining Eqn 1.2 and 1.5 it is possible to obtain the value for the oscillator strength of the monolayer by integrating the measured reflection band:

$$f = \frac{1.44 \times 10^{-19} N_A}{2.303 \times 10^{17} f_0 \sqrt{R_S}} \int_{band} \Delta R \times S \, d\nu = \frac{2.6 \times 10^{12}}{f_0} \int_{band} \Delta R^N \, d\nu \quad (1.6)$$

In this expression  $\Delta R^N = \Delta R \times S$  takes into account the increase on  $\Delta R$  when compressing the monolayer due to a change in  $S$ , avoiding its influence during compression. Thus, if  $\Delta R^N$  decreases when compressing the monolayer, it can be

explained by two different phenomena: the loss of some molecules to the subphase, or a reorientation of the molecules in the monolayer. As a consequence, assuming no loss of molecules to the subphase, Eq. 1.6 allows the evaluation of changes in the orientation of the transition dipole with the compression of the monolayer, thus obtaining information about their organization.

### Brewster Angle Microscopy (BAM)

This technique is based in the polarization induced by reflection that takes place when an incident non-polarized radiation is refracted at an interface between two materials ( $n_1$  and  $n_2$ ) with a refracting angle perpendicular to the incident light. Under such conditions, if the refractive indexes of both materials are  $n_1 < n_2$ , the parallel component of the electric field (p-) in the reflected light is zero, or equivalently, the reflected light is s-polarized, and the incident angle is called Brewster Angle ( $\theta_B$ ). The value of  $\theta_B$  can be calculated by using the Snell's law:

$$\tan \theta_B = n_2/n_1 \quad (n_2 > n_1) \quad (1.7)$$

The air-water interface presents a value for  $\theta_B = 53.1^\circ$ . Experimentally, the BAM technique uses a p-polarized light that affects the air-water interface at  $53.1^\circ$ , so the reflected light is zero. Nevertheless, when a monolayer is spread at the same air-water interface, a new interface between air-monolayer will appear, with  $n_1 = n_{\text{air}}$  and  $n_2 = n_{\text{monolayer}}$ , modifying slightly the  $\theta_B$  value, thus reflecting a low part of the radiation at an incident angle of  $53.1^\circ$  (see Fig. 1.3).

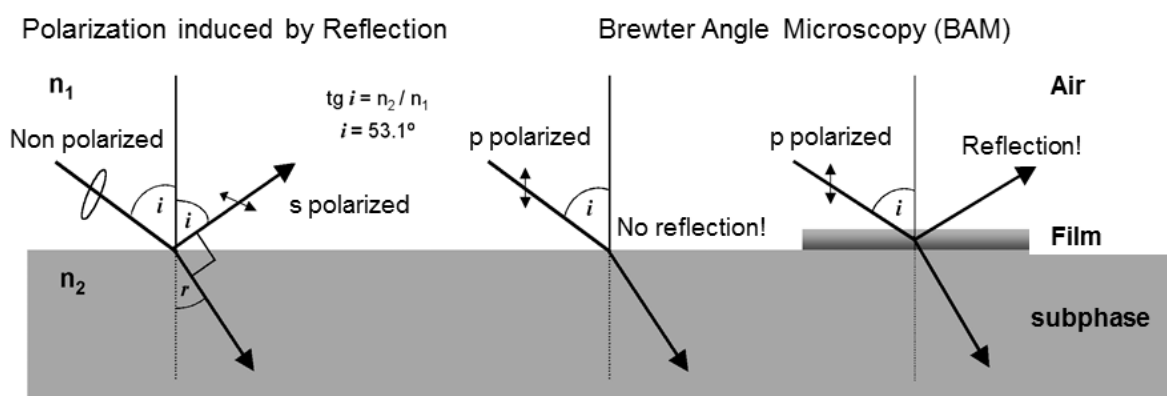


**Fig. 1.3.** Physic principle for Brewster Angle Microscopy (BAM).

As a consequence, the reflected radiation is originated directly from the monolayer. Moreover, organic monolayers are often anisotropic films, showing different polarizabilities depending on the direction (parallel or perpendicular) respect to the molecule axes (so different refractive indexes  $n_x$ ,  $n_y$ ,  $n_z$ ). Under these conditions, by using a special detector (camera), the BAM technique can be used to obtain information about the changes in the morphology of the film during its compression, allowing the direct observation of the optical anisotropy existing inside the monolayer domains.

## Langmuir Blodgett and Langmuir-Schaefer techniques

There are several techniques to transfer the monolayer from the air-water interface to a solid substrate<sup>49-51</sup> but the most popular methods are the Langmuir-Blodgett (LB) and the Langmuir-Schaefer (LS) depositions.<sup>34,35,52-54</sup> These two methods differ basically in the orientation between substrate and monolayer during the transference. Thus, LB consists of a vertical deposition technique, where the monolayer and the substrate are perpendicular between them. During the transference, the substrate crosses slowly the interface and the monolayer starts transferring to it. Depending on the initial phase (air or water) from which the substrate starts moving, the monolayer is transferred with the hydrophobic or hydrophilic region close to the

solid substrate. On the contrary, the LS technique is based on a horizontally deposition where both monolayer and substrate are parallel to each other. Once the substrate touches softly the interface it moves out, carrying with it a deposited monolayer. In Fig. 1.4 it is shown both processes in more detail.

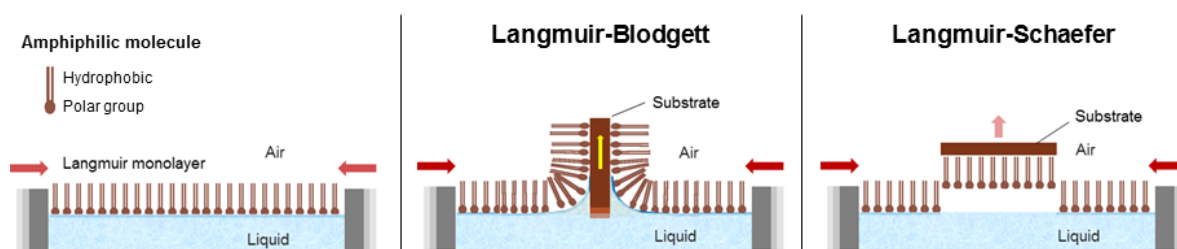


**Fig. 1.4.** Langmuir Blodgett and Langmuir Schaefer transference processes.

In order to quantify the effectiveness of the transference it is useful to define the *transference ratio* ( $\tau$ ) as the ratio between the area of the monolayer lost due to the transference and the area of the covered substrate,  $\tau = A_L/A_S$ . For an ideal transference  $\tau=1$ , which means that the 100% of the substrate has been covered.

The films obtained can be highly organized ranging from an ultrathin monolayer to multilayer structures built up of hundreds of monolayers and combining different properties. These properties, together with the precise control of the monolayer thickness and the homogeneous deposition, make it a very suitable technique for preparing organized thin films.

## 1.2.2 Techniques with low control on the molecular organization

### Spin coating

This technique is a widespread practice in modern science and engineering.<sup>55,56</sup> The various steps involved in the process are illustrated in Fig. 1.5(a). A quantity of solution is first placed on a planar substrate, which after some seconds is rotated at a fix speed of several thousand revolutions per minute. As the substrate rotates, the

solution flows radially outwards reducing the fluid layer thickness, leading to uniform and homogeneous films after the evaporation of the solvent. The main parameters that determine the final thickness and quality of the films are the viscosity and density of the solution, the rotating speed (r.p.m.), as well as the temperature during the process. It is a relatively high reproducible technique, fast and easy to use, as well as very cheap compared to other alternatives. Nevertheless its discontinuous character and the appearance of film imperfections due to non-perfect substrate wetting, makes it not so desirable for industrial applications.

### **Meniscus coating**

In this technique capillary forces are used to place a volume of the solution in between the substrate and the bottom of a flat blade (~ 3 by 20 mm) with a very small gap (< 0.2 mm) between them. The drop is maintained within the gap creating the so called meniscus, which is stretched when moving the blade over the substrate, leaving behind a thin film of the organic material.<sup>57</sup> The resulting dry film thickness is primarily determined by the drawing speed of the blade and its distance to the substrate, as well as the solution parameters such as density, viscosity and contact angle. Uniform coating thicknesses can be obtained without the need for precise mechanical specifications or adjustments.<sup>58</sup> The entire process is illustrated in Fig. 1.5 (b).

In a lab-scale meniscus coater the deposition implies a discontinuous method, but it can be easily adapted to a continuous process for industry.<sup>59</sup> This technique allows the preparation of reproducible films, with homogeneous thicknesses as thin as 20 nm by using few amounts of solution (~ 1-2.5  $\mu\text{L cm}^{-2}$  compared to ~ 15-20  $\mu\text{L cm}^{-2}$  in spin-coating, depending on the material). Moreover, as it is less aggressive than spin-coating, it becomes a suitable technique for carrying on sequential deposition, which is of crucial importance for preparing multilayered systems. All these characteristics make meniscus-coating one of the most versatile and simplest technique for thin film deposition.

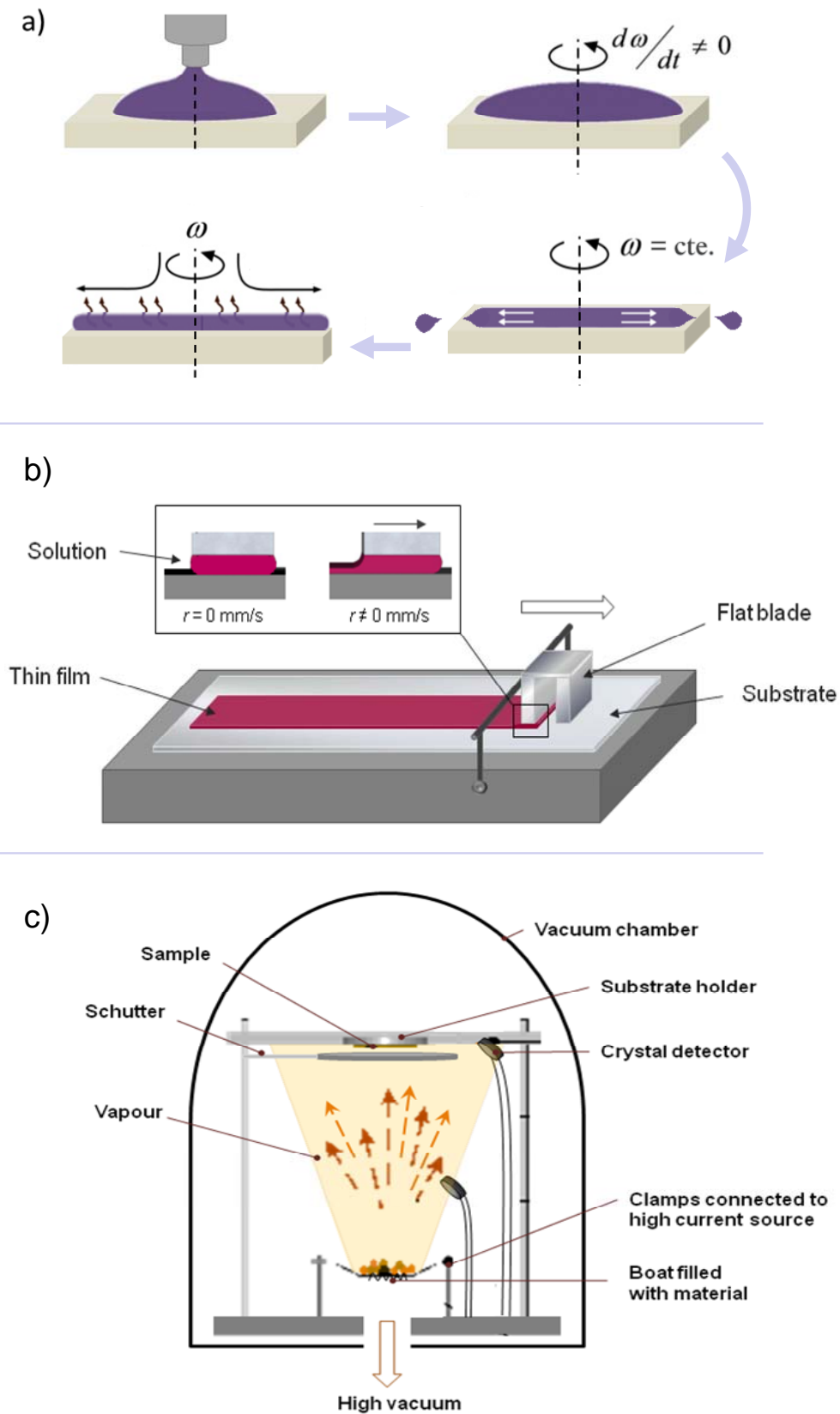


**Fig. 1.5.** a) Diagram of the steps involved in the spin-coating process; b) Illustration of the meniscus-coater technique before moving the blade ( $r = 0$  mm/s) and after moving the blade ( $r \neq 0$  mm/s); c) Resistive thermal-vapor deposition technique.

## **Thermal vapor deposition: inorganic and organic molecular evaporation**

The vapor deposition process takes place normally inside an ultra-high vacuum evaporator, which reaches values of pressure between  $10^{-4}$  -  $10^{-6}$  mbar. The vacuum chamber consists on a metallic or glassy chamber, where the samples are located on a sample holder, normally situated in the upper part. Below the sample holder it is situated the evaporating material, located in a thermal source from where it will firstly sublime and secondly condensate onto the solid substrate. To control the rate during the evaporation and thus the deposited thickness, several film thickness sensors based on oscillating quartz crystals are normally located inside the vacuum chamber, close to the substrate and the thermal source. Fig. 1.5 (c) shows a schedule diagram about the process.

This technique allows the deposition of inorganic and low molecular weight organic materials (metals and their alloys, fullerene...). Nevertheless, one of the most interesting approaches is the dual source evaporating process, which allows the co-evaporation of different materials during the same deposition. As a result, it is possible to carry on a sequential deposition free of contaminants, a doping process to modify some material's properties or even the formation of a new material by chemical reaction between precursors. Nevertheless the high cost of the process, the waste of material and its discontinuous character, are their main disadvantages.

### **1.3 Thin films in optoelectronics:**

#### **Light emitting and photovoltaic devices**

Nowadays, saving energy and reducing the greenhouse gases is being the main objective for new technologies, becoming one of the main challenges for sustaining the energy demand from developed and developing countries. For this purpose, it is necessary to combine the efficiency with low cost technologies, making them more easily accessible. In this context, organic semiconductors offer many advantages as

they can be really cheap, they allow the fabrication of light-weight and very thin devices, their electrical and optical properties can be easily tuned and they can be solution processed on flexible and large-area substrates.<sup>60,61</sup>

Organic optoelectronic devices are often based on one or more thin films of an organic semiconductor sandwiched between two inorganic electrodes, as it is shown in Fig. 1.6. The cathode is normally based on a metal or an alloy of metals (Al, Ca, Li-Al, Mg-Ag...) with a low work function, while the anode presents a high work function and normally is transparent to the visible light (such as indium tin oxide (ITO) or fluorine doped tin oxide (FTO)) to allow the incoming/ outgoing of light through the device. The design of suitable device architectures, as well as the use of appropriate materials, would considerably affect the performance of these devices.

Interlayers inside the device can adopt very different roles, conditioning the injection/extraction of carriers (electrons and holes) at the electrode interfaces, their transport inside the device or even a desirable charge blocking effect specific for one type of carrier. In the case of light emitting or photovoltaic devices, the recombination/separation of charges also takes place in a thin film or between two thin films (called active layer or active interface), to produce the desirable light or electrical current respectively. Although sometimes the same material can play several roles, a breakthrough in terms of improved performance was achieved when the charge transport inside the device was better controlled by introducing multilayer structures<sup>62-64</sup>

A special case is provided by the tandem structure, which combines two individual devices one on top to the other, joined through an intermediate layer that connects physically and electrically both units in a single architecture. In such structures, the intermediate layer has to compensate the carriers generated in both single devices by supplying electrons to one unit and holes to the other. For that reason it is called “charge generation layer” (CGL) and nowadays is being the focus of an important amount of research.<sup>65-67</sup>



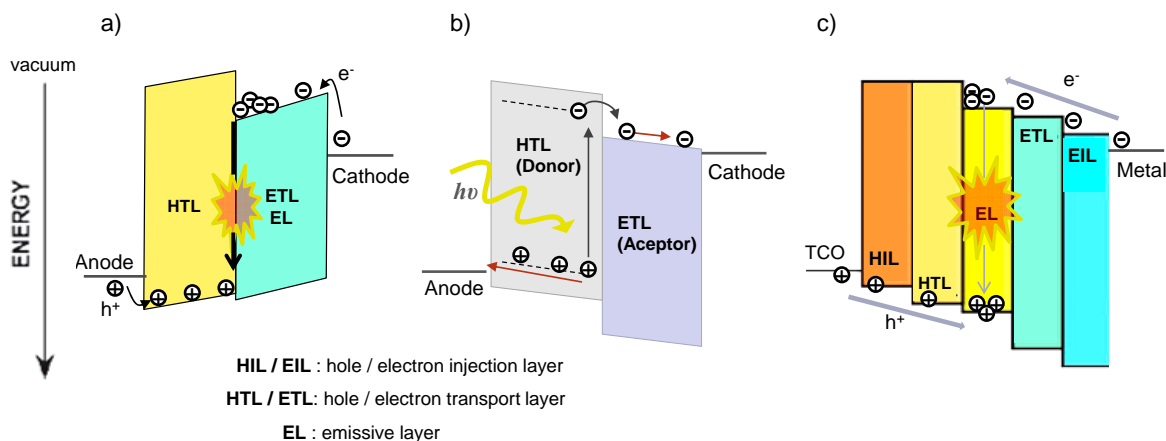


**Fig. 1.6.** Example of a bilayer OLED (a) and a bilayer solar cell (b), where the active layer behaves both as charge transporting and as emissive/photoactive material respectively. Figure (c) shows a multilayer structured OLED (right). The incorporation of charge transporting materials (HIL, HTL, EIL and ETL) facilitates the injection and transport of the carriers when the injection barriers are high.

### 1.3.1 Some fundamentals

Organic materials useful for some optoelectronics behave often as insulators under a low electric field. Nevertheless, the chemical doping and/or the formation of ultrathin organic films provide a possible way to produce organic semiconductors.

In the following text an overview of the fundamental models will be given, describing the injection and transport in organic materials. The principles are discussed only for injection of electrons but it can be adapted for hole/electron injection or extraction. Nevertheless, each metal/semiconductor interface presents different chemical interaction and inherent material's properties, being necessary to analyze each system case-by-case.<sup>68-70</sup>

## Carrier injection/extraction at the organic/metal interface.

When a metal and a semiconductor (with different work functions,  $\Phi_m$  and  $\Phi_s$  respectively) are placed in contact, there is a redistribution of electrons from one material to the other. These transferred electrons accumulate at the interface, leaving behind them an electron-depleted region with uncompensated positively-charged donor positions (which is called *the image force*). The generated space-charge separation leads to a contact potential ( $V_o$ ) at the interface, which, once the equilibrium is reached, prevents further net electron diffusion through it. As a consequence, the energy bands at the region close to interface bends, leading to the appearance of a potential barrier which is called the “Schottky barrier height” ( $\Phi_B$ ). This parameter is related with the energy barrier that electrons may overcome to cross the interface and is ideally proportional to the difference between the metal-vacuum work function ( $\Phi_m$ ) and the semiconductor-vacuum electron affinity ( $\chi$ ) [Ref]. Nevertheless in real interfaces it can be unpredictable due to the specific chemical interactions between metal-semiconductor and impurities at the contact. As a consequence of the bending, the energy necessary for electrons to cross the metal-semiconductor interface would depend on the direction of the flow, leading to the so-called Schottky rectifier behavior. (See Fig. 1.7.a).

Not all the metal-semiconductor interfaces lead to rectifying contacts, as the Schottky barrier can be very low allowing the injection to take place. If under the application of an electric field the barrier height at the interface is high enough, the transport capability at the organic layer can be faster than the charge injection at the electrode, leading to an *injection limited current*. There are two main models to describe the injection in such conditions, which are the *Schottky thermal injection*,<sup>71-73</sup> via localized levels at the interface due to impurities or structural disordered levels, or the *Fowler-Nordheim tunneling injection* processes (FN),<sup>74-76</sup> favored by a local high electric field (see Fig. 1.7.b and Fig. 1.7.c).

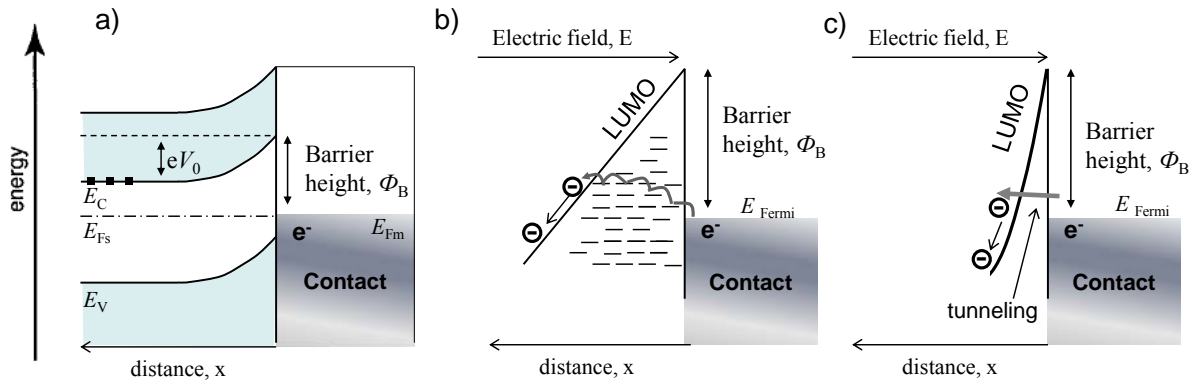


**Fig. 1.7** (a) Formation of the Schottky barrier between a metal and a n-type semiconductor.  $E_C$  and  $E_V$  are the edges of the conduction and valence band, respectively.  $E_F$  and  $E_{FS}$  are the Fermi level of the metal and semiconductor, respectively;  $\Phi_B$  is the Schottky barrier height and  $V_0$  is the contact potential. Additionally, two possible carrier injection mechanisms at the organic/metal interface are shown: (b) Schottky-type carrier injection via structural disordered levels or impurities with thermal assistance and (c) Fowler-Nordheim tunneling carrier injection with the assistance of a local high electric field ( $10^6 - 10^7 \text{ V cm}^{-1}$ ).

However, these two models are insufficient to handle disordered organic materials<sup>77-79</sup> and there is still a lack of satisfactory description of the physical processes that govern the charge injection in such interfaces.

On the other hand, in devices such as OLEDs or solar cells, a good injection and extraction of carriers through the electrodes is desired. For this purpose, a suitable combination of electrode-semiconductor materials is required to keep the barrier height as small as possible. When the barrier height is very low, the charges can be injected easily and the current is no more inject-limited. In this situation the current flow is governed by the Ohm's law. There are different strategies to achieve such situation. For example in OLEDs, it is usually to inject electrons from a low work-function contact and holes from a high work-function contact to decrease the barrier height potential between the electrode and the active layer. Another approach is to incorporate additional interlayers with energy levels that are between those corresponding to the work function of the electrode and the HOMO/LUMO of the active layer, depending on the type of carrier to be injected (holes or electrons respectively). Hence, it is often the use of hole transporting layers (HTL) close to the

anode, and electron transporting layers (ETL) close to the cathode, to minimize the barrier and ensure an optimal extraction/injection of carriers from the electrodes to the active material (see Fig. 1.6(c)). The presence of those interlayers plays a crucial role on the performance of such devices, being indispensable for obtaining the high efficiencies.

## Charge carrier transport

The electronic structure of organic thin films are based on the HOMO (highest occupied molecular orbital) and LUMO (lowest unoccupied molecular orbital) of individual molecules that interact together via Van der Waal's forces, creating narrow conduction and valence bands between them.<sup>80</sup> As a consequence, it is frequent to describe them by using typical parameters of inorganic semiconductors such as electron affinity ( $E_a$ ), ionization potential ( $I_p$ ), charge carrier mobility ( $\mu_h, \mu_e$ ) or charge carrier densities ( $n_h, n_e$ ), although the amount of carriers and their mobility are often very low compared to inorganic materials.

One first consequence of their different nature is that in organic materials charges are localized to single molecules and not delocalized in large bands, being the carrier transport based on a hopping process from one localized state to the next. The transition rate depends on the overlap of the relevant molecular orbitals, which will depend on the orientation between molecules and their aggregation, as well as the level of disorder of the film. These processes will determine the localization length and the energy difference between the hopping sites.<sup>81-83</sup>

Once the carriers are inside the device, they travel through the organic layer influenced by an applied or induced internal voltage, which guide them to the desirable direction. If charges can be injected/extracted without any limitation (Ohm's contacts) the currents will be limited by the bulk properties of the organic film. At very low current, the "additional" carriers ( $n_a$ ) (injected or generated) are lower than

the intrinsic carriers ( $n_i$ ) that are initially in the film, and the current follows the Ohm's law. Nevertheless, if  $n_a$  exceeds  $n_i$ , the current can be transport-limited. Because of impurities or imperfections in the film, there are often electronic states below the LUMO, which can trap electrons, decreasing the amount of carriers available for the charge transport. This situation leads to a *trap limited current* (TLC),<sup>84</sup> which produces a different behavior in the  $J - V$  curve depending on the distribution of traps. Nevertheless, if enough current is flowing all the traps will become and remain filled, leading to a strong increase in the resulting current that can be observed in the  $J - V$  curve. When there are more injected carriers per unit time than the sample can transport, for example due to the low carrier mobility, space charges will appear at the organic film and the current will be *space charge limited* (SCLC)<sup>71,85-89</sup>

### Charge blocking effect

In some cases it is desirable the use of interlayers with a high energy barrier at the interface with its neighbor film. In such a situation the carrier transport is limited through such interface, leading to a decrease in the whole device current. Nevertheless, if the blocking layer is well positioned, it can be used to avoid undesirable losses and optimize the main central process in the device, obtaining higher efficiencies. This can be explained if the material behaves as a blocker for one type of carrier, for instance electrons, but it is a good transporter for holes. These interlayers are called hole blocking (HBL) or electron blocking layers (EBL) and have been extensively used in OLEDs.<sup>90-91</sup>

By combining different interlayers with different charge injection or blocking effects it is possible to modify substantially the performance of organic electronic devices.

### 1.3.2. Light emitting electrochemical cells (LECs)

Artificial lighting is one of the primary needs for the development of the social, commercial and industrial activities in modern society. The consumption of electrical energy in the lighting sector was ca. 3500 TWh in 2012, corresponding to an equivalent CO<sub>2</sub> production of 1900 Mt.<sup>92</sup> In this context, it is necessary a massive change from the conventional technology to efficient and low cost alternatives. One of the most developed type of alternative is the organic light emitting diode (OLED)<sup>7,8,93</sup> which has already reached efficiencies very close to the typical values obtained for fluorescent tubes.<sup>94-96</sup> Nevertheless, high efficient OLEDs are based on multi-layer stacks of organic materials which normally requires high vacuum processes and the use of reactive metals for an efficient injection of electrons. That implies rigorous encapsulation to prevent degradation of the air-sensitive materials and higher production costs, undesirable for a large-scale market of lighting.

Solid-state light emitting electrochemical cells (LECs) provide a promising alternative to OLEDs.<sup>97,98</sup> In their simplest configuration they are based on a single emissive layer of a polymer (p-LEC) or an ionic transition metal complex (iTMC-LEC) that contains mobile ions, sandwiched between two electrodes.<sup>99-101</sup> When an external bias is applied, the ions migrate and accumulate at the electrodes lowering the energy barrier needed for the injection of carriers. As a consequence, LECs can use air-stable electrodes such as aluminum or gold and can be reduced to a single-layer structure, being compatible with solution processing prepared in ambient conditions.<sup>101-103</sup> Fig. 1.8 shows the main differences between OLEDs and LECs.

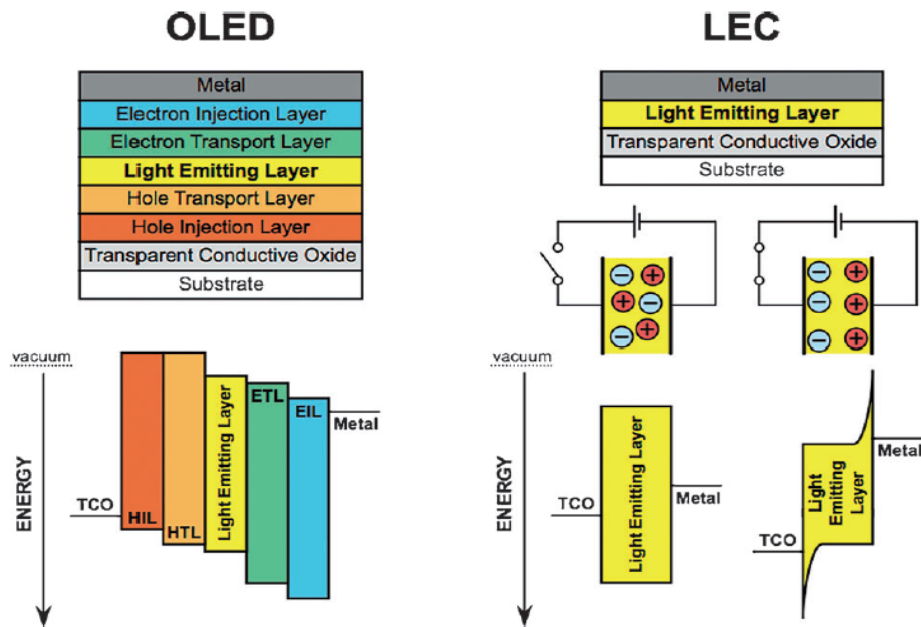


**Fig 1.8.** a) State-of-the-art OLED. b) State-of-the-art LEC. OLEDs require multiple layers, some of them processed by evaporation under high-vacuum conditions. Air sensitive low work function metals or electron injecting layers are needed for efficient charge carrier injection. LECs can be prepared from just a single active layer. The movement of ions in the layer under an applied bias allows for efficient charge carrier injection from air-stable electrodes. (Taken from reference 110).

Both polymer and iTMC-LECs have experienced a lot of progress in the state-of-the-art of LECs.<sup>97,102,104-109</sup> However, one advantage with respect to polymer-based devices is that the ionic complex in iTMC-LECs is responsible for injection, transport and emission, allowing in principle for single component devices that do not suffer from phase separation.<sup>100,101,110-112</sup> Additionally, iTMC are phosphorescent so they can harvest both singlet and triplet states, leading to higher efficiencies than fluorescent emitters.<sup>93,113,114</sup>

### Operation mechanism: Dynamic Interlayers

During the last decades there have been some controversies about the mechanism that govern the charge transport and ionic distribution along LECs. Two principal models have been intensively discussed and contrasted with the experimental

results<sup>97,102,115-119</sup> but recent studies have demonstrated that both models are limiting cases of a unifying description.<sup>120</sup>

The working principle of LECs implies the movement of the ionic species present at the active layer, leading to a continuous evolution of the system. Due to its ionic nature, under an applied bias anions and cations migrate to the respective electrodes and accumulate at the interface as very thin layers of uncompensated charge, forming the so called electric double layers (EDL).<sup>115-118</sup> At very low voltage ( $< 2.5$  V) the current injection is limited and the luminance is very poor. In such a situation the device current is based fundamentally on ionic transport and the diffusion of some electronic charge carriers. As a consequence, the entire applied potential drops at the EDLs, remaining the bulk of the active layer field-free.<sup>120</sup> However, at high voltage ( $> 2.5$  V), more carriers are injected and the semiconducting material is partially oxidized and reduced, forming redox species that are stabilized by the uncompensated oppositely charged ions presented at the electrode interface. These oxidized and reduced species are identical to their analogues used in doped organic devices, and thus the process is referred to as p- and n-doping. As a result, a p-i-n internal structure is formed in a similar way than p-i-n OLEDs, and both injection and luminance level increase considerably.

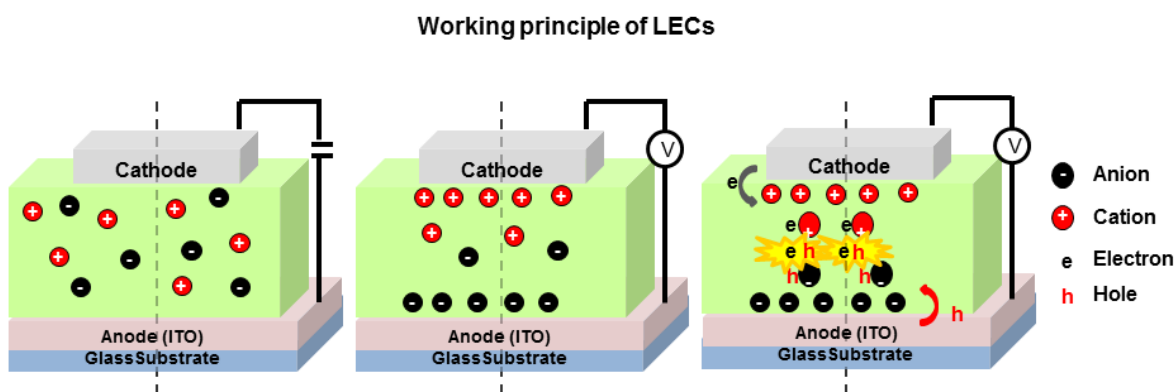


**Fig. 1.9.** Schematic representation of the operation mechanism of LECs. Before an applied bias the ions are randomly distributed. After applying the bias, the formation of the EDLs and the p- and n- type zones occurs, leading to the injection and emission of light.



Unfortunately, during device operation these highly conductive doped zones grow slowly through the middle region of the LEC, decreasing the remaining intrinsic (non-doped) region of the emissive layer.<sup>121-123</sup> In this situation, part of the applied potential is used for charge injection and the remaining bias drop over the intrinsic zone, where emission takes place. That growing of the doped zones constitutes one of the main problems of LECs, as the quenching of excitons inherent to doped zones produces a decrease in the photoluminescence and efficiency of the device. When no precaution is used, doped zones continue growing until both zones make contact and no light is emitted.<sup>124,125</sup> Different strategies<sup>126-131</sup> have been taken to prevent or retard the growing of doped zones, trying to fix it once the p-i-n configuration have been achieved. Nevertheless it is still one of the main challenges for future advances towards a real application.

### **State-of-the-art LECs and challenges**

The main inconvenient of LECs is related to their dynamic nature, which makes them self-limiting devices. The need of the EDLs formation increases the turn-on time of the device, which is the time needed for detecting light emission since the bias is applied. This leads to turn-on times ranging from milliseconds to hours depending on the ionic conductivity of the light-emitting layer. Different strategies have been adopted to solve that problem,<sup>127,132</sup> but one of the most successful consisted on driving the device with a pulse current at a high frequency (1000Hz), which allows, by retarding the growth of the doped zones during the off-time of the pulse, to achieve faster turn-on times ( $t_{\text{on}} < 1$  s), longer lifetimes ( $> 4000$  hours at a maximum luminance of  $670 \text{ cd m}^{-2}$ ) and more stable efficiencies over time.<sup>130</sup>

Additionally, some LECs can also show a reduced efficiency due to an exciton-quenching with the presence of impurities or imperfections in the active layer, or even if the emission zone is not well centered in the intrinsic region. All these disadvantages have been studied by several groups, adopting different approaches

such as controlling one carrier mobility with a carrier trap,<sup>131</sup> separating physically the p-i-n junction in a tri-layer LEC,<sup>133</sup> or even using a host-guest approach similar to the one used in OLEDs.<sup>134-136</sup>

Although some problems have to be solved, LECs are suitable alternatives for lighting applications.<sup>137-139</sup> Nevertheless, one of the main challenges on that purpose is the achievement of white light. There are iTMC-LECs performed on different transition metals,<sup>129,140-152</sup> but the most extended used iTMC are the iridium (III) based complexes. The structure consists usually on two different ligands: two negatively charged cyclometalating C<sup>N</sup> ligands, being typically responsible of the HOMO level, and one neutral ancillary N<sup>N</sup> ligand, responsible of the LUMO level.<sup>153,154</sup> This archetype-complex exhibits high photoluminescence quantum yields, enhanced photostability<sup>152,155,156</sup> and its emission can be easily tuned from red to blue by modifying chemically both ligands, tuning the HOMO-LUMO gap. As a consequence, it has been obtained LEC emission from blue to even infrared.<sup>157-168</sup> Nevertheless white emissive iTMC-LEC are not so frequent and the efficiency is normally very low.<sup>163,169-173</sup> One strategy to achieve the white emission consists on mixing a blue-green host with an orange-red guest, but the low stability and low luminance of blue-iTMCs, together with the need of deeper blue colors are the main difficulties.<sup>170,174</sup> By this approach, He *et al.* achieved a warm white LEC (CIE<sub>x,y</sub> coordinates (0.40, 0.45)) with EQE values of 4.4 % and a luminance value of 115 cd m<sup>-2</sup>. Additionally Tang *et al.*<sup>175</sup> used a conjugated polymer to produce single emitters white LECs reaching an efficacy of 3.8 cd A<sup>-1</sup>. However, the dynamic nature of LECs can complicate the stability of white color over time if the active layer contains a mixture of blue and orange/red emitting molecules, suggesting the necessity of adopting new strategies for achieving stable and efficient white emission.

### 1.3.3. Thin film solar cells

The surface of the earth receives, on average, about  $1.2 \times 10^{17}$  W of solar power, so more than the global demand on energy of an entire year is received in less than one hour from the sun.<sup>176</sup> Solar energy for photovoltaic conversion into electricity is abundant, inexhaustive and clean, yet nowadays photovoltaic solar cell technology represent less than 0.5 % of the produced electricity in the world<sup>177</sup> Since the photovoltaic effect was first observed by Becquerel E. in 1839,<sup>178</sup> and the first silicon based p-n junction photovoltaic cell was reported in 1954,<sup>179</sup> a tremendous advance in their manufacturing and performance have been experienced until now, being nowadays extensively used in many applications.<sup>180</sup> More than 80% of the solar cells in the market in 2010 were based on crystalline and multicrystalline silicon, with power conversion efficiencies (PCE) up to 25% and 20.4% respectively.<sup>181</sup> Nevertheless, to become an accessible source of energy ready to play a major role in the future energy production, it is necessary to reduce the cost of produced electricity by increasing the power conversion efficiency, reducing the amount of absorbing material or by lowering the manufacturing cost.

There are several emerging technologies that have not seen yet broad commercial availability but are still being heavily investigated in the laboratory for future applications. Some of these alternatives are the inorganic thin film solar cells, which need less active material and reduce some manufacturing costs. The main examples are amorphous silicon (a-Si), Cu(InGa)Se<sub>2</sub> (CIGS), and CdTe with highest PCE of 10.1%, 20.4%, and 16.7%, respectively.<sup>181,182</sup> However, the reduced efficiency of a-Si, together with the toxicity of cadmium or the limited amount of indium reserves suggest that novel alternatives might be found. Another type of thin film solar cells are organic photovoltaics (OPVs). They represent a potential affordable energy technology which offers the possibility of large-scale production with abundant, light and flexible materials, together with properties easy to tune and optimize. The main disadvantages in such organic cells are the low efficiencies achieved due to the difficulties on extracting the generated charges from the organic material. These types

of cells have been extensively studied and a huge amount of materials have been tested.<sup>17,183-187</sup> As a result, in the last ten years, the highest efficiency obtained from organic solar cells has risen from 2.5 to 11 %, a considerable advance in performance.<sup>188</sup> However, organic photovoltaic efficiencies still lag behind their inorganic counterparts and new materials are needed to enhance it.

A very new member on the thin film solar cell family is the one using hybrid organic-inorganic perovskite materials as the absorber material. The first report on solar cells employing hybrid methylammonium lead halide perovskite,  $\text{CH}_3\text{NH}_3\text{PbBr}_3$ , took place in 2006 in the annual meeting of the International Electrochemical Society (IES).<sup>189</sup> The cell consisted on a dye sensitized solar cell (DSSC), with a perovskite-sensitized mesoscopic  $\text{TiO}_2$  film, which showed a PCE of 2.2%. Three years later the efficiency was improve to 3.8% by replacing bromine with iodine and spin-coating the perovskite layer on top of the mesoporous  $\text{TiO}_2$  film.<sup>190</sup> These results did not gain much attention as all devices were unstable. Two years later, in 2011, again the efficiency was doubled to 6.5% by changing the electrolyte formulation and the growing of perovskite as nanodots on the  $\text{TiO}_2$  scaffold.<sup>191</sup> Unfortunately, these devices were limited by the solubility of the employed perovskite in polar solvent, which are used commonly in DSSC. However, they pointed out perovskite materials as suitable absorbers for solid state solar cells, especially  $\text{CH}_3\text{NH}_3\text{PbI}_3$ , due to its very high absorption coefficient over the whole visible solar emission spectrum. Moreover, these materials were easy to synthesize, cheap, compatible with solution process techniques and presented optical and electrical properties easy to be tuned.<sup>192-195</sup>

Only some months later, by replacing the liquid electrolyte with a solid HTM, the first stable, solid-state and high efficient perovskite solar cell arrived, showing a breakthrough in efficiency as high as 9.7% and 10.7%.<sup>196,197</sup> New results from these studies demonstrated that  $\text{CH}_3\text{NH}_3\text{PbI}_3$  was able to transport both holes and electrons, and could be used in non-scaffold but single planar thin film cells. Efficiencies over 12% were achieved in devices where the perovskite film capped the scaffold  $\text{TiO}_2$  layer, reducing the thickness of the mesoscopic component to 200-300 nm.<sup>198,199</sup> However, most of the results from perovskite solar cells (PSC) were very

irreproducible due to the uncontrolled growing of the material through the solution processing method. By improving the morphology of the layer a new record in efficiency was soon announced, with values of PCE over 15 %.<sup>200,201</sup> At the same time, high efficient planar configurations<sup>201,202</sup> and HTL-free devices were also demonstrated,<sup>203</sup> showing the potential of PSC on very simple high efficient architectures. At the beginning of 2014 Seok's group announced an efficiency of 17.94% by using different perovskite compositions  $\text{CH}_3\text{NH}_3\text{PbI}_{3-x}\text{Br}_x$  (10–15% Br), and some months later a 19.3% efficiency was achieved by Y. Yang's group,<sup>204</sup> which is very close to the theoretical limit.

Numerous studies appeared in the last two years, showing different architectures and compositions of the perovskite active layer, but still a deep understanding of the underlying physical and chemical processes is needed.

In view of the rapidly advance of PSC field it is appropriate to contextualize that the results showed in this Thesis were carried out in the second half of 2013 and early 2014.

## **A hybrid organic-inorganic material:**

### **Methylammonium lead iodide perovskite ( $\text{CH}_3\text{NH}_3\text{PbI}_3$ )**

Methylammonium lead iodide is an organic-inorganic crystalline material with the generic formula  $\text{ABX}_3$ , which adopts a perovskite structure<sup>192</sup> where position A is occupied by the organic cation  $\text{CH}_3\text{NH}_3^+$ , and positions B and X are occupied with the  $\text{Pb}^{+2}$  and the I ions respectively. Due to the low size of the methylammonium compared to other organic cations, the complete structure is a 3D network where  $[\text{PbI}_6]^{-4}$  octahedron share their corners and the organic cation fills the interstitial space between them. Fig. 1.10 shows a schedule of the crystalline structure.

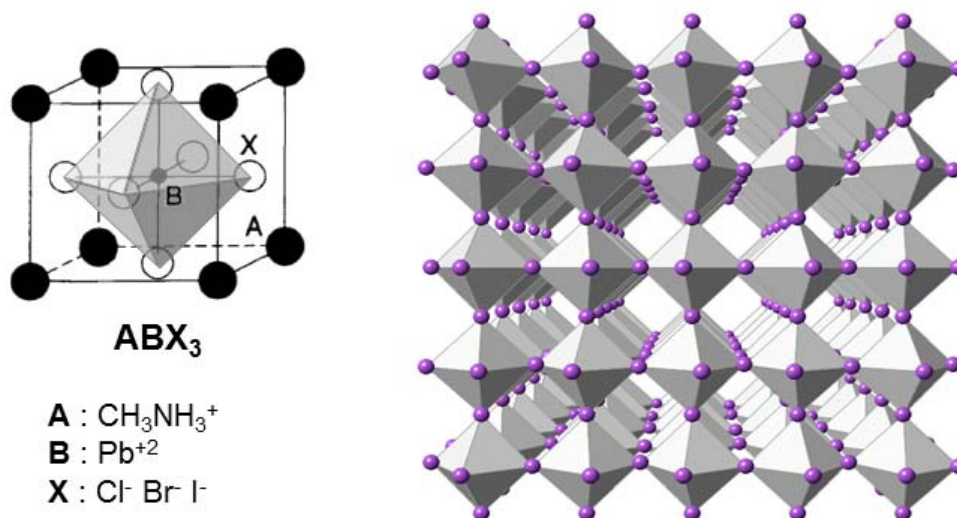


**Fig. 1.10.** Crystalline structure of methylammonium lead iodide perovskite. Left: building unit. Right: 3D crystalline structure of [PbI<sub>6</sub>]<sup>-</sup> octahedron, without including the organic methylammonium cation for clarity.

This hybrid organic-inorganic perovskite presents a band gap of 1.55 eV, which makes it a suitable semiconductor for photovoltaic applications, showing really high absorption coefficients and a broad absorption spectrum below 800 nm. Its organic-inorganic nature allows it to combine properties typical from inorganic materials with some of the advantages from organic compounds, such as its flexibility. As a consequence, this material has shown unique electrical and optical properties that are the focus of an intense debate.<sup>205-210</sup>

In most organic materials, the photovoltaic process implies firstly the formation of an exciton, which is a strongly bonded electron-hole pair, contrary to inorganic solids where free charges are directly generated.<sup>211,212</sup> This is mainly due to the low dielectric constant in organic materials,<sup>213</sup> which favors a high binding energy between hole and electron of 0.5 - 1 eV.<sup>214</sup> Thus, in order to split the charges, it is necessary a built-in potential higher than the binding energy which can be achieved, for example, through incorporating an electron acceptor material. In such a case, once the exciton is formed, it diffuses to the active interface, where it dissociates into free charges that are then transported to the respective electrodes (see Fig. 1.11). Unfortunately, the exciton

transport is in competition with other decay processes such as luminescence or non-radiative recombination to the ground state, limiting the exciton diffusion to a specific length, called diffusion length ( $L_D$ ), that in most organic materials is around 10 nm.<sup>17</sup> Different strategies in the state-of-the-art devices are focused on reducing the distance to the active interface, minimizing the recombination of excitons.

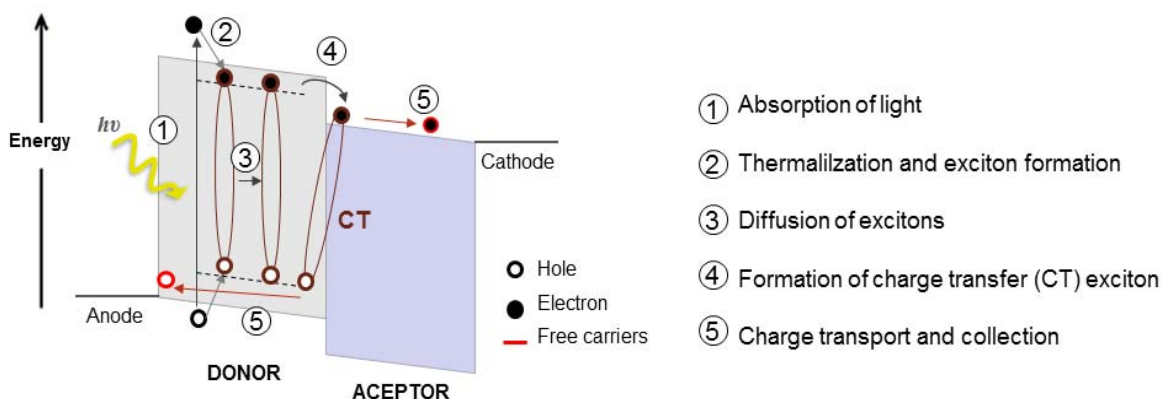


**Fig. 1.11.** Diagram of the five steps involved in the photon-to-conversion process in bilayer organic solar cells.

Nevertheless, in perovskite materials the excitons produced by light absorption have a very weak binding energy of about 0.03 eV,<sup>215</sup> which is comparable to the thermal energy ( $kT$ ) at room temperature. That means that most of the excitons are separated into free charges very rapidly. Moreover, high carrier mobilities have been measured for electrons and holes, resulting in values of  $7.5 \text{ cm}^2 \text{ V}^{-1} \text{ s}^{-1}$  and  $12.5 - 66 \text{ cm}^2 \text{ V}^{-1} \text{ s}^{-1}$  respectively,<sup>216,217</sup> which are much higher than typical mobilities for organic materials ( $10^{-6}$  to  $1 \text{ cm}^2 \text{ V}^{-1} \text{ s}^{-1}$ ).<sup>218</sup> All these characteristics are accompanied by very long carrier-diffusion lengths ( $L_D$ ), which prevents free carriers to recombine once they have been separated. Compared to organic materials, methylammonium lead iodide perovskite has shown diffusion lengths from 10 to more than 100 times higher, depending on the method of synthesis,<sup>219,220</sup> with some recent results concluding that they are even in the range of  $3 \mu\text{m}$ .<sup>221</sup> All these characteristics have converted hybrid organic-inorganic perovskite in one of the most promising materials for next-

generation photovoltaic technologies, which is pointing out as a serious alternative to the actual market.

## Challenges and outlook

Organic–inorganic halide PSC has been the most significant development in the field of photovoltaic in the present decade. They represent for the first time a real alternative to substitute the established inorganic technology, satisfying at the same time the need for high efficiencies and low cost solution based manufacturing. Nevertheless, there are still some questions that need to be understood and improved before advancing one step more in the introduction of these products on the real market.

The rising efficiency achieved by these new solar cells since 2012 have considerable impacted to all the solar cell community, and nowadays there is an increasing number of groups researching on that topic that produce PSC with very good performances. Nevertheless, one inconvenient has highlighted: the influence of the voltage background on the cell performance. As a consequence, some of the most efficient reported cells have shown a strong hysteresis when they are reversed or direct biased<sup>222,223</sup> what can lead to overestimated values if they have not been certified.<sup>224,225</sup> The influence of the perovskite morphology on the performance and photocurrent behavior of the solar cells is not yet understood, but different methods of synthesis leads to different perovskite behavior. Many groups are working now on controlling the morphology of the perovskite during the formation process, which is urgently needed for carrying on reliable fundamental studies.<sup>226,227</sup>

Additionally, very few reports on stability studies have appeared in the literature, which is somehow comprehensible due to the fast evolution of this field. However, methylammonium lead iodide perovskite is very sensitive to water and degrades easily under humid conditions. For that reason, long term stability tests in humid atmosphere as well as temperature dependent studies versus time should be carried out, to probe the potential of  $\text{CH}_3\text{NH}_3\text{PbI}_3$  in practical conditions. On the other



hand, the enormous potential of PSC relies on the easy processing from solution, the low cost of the material as well as their fantastic photoactive behavior. Nevertheless, other exceptional properties may be exploited to extend their application from the traditional rough solar cell panel to innovative designs, such as portable-flexible solar cells for clothes, beach umbrellas... or semitransparent solar cells for building integrated windows, tandem structures... with other organic or inorganic photoactive materials for highly efficient devices. For this purpose, new configurations and new compatible materials need to be developed to draw on all the perovskite potential.

The toxicity is another important point to remark here, as almost the totality of perovskite solar cells investigated in the last two years contains lead, which is very toxic for the human health and the environment. Moreover, one of the main precursors of  $\text{CH}_3\text{NH}_3\text{PbI}_3$  is  $\text{PbI}_2$ , a very carcinogenic compound, partially soluble in water, and which is also produced as a result of degradation of the perovskite. This point gain even more importance if photovoltaic technology tends to be a clean and sustainable source of energy. Several studies suggested the substitution of  $\text{Pb}^{+2}$  by other metals such as  $\text{Sn}^{+2}$ , but very few reports have appeared until now.<sup>228-230</sup>

Finally, hybrid organic-inorganic perovskites are very versatile materials, which have a lot of possibilities for tuning their properties depending on their composition. It is possible to change not only the halide, which have been demonstrated to modify the optical properties and stability in air, but also the organic compound, which can be very desirable for avoiding the main degradation problem of the perovskite, related with the evaporation of the organic  $\text{CH}_3\text{NH}_3^+$  cation into  $\text{CH}_3\text{NH}_2$ , gas at normal conditions.<sup>231-233</sup>

## 1.4. About this work

In the previous Sections the importance of organic thin films in technological applications has been pointed out. Thin films have been widely used in complex applications such as interlayers in organic electronics or ultrathin nanostructured films for gas sensing or magnetic displays. In some cases, the organization of the molecules in such films can have an important impact in the performance of the devices, being possible the appearance of new properties in highly organized systems. The main purpose of this work is to study the influence of interlayers in the performance of optoelectronic devices, as well as to introduce some useful studies for the preparation and characterization of organized organic thin films composed by typical emissive molecules used in optoelectronics, such as Ir-complexes, rhodamine or porphyrine derivatives. Nevertheless, the study and preparation of organized thin films are also interesting for fundamental studies, to prepare engineered ultrathin films for achieving specific desirable properties or, for example, for mimicking organized biological systems such as cellular lipid based membranes. For this purpose it is necessary the availability of techniques that allow the preparation and characterization of such organized systems.

With that in mind, Chapter 3 is focused on the physical control of organized thin films prepared by the Langmuir technique at the air-water interface. This chapter starts with a review of one of the most used techniques to characterize the morphology of such thin films, the Brewster Angle Microscopy (BAM), from a perspective very different than the classical. This study shows the influence of the polar-group in the reflectivity of the monolayer, and demonstrates the importance of including this part in the theoretical analysis of the BAM pictures. The results are very relevant for the case in which the polar group is big and/or absorbs light at the wavelength of the incident light source, what can be very frequent when studying absorbent molecules for lighting or solar cell applications. Additionally, in this chapter a novel reflection spectroscopy method is introduced for obtaining valuable information about the tilt

and aggregation of chromophores in the Langmuir monolayers, which are normally located in a region hardly accessible by other experimental techniques. This new method is based on the Reflection Spectroscopy technique, similar to that with normal incidence, but using s- and p-polarized radiation at different incidence angles, obtaining reach detail information about the organization in the monolayer. At the same time, mixed Langmuir monolayers of Ir-complex / porphyrin derivatives and multilayered structures based on this system have been prepared and transferred to a solid substrate to study energy transference processes through steady-state fluorescence and lifetime measurements.

In Chapter 4 the influence of different inorganic thin films as interlayers in light emitting electrochemical cells as well as the formation of typical dynamic interlayers will be discussed. Although these devices are in principle independent of the electrode material used for injecting the charge carriers, additional studies will show that the performance can be seriously affected depending on the material used. Different metals such as Al or Au, as well as metal oxides such as MoO<sub>3</sub> or ZnO will be used to tune the emission zone far or close from the electrodes, leading to a change in the luminance level. On the other hand, these new inorganic-based interfaces will inspire the preparation of white tandem-LEC devices, where no complex CGL is needed. Due to the ionic nature of LECs, very thin metallic interlayers lead to the generation of dynamically doped regions adjacent to the electrodes (analogue to the CGL), resulting in an ideal “self-regulated” junction formation. Thus, by introducing a simple metallic interlayer, a new concept of tandem will be shown, extending the possibilities for a real lighting application as white-LECs.

In Chapter 5 a new photoactive perovskite material (CH<sub>3</sub>NH<sub>3</sub>PbI<sub>3</sub>) will be analyzed under the influence of two organic electron and hole blocking layers. The development of the perovskite material synthesis through a dual source evaporating method, as well as the solution process compatibility of the rest of the sandwiched structure, including the charge blocking layers, converts it in a very promising solar cell architecture for future applications. This new architecture does not need high temperature steps and can be prepared using large coating or printing methods. In this

chapter will be shown high efficient flexible perovskite solar cells, where the high resistance of perovskite materials to extended bending and thus, its suitability to roll to roll processes (R2R) will be demonstrated. Moreover, high efficient single-junction semitransparent solar cells will be also prepared, suggesting their use in building integrated applications such as facade or colored windows, necessary for self-sustaining buildings at low cost.

## References

1. Petty, M. *Molecular Electronics: From principles to practice*, 2007.
2. Forrest, S.R.; Thompson, S.E. *Chem. Rev.* 2007, 107, 923.
3. Pope M. and Swenberg C.E. “*Electronic processes in organic crystals*”, Clarendon Press, 1982.
4. Berets, D.J. and Smith, D.S. *Trans. Faraday Soc.* 1968, 64, 823.
5. Bredas, J.L.; Chance, R.R. and Silbey, R. *Phys. Rev. B* 1982, 26, 5843.
6. Heeger, A.J.; Kivelson, S.; Schrieffer, J.R. and Su, W.P. *Reviews of Modern Physics* 1988, 60, 781.
7. Tang, C.W. and Van Slyke, S.A. *Appl. Phys. Lett.* 1987, 51, 913.
8. Burroughes, J. H.; Bradley, D. D. C.; Brown, A.R.; Marks, R. N.; Mackay, k.; Friend, R. H.; Burns, P. L.; Holmes, A. B. *Nature*, 1990 347, 539.
9. Horowitz, G. “Physics of Organic Field-Effect Transistors”, in “*Semiconducting Polymers*”, Eds. Hadziioannou Gandvan Hutten P.F., Wiley-VCH, 2000.
10. Geacintov, N.E. and Pope, M. *J. Chem. Phys.* 1966, 45, 3884.
11. Geacintov, N.E.; Pope, M. and Kallmann, H. *J. Chem. Phys.* 1966, 45, 2639.
12. Kao, K.C. and Hwang, W. “*Electrical Transport in Solids*”, Pergamon Press 1981.
13. Reichmanis, E.; Katz, H.; Kloc, C. and Maliakal, A. *Bell Labs Technical Journal* 2005, 10, 87.
14. Friend, R. H.; Gymer, R. W.; Holmes, A. B.; Burroughes, J. H.; Marks, R. N.; Taliani, C.; Bradley, D. D. C.; Dos Santos, D. A.; Brédas, J. L.; Lögdlund, M. & Salaneck, W. R. *Nature*, 1999, 397, 121.
- 15 Garnier, F.; Hajlaoui, R.; Yassar, A. and Srivastava, P. *Science*, 1994, 265, 1684.
- 16 Dimitrakopoulos, C. D. and Malenfant, P. R. L. *Adv. Mater.* 2002, 14, 99.
- 17 Peumans, P.; Yakimov, A. and Forrest, S. R. *J. Appl. Phys.* 2003, 93, 3693.
- 18 You, J.; Dou, L.; Yoshimura, K.; Kato, T.; Ohya, K.; Moriarty, T.; Emery, K.; Chen, C.C.; Gao, J.; Li, G. and Yang Y. DOI: 10.1038/ncomms2411
- 19 Owens, R. M. and Malliaras, G. G. *Mrs Bulletin* , 35, 2010, 449

20. Temirov, R.; Soubatch, S.; Luican, A.; Tautz, F.S. *Nature* 2006, 444, 350.
21. Agranovich, V.M.; Basko, D.M.; La Rocca, G.C.; Bassani, F. *J. Phys., Condens. Matter* 1998, 10, 9369.
22. Zhu, X.-Y.; Yang, Q. and Muntwiler, M. *Acc. Chem. Res.* 2009, 42, 1779.
23. Deutsch, D.; Natan, A.; Shapira, Y.; Kronik, L. *J. Am. Chem. Soc.* 2007, 129, 2989.
24. Duhm, S.; Heimel, G.; Salzmann, I.; Glowatzki, H.; Johnson, R.L.; Vollmer, A.; Rabe, J.P. and Koch, N. *Nat. Mater.* 2008, 7, 326.
25. Pope, M.; Swenberg, C. E. *Electronic processes in Organic Crystals and Polymers*, Oxford University Press, 1999.
26. Jimenez-Millan, E; Giner-Casares, J.J.; Martin-Romero, M.T.; Brezesinski, G.; Camacho, L. *J. Appl. Chem. Soc.* 2011, 133 (47), 19028.
27. Naaman, R. and Vager, Z. *Mrs Bulletin* 2010, 35, 420.
28. Helgesen, M.; Sondergaard, R. and Krebs, F. C. *J. Mater. Chem.* 2010, 20, 36.
29. Li, G.; Shrotriya, V.; Huang, J. S.; Yao, Y.; Moriarty, T.; Emery, K. and Yang, Y. *Nat. Mater.* 2005, 4, 864.
30. Shoaee, S.; Eng, M. P.; Espildora, E.; Delgado, J. L.; Campo, B.; Martin, N.; Vanderzande, D. and Durrant, J. R. *Energy Environ. Sci.* 2010, 3, 971.
31. McNeill, C. R.; Westenhoff, S.; Groves, C.; Friend, R. H. and Greenham, N. C. *J. Phys. Chem. C*, 2007, 111, 19153.
32. X. Yang, J. Loos, S. C. Veenstra, W. J. H. Verhees, M. M. Wienk, J. M. Kroon, M. A. J. Michels and R. A. J. Janssen, *Nano Lett.*, 2005, 5, 579–583.
33. Petty, M. *Molecular Electronics: From principles to practice*, 2007
34. Roberts, G. G. *Langmuir-Blodgett Films*; Plenum: New York, 1990.
35. Ulman, A. *An Introduction to Ultrathin Organic Films from Langmuir-Blodgett to Self Assembly*; Academic Press: San Diego, 1991.
36. Mijama, S; Nalwa, H. S. *Organic Electroluminescent Materials and Devices*; Gordon and Breach: Amsterdam, 1997.
37. Stapff, I. H. Stumpfpln, V.; Wendorff, J. H.; Spohn, D.B; Mobius, D. *Liq. Cryst.* 1997, 23, 613.

38. Addadi, L.; Weiner, S. *Angewandte Chemie International Edition in English*, 1992, 31, 153.
39. Magnet-Dana, R. *Biochimica et Biophysica Acta-Biomembranes*, 1999, 109, 1462.
40. Berger, R.; Delamarche, E.; Lang, H.P.; Gerber, CH, Gimzewsky, J.K., Meyer, E. and Güntherodt H.J. *Science*, 1997, 276.
41. Leblanc, R.M. *Current Opinion in Chemical Biology*, 2006, 6, 529.
42. Pavinatto, FJ ; Pavinatto, A; Caseli, L; dos Santos, DS; Nobre, TM; Zaniquelli, MED; Oliveira, ON. *Biomacromolecules* 2007, 8, 1633.
43. Ariga, K.; Hill, J. P.; Endo, H. *International Journal of Molecular Sciences* 2007, 8, 864.
44. Gaines, G. L. J. *Insoluble Monolayers at the Liquid-Gas Interfaces*; Wiley Interscience: New York 1996.
45. Kaercher, T.; Hönig, D.; Möbius, D. *Orbit* 1995, 14, 17.
46. Kuhn, H.; Forsterling, .. *Principles of Physical Chemistry*, John Wiley & Sons: New York 1999.
47. Grüninguer, H.; Möbius, D.; Meyer, H. *J. Chem. Phys* 1983, 79, 3701.
48. Pedrosa, J.M; Martin-Romero, M.T.; Camacho, L.; Mobius, D. *J. Phys. Chem. B* 2002,106, 2583.
49. Schulmann, J. H.; Waterhouse, R. B.; Spink, J. A. *Kolloid. Z.* 1956, 146, 77.
50. Kossi, C. N.; Leblanc, R. M. *J. Colloid Interface Sci.* 1981, 80, 426.
51. G. Fariss, J. B. Lando, S. E. Rickert, *Journal of Materials Science* 18 (1983) 3323-3330
52. Kuhn, H. Mobius, D. *Monolayer Assemblies. Investigation of Surfaces and Interfaces*; Rossister, B. W. Baetzold, R. C. Ed.; John Wiley & Sons, Inc: New York, 1993: Vol. IXB; pp 375.
53. Langmuir, I.; Schaefer, V. J. *J. Am. Chem. Soc.* 1938, 60, 1351.
54. Petty, M.C. *An introduction to Langmuir-Blodgett films*. Cambridge. Cambridge University Press. 1996.
55. Burroughs, J. H.; Bradley, D. D. C.; Brown, A. R.; Marks, R. N.; Mackay, K.; Friend, R. H.; Burns, P. L. & Holmes, A. B. *Nature* **347**, 539 (1990)
56. Mihi, A.; Ocaña, M. & Míguez, H. *Adv. Mat.*, **18**, 2244 (2006)

57. Malinkiewicz, O.; Lenes, M.; Brine, H. and Bolink, H. J. *RSC Advances*, 2012, 2, 3335–3339
58. C. S. Herrick, *Ind. Eng. Chem. Prod. Res. Dev.* 1980, 19, 314-316
59. Bhattacharya, S.K. ; Moon, K.S. ; Tummala, R.R. ; May, G.S. *IEEE Transactions on Electronics Packaging Manufacturing* 26, 2, 2003.
60. W. Brutting, C. Adachi, R.J. Holmes, *Physics of Organic Semiconductors*, Wiley-VCH, Weinheim, Germany, 2012.
61. R.R. Søndergaard, M. Hösel, F.C. Krebs, *J. Polym. Sci. B: Polym. Phys.* 51 (2013) 16–34.
62. C. Adachi, T. Tsutsui, S. Saito, *Optoelectron: Devices Technol.* 6, 25 (1991)
63. C. W. Tang, S.A. VangSlyke, and C. H. Chen, *J. Appl. Phys.* 65, 3610, (1989)
64. Chunfu Z.; Tong, S. W.; Jiang, C.; Kang, E. T.; Chan, D. S. H. and Zhu, C. *Appl. Phys. Lett.* 2008, 93, 043307.
65. Gao, X. D.; Zhou, J.; Xie, Z. T.; et al. *Applied Physics Letters*, 93, 083304, (2008).
66. Hamwi,S.; Meyer, J.; Kröger, M.; Winkler, T.; Witte, M.; Riedl, T.; Kahn,A. and Kowalsky, W. *Adv. Funct. Mater.* 20, 1762, (2010).
67. Chen, Y. and Ma, D. *Journal of Materials Chemistry*, 22, 18718, (2012).
68. Gartstein, Y.N. and Conwell, E.M. *Chem.Phys. Lett.* 255, 93 (1996).
69. Conwell, E.M. and Wu, M.W. *Appl. Phys. Lett.* 70,1867 (1997).
70. Savvateev, V. N and Ovadyahu, Z. "Slow Relaxation in a Fermi Glass," in Hopping and Related Phenomena: Proceedings of the 6th International Conference on Hopping and Related Phenomena, edited by O. Millo and Z. Ovadyahu, p. 44 (1995).
71. S. M. Sze, *Physics of Semiconductor Devices*, Wiley, New York, 1981.
72. Wolf,; Arkhipov, V. I. and Bäessler, H. *Phys. Rev. B* 59(11), 507-7513 (1999)
73. Matsumura, M.; Akai, T.; Saito, M. and Kimura, T. *J. Appl. Phys.* 79, 264 (1996).
74. Arkhipov, V. I. ; Emelianova, E. V.; Tak, Y. H. and Bäessler, H. *J. Appl. Phys.* 84(2), 848 (1998)
75. Parker, I. D. *J. Appl. Phys.* 75(3), 1656-1666 (1994)
76. Koehler, M. and Hümmelgen, I. A. *Appl. Phys. Lett.* 70(24), 3254-3256 (1997)
77. H. Bassler *Phys. Stat. Sol.(b)*, 175, 15-55, 1993.



78. Conwell, E.M. and Wu, M.W. *Appl. Phys. Lett.* 70,1867 (1997).
79. Lampert, M. A. and Mark, P. *Current Injection in Solids* (Academic Press, NY, 1970).
80. Shinar, J. *Organic Light Emitting Devices. A Survey.* **2002**
81. Raikh, M. and Wei, X. *Mol. Cryst. Liq. Cryst.* 256, 563 (1994).
82. Lemmer, U.; Scheidler, M.; Kersting, R.; Mahrt, R. E; Kurz, H.; Bäessler, H.; Gobel, E. and Thomas, P. in Ropping and Related Phenomena: Proceedings of the 6th International conference on Ropping and Related Phenomena, edited by O. Millo and Z. Ovadyahu, p. 400 (Jerusalem, Israel. 1995).
83. (a) A. Miller and E. Abrahams, *Phys. Rev.* 120,7455 (1960) ; (b) S. V. Frolov, M.Leiss, P. A. Lane, W. GeHerman and Z. V. Vardeny, *Phys. Rev. Lett.* 78,4285 (1997).
84. Murray A. Lampert and Peter Mark *Current injection in solids* Academic Press, New York and London (1970)
85. Murray A. Lampert Simplified Theory of Space-Charge-Limited Currents in an Insulator with Traps *Phys. Rev.* 103(6), 1648-1656 (1956)
86. Murray A. Lampert Injection Currents in Insulators *Proceedings of the IRE* 50(8), 1781-1795 (1962)
87. N. F. Mott and R. W. Gurney *Electronic Processes in Ionic Crystals* Oxford University Press, New York (1940)
88. A. Rose Space-Charge-Limited Currents in Solids *Phys. Rev.* 97(6), 1538-1544 (1954)
89. Tredgold R.H., *Space Charge conduction in solids.* Amsterdam. Elsevier. 1966
90. Hancox, I.; Chauhan, K. V.; Sullivan, P.; Hatton, R. A.; Moshar, A.; Mulcahy, C. P. A. and Jones, T. S. *Energy Environ. Sci.*, 2010, 3, 107–110.
91. Dennler, G.; Scharber, M. C. and Brabec, C. J. *Adv. Mater.* 2009, 21, 1323.
92. International Energy Agency, Light's Labour's Lost, <http://www.iea.org/>.
93. Baldo, M. A.; O'Brien, D. F.; You, Y.; Shoustikov, A; Sibley, S.; Thomson, M.E., Forrest, S. R. *Nature* 1998, 395, 151.
94. Reineke, S.; Lindner, F.; Schwartz, G.; Seidler, N.; Walzer, K.; Lüssem, B. & Leo, K. *Nature* 459 (2009), 234-U116.

95. Walzer, K.; Maenning, B.; Pfeiffer, M.; Leo, K. *Chem. Rev.* 2007, 107, 1233.
96. Sasabe, H.; Kido, J. *J. Mater. Chem. C.* 2013, 1, 1699.
97. Pei, Q.B.; Yu, G.; Zhang, C.; Yang, Y.; Heeger, A. J. *Science* 1995, 296, 1086.
98. Dumur, F.; Bertin, D.; Gigmes, D. *Int. J. Nanotechnol.* 2012, 9, 377.
99. Costa, R.D. ; Ortí, E.; Bolink, H.J.; Graber, S.; Schaffner, S.; Neuburger, M.; Housecroft, C.E.; Constable, E.C. *Adv. Funct. Mater.* 19 (2009) 3456.
100. Slinker, J. ; Bernards, D.; Houston, P.L.; Abruña, H.D.; Bernhardand, S.; Malliaras, G.G. *Chem. Commun.* 19 (2003) 2392.
101. Slinker, J.D.; Rivnay, J.; Moskowitz, J.S.; Parker, J.B.; Bernhard, S.; Abruña, H.D.; Malliaras, G.G. *J. Mater. Chem.* 17 (2007) 2976.
102. Pei, Q. B.; Yang, Y.; Yu, G.; Zhang, C.; Heeger, A. J. *J. Am. Chem. Soc.* 1996, 114, 3922.
103. Matyba, P. Yamaguchi, H.; Chhowalla, M. Robinson, N.D.; Edman, L. *Acs. Nano* 2011, 5, 574.
104. Dick, D.J.; Heeger, A.J.; Yang, Y.; Pei, Q.B. *Adv. Mater.* 1996, 8, 985.
105. Fang, J.; Matyba, P.; Edman, L. *Adv. Funct. Mater.* 2009, 19, 2671.
106. Sandstrom, A.; Matyba, P.; Edman, L. *Appl. Phys. Lett.* 2010, 96, 053303.
107. Asarpoordarvish, A.; Sandstrom, A.; Tang, S.; Ganstrom, J. Edman, L. *Appl. Phys. Lett.* 2012, 100, 193508.
108. Costa, R.D.; Pertegás, A.; Tordera, D.; Lenes, M.; Ortí, E.; Bolink, H.; Graber, S.; Constable, E. C. and Housecroft, C. E. *NSTI-Nanotech* 2010, 2, 49.
109. Costa, RD.; Ortí, E.; Tordera, D.; Pertegás, A.; Bolink, H. J.; Graber, S.; Housecroft, C.E. ; Sachno, L.; Neuburger, M. and Constable, E. C. *Adv. Ener. Mater.* 2011, 1, 282.
110. Costa, R.D.;Ortí, E.; Bolink, H.J.; Monti, F.; Accorsi, G. and Armaroli, N.. *Angew. Chem. Int. Ed.* 51 (2012) 8178–8211.
111. Mannes, K.M.; Terrill, R.H.; Meyer, T.J.; Murray, R.W. and Wightman, R.M.. *J. Am. Chem. Soc.* 118 (1996) 10609–10616.
112. Hu, T.; He, L.; Duan, L. and Qiu, Y. *J. Mater. Chem.* 22 (2012) 4206–4215.
113. Bolink, H. J.; Coronado, E.; Costa, R. D.; Lardies, N.; Ortí, E. *Inorg. Chem.* 2008, 47, 9149.

114. He, L.; Qiao, J.; Wang, R.J.; Wei, P.; Wang, L. D.; Qiu, Y. *Adv. Funct. Mater.* 2009, 19, 2950.
115. deMello, J.C.; Tessler, N.; Graham, S.C.; Friend, R.H. *Phys. Rev. B* 57 (1998) 12951–12963.
116. deMello, J.C. *Phys. Rev. B* 66 (2002) 235210.
117. deMello, J.C.; Halls, J.J.M.; Graham, S.C.; Tessler, N.; Friend, R.H. *Phys. Rev. Lett.* 85 (2000) 421.
118. Slinker, J.D.; DeFranco, J.A.; Jaquith, M.J.; Silveira, W.R.; Zhong, Y.W.; Moran-Mirabal, J.M.; Craighead, H.G.; Abruña, H.D.; Marohn, J.A.; Malliaras, G.G. *Nat. Mater.* 6 (2007) 894.
119. Matyba, P.; Maturova, K.; Kemerink, M.; Robinson, N. D. & Edman, L. *Nat. Mater.* 8 (2009) 672–676.
120. S. van Reenen, P. Matyba, A. Dzwilewski, R. A. J. Janssen, L. Edman, M. Kemerink *J. Am. Chem. Soc.* 132 (2010) 13776.
121. Lenes, M.; Garcia-Belmonte, G.; Tordera, D.; Pertegás, A.; Bisquert, J. and Bolink, H. J. *Adv. Funct. Mater.* 21 (2011) 1581–1586.
122. Lenes, M.; Tordera, D.; Bolink, H.J. *Org. Electron.* 14 (2013) 693–698.
123. Meier, S. B.; van Reenen, S.; Lefevre, B.; Hartmann, D.; Bolink, H. J.; Winnacker, A.; Sarfert, W.; Kemerink, M. *Adv. Funct. Mater.* 23 (2013) 3531–3538.
124. Reenen, S.V.; Janssen, R.A.J.; Kemerink, M. *Org. Electron.* 12 (2011) 1746.
125. Meier, S. B.; Hartmann, D.; Tordera, D.; Bolink, H. J.; Winnacker, A.; Sarfert, W. *Phys. Chem. Chem. Phys.* 14 (2012) 10886–10890.
126. Tang, S. ; Edman, L. *Electrochim. Acta* 56 (2011) 10473–10478.
127. Yu, Z.; Wang, M.; Lei, G.; Liu, J.; Li, L. and Pei, Q. *J. Phys. Chem. Lett.* 2 (2011) 367–372.
128. Yu, G.; Cao, Y.; Zhang, C.; Li, Y. F.; Gao, J.; Heeger, A. J. *Appl. Phys. Lett.* 73 (1998) 111–113.
129. Rudmann, H.; Rubner, M.F. *J. Appl. Phys.* 90 (2001) 4338.
130. Tordera, D.; Meier, S.; Lenes, M.; Costa, R.D.; Ortí, E.; Sarfert, W. and J. Bolink, H. *Adv. Mater.* 2012, 24, 897.

131. Liao, C. H.; Chen, h. f.; Su, H. C. and Wong, K. T. . *J. Mat. Chem.* 21, 2011, 17855.
132. Asadpoordarvish, A.; Sandström, A.; Tang, S.; Granström, J.; Edman, L. *Appl. Phys. Lett.* 100, (2012), 193508.
133. Tang, S.; Sandström, A.; Fang, J.; Edman, L. *J. Am. Chem. Soc.* 134 (2012) 14050.
134. Hosseini, A.R.; Koh, C.Y.; Slinker, J.D.; Flores-Torres, S.; Abruña, H. D. and Malliaras, G. G. *Chem. Mater.* 17 (2005) 6114.
135. Su H. C.; Wu, C. C. *Appl. Phys. Lett.* 89 (2006) 261118.
136. Liao, T.; Chen, H.F.; Su, H.C.; Wong, K.T. *Phys. Chem. Chem. Phys.* 14 (2012) 1262.
137. Sandström, A.; Dam, H. F.; Krebs, F. C. and Edman, L. *Nat. Commun.* 3 (2012) 1002.
138. Filiatrault, H. L., Porteous, G. C., Carmichael, R. S., Davidson, G. J. E. & Carmichael, T. B. *Adv. Mater.* 24 (2012) 2673.
139. European Energy Innovation Spring, 2013, p. 36.
140. Lee, J.; Yoo, D. S.; Handy, E.S.; M.F. *Appl. Phys. Lett* 1996, 69, 1986.
141. Rudmann, H.; Shimada, S.; Rubner, M. F. *J. Appl. Phys.* 2003, 94, 115.
142. Rudmann, H.; Shimada, S.; Rubner, M.F. *J. Am. Chem. Soc.* 2002, 124, 4918.
143. Rudmann, H.; Shimada, S.; Rubner, M. F.; Oblas, D. W.; Whitten, J. E. *J. Appl. Phys.* 2002, 92, 1576.
144. Armaroli, N.; Accorsi, G.; Holler, M.; Moudam, O.; Nierengarten, J. F.; Zhou, Z.; Wegh, R. T.; Welter, R. *Adv. Mater.* 2006, 18, 1313.
145. Moudam, O.; Kaeser, A.; Delavaux-Nicot, B.; Duhayon, C.; Holler, M.; Accorsi, G.; Armaroli, N.; Seguy, I.; Navarro, J.; Destruel, P.; Nierengarten, J.F. *Chem. Commun.* 2007, 3077.
146. Xia, H.; He, L.; Zhang, M.; Zeng, M.; Wang, X. M.; Lu, D.; Ma, Y.G. *Opt. Mater.* 2007, 29, 667.
147. Zhang, Q. S.; Ding, J. Q.; Cheng, Y.X.; wang, L.X.; Xie, Z.Y.; Jing, X.B; Wang, F. S. *Adv. Funct. Mater.* 2007, 17, 2983.

148. Costa, R.D.; Tordera, D.; Ortí, E.; Bolink, H.J.; Schonle, J.; Graber, S.; Housecroft, C.E.; Constable, E.C.; Zampese, J.A. *J. Mater. Chem.* 2011, 21, 10108.
149. Bernhard, S.; Gao, X.C.; Malliaras, G.G.; Abruña, H.D. *Adv. Mater.* 2002, 14, 433.
150. Buda, M.; Kalyuzhny, G.; Bard, A. j. *J. Am. Chem. Soc.* 2002, 124, 6090.
151. Bernhard, S.; Barron, J.A.; Houston, P.L.; Abruña, H.D.; Ruglovsky, J.L.; Gao, X.C.; Malliaras, G. G. *J. Am. Chem. Soc.* 2002, 124, 13624.
152. Slinker, J.D.; Gorodetsky, A.A.; Lowry, M.S.; Wang, J.J.; Parker, S.; Rohl, R.; Bernhard, S.; Malliaras, G.G. *J. Am. Chem. Soc.* 2004, 126, 2763.
153. Lowry, M.S.; Goldsmith, J.I.; Slinker, J.D. Rohl, R.; Pascal, R.A.; Malliaras, G.G.; Bernhard, S. *Chem. Mater.* 2005, 17, 5712.
154. Terki, R.; Simoneau, L.P.; Rochefort, A. *J. Phys. Chem. A.* 2009, 113, 534.
155. Durham, B.; Caspar, J.V.; Nagle, J.K.; Meyer, T.J. *J. Am. Chem. Soc.* 1982, 104, 4803.
156. Thompson, D.W.; Wishart, J.F.; Brunshwig, B.S.; Sutin, N. *J. Phys. Chem. A.* 2001, 105, 8117.
157. Costa, R. D.; Cespedes-Guirao, F. J.; Ortí, E.; Bolink, H. J.; Gierschner, J.; Fernandez-Lazaro, F.; Sastre-Santos, A. *Chem. Commun.* 2009, 3886.
158. He, L.; Duan, L..A.; Qiao, J. A.; Zhang, D.Q.; Wang, L.D.; Qiu, Y. *Org. Electron.* 2010, 11, 1185.
159. Tamayo, A.B.; Garon, S.; Sajoto, T.; Djurovich, P.I.; Tsyba, I.M.; Bau, R.; Thompson, M.E. *Inorg. Chem.* 2005, 44, 8723.
- 160.[Su, H.C.; Fang, F.C.; Hwu, T.Y.; Hsieh, H.H.; Chen, H.F.; Lee, G.H.; Peng, S.M.; Wong, K.T.; Wu, C.C. *Adv. Funct. Mater.* 2007, 17, 1019.
161. Slinker, J.D.; Koh, C.Y.; Malliaras, G.G.; Lowry, M.S. Bernhard, S. *Appl. Phys. Lett.* 2005, 86, 173506.
162. Bolink, H.J.; Coronado, E.; Costa, R.D.; Lardies, N.; Nazeeruddin, M.K.; Ortí, E. *P. Soc. Photo-Opt. Ins.* 2008, 6999, L9992.
163. He, L.; Qiao, J.; Duan, L.; Dong, G.F.; Zhang, D.Q.; Wang, L.D.; Qiu, Y. *Adv. Funct. Mater.* 2009, 19, 2950.

164. Nazeeruddin, M.K.; Wegh, R.R.T.; Zhou, Z.; Klein, C.; Wang, Q.; De Angelis, F.; Fantacci, S.; Gratzel, M. *Inorg. Chem.* 2006, 45, 9245.
165. Hu, T.; Duan, L.; Qiao, J.; Zhng, D.Q.; Wang, L.D.; Qiu, Y. *Chem. Commun.* 2011, 47, 6467.
166. Bolink, H.J.; Cappelli, L.; Cheylan, S.; Coronado, E.; Costa, R.D.; Lardies, N.; Nazeeruddin, M.K.; Ortí, E. *J. Mater. Chem.* 2007, 17, 5032.
167. Mydlak, M.; Bizzarri, C.; Hartmann, D.; Sarfert, W. Schmid, G.; De Cola, L. *Adv. Funct. Mater.* 2010, 20, 1812.
168. Yang, C.H.; Beltran, J.; Lemaun, V.; Cornil, J.; Hartmann, D.; Sarfert, W.; Frohlich, R.; Bizzarri, C.; De Cola, L. *Inorg. Chem.* 2010, 49, 9891.
169. He, L.; Duan, L.; Qiao, J.A.; Dong, G.F.; Wang, L.D.; Qiu, Y. *Chem. Mater.* 2010, 22, 3535.
170. Su, H.C.; Chen, H.F.; Shen, Y.C.; Liao, C.T.; Wong, K.T. *J. Mater. Chem.* 2011, 21, 9653.
171. Wu, H.B.; Chen, H.F.; Liao, C.T.; Su, H.C.; Wong, K.T. *Org. Electron.* 2012, 13, 483.
172. Su, H.C.; Chen, H.F.; Chen, P.H.; Lin, S.W.; Liao, C.T.; Wong, K. T. *Phys. Chem. Chem. Phys.* 2011, 24, 1896.
173. Sessolo, M.; Toderà, D.; Bolink, H.J. *Acs Appl Mater. Inter.* 2013, 5, 630.
174. He, L.; Duan, L.; Qiao, J.; Wang, R. J.; Wei, P.; Wang, L. D.; Qiu, Y. *Adv. Funct. Mater.* 19 (2009) 2950–2960.
175. Tang, S.; Pan, J.; Buchholz, H. A. and Edman, L. *J. Am. Chem. Soc.* 135 (2013) 3647–3652.
176. Markvart, T. *Electricity from the sun*. In T. Markvart (Ed.), *Solar Electricity* (pp. 1-4). (2000). Chichester, England: John Wiley
177. Fifteenth Inventory – Edison 2013. Worldwide electricity production from renewable energy sources. (<http://www.energies-renouvelables.org/observ-er/html/inventaire/Eng/sommaire.asp#chapitre3>).
178. Becquerel, E. *Comptes Rendus*, 9, 561, 1839.
179. Chapin, D. M.; Fuller, C. S. and Pearson, G. L. *J. Appl. Phys.*, 1954, 25, 676

180. Green, M. A. *Solar Cells*, The University of New South Wales, Kensington, Australia, 1998.
181. Green, M. A., Emery, K., Hishikawa, Y., & Warta, W. (2010). Solar cell efficiency tables (version 36). *Progress in Photovoltaics: Research and Applications*, 18, 346-352.
182. Jackson, P.; Hariskos, D.; Lotter, E.; et al. *5th World Conference on Photovoltaic Energy Conversion (WCPEC-5)*, *Progress in Photovoltaics*, 2010, 19, 7.
183. Nelson, J. *Curr. Opin. Solid State Mater. Sci.*, 2002, 6, 87.
184. *Organic Photovoltaics: Mechanisms, Materials and Devices*, ed. S. S. Sun and N. S. Sariciftci, Taylor and Francis, Boca Raton, FL, 2005.
185. Shaheen, S.E.; Ginley, D. S. and Jabbour, G. E. *MRS Bull.*, 2005, 30, 10.
186. Hoppe, H. and Sariciftci, N. S. *J. Mater. Res.*, 2004, 19, 1924.
187. Spanggaard, H. and Krebs, F. C. *Sol. Energy Mater. Sol. Cells*, 2004, 83, 125.
188. <http://www.nrel.gov/ncpv/>
189. Kojima, A.; Teshima, K.; Miyasaka, T. and Shirai, Y. *Novel photoelectrochemical cell with mesoscopic electrodes sensitized by lead-halide compounds*(2). Books of Abstracts (#397), 210th ECS Meeting, Cancun, Mexico, October 29–November 3, 2006, The Electrochemical Society, Pennington, New Jersey, 2006.
190. Kojima, A.; Teshima, K.; Shirai, Y. and Miyasaka, T. *J. Am. Chem. Soc.* 131, 6050 (2009).
191. Im, J.-H., Lee, C.-R., Lee, J.-W., Park, S.-W. & Park, N.-G. *Nanoscale* 3, 4088–4093 (2011).
192. Mitzi, D.B. *Progress in Inorganic Chemistry* Vol. 48, 1999. ISBN 0-471-32623-2
193. Kitazawa, N.; Watanabe, Y.; Nakamura, Y. *Journal Of Materials Science* **37** (2002) 3585.
194. Mitzi, D. B. *J.Mater. Chem.* 2004, 14, 2355.
195. Kojima, A.; Ikegami, M.; Teshima, K. and Miyasaka, T. *Chem. Lett.* 2012, 41, 397399.

196. Kim, H.-S.; Lee, C.-R.; Im, J.-H.; Lee, K.-B.; Moehl, T.; Marchioro, A.; Moon, S.-J.; Humphry-Baker, R.; Yum, J.-H.; Moser, J. E.; Grätzel, M.; Park, N.-G. *Sci. Rep.* 2012, 2, 591.
197. Lee, M. M.; Teuscher, J.; Miyasaka, T.; Murakami, T. N.; Snaith, H. J. *Science* 2012, 338, 643–647.
198. Heo, J. H.; Im, S. H.; Noh, J. H.; Mandal, T. N.; Lim, C.-S.; Chang, J. A.; Lee, Y. H.; Kim, H.-J.; Sarkar, A.; Nazeeruddin, M. K.; Grätzel, M. and Seok, S. I. *Nature Photon.* 7, 486–491 (2013).]
199. Noh, J. H., Im, S. H., Heo, J. H., Mandal, T. N. & Seok, S. I. *Nano Lett.* 13, 1764, (2013).
200. Burschka, J.; Pellet, N.; Moon, S.-J.; Humphry-Baker, R.; Gao, P.; Nazeeruddin, M. K. and Grätzel, M. *Nature* 499, 316–319 (2013).
201. Liu, M., Johnston, M. B. & Snaith, H. J. *Nature* 501, 395–398 (2013)
202. Malinkiewicz, O.; Aswani, Y.; Lee, Y. H.; Minguez-Espallargas, M.; Graetzel, M.; Nazeeruddin, M. K.; Bolink, H. J. *Nature Photon.* 8, 128–132 (2014)
203. Etgar, L.; Gao, P.; Xue, Z.; Peng, Q.; Chandiran, A.K.; Liu, B.; Nazeeruddin, M.K.; Grätzel, M. *J. Am. Chem. Soc.* 134, 17396–17399 (2012).
204. Zhou, H.; Chen, Q.; Li, G.; Luo, S.; Song, T.-b.; Duan, H.-S.; Hong, Z.; You, J.; Liu, Y.; Y. Yang, *Science*, 345, 542 (2014)
205. Yin, W.-J.; Shi, T. and Yan, Y. *Appl. Phys. Lett.* 104 , 063903 (2014)
206. Wan-Jian Yin , Tingting Shi , and Yanfa Yan *Adv. Mater.* 2014, 26, 4653–4658
207. Sun, S.; Salim, T.; Mathews, N.; Duchamp, M.; Boothroyd, C.; Xing, G.; Sumb, T. C. and Lam, Y. M. *Energy Environ. Sci.*, 2014, 7, 399–407
208. Roiati, V.; Colellad, S.; Lerario, G.; De Marco, L.; Rizzo, A.; Listorti, A. and Giglia, G. 10.1039/x0xx00000x
209. Aharon, S.; Gamliel, S.; Cohen, B.E. and Etgar, L. DOI: 10.1039/c4cp00460d
210. Schulz, P.; Edri, E.; Kirmayer, S.; Hodes, G.; Cahenb, D. and Kahn, A. *Energy Environ. Sci.*, 2014, 7, 1377
211. Halls, J. J. M.; Cornil, J.; dos Santos, D. A.; Silbey, R.; Hwang, D. H.; Holmes, A. B.; Bredas, J. L. and Friend, R. H. *Phys. Rev. B: Condens. Matter*, 1999, 60, 5721.



212. Barth, S. and Bassler, H. *Phys. Rev. Lett.*, 1997, 79, 4445.
213. Deibel, C. and Dyakonov, V., *Rep Prog Phys* (2010) 73 (9), 096401.
214. Forrest, S. R., *Nature* (2004) 428 (6986), 911.
215. Ponseca, C. S.; Savenije, T. J.; Abdellah, M.; Zheng, K.; Yartsev, A.; Pascher, T.; Harlang, T.; Chabera, P.; Pullerits, T.; Stepanov, A.; Wolf, J.-P. and Sundström, V. *J. Am. Chem. Soc.* 136, 5189 (2014).
216. Mitzi, D. B. *J. Chem. Soc. Dalton Trans.* 1, 1 (2001).
217. Stoumpos, C. C., Malliakas, C. D. & Kanatzidis, M. G. *Inorg. Chem.* 52, 9019 (2013).
218. Coropceanu, V.; Cornil, J.; da Silva Filho, D. A.; Olivier, Y.; Silbey, R. and Brédas, J.-L. *Chem. Rev.*, 2007, 107, 926.
219. Xing, G.; Mathews, N.; Sun, S.; Lim, S. S.; Lam, Y. M.; Grätzel, M.; Mhaisalkar, S.; Sum, T. C. *Science* 342, 344–347 (2013).
220. Stranks, S. D.; Eperon, G. E.; Grancini, G.; Menelaou, C.; Alcocer, M. J. P.; Leijtens, T.; Herz, L. M.; Petrozza, A.; Snaith, H. J. *Science* 342, 341–344 (2013).
221. Wehrenfennig, C.; Liu, M.; Snaith, H. J.; Johnston, M. B. and Herz, L. M. *Energy Environ. Sci.*, 2014, 7, 2269.
222. Snaith, H. J.; Abate, A.; Ball, J. M.; Eperon, G. E.; Leijtens, T.; Noel, N. K.; Stranks, S. D.; Wang, J. T-W; Wojciechowski, K. and Zhang, W. <http://pubs.acs.org> on March 25, 2014.
223. Jeon, N. J.; Noh, J. H.; Kim, Y. C.; Yang, W. S.; Ryu, S. and Seok, S. I. *Nature Mater.* 13, 897–903 (2014).
224. Juarez-Perez, E. J.; Sanchez, R. S.; Badia, L.; Garcia-Belmonte, G.; Kang, Y. S.; Mora-Sero, I.; Bisquert, J. *J. Phys. Chem. Lett.* 5, 2390–2394 (2014).
225. Dualeh, A.; Moehl, T.; Nazeeruddin, M. K.; Gratzel, M. *ACS Nano* 8, 362–373 (2014)
226. Jeon, N. J.; Noh, J. H.; Kim, Y. C.; Yang, W. S.; Ryu, S. and Seok, S. DOI: 10.1038/NMAT4014
227. Liang, P-W; Liao, C.-Y; Chueh, C.-C.; Zuo, F.; Williams, S. T.; Xin, X-K; Lin, J.; and Jen, A. K.-Y. DOI: 10.1002/adma.201400231

228. Hao, F.; Stoumpos, C. C.; Cao, D. H.; Chang, R. P. H. & Kanatzidis, M. G. *Nature Photon.* 8, 489 (2014).
229. Noel, N. K.; Stranks, S. D.; Abate, A.; Wehrenfennig, C.; Guarnera, S.; Haghighirad, A.-A.; Sadhanala, A.; Eperon, G. E.; Pathak, S. K.; Johnston, M. B.; Petrozza, A.; Herza, L. M. and Snaith, H. J. *Energy Environ. Sci.* [http://dx.doi.org/ 10.1039/c4ee01076K](http://dx.doi.org/10.1039/c4ee01076K) (2014)
230. Hao, F.; Stoumpos, C. C.; Chang, R. P. H. and Kanatzidis, M. G. [dx.doi.org/10.1021/ja5033259](http://dx.doi.org/10.1021/ja5033259).
231. Lee, J.-W.; Seol, D.-J.; Cho, A.-N and Park, N.-G *Adv. Mater.* 2014, 26, 4991.
232. Amat, A.; Mosconi, E.; Ronca, E.; Quarti, C.; Umari, P.; Nazeeruddin, Md. K.; Grätzel, M. and De Angelis, F. DOI: 10.1021/nl5012992.
233. Lv, S.; Pang, S.; Zhou, Y.; Padture, N. P.; Hu, H.; Wang, L.; Zhou, X.; Zhu, H.; Zhang, L.; Huang, C. and Cuia, G. DOI: 10.1039/x0xx00000x

# **Chapter 2**

## **Experimental**



## 2. Metodology & characterization techniques

All the experimental details related with the content of this memory are specifically described in each chapter. A brief description of some techniques and global information can be found below.

All the experiments were carried out in a clean atmosphere, inside two class 10000 clean rooms, both shown in Fig. 2.1. The evaporation process and the characterization of the devices were completed inside an MBrawn glove box to ensure an appropriate atmosphere for the non-encapsulated devices ( $<0.01$  ppm  $O_2$  and  $<0.01$  ppm  $H_2O$ )



**Fig. 2.1** Clean-room class 10000 at the Molecular Science Institute, at the University of Valencia (left), and clean-room at the Department of Physical Chemistry in the University of Cordoba (right).

### 2.1 Organized thin films

All the Langmuir monolayers studied during the realization of this memory were prepared in a Langmuir trough with a Wilhelmy System. This system is based on a highly sensitive electronic microbalance that is connected to the air-water interface through a small piece of paper. When the monolayer is spread over the water surface, the surface tension ( $\gamma$ ) changes, and it is possible to measure the surface

pressure  $\pi$  (see Eq. 1.1). The Langmuir trough used in this memory are NIMA models 611D and 601BAM.

## UV-Vis-Normal Reflection Spectroscopy

The reflection measurements were carried out in a *Nanofilm RefSpec2* equipment supplied by *Nanofilm GmbH* (nowadays *Accurion GmbH*, Göttingen, Germany).<sup>1</sup> In this technique the light source is composed by both tungsten and deuterium lamps. The produced light is first collimated and then directed perpendicular to the air-water interface through a double head optic fiber. Hence the angle of incidence is  $\theta_i = 0^\circ$ . Once the light reaches the interface, it is partially reflected and directed, via a second optic fiber, to a charge-couple detector, where it is analyzed. To avoid multiple reflections and contamination from the subphase, a light trap is positioned at the bottom of the trough. Two choppers connected electronically, one close to the light source and a second one at the edge of the optic fiber, alternate the incident and reflected light. A schedule of the process is shown in Fig. 2.2.

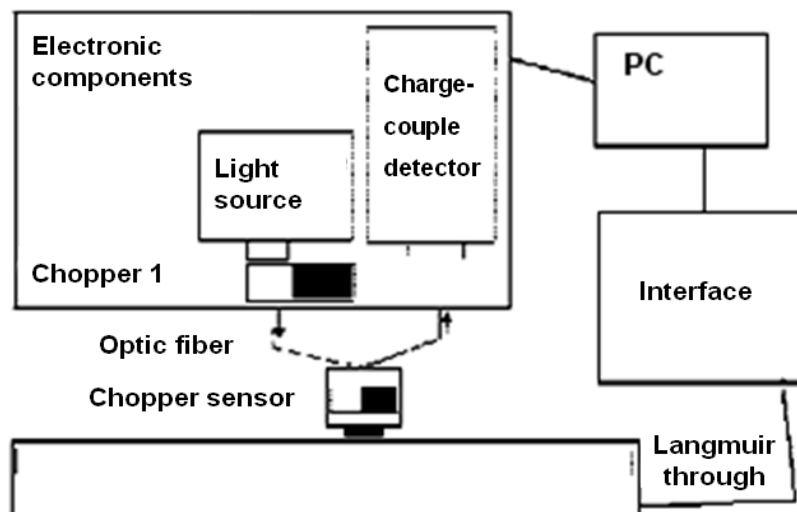


**Fig. 2.2.** Schedule of the ReflSpec equipment.

## UV-Vis-va Reflection Spectroscopy

The equipment used for these measurements is an extended version of the ReflSpec explained in the above Section, model RefSpec2 VA (supplied by Accurion GmbH, Göttingen, Germany). In this case the equipment is provided by two motorized arms that allows a precision motorized adjustment of the angle-of-incidence. At the same time, it contains a motorized polarizer and analyzer that can be easily and precisely controlled (p&s polarization flip).<sup>2</sup> The lamp is a Xe-light source that allows to work in a spectral region in the range from 240-980 nm. Due to its innovative configuration, the study of orientation effects and optical dichroism in absorbing thin films is possible. Fig. 2.3 shows a schedule of the equipment.

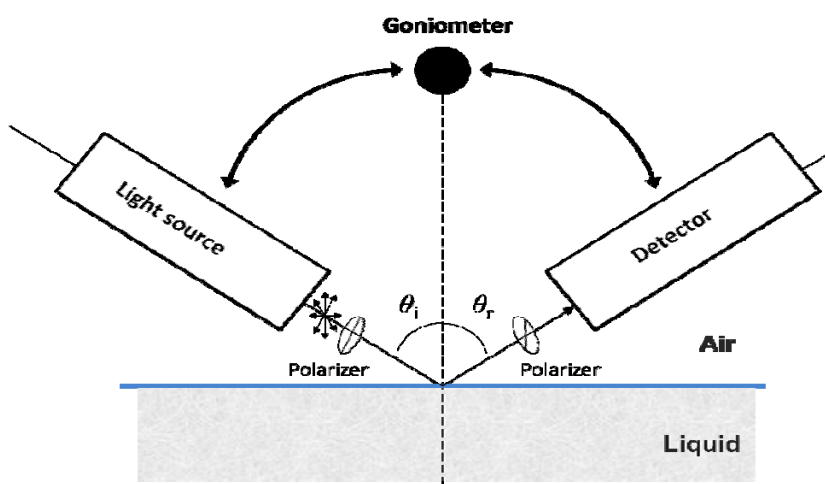


**Fig. 2.3.** Diagram of the RefSpec2 VA equipment.

## Brewster Angle Microscopy (BAM)

BAM pictures were taken in a commercial BAM equipment *Nanofilm I-Elli2000*.<sup>1,3</sup> This equipment is based on a laser source (Nd:YAG, 50 mW, 532 nm) with a light diameter  $\sim 1.3$  mm that is p-polarized before affecting the air-water interface at an angle  $\theta = 53.1^\circ = \theta_{B \text{ air-water}}$ . To avoid contamination from the refracted light it is used a black light tramp at the bottom of the trough. The reflected light is

then collected by an analyzer with a focal length of 20 mm and directed to a high sensitive charge-coupled detector. This detector converts the intensity of the reflected light from very small regions of the monolayer into a pixel picture (768 x 562 pixels), which allows an easier analysis. The lateral resolution of the optic system is 2  $\mu\text{m}$ . Additionally, the analyzer allows to observe the possible anisotropy existing inside the domains, which results from the different organization of the molecules in the monolayer. This is possible by rotating the analyzer respect to the p-direction of the light. All the equipment is located on anti-vibration table Halcyonics MOD-2 S.

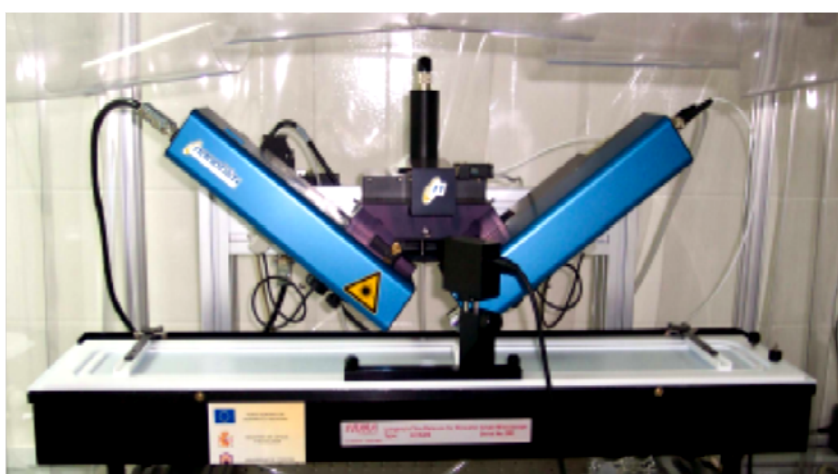


**Fig. 2.4.** Photograph of the Brewster Angle Microscopy used in this memory.

## **2.2 Thin films in optoelectronics**

The solution processed layers were prepared in a Spin-coater Model *Chemsols CSS-05* and a Coatmaster Model 510, inside the cleanroom. For the evaporated films two different high vacuum evaporators were used: an Edwards Auto500 evaporator for the inorganic films such as metal or metal oxides films, and an MBraun MOLevap, with two temperature controlled evaporation sources from Creaphys fitted with ceramic crucibles, for evaporating the hybrid perovskite.

All the thicknesses were determined with an Ambios XP-1 profilometer, a computerized, high sensitivity surface profiler that measures roughness and step



heights. It consists on a diamond stylus, which is moved vertically in contact with a sample and then moved laterally across the sample for a specified distance and specified contact force. It features the ability to measure precision step heights from under 10 angstroms to as large as 1 millimeter as a function of position, with a vertical resolution of 1Å at 10µm and 15Å at 100µm.

## Light emitting electrochemical cells (LECs)

The typical response of a LECs under an applied voltage (or current density), follows a slow increase on luminance and current density with time (or decrease on voltage), which after reaching a maxima value of luminance ( $L_{max}$ ) decreases. This behavior is due to the previously described dynamic nature of these devices, which are self-limited due to the growing of the doped zones. In the following text are describe the most important parameters of LECs, which determine the performance of such devices.

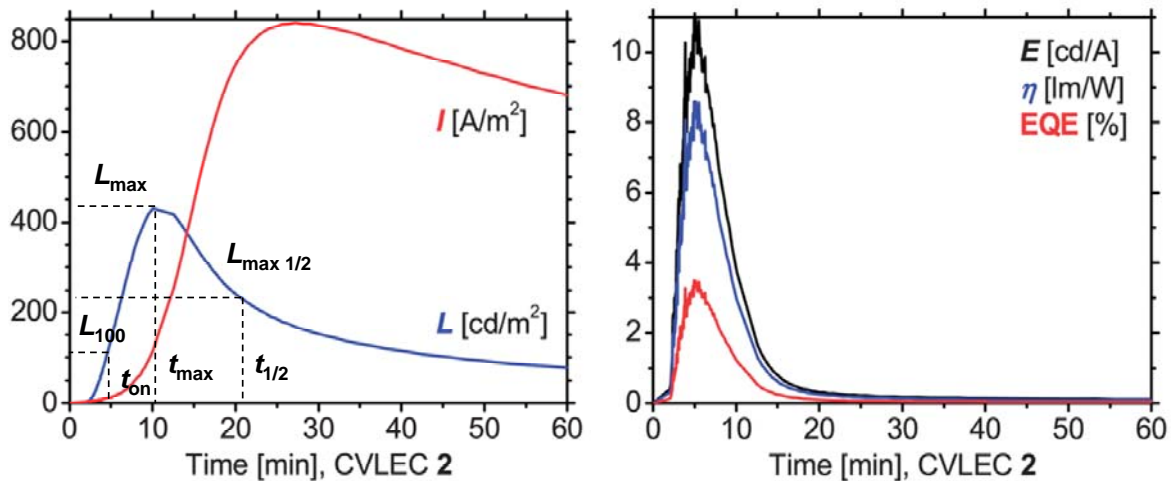


**Fig. 2.5.** Typical time-dependence of luminance, current, efficacy, power-efficiency and EQE of a constant-voltage LEC device.<sup>4</sup>

- *Luminance (L)*: Flux of light measured in candela per surface unit ( $\text{cd m}^{-2}$ ) that the device emits at a given moment.
- *Current density (J)*: Flux of current measured in ampere per surface unit ( $\text{A m}^{-2}$ ).

- *Voltage (V)*: The voltage applied or measured in a working device. For a pulsed driving cell, the voltage is the averaged between the on- and off- time of the pulse.
- *Turn-on time ( $t_{on}$ )*: Time to reach the maximum luminance ( $t_{on}$ ) or time to reach  $100 \text{ cd m}^{-2}$  ( $t_{100}$ ).
- *Lifetime ( $t_{1/2}$ )*: Time to reach the half of the maximum luminance. This parameter is related with the stability of the LEC. Sometimes, an alternative definition is the time to reach one fifth of the maximum luminance ( $t_{1/5}$ ).
- *Current efficiency*: The flux in candela per electrical ampere ( $\text{cd A}^{-1}$ ).
- *Power efficiency ( $\eta$ )*: The flux of light measured in lumens per electric watt ( $\text{Lm W}^{-1}$ ). The stated values in literature correspond normally to the maximum value observed. In pulsed-driving cells, the duty cycle has to be taken into account.
- *External Quantum Efficiency (EQE)*: The ratio of photons emerging from the device per injected electron. Theoretically, it can be defined as

$$EQE = \frac{b\Phi}{2n^2} \quad (2.1)$$

where  $b$  is the recombination efficiency (equal to unit for two ohmic contacts),<sup>5</sup>  $\Phi$  is the fraction of electrons that decay radiatively, and  $n$  is the refractive index of the glass substrate, equal to 1.5 (the factor  $1/2n^2$  accounts for the coupling of light out of the device).

- *Electroluminescent spectrum (EL spectrum)*: Gives the information about the color of emission of the device. The peak of the EL spectrum is often reported as  $\lambda_{\text{max}}$ .
- *Commission Internationale de l'Eclairage coordinates ( $CIE_{x,y}$ )*: These coordinates provide the color purity relative to the red, green and blue receptors of the human

eye, giving an exact definition of the emission color according to universally accepted international standards.

The photoluminescence spectra and the quantum yield were measured in a Hamamatsu C9920-02 Absolute PL Quantum Yield Measurement System. It consists on an excitation system based on a Xe lamp linked to a monochromator. The light is first collimated to an optic fiber and guided to an integrated sphere where the sample is fitted. Once the light reaches the sample, a second optic fiber guides the global light from the sphere (resulted from the difference between the incident, absorbed and emitted light) through a multi-channel spectrometer, from where it is processed and analyzed.

The electroluminescence spectra were obtained by using an Avantes fiberoptics photospectrometer. The voltage versus time ( $V - t$ ) and electroluminescence versus time ( $Lum - t$ ) characteristics at a constant current density were collected using a Keithley Model 2400 source measurement unit and a Si-photodiode (Hamamatsu S1336-8BK) coupled to a Keithley Model 6485 pico-amperometer, respectively. The calibration of the photocurrent was carried out using Minolta LS100 luminance meter.

The device lifetime data of pulsed-current were carried out by applying a pulsed current ( $200 \text{ mA cm}^{-2}$ , duty cycle 50%) and monitoring the luminance and the voltage versus time with a Botest OLT OLED Lifetime-Test System equipped with a True Colour Sensor MAZeT (MTCSiCT Sensor).

## Photovoltaic devices

The current-density vs. voltage ( $J-V$ ) characteristics of most efficient inorganic and organic solar cells resembles the exponential response of a diode when they are measure in the dark, without illumination of sun. Under forward bias they exhibit high current densities, which considerably decrease in reverse bias. Shining light on a device generates a photocurrent in the cell in addition to the diode behavior, and the resulting  $J-V$  curve is ideally the superposition of both dark and photocurrent.

In the following text will be described the most important parameters for solar cells, which determines their performances. Fig. 2.5 shows the ideal  $J$ - $V$  curve for an illuminated solar cell, where main figures of merits are shown.

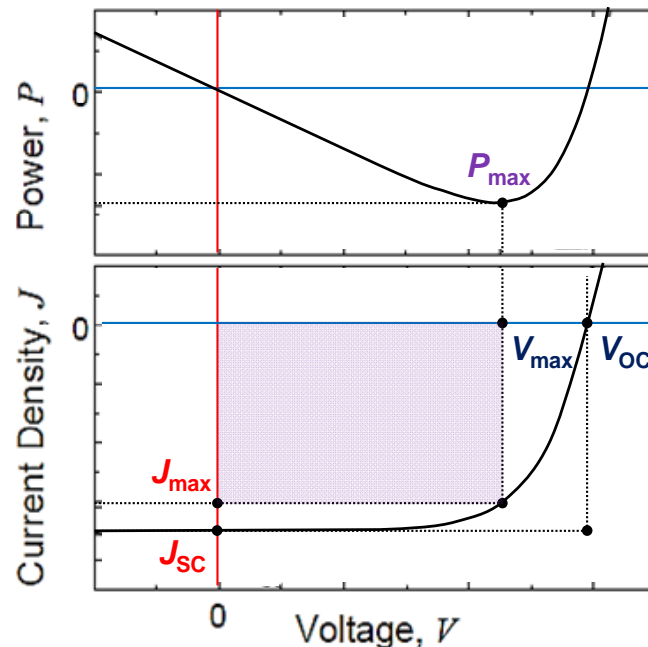


**Fig. 2.5** depicts the  $J$ - $V$  plot for an idealized solar cell in the region of power generation.

- *Open-circuit voltage* ( $V_{OC}$ ): Voltage across the solar cell when the device is open-circuited under illumination ( $J = 0 \text{ A m}^{-2}$ ). This voltage represents the point at which the photocurrent generation and dark compensates, thus marks the limit in the voltage for generating power.
- *Short-circuit current density* ( $J_{SC}$ ): Current density when  $V=0$ , which is the same condition as the two electrodes of the cell being short-circuited together. In ideal devices  $J_{SC}$  equals to the photocurrent density ( $J_{ph}$ ), and marks the limit of the power generation.
- *Power density* ( $P$ ): Product of voltage and current density ( $V \times J$ ). The maximum value ( $P_{max}$ ) occurs at the voltage and current-density where the product of both is maximum in absolute value ( $V_{max}$  and  $J_{max}$  respectively). Ideally it would be  $V_{OC}$

and  $J_{SC}$ . Nevertheless, real cells exhibit  $V_{max} < V_{OC}$  and  $J_{max} < J_{SC}$ , thus  $P_{max}$  normally differs from ideality.

- *Fill factor* (FF): Ratio between  $P_{max}$  and  $P_{ideal}$ , thus it indicates how far from ideality is the power density ( $P$ ) of the cell. FF is always lower than unity, being normally related with a bad device quality. It is define as

$$FF = \frac{J_{max}V_{max}}{J_{sc}V_{oc}} \quad (2.2)$$

- *Power conversion efficiency* ( $\eta$  or PCE): The percentage of incident irradiance  $I_L$  (light power per unit area) that is converted into output power. For consistency, the maximum value  $P_{max}$  is used to avoid dependencies on voltage and is expressed as

$$\eta = \frac{|J_{max}| \times V_{max}}{I_L} \times 100\% = \frac{FF \times |J_{sc}| \times V_{oc}}{I_L} \times 100\% \quad (2.3)$$

- *External quantum efficiency* (EQE): Fraction of incident photons converted into current at a specific wavelength. Knowing the spectral irradiance from the light source and the  $EQE(\lambda)$ , it is possible to estimate the  $J_{SC}$ .

Solar cells were measured with a MiniSun simulator (ECN the Netherlands) based on a white light halogen lamp in combination with interference filters for the EQE and current-voltage ( $J$ - $V$ ) measurements. To delimit the active area of the device and avoid possible errors in efficiency, a black mask was positioned on top of the cell. Before each measurement, the exact light intensity was determined using a calibrated Si reference diode. An estimation of the short-circuit current density ( $J_{SC}$ ) under standard test conditions was calculated by convolving the EQE spectrum with the AM1.5G reference spectrum, using the premise of a linear dependence of  $J_{SC}$  on light intensity. Current-voltage ( $J$ - $V$ ) characteristics were measured using a Keithley 2400 source measure unit. The scan was performed with steps of 0.01 V starting from  $-0.2$  V to 1.1 V with a time delay between each point set to 0.01 s.

## References

1. Grüniger, H.; Möbius, D.; Meyer, H.; *J. Chem. Phys.* 1983, 79, 3701
2. <http://www.accurion.com>
3. Hönig, D.; Möbius, D.; Overbeck, G. *Adv. Mater.* 1992, 4, 419
4. Shavaleev, N. M.; Scopelliti, R.; Grätzel, M.; Nazeeruddin, M.K.; Pertegás, A.; Roldán-Carmona, C.; Tordera, D. and H.J. Bolink *J. Mater. Chem. C*, 2013, 1, 2241
5. Malliaras, G.G.; Scott, J.C. *J. Appl. Phys.* 1998, 83, 5399.

## **Results & Discussion**





This Thesis reprints a selection of papers in refereed journals in which the author of this Thesis was author or co-author. The articles themselves contain an introduction to their special topic, the experimental setup, the results and discussion, and the conclusions. They are reprinted in the style of this Thesis. An overview and summary of the research described in the publications is found in Chapter 6, as well as the summary of the most important conclusions, which can be found in Chapter 7.



## **Chapter 3**

# **Physical control of thin films at the air–water interface**



## 3.1 Revisiting the Brewster Angle Microscopy:

### The relevance of the polar headgroup

**Roldán-Carmona, C.;** Giner-Casares, J.J.; Perez-Morales, M.; Martin-Romero, M.T. and Camacho, L.

<sup>1</sup>*Dept. of Physical Chemistry, University of Córdoba, C. Rabanales, Ed. C3, Córdoba, 14014 (Spain).*

<sup>2</sup>*Max Planck Institute of Colloids and Interfaces, 14476 Potsdam (Germany).*

The Brewster Angle Microscopy (BAM) is a powerful microscopy technique allowing the in situ visualization of the morphology of Langmuir monolayers at the air/water interface. The use of the BAM for attaining structural insights in the molecular arrangement of the Langmuir monolayers is widespread. In this review, we examine the reflection of a Langmuir monolayer under a rather different perspective than classical: the influence of the polar headgroup of the amphiphiles in the BAM images is taken into account. The relevance of the polar headgroup as the main cause of the BAM features has been the focus of a reduced number of BAM studies. An emerging experimental and theoretical framework from recent bibliography is discussed.

Different theoretical scenarios are considered, concerning the size and absorption of radiation of the polar headgroup. Two qualitative examples showing physical phenomena regarding the reflectivity changes in a BAM experiments are discussed. The anisotropy in the BAM images as inner textures is of special interest. Quantitative structural information of the molecular arrangement of the monolayer is obtained by simulating the textures of the domains observed. The quantitative assessment of the detailed molecular arrangement of the polar headgroup by BAM is highly valuable, as this information can hardly be obtained from other experimental techniques. The procedure for extracting quantitative structural data from the experimental BAM pictures is revised in detail from the recent bibliography for further application of this model to different Langmuir monolayers.

Paper published in *Advances in Colloid and Interface Science* 173 (2012) 12–22

### 3.1.1. Introduction

The Brewster Angle Microscopy (BAM) was proposed in 1991 as a direct and non-invasive method to study the micrometric morphology of Langmuir monolayers. The BAM has become one of the most attractive and powerful techniques for the in situ studies of the amphiphilic molecules forming Langmuir monolayers at the air/water interface.<sup>1,2</sup> The BAM technique is based on the change of the refractive index by a Langmuir monolayer at the air/water interface with respect to the bare air/water interface. By imaging a p-polarized laser beam reflected off the interface at the Brewster angle of the bare air/water interface no radiation is reflected. When a Langmuir monolayer is placed on the air/water interface, the change in the refractive index leads to a change on the value of the Brewster angle. A certain percentage of the incident light is reflected from the Langmuir monolayer. The recording of this reflected light by a video camera allows the direct observation of micrometer-sized structures in the Langmuir monolayer. The BAM is suitable for the study of Langmuir monolayer formed by a wide variety of amphiphilic molecules, most commonly fatty acids and alcohols, phospholipids, liquid crystals, and polymers.<sup>1-12</sup>

The morphology of Langmuir monolayers can also be visualized with fluorescence microscopy.<sup>13,14</sup> In contrast to fluorescence microscopy, BAM has the unique advantage that it does not require the introduction of probe molecules, but rather uses the intrinsic optical properties of the monolayer. Furthermore, mono- and multilayers transferred onto solid substrates by the Langmuir–Blodgett method can also be studied by BAM.<sup>15,16</sup> Therefore, a wide range of applications for the BAM in colloid and interface science has been exploited. An exhaustive revision of these applications is beyond the scope of this review. The interested reader is referred to previous reviews by Vollhardt.<sup>15-17</sup> As representative examples, the following processes as monitored by BAM are highlighted: domain formation as consequence of ordering phenomena,<sup>18-20</sup> 2D into 3D transitions,<sup>21-23</sup> monitoring of interfacial chemical reactions,<sup>24,25</sup> and formation of films by inorganic nanoparticles.<sup>26,27</sup>

The phase transitions of a given Langmuir monolayer are usually observed in BAM by the appearance of domains. In the absence of anisotropy in the Langmuir monolayer, the domains are related to a condensed phase. The observance of the domains arises from the reflection from the alkyl chains and the polar headgroup.

Of special interest concerning the molecular arrangement is the occurrence of inner textures within the domains observed by BAM. The inner textures are related with the anisotropy. The appearance of inner textures within the domains is indicative of the existence of a high molecular ordering in the Langmuir monolayer. Extensive studies have been successfully performed for the scenario of anisotropy in the arrangement of the hydrophobic chains. In the examples shown in Fig. 1, the molecular organization of Langmuir monolayers of new surface-active derivatives of amino acids was analyzed by Ignés-Mullol et al., observing inner textures within the domains corresponding to different values of azimuthal angle.<sup>28</sup> A relevant example is the study of the lipid dipalmitoyl-phosphatidylglycerol (DPPG) performed by Vollhardt et al., in where the whole domains display different azimuthal angle with respect to each other, displaying instead an homogeneous texture within each single domain.<sup>20</sup> In a further investigation by Vollhardt concerning the arrangement of the alkyl chains leading to changes in the domain morphology observed by BAM, pyrimidine derivatives present in the subphase could be attached to amphiphilic melamine monolayers by complementary hydrogen bonding of the headgroups. Remarkably, in this case highly specific changes of the domain morphology observed by BAM do not correspond to large modifications of the alkyl chain arrangement. On the contrary, the pyrimidine derivatives play a main role being attached to the polar headgroup by a specific recognition process.<sup>29</sup>

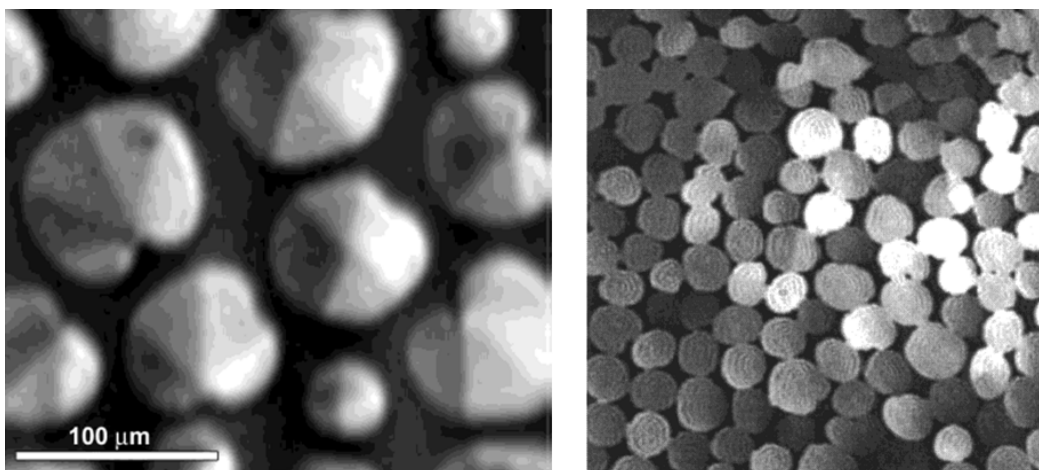


**Fig. 3.1.** Left: Langmuir monolayer of a diacyl amino acid-based surfactant in the LC–LE coexistence.<sup>28</sup> Right: Langmuir monolayer of dipalmitoyl-phosphatidylglycerol (DPPG).<sup>20</sup> Both pictures were acquired with the position of the BAM analyzer at 60° to maximize the contrast in the inner texture. Copyright from the American Chemical Society, 2003 and 2000.

Traditionally, the information provided by BAM has been related with the molecular organization of the alkyl chains of the surfactants, although some authors study the sensitive effect in a not declared way of head group changes on the domain morphology.<sup>29–32</sup> Most of the early BAM studies focused in amphiphilic compounds with simple polar groups, such as hydroxyl,<sup>6</sup> carboxylic,<sup>33</sup> or ammonium.<sup>34</sup> These head groups display a smaller surface area than the alkyl chains, being strongly hydrated. A strong hydration of the headgroup leads to a value of the refractive index for the headgroup similar to that of pure water. Remarkably, the mentioned polar groups do not absorb radiation at the wavelength of the lasers that are commonly used in BAM experiments. In fact, given the following conditions for a polar headgroup: small surface area, strong hydration, and non-absorption, the structures observed by BAM are almost exclusively related to the organization of the alkyl chains. The use of BAM for obtaining information on the arrangement of the non-polar alkyl chains of the surfactants is still widespread and successful.<sup>31,35,36</sup>

However, there is a vast array of Langmuir monolayers in which the polar headgroup does not fulfill the requirements mentioned above. For large and UV–vis absorbing headgroups, the molecular arrangement of the headgroup of the surfactant



can be most significant to the BAM experiments.<sup>37,38</sup> Unfortunately, the relevance of the headgroup as the main agent of picture formation in a BAM experiment has been the focus of a reduced number of reports. This review is aimed to state a framework for the experimental conditions in a BAM experiment with significant reflection from the polar headgroup, as well as for the quantitative analysis of the experimental data. Experimental and theoretical evidence is presented from recent examples in the bibliography. For the case of reflection of the incoming light caused mainly by the polar headgroup, quantitative structural information can be attained by analyzing the inner textures of the domains. The analysis of the BAM pictures requires the simulation of the textures. The simulated domains should reproduce the textures observed by BAM. We would like to highlight that the quantitative information on the molecular arrangement of the headgroups can hardly be obtained from other experimental techniques, such as X-ray.

This review is structured as follows. First, the theoretical framework is presented. Second, two experimental qualitative examples of significant reflection from the polar headgroup are shown. Third, an example of the quantitative assessment of the molecular organization of the polar headgroup is provided. An account of the instrumental parameters during a BAM experiment is included. The appendixes detail the model for the simulation of the domains.

### **3.1.2. Theoretical model**

A Langmuir monolayer at the air/water interface can be analyzed using a two-layer model. The two-layer model is simple, yet useful. The first layer corresponds to the hydrophobic alkyl chain. The second layer corresponds to the hydrophilic headgroup. Two phases of infinite thickness, air and water are placed above and below the monolayer, respectively. See Fig. 3.2 for a sketch. A similar model has been successfully applied to the analysis of X-ray reflectivity measurements of Langmuir monolayers.<sup>39</sup> The two-layer model has been successfully applied in a large number of

reports from the bibliography. However, the question of the transition region is still open. One classical solution has been the application of a smearing zone around the boundaries of the boxes. The smearing of the different regions does not include an explicit transition region, but it has been proven useful for the quantitative analysis of X-ray reflectivity data and it is mathematically simple to apply.<sup>39,40</sup>

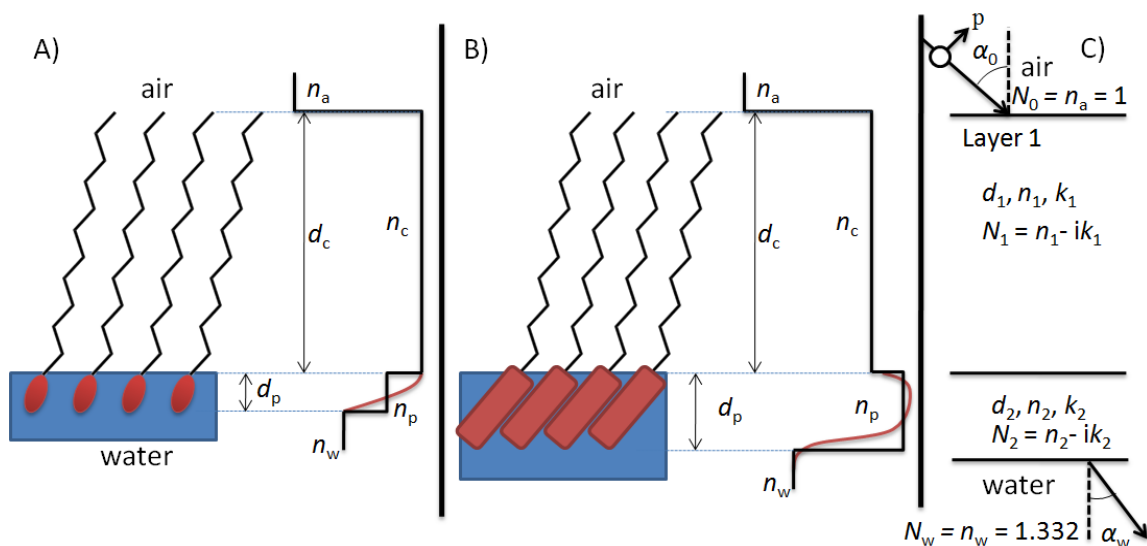


**Fig. 3.2.** Simplified sketch of a Langmuir monolayer divided in two layers. The layers 1 and 2 correspond to the alkyl chains and polar headgroup region, respectively. A) Langmuir monolayer of a surfactant with a small polar headgroup. B) Langmuir monolayer of a surfactant with a large polar headgroup. C) Optical parameters as used in the theoretical simulations.

In most of the cases, the alkyl chains are able to adopt a highly packed organization. However, the polar headgroup can be organized in a broad range of arrangements. The different possibilities for the arrangements are a function of the size of the headgroup. The chemical nature of the polar headgroup also plays a role, leading to different interactions headgroup–headgroup and/or headgroup-subphase. Four limiting scenarios of study are discussed herein, accounting for the relation between the molecular arrangement of the polar headgroup and the BAM pictures. The four scenarios are noted as scenarios I, II, III and IV. The values of the optical parameters as considered for these four scenarios are shown in Table 3.1.  $n_{\text{chain}}$  and  $n_{\text{polar}}$  are the refractive indexes of the alkyl chain and the polar headgroup layers,

respectively.  $d_{\text{chain}}$  and  $d_{\text{polar}}$  are the thicknesses (expressed in nanometers) of the alkyl chain and the polar headgroup layers, respectively.  $k$  is the absorption coefficient of the polar headgroup.  $R$  is the total reflection of the incident light from the Langmuir monolayer.  $\Delta R_p/R$  is the ratio of the enhancement of reflection originated by the polar headgroup and the total reflection from the Langmuir monolayer. The parameter  $\Delta R_p/R$  indicates the relative importance of the polar headgroup to the total reflection of the incident light from the Langmuir monolayer, leading in turn to the pictures obtained in a BAM experiment. Scenario 0 is defined as a Langmuir monolayer in which exclusively the alkyl chain layer is considered, thus ignoring the existence of the polar headgroup layer. Scenario 0 is used as a reference for calculating the relative amount of reflection from the polar headgroup in scenarios I, II, III and IV. The scenarios (I–IV) correspond to the reflection of the two regions of the Langmuir monolayer, i.e., alkyl chain and polar headgroup. In other words, in the scenarios (I–IV), the polar headgroup is taken into account. Additionally, scenarios I-p, IIp, III-p and IV-p are considered. In scenarios (I–IV)-p, exclusively the reflection from the box corresponding to the polar headgroup is considered, ignoring the reflection from the alkyl chain layer. As a general assumption for simplicity, average values of  $n$  and  $k$  of each box are considered (black line in Fig. 3.2 A–B.  $c$  and  $p$  denotes chain and polar layer, respectively). Appendix 1 provides the theoretical model for the calculation of the reflection from the Langmuir monolayer in the different scenarios considered herein.

The different scenarios of study are defined as a function of both the size and the absorption of radiation from the polar headgroup. It is of maximum importance to highlight that the reflection of the incident light from the two different regions of the Langmuir monolayer is not additive. In other words, the total reflection of the incident light from the Langmuir monolayer cannot be obtained as the sum of the separate alkyl chain and polar headgroup layers (see Appendix 1 for details). As a general statement, it is not feasible to neglect any of the chains and headgroup layers. The relative importance of reflection significantly depends on the optical parameters of each case. When both layers contribute significantly to the reflection, the image

obtained will be difficult to interpret correctly without an accurate knowledge of the optical parameters of both regions.

Scenario	$n_{\text{chains}}$	$d_{\text{chains}}$ , nm	$n_{\text{polar}}$	$d_{\text{polar}}$ , nm	$k$	$R \times 10^5$	$\Delta R_p/R$ %
Contribution of alkyl chains							
0 (reference)	1.42	2	-	-	-	0.075	-
Contribution of polar headgroup							
I-p			1.4	0.4	0	0.002	
II-p			1.6	0.8	0	0.184	
III-p	-	-	1.4	0.4	0.5	0.198	-
IV-p			1.6	0.8	0.5	1.227	
2-layers model: Alkyl chain and polar headgroup							
I			1.4	0.4	0	0.099	24.2
II			1.6	0.8	0	0.494	84.8
III	1.42	2	1.4	0.4	0.5	0.158	54.4
IV			1.6	0.8	0.5	1.304	94.3

**Table 3.1.** Optical parameters for the different scenarios considered in this study.  $n_{\text{chains}}$  and  $n_{\text{polar}}$  are the refractive indexes of the alkyl chains and the polar headgroup layers, respectively.  $d_{\text{chains}}$  and  $d_{\text{polar}}$  are the thicknesses (expressed in nanometers) of the alkyl chains and the polar headgroup layers, respectively.  $k$  is the absorption coefficient of the polar headgroup.  $R$  is the total reflection of the incident light from the Langmuir monolayer.  $\Delta R_p/R$  is the ratio of the enhancement of reflection originated by the polar headgroup and the total reflection.

### Scenario I. Non-absorbent small polar headgroup

Scenario I considers the Langmuir monolayers with a polar headgroup that does not absorb radiation at the wavelength of the BAM laser. A small size of the headgroup is also assumed, thus being strongly hydrated. Note that scenario I includes most of the simple surfactants, such as fatty acids and esters, as well as long chain alcohols and amines. In scenario I the contribution of the polar headgroup can be considered as not significant with respect to the total reflection of the monolayer. Thus, it is a suitable approximation not to consider the polar headgroup in the

simulations, see Fig. 3.2A. Table 3.1 shows the typical values of the optical parameters for this scenario,  $n_{\text{polar}} = 1.4$ ,  $d_{\text{polar}} = 0.4$  nm, and  $k = 0$ .  $n_{\text{polar}}$  is the refractive index of the headgroup, with no significant difference to the refractive index of the alkyl chains ( $n_{\text{chains}} = 1.42$ ).  $d_{\text{polar}}$  is the thickness of the polar headgroup in nanometers.  $k$  is the absorption coefficient. The relative increase of reflection of the incident light from the Langmuir monolayer provoked by the polar headgroup is only 24.2%. As mentioned previously, it should be emphasized that the reflection is not additive.

## **Scenario II. Non-absorbent large polar headgroup**

Scenario II considers the Langmuir monolayers with a bulky polar headgroup. A polar headgroup is considered large when occupying a similar surface area to the surface area of the alkyl chain. An array of large polar headgroups at the air/water interface can be arranged in highly packed supramolecular structures. The hydration shell of the polar headgroups is small. Under these circumstances, the refractive index of the polar layer is usually larger than the refractive index of the alkyl chains layer. Note that for most of the cases, the thickness of the polar headgroup is smaller than the thickness of the alkyl chain. Table 3.1 shows the optical parameters for a typical Langmuir monolayer described by the scenario II, where  $n_{\text{polar}} = 1.6$ ,  $d_{\text{polar}} = 0.8$  nm, and  $k = 0$ .  $n_{\text{polar}}$  is the refractive index of the headgroup, in this scenario significantly different to the refractive index of the alkyl chain, *i. e.*,  $n_{\text{chain}} = 1.42$ . The relative increase of reflection of the incident light from the Langmuir monolayer provoked by the polar headgroup is 84.8%. The reflection provoked by the alkyl chain might be ignored, as the reflection from the polar headgroup is rather significant. Moreover, in this scenario a small change in  $n_{\text{polar}}$  and/or  $d_{\text{polar}}$  significantly affects the amount of incident light that is reflected from the monolayer.

### **Scenario III. Absorbent small polar headgroup**

Scenario III considers a Langmuir monolayer with similar features to scenario I. However, the scenario III includes the absorption of radiation by the headgroup,  $k \neq 0$ . In the example shown in the Table 3.1, a value of  $k = 0.5$  has been included, see Appendix 2 for details. The relative increase of reflection of the incident light from the Langmuir monolayer provoked by the polar headgroup is 54.4%. Note that small  $k$  values lead to intermediate situations between scenarios I and III. It is suitable to consider that both alkyl chain and polar headgroup layers contribute significantly to the total reflection of the monolayer in scenario III. For the case of very intense absorption from the polar headgroup, the reflection from the polar headgroup might be the most relevant contribution to the total reflection of the monolayer, even when  $n_p < n_c$ . In such a case, the reflection of the chains is screened by the polar groups.

### **Scenario IV. Absorbent large polar headgroup**

Scenario IV considers a Langmuir monolayer with a similar structure to that described in scenario II. However, scenario IV includes the absorption from the polar headgroup,  $k = 0.5$ . In this scenario, the reflection caused by the polar headgroup layer is rather significant than the reflection from the alkyl chain layer. The relative increase of reflection of the incident light from the Langmuir monolayer provoked by the polar headgroup is 94.3%. Under these circumstances, the total reflection from the monolayer can be analyzed without taking into account the alkyl chains layer.

Note that even with a tight arrangement of the polar headgroups in the Langmuir monolayer, the reflection of radiation is most likely influenced from both the alkyl chain and the polar headgroup. Two experimental examples are provided right below qualitatively illustrating the origin of the reflection in a BAM experiment.

### 3.1.3 Optical behavior at the air/water interface of octadecyl rhodamine b (C18RhB). Scenario IV

Herein a not previously published experimental example of the above described Scenario IV is presented. The experimental conditions were identical to those of our previous study.<sup>41</sup> Fig. 3.3 shows the surface pressure–molecular area isotherm of the mixed Langmuir monolayer composed by an amphiphilic derivative of Rhodamine, named as C<sub>18</sub>RhB, and a surface active benzyl ester. The C<sub>18</sub>RhB surfactant has a bulky polar headgroup. The surface pressure–molecular area isotherm displays the offset of the surface pressure at a molecular area of ca. 1.1 nm<sup>2</sup>. The surface pressure at the collapse is ca. 33 mN/m at a molecular area of 0.42 nm<sup>2</sup>. The temperature is 21 °C. Fig. 3.3 includes BAM pictures obtained simultaneously to the recording of the surface pressure–molecular area isotherm. At large values of molecular area and expanded state of the monolayer, the mixed monolayer appears homogeneous. Dark irregularly shaped domains appear for a surface area of ca. 0.8 nm<sup>2</sup> per C<sub>18</sub>RhB molecule. With the compression of the monolayer, these dark domains grow in size, resulting in dark branched shapes. The dark domains appearing after compression of the monolayer are due to the formation of a condensed phase. As previously described, for most BAM experiments, the formation of a condensed phase leads to increased reflection, and therefore domains brighter than the environment appear.

On the contrary, in the case of the mixed monolayer C<sub>18</sub>Rh B:benzyl ester, the dark domains are mainly composed of segregated benzyl ester. Given that there is no absorption from the polar headgroup of benzyl ester, the bright part of the monolayer corresponds to C<sub>18</sub>RhB-enriched regions. The C<sub>18</sub>RhB molecule bears a polar headgroup with a large absorption coefficient at the wavelength of the laser used for the BAM experiment. Therefore, for the mixed monolayer C<sub>18</sub>RhB:benzyl ester, the more condensed domains appear darker than the environment, as regions with low content of C<sub>18</sub>RhB. The existence of dark domains is therefore the result of the lateral separation of the C<sub>18</sub>RhB, leading to a reduced absorption of radiation in these dark

regions. The behavior of the mixed monolayer  $C_{18}RhB$ :benzyl ester is an example of scenario IV, as discussed above.

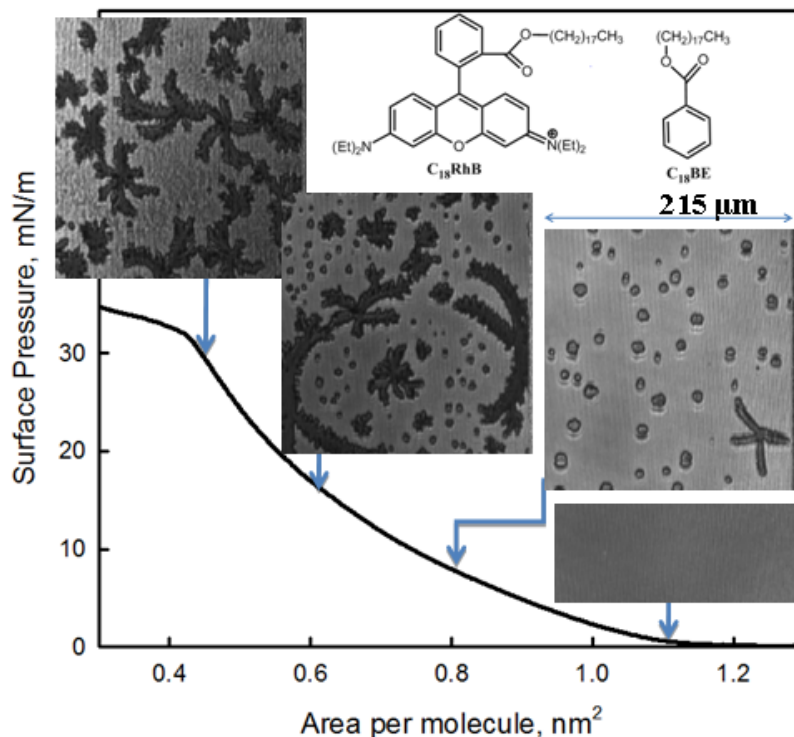


**Fig. 3.3.** Surface pressure–area isotherms of  $C_{18}RhB$ :benzyl ester mixed monolayer in molar ratio 1:2 at  $T=21$  °C. BAM images of  $C_{18}RhB$  under different surface pressures at the air/water interface. Image size:  $215 \mu\text{m}$  width. Inset: molecular structure of the two components of the mixed Langmuir monolayer.

### 3.1.4 Inversion of reflectivity during a BAM experiment. Segregation of lipid in the mixed monolayers with an organometallic complex Ir-dye/DMPA. Scenarios I and II

The mixed monolayers formed by the phospholipid DMPA (dimyristoyl-phosphatidic acid) and the Iridium (III) organometallic complex named as Ir-dye,  $[\text{Ir}(\text{F}_2\text{-ppy})_2(\text{bpy})]$ , where  $\text{F}_2\text{-ppy}=2\text{-(2,4- difluoro) phenylpyridine}$  or  $\text{bpy}=2,2'\text{-bipyridyl}$ ] have been studied in our group.<sup>42,43</sup> The Ir-dye molecule is water-insoluble and does not form Langmuir monolayers on the air/water interface. On the contrary,



the mixed monolayer Ir-dye:DMPA in a molar ratio 1:1 forms a stable Langmuir monolayer, displaying homogeneity along the complete surface pressure–molecular area isotherm. The stability and homogeneity of the equimolecular mixed Langmuir monolayer are ascribed to the ion pair interaction among the anionic DMPA polar head and the cationic Ir-dye molecule.

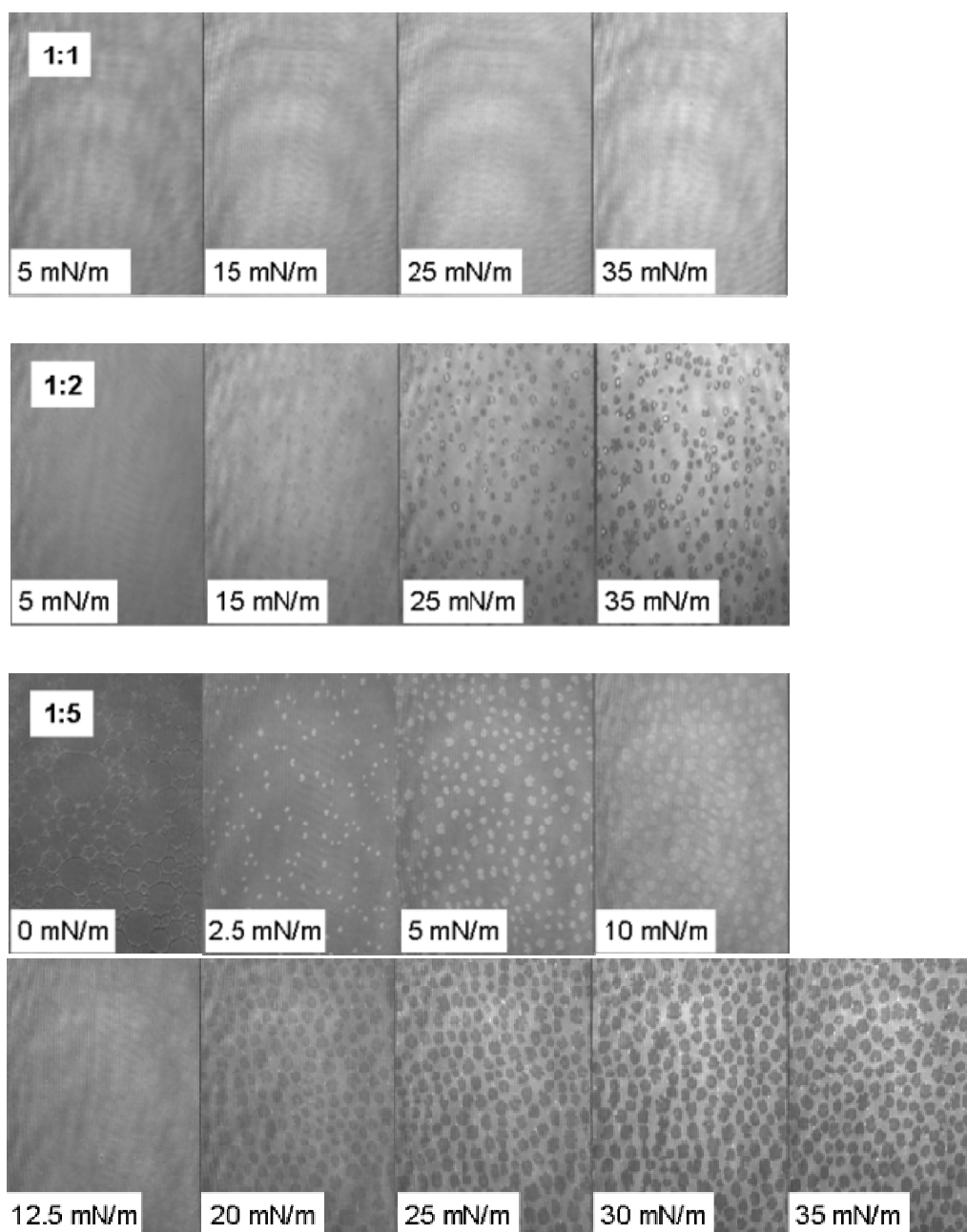


**Fig. 3.4.** BAM images recorded simultaneously to the compression of the mixed monolayers Ir-dye:DMPA=1:1 and 1:2 (top row, left and right, respectively), and 1:5 bottom row). Image size: 430  $\mu\text{m}$  width. Copyright from Royal Society of Chemistry, 2008.

In the spirit of generalize the statement concerning the molecular structure of the mixed monolayers Ir-dye:DMPA, different molar ratios were studied by BAM. The Ir-dye:DMPA=1:x mixed monolayers were considered. For an excess of DMPA ( $x>1$ ), the equimolar mixture Ir-dye:DMPA is formed at the air/water interface, while the excess of DMPA is segregated to form pure DMPA domains upon compression of the film. Fig. 3.4 shows representative BAM pictures from the mixed monolayers with different molar ratios, as previously published.<sup>42</sup> For the mixed monolayer Ir-dye:DMPA=1:5 at large values of molecular area, the mixed monolayer appears homogeneous.

At an early stage of compression, under a surface pressure of ca. 2 mN/ m, small bright domains are detected. The size and number of these domains increase with increasing surface pressure. A remarkable phenomenon is observed at the intermediate surface pressure of 12.5 mN/ m: the relative reflectivity of domains and bulk phase is inverted. In other words, for values of surface pressure of  $\pi > 12.5$  mN/m, the surrounding area is brighter than the domains, which become darker. The reflectivity of the domains at both small and large values of surface pressure is constant, while the reflectivity of the surrounding area increases gradually during the compression process. The reflection intensity of the images had to be rescaled to improve the contrast, leading to the inversion of the reflectivity of the BAM pictures.

The domains observed in the mixed monolayer Ir-dye: DMPA=1:5 monolayer are originated from the segregation to a new phase of pure DMPA lipid of the excess of DMPA lipid molecules from the Ir-dye/DMPA 1:1 complex. The organometallic complex Irdye does not absorb radiation at the wavelength of the BAM laser, and therefore the absorption constant is zero,  $k = 0$ . At small values of surface pressure, the bulk phase contains a reduced surface density of Ir-dye molecules. In spite of the large molecular size of the Ir-dye molecule, the polar layer is assumed to be strongly hydrated, thus showing low reflectivity. Therefore, the bulk phase appears darker than the brighter domains. This behavior has been described herein as scenario I. The reflectivity of the bulk phase  $R_B$  is mainly due to the alkyl chains. In the segregated

phase, composed mainly of pure DMPA domains, the alkyl chains are more packed, leading to a larger reflectivity for the domains,  $R_D$ , being  $R_D > R_B$ , see Fig. 3.5I.

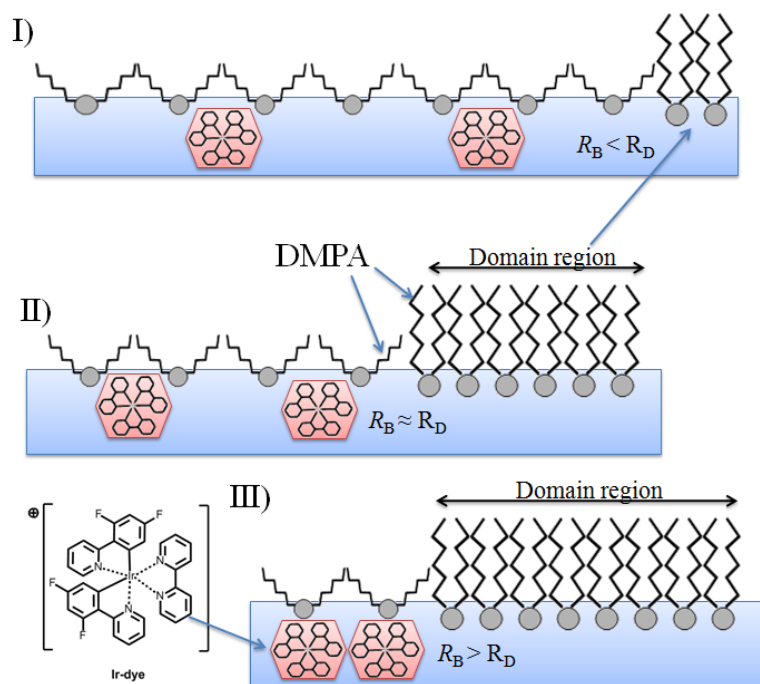


**Fig. 3.5.** Schematic representation of Ir-dye:DMPA=1:5 segregation monolayer. I) Small values of surface pressure, with low molecular density of Ir-dye in the environment region. The domains of the segregated DMPA are brighter than the surrounding area. II) Intermediate values of surface pressure, with increased molecular density of Ir-dye in the environment region. Domain and surrounding area display similar values of reflectivity. III) Large values of surface pressure and molecular density of Ir-dye in the environment region. The surrounding area is brighter than the domain area. Domains contain exclusively of the segregated DMPA lipid.

With the compression of the mixed monolayer Ir-dye:DMPA, the segregation of DMPA lipid molecules from the bulk phase to the domains is promoted. The surface density of Ir-dye molecules increases in the surrounding areas to the domains, leading to a decrease on the hydration of the polar headgroup layer. As a consequence, the reflectivity of the polar headgroup layer increases. For a surface pressure of  $\pi \approx 12.5$  mN/m, the reflectivity of bulk phase and the domains have similar values,  $R_D \approx R_B$ , see Fig. 3.5II. For values of surface pressure of  $\pi > 12.5$  mN/m, the Ir-dye molecules are tightly packed. Therefore, the polar headgroup layer consists in highly packed bulky

polar groups, with a small amount of hydration water. Thus, the reflectivity of the polar layer is larger than the reflectivity of the alkyl chains. This situation can be represented by scenario II described above. The BAM pictures show an inversion of the reflectivity, as the bulk phase shows a higher reflectivity than the pure DMPA domains,  $R_B > R_D$ , see Fig. 3.5III.

Similar phenomena have been reported previously. A mixed monolayer of a Dicholesteryl-Cyclodextrin (TBdSC) derivative and dipalmitoyl-phosphatidylcholine lipid (DPPC) in a ratio of 33 mol % TBdSC in DPPC showed an inversion of the relative reflectivity of domains and bulk phase with compression.<sup>38</sup> Bioactive new derivatives of oligosquaramide promoted inversion of reflectivity upon inclusion of the derivatives in the hydrophobic region of a DPPC monolayer.<sup>44</sup>

### **3.1.5 Quantitative assessment of the molecular arrangement of the polar headgroups. Inner textures within the domains: anisotropy caused by the coherent organization of polar groups**

Although the above mentioned examples demonstrate the significant role of the polar headgroup in the BAM images, the information that has been obtained in the two previous examples is merely qualitative. It is possible to obtain quantitative structural information on the molecular arrangement for those cases of domains displaying anisotropy. In this case, the reflection is originated exclusively from one region of the monolayer, either the alkyl chains or polar headgroup layer.

For the case of reflection mainly originated from the alkyl chain, calculations of the different textures of the domains have been effectively used for attaining quantitative information on the alkyl chain arrangement. We cite here representative examples, albeit the work in this direction is extensive.<sup>10,31,45</sup> The information on the arrangement of the alkyl chain as obtained by BAM can be used as complementary to

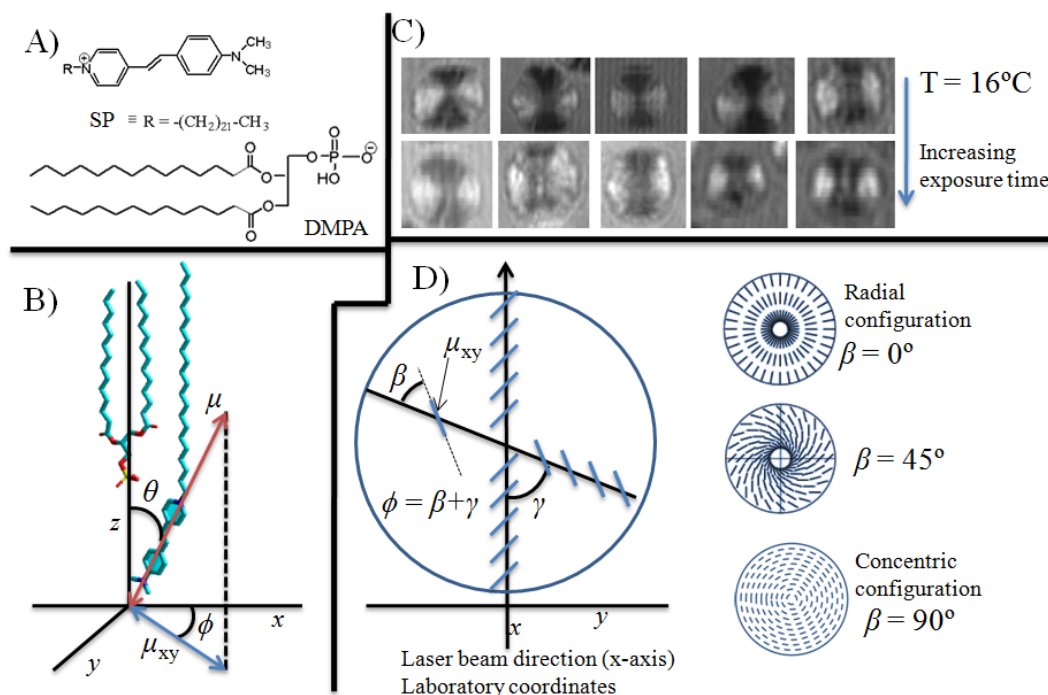


**Fig. 3.6.** A) Molecular structures of the hemicyanine (SP) and the dimyristoyl-phosphatidic acid (DMPA) molecules. B) Sketch of the mixed monolayer SP:DMPA 1:1. Graphical definitions of the transition dipolar moment  $\mu$ , its projection on the x-y plane  $\mu_{xy}$ , the polar tilt angle  $\theta$ , and the azimuthal angle  $\phi$ , of the SP molecules in presence of the DMPA molecule (the interface plane coincides with x-y plane). C) Zoom of experimental circular domains observed by BAM with increasing the opening time of the BAM camera lens. D) Organization model of the 2D circular domain. Definition of  $\gamma$  (the angle formed between the x axis and any radial circle), and  $\beta$  (angle between  $\mu_{xy}$  and the radial direction). Dashed blue line represents the projection of the transition dipole on the x-y plane. Right; examples of configurations with  $\beta = 90^\circ$  (concentric),  $\beta = 45^\circ$  and  $\beta = 0^\circ$  (radial). Temperature was  $16^\circ\text{C}$ . Copyright from the American Chemical Society, 2010.

the quantitative data obtained by X-ray scattering or vibrational spectroscopy techniques. The main focus of this review is the case for reflection of the incident light from the Langmuir monolayer mainly due to the polar headgroup. The quantitative information on the molecular arrangement of the headgroup is most valuable, as there are few experimental techniques to obtain detailed information about the organization of such groups. The quantitative analysis of the arrangement of the polar headgroup requires the existence of inner textures within the domains as observed by BAM. The textures are analyzed with a relatively simple theoretical simulation using the Fresnel equations. In order to illustrate the procedure for extracting quantitative information

from the BAM pictures, an experimental example is presented from a previous paper. The mathematical details that should be performed for gaining the quantitative insights on the arrangement of the polar headgroup are described in the Appendix. Previous studies on mixed monolayers composed by a phospholipid and an organic dye have been reported by our group and successfully characterized using this procedure.<sup>41,46–48</sup>

A mixed Langmuir monolayer formed by the anionic phospholipid dimyristoylphosphatidic acid (DMPA) and a cationic amphiphilic hemicyanine dye (SP) in a molar ratio 1:1 was studied by BAM. See Fig. 3.6A for the molecular structures. The anionic DMPA lipid and the cationic SP dye form an ionic pair, resulting in a stable mixed Langmuir monolayer. The alkyl chains of the DMPA molecule (12 methylene units) are shorter than those of the SP molecule (22 methylene units). Thus, the DMPA small polar headgroup does not interfere with the ordered aggregation of the polar headgroup of the SP molecules (Fig. 3.6B). Therefore, formation of well-defined 2D structures of the polar headgroup of the SP molecule driven by the lateral self-aggregation of hemicyanine groups is feasible.

The BAM images of the mixed Langmuir monolayer DMPA:SP show well-defined 2D domains. The domains present anisotropy as inner textures within the domains. Circular domains with both bright horizontal regions and dark vertical regions have been observed (see Fig. 3.6C). The alkyl chains of the DMPA and SP molecules are not tilted for the complete range of surface pressure studied, as revealed by GIXD experiments.<sup>41</sup> The polar headgroup of the SP molecule is a hemicyanine dye derivative, displaying a strong absorption band at the wavelength of the laser used for the BAM experiments. Therefore, the inner texture of the domains observed by BAM is due to the combination of the ordered arrangement of the polar headgroup and the absorption of radiation from the polar headgroup.

Fig. 3.6B shows a scheme of the structural parameters of the polar headgroup of the SP molecule in the mixed Langmuir monolayer DMPA:SP.  $\mu$  is defined as the main transition dipole of the hemicyanine headgroup.  $\mu_{xy}$  is the projection of  $\mu$  on the

air/water interface plane. The inner textures of the domains can be simulated ignoring the presence of the alkyl chains. This simulation corresponds to scenario IV, in which the polar headgroup layer is most relevant for the reflection. In other words, the mixed monolayer DMPA:SP is considered as a biaxial material with the complex refractive indices of  $N_q = n_q - ik_q$  ( $q \equiv x, y$  and  $z$ , see Appendix 3).

The BAM images shown in Fig. 3.6C were recorded with the polarizer at the camera, also named analyzer, at  $0^\circ$ . This polarization angle implies that exclusively the p component of the reflected radiation is detected. Thus, the  $N_y$  ( $N_y$  is the complex refractive index in the y axis, laboratory coordinates) component of the mixed monolayer SP: DMPA does not play a role in the acquired BAM pictures. The x axis (laboratory coordinates) is defined as the projection of the laser incidence axis on the air/water interface, see Fig. 3.6D. The absorption coefficients of the mixed monolayer can be expressed as follows:  $k_x = k_0 \times \sin(\theta) \times \cos(\phi)$ , and  $k_z = k_0 \times \cos(\theta)$ .

The reflectivity is almost constant for any radius of the circle. Thus, the azimuthal angle ( $\phi$ ) is considered constant for any radial direction, see Fig. 3.6D. The angle formed between the x axis and any radius of the circle is the circle rotation angle, and named as  $\gamma$ . The angle formed between the projection of the dipolar moment on the x-y plane  $\mu_{xy}$ , and the radial direction is defined as  $\beta$ . The azimuthal angle is  $\phi = \gamma + \beta$ . Fig. 3.6D shows sketches for  $\beta = 90^\circ$  (concentric configuration),  $\beta = 45^\circ$ , and  $\beta = 0^\circ$  (radial configuration). The dashed blue lines represent the projection of the transition dipole of the SP headgroup on the x-y plane.

Given a concentric configuration, a value of  $\beta = 90^\circ$  is defined. The following parameters are assumed to simulate the inner textures of the domains:  $\theta = 50^\circ$ ,  $k_0 = 0.5$ ,  $n_x = n_z = 1.6$ , and  $d = 0.8$  nm. See Appendix 3 for details. The reflectivity of the domains can be expressed as a function of the single parameter angle  $\phi = \gamma + \beta$ . Note that  $\beta$  is a constant value dependent on  $\gamma$ . The total reflection from the mixed monolayer  $R_p$  is calculated as a function of the angle  $\gamma$ . The total reflection can be expressed in terms of a relative grey level scale. The grey scale ranges from 0 to 255, being these values a complete black and a complete white colors, respectively. The

simulated values of reflectivity are shown in Fig. 3.7, left. The reflectivity values are shown in a polar plot (Fig. 3.7 center), which resembles the circular domain observed by BAM. The reflectivity values can be expressed in a polar plot using the gray scale from 0 to 255, see Fig. 3.7, right. The latter picture is the simulated domain that should be compared with the experimental BAM picture.

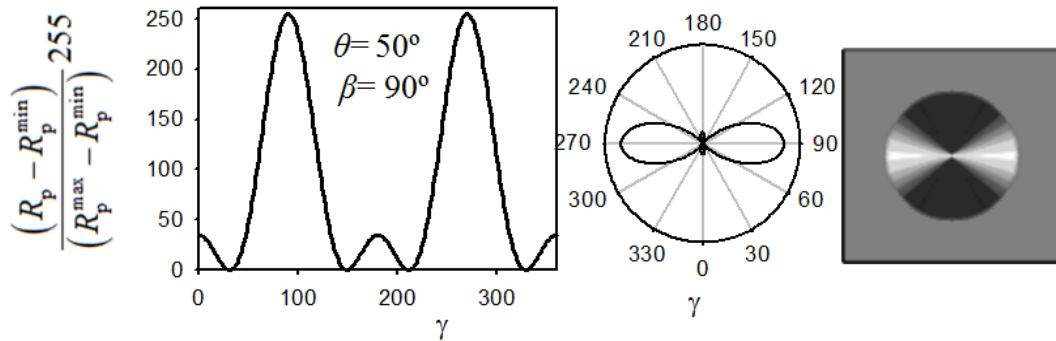


**Fig. 3.7.** Plot of the relative reflection vs  $\gamma$ , for  $\beta = 90^\circ$ ,  $\theta = 50^\circ$ ,  $k_0 = 0.5$ ,  $n_x = n_z = 1.6$  and  $d = 0.8$  nm. The reflection is transformed into a grey level scale (from 0 to 255).

The contrast and clarity of the BAM picture can be improved by the rationale adjusting of the experimental parameters of the BAM instrument. A remarkable option in the commercial models of the BAM instrument is the so-called “auto set gray level”. The autoset option rescales automatically the gray level in the BAM picture by adjusting the exposure time of the BAM camera. This adjustment places the maximum light detected by the camera under the threshold value of 255. Note that a reflectivity value of 255 is the value of maximum reflectivity in the grey scale, and corresponds to a pure white color. The increase of reflectivity can be taken into account quantitatively by our model. It should be remarked that the increase/decrease of reflectivity can be set manually adjusting certain experimental parameters such as the laser power or the camera iris. Starting from the situation described in Fig. 3.7, an increase of the exposure time 3/2-fold enhances the reflectivity to the threshold of 255. The calculated values of increased reflectivity are shown in Fig. 3.8, where the domain is also simulated.



When the exposure time is increased for  $\theta = 50^\circ$  and  $\beta = 90^\circ$ , the model predicts the appearance of a narrow gray region along the vertical direction of the circular domain, surrounded by darker regions, see Fig. 3.8. These calculated textures agree with the experimentally observed textures, as shown in Fig. 3.6C.

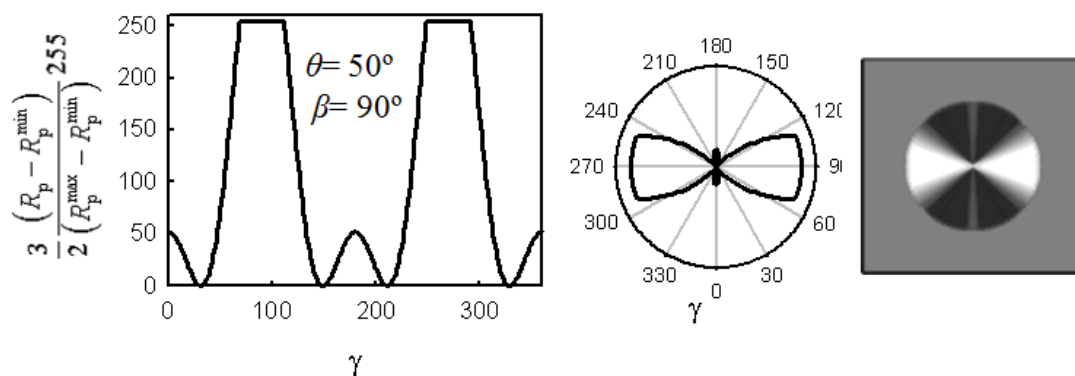


**Fig. 3.8.** Plot of the relative reflection against  $\gamma$  (using the same constants as Fig. 3.7). The relative reflectivity is increased 3/2 for simulate the increasing exposure time, but the cutoff is again 255 (maximum value of the grey level scale).

Therefore, the procedure described herein to simulate the inner textures of the domains allows obtaining information on the molecular organization of the polar headgroup. The experimentally obtained circular domains have been related to a concentric configuration of the transition of the dipole hemicyanine polar headgroup with an angle of  $\theta \approx 50^\circ$ .<sup>41</sup>

This procedure can be extended to different values of the polar tilt angles, therefore being suitable for a general application to different Langmuir monolayers. Fig. 3.9 shows the results of the simulation of the circular domains for different values of either polar tilt angle  $\theta$  or angle  $\beta$ . The values of the optical parameters  $k_0$ ,  $n_y$ ,  $n_z$  and  $d$  and exposure time are similar as previously indicated for the simulations shown in Fig. 3.7. The maximum value of the reflectivity inside the domains is 3/2 the maximum value of reflectivity allowed by the instrument. The simulated reflectivity of the inner texture of the domains is a relative parameter, which is related to the minimum and maximum of reflectivity for each case.

The simulations shown in Fig. 3.9 show that for a given configuration, radial, concentric or intermediate, the relative reflectivity of the inner texture of the domain is a function of the polar dipole transition angle,  $\theta$ . The dependence in the reflectivity with  $\theta$  might lead to an inversion of the reflectivity of the domain texture.

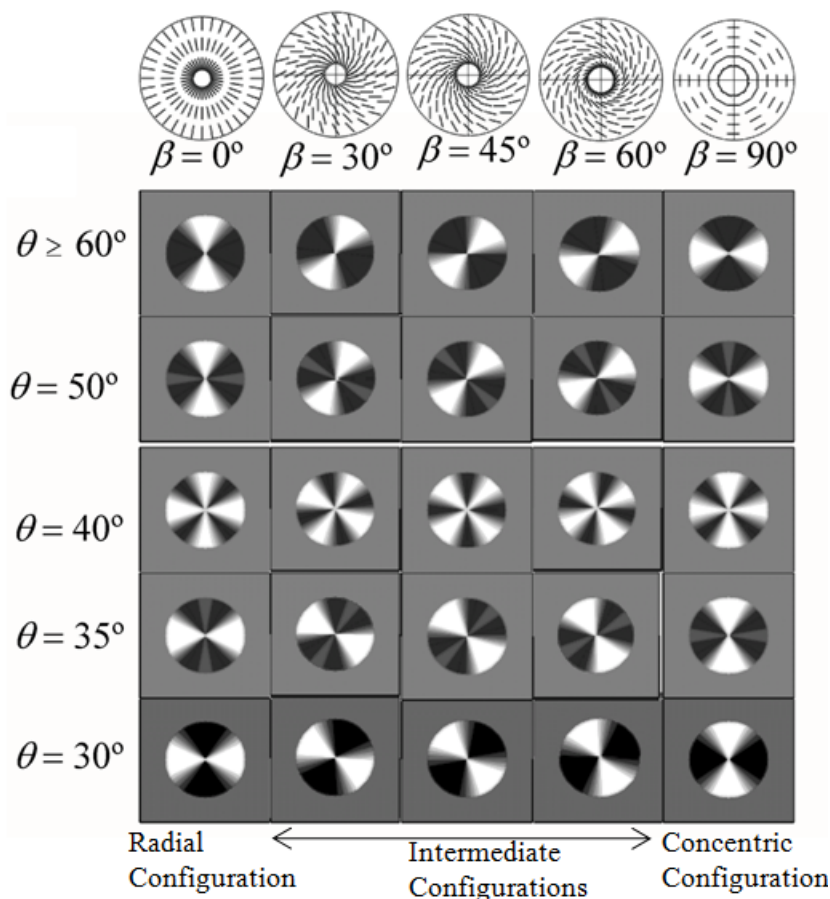


**Fig. 3.9.** Circular domain simulation for different polar angle tilt,  $\theta$ , and different angle, by using  $k_0 = 0.5$ ,  $n_y = n_z = 1.6$ , and  $d = 0.8$  nm. Copyright from the American Chemical Society, 2010.

Traditionally, the bright regions within the domains have been related to dipole orientations parallel to the direction of polarization of light. On the contrary, dark regions are associated with perpendicular orientations of the dipole orientations with respect to the direction of polarization of light. This interpretation is correct when the transition dipoles are located parallel to the air/water interface, at least qualitatively.

However, this interpretation is not correct when the relative value of reflection in the experimentally obtained BAM images is quantitatively analyzed. In this case the

reflectivity depends on the value of the angle  $\theta$ . Indeed, the typical Langmuir monolayer gives rise to different values of  $\theta$ . Therefore, a detailed simulation of the inner textures should be performed in order to assess the quantitative information offered by the BAM pictures.

In the case of a concentric configuration, with a value of  $\beta = 90^\circ$ , and a range of value of  $\theta = 50\text{-}35^\circ$ , remarkable inner textures are observed: the appearance of a vertical thin gray line, as an example. The appearance of eight sections of alternative bright and dark textures is observed for  $\theta = 40^\circ$ . Note that the changes of the inner textures with the change in the value of  $\theta$  do not indicate a modification in the orientation of transition dipoles. In fact, all the dipoles are uniformly distributed about the center in the circular domains. The occurrence of these special textures should be interpreted as an optical phenomenon resulting from the complexity of the Fresnel equations, for intermediates and low values of  $\theta$ , see Appendix 3.

Similar cases have been reported previously by several groups. For example, inner textures were formed in eight alternative dark and bright sections for monolayers of polymerized 10,12-pentacosadiynoic acid, as observed by BAM.<sup>49,50</sup> The BAM images were not originated from the reflection of the polar headgroup in this case.

The inner textures within the domains were instead originated from the conjugate polymerized diacetylene group, which absorbs radiation in the visible region of the UV–visible spectra.<sup>51</sup> The anisotropy observed in this case can be analyzed by the model described in Appendix 3. The model can effectively simulate the reflectivity of the polymerized layer, ignoring the existence of the different regions of the polar group and the alkyl chain.

Finally, it should be noted that the model described in Appendix 3 is a simplified model that exclusively relates anisotropy to the absorption of radiation, assuming that  $n_x \approx n_z$ . This assumption can be considered correct only in the case of a large extent of absorption of radiation. The model can also be used to explain the anisotropy caused by the alkyl chains in the absence of absorption,  $k = 0$ . The following relation should be assumed in case of no absorption:  $n_x \neq n_z$ . The degree of

difference in the refraction indexes is a function of the inclination of the alkyl chains. The textures observed in the case of no absorption are very similar to that shown in Fig. 3.9.

In summary, we have described experimental evidence from the recent bibliography of the most relevant influence of the polar headgroup in the BAM images for Langmuir monolayers under well defined conditions. The relevance of the polar headgroup has been traditionally overlooked. A simple mathematical procedure using the Fresnel equations has been introduced, in the aim of offering a quantitative tool for further research in the detailed molecular arrangement of the polar headgroups in Langmuir monolayers.

### 3.1.6 Conclusions

Traditionally, exclusively the structure of the alkyl chain of the amphiphilic molecules has been studied by BAM, although some authors studies the sensitive effect in a not declared way of head group changes on the domain morphology.<sup>29–32</sup> In the cases of molecular recognition at the polar headgroup, the effect of the recognition agents has been successfully described. On the contrary, the relevance of the polar headgroup as the main contribution to the BAM pictures has not been described to a large extent. This review attempts to show that this is strictly correct only in the case of small polar headgroup, implying a strong hydration, with no absorbance of radiation. On the contrary, for bulky and absorbing polar headgroups, low hydration degree is expected: for such cases, the BAM images must be related to the reflectivity of these polar headgroups. The different experimental situations have been analyzed in terms of four different scenarios of study, allowing the correlation of the BAM pictures with a specific region of the Langmuir monolayer, either the alkyl chain or the polar headgroup. The significant influence of the polar headgroup in the BAM pictures has been demonstrated qualitatively for the mixed monolayers C<sub>18</sub>RhB: benzyl ester and Ir-dye: DMPA.

The anisotropy in the BAM pictures is of special interest, being indicative of the existence of a high degree of order in the Langmuir monolayer. In those cases in which reflection is caused mainly by the polar groups, it is possible to obtain quantitative structural information of this region of the monolayer. This information can hardly be obtained from other experimental techniques. An example of this procedure has been discussed for the mixed monolayer SP:DMPA.

The simulation of the different textures of the domains has been used as a tool to attain the structural information. The reflected light (p-polarized) of thin films under Brewster angle incidence is not a linear phenomenon and the simulation is necessary to match the experimental results. The mathematical procedure has been described in great detail, allowing its application to different Langmuir monolayers.

A new experimental and theoretical framework has been revised from the recent bibliography, allowing the extraction of quantitative information on the arrangement of the polar headgroup from the BAM pictures.

### 3.1.7 Outlook

It would be intriguing to perform BAM experiments with different lasers at different wavelengths, which would allow enhancing the reflection of one of the regions within the domains at the expense of another, increasing or decreasing the absorption of the polar region. For the case of not relevant absorption of radiation from the polar headgroup at the different wavelengths, the BAM pictures would not be modified to a large extent when using different lasers. On the contrary, a substantial modification of the BAM pictures with the use of different lasers would be expected for an absorbing polar headgroup. The modification of the BAM pictures with the modification of the wavelength of the illuminating radiation is of special interest regarding the anisotropy within the domains. For anisotropical domains, one would expect noticeable changes in the morphology of the textures with the different wavelengths. A multiple-wavelength BAM instrument might offer the chance of visualizing either the polar headgroup or the alkyl chain at the Langmuir monolayer. For this selective visualization, a radiation with a wavelength that falls either inside or outside the absorption region of the polar headgroup could be used. Moreover, in case of different absorption maxima of the same polar headgroup, the selective excitation of a maximum of absorption would lead to a change in the morphology of the domains. The different observed morphologies could be related with the orientations of the different transition moments of the same chromophore headgroup, allowing for a sub-molecular resolution of the arrangement. Therefore, the use of different wavelengths in a single BAM experiment might lead to a new concept in the molecular description of the Langmuir monolayers.

## Appendix 1. Reflection of incident light from a Langmuir monolayer

Consider a system consisting of L layers (see Fig. 3.2C), located between two environments, air and water. P-polarized monochromatic radiation affects at the water Brewster angle  $\alpha_0 = 53.1^\circ$ . In this case, reflection can be determined from the following relations

$$\eta_0 = \frac{N_0}{\cos(\alpha_0)} \quad \eta_w = \frac{N_w^2}{\sqrt{N_w^2 - N_0^2 \sin^2(\alpha_0)}} \quad (3.1)$$

$$\eta_j = \frac{N_j^2}{\sqrt{N_j^2 - N_0^2 \sin^2(\alpha_0)}} \quad D_j = 2\pi d_j \sqrt{N_j^2 - N_0^2 \sin^2(\alpha_0)} \quad (3.2)$$

where  $j=1, 2 \dots L$  (for a two-layer model,  $L=2$ ).

$$\begin{pmatrix} B \\ C \end{pmatrix} = \prod_{j=1}^L \begin{pmatrix} \cos(D_j/\lambda) & i \cdot \sin(D_j/\lambda) \\ i \cdot \eta_j \cdot \sin(D_j/\lambda) & \cos(D_j/\lambda) \end{pmatrix} \begin{pmatrix} 1 \\ \eta_w \end{pmatrix} \quad (3.3)$$

$$R_p = |r_p|^2 = \left| \frac{\eta_0 \cdot B - C}{\eta_0 \cdot B + C} \right|^2 \quad (3.4)$$

## Appendix 2. Absorption of radiation from the polar headgroup

The absorption constant,  $k$ , may be related to the absorbance,  $Abs$ , by

$$k = \frac{2.303 \cdot \lambda \cdot Abs}{4 \cdot \pi \cdot d} = \frac{2.303 \cdot \lambda \cdot \varepsilon}{4 \cdot \pi \cdot d \cdot A \cdot N_A} \quad (3.5)$$

where we used  $Abs = \varepsilon \Gamma = \varepsilon / A N_a$ , being,  $N_a$  the Avogadro constant,  $\Gamma$  the surface concentration,  $\varepsilon$  the extinction coefficient,  $A$  the area per molecule and  $d$  the thickness of the absorbent layer. For example if we used  $\lambda = 532$  nm,  $d_p = 0.4$  nm,  $\varepsilon = 5 \times 10^3$  M<sup>-1</sup>cm<sup>-1</sup>,  $A = 0.4$  nm<sup>2</sup>, we can obtain  $k \approx 0.5$ . In any case, the above expression is only approximate, and valid for normal incidence and isotropic films.

### Appendix 3. Simulation of the inner textures of domains caused by anisotropy in the arrangement of the polar headgroup

The anisotropic thin film is assumed to be a biaxial material with complex refractive indices ( $N_{1x}$ ,  $N_{1y}$ ,  $N_{1z}$ ). The incidence angle,  $\alpha_0$ , and transmission angle,  $\alpha_w$ , of multiply reflected waves are constants and related by  $n_0 \sin(\alpha_0) = n_w \sin(\alpha_w)$ , where  $n_0 = 1$  (air) and  $n_w = 1.333$  (water) show the real refractive indices of the ambient and substrate, respectively (see Fig. 3.2C). In this case, we ignored the alkyl chain layer.

In BAM microscopy, the incident light is p-polarized and when the analyzer is set to  $0^\circ$ , only the p component of the reflection is observed. In such a case, the light reflection at the ambient/film interface can be expressed as follows (Fujiwara, H. *Spectroscopic Ellipsometry. Principles and Applications*; John Wiley & Sons: Chichester, England, 2007):

$$r_{01pp} = \frac{N_x N_z \cos(\alpha_0) - n_0 \left( N_z^2 - n_0^2 \sin^2(\alpha_0) \right)^{1/2}}{N_x N_z \cos(\alpha_0) + n_0 \left( N_z^2 - n_0^2 \sin^2(\alpha_0) \right)^{1/2}} \quad (3.6)$$

$$r_{12pp} = \frac{n_w \left( N_z^2 - n_w^2 \sin^2(\alpha_w) \right)^{1/2} - N_x N_z \cos(\alpha_w)}{n_w \left( N_z^2 - n_w^2 \sin^2(\alpha_w) \right)^{1/2} + N_x N_z \cos(\alpha_w)} \quad (3.7)$$

The total reflection coefficients for p-polarizations

$$r_{012pp} = \frac{r_{01pp} + r_{12pp} \exp(-i2\beta_p)}{1 + r_{01pp} r_{12pp} \exp(-i2\beta_p)} \quad (3.8)$$

Where

$$\beta_p = \frac{2\pi d}{\lambda} \frac{N_x}{N_z} \left( N_z^2 - n_0^2 \sin^2(\alpha_0) \right)^{1/2} \quad (3.9)$$



being  $\lambda = 532$  nm the wavelength of the laser beam and  $d$  the thickness of the biaxial thin film. The reflectances for p-polarized waves are obtained by

$$R_p = |r_{012pp}|^2 \quad (3.10)$$

The complex refractive indices of anisotropic materials along the x, y, and z axes are given by  $N_x = n_x - ik_x$ ,  $N_y = n_y - ik_y$ , and  $N_{1z} = n_{1z} - ik_{1z}$ , respectively. As only the p-component of the reflection is analyzed, the  $N_y$  component does not affect to the final result. On the other hand, the absorption coefficients can be expressed by means of

$$k_x = k_0 \sin(\theta)^2 \cos(\phi)^2 \quad k_z = k_0 \cos(\theta)^2 \quad (3.11)$$

where the angles  $\theta$  and  $\phi$  are those defined in Fig. 3.6B and  $\alpha_0 = 53.15^\circ$  (Brewster angle).

## Acknowledgments

The authors thank the Spanish CICYT for financial support of this research in the framework of projects CTQ2010-17481 and also thank the Junta de Andalucía (Consejería de Innovacion, Ciencia y Empresa) for special financial support (P08-FQM-4011 and P10-FQM-6703). We thank M. Sc. Carlos Rubia-Payá and M. Sc. Antonio González-Delgado for invaluable help with the experiments. C.R-C. acknowledges the MEC (Spanish Ministry of Education, Culture, and Sport) for an FPU grant. Juan J.Giner-Casares acknowledges the Alexander von Humboldt foundation for a postdoctoral fellowship.

## References

1. Henon S, Meunier J. *Rev Sci Instrum* 1991;62:936.
2. Honig D, Mobius D. *J Phys Chem* 1991;95:4590.
3. Honig D, Mobius D. *Chem Phys Lett* 1992;195:50.
4. Honig D, Mobius D. *Thin Solid Films* 1992;210:64.
5. Honig D, Overbeck GA, Mobius D. *Adv Mater* 1992;4:419.
6. Overbeck GA, Honig D, Mobius D. *Langmuir* 1993;9:555.
7. Kaercher T, Honig D, Mobius D. *Int Ophthalmol* 1993;17:341.
8. Riviere S, Henon S, Meunier J, Schwartz DK, Tsao MW, Knobler CM. *J Chem Phys* 1994;101:10045.
9. Wolthaus L, Schaper A, Mobius D. *J Phys Chem* 1994;98:10809.
10. Overbeck GA, Honig D, Mobius D. *Thin Solid Films* 1994;242:213.
11. Brezesinski G, Scalas E, Struth B, Mohwald H, Bringezu F, Gehlert U, et al. *J Phys Chem* 1995;99:8758.
12. FriedenberG MC, Fuller GG, Frank CW, Robertson CR. *Langmuir* 1996;12:1594.
13. Losche M, Mohwald H. *Rev Sci Instrum* 1984;55:1968.
14. Losche M, Sackmann E, Mohwald H. *Phys Chem Chem Phys* 1983;87:848.
15. Nandi N, Vollhardt D. *Chem Rev* 2003;103:4033.
16. Vollhardt D, Fainerman VB. *Adv Colloid Interface Sci* 2010;154:1.
17. Vollhardt D. *Adv Colloid Interface Sci* 2006;123:173.
18. Nandi N, Vollhardt D, Brezesinski G. *J Phys Chem B* 2004;108:327.

19. Vollhardt A, Weidemann G, Lang S. *J Phys Chem B* 2004;108:3781.
20. Vollhardt D, Fainerman VB, Siegel S. *J Phys Chem B* 2000;104:4115.
21. Filosof-Mazor L, Volinsky R, Jopp J, Blumberg P, Rapaport H, Marquez VE, et al. *Chem Phys Chem* 2009;10:2615.
22. El-Khoury RJ, Frey SL, Szmodis AW, Hall E, Kauffman KJ, Patten TE, et al. *Langmuir* 2011;27:1900.
23. Gonzalez-Delgado AM, Perez-Morales M, Giner-Casares JJ, Munoz E, Martin-Romero MT, Camacho L. *J Phys Chem B* 2009;113:13249.
24. Sharbaugh DM, Talham DR. *Langmuir* 2010;26:4925.
25. El Kirat K, Chauvet JP, Roux B, Besson F. *Biochim Biophys Acta Biomembr* 2004;1661:144.
26. Santini E, Guzmán E, Ravera F, Ferrari M, Liggieri L. *Phys Chem Chem Phys*. 2012;14:607–615.
27. Mogilevsky A, Volinsky R, Dayagi Y, Markovich N, Jelinek R. *Langmuir*. 2010;26:7893.
28. Albalat R, Claret J, Iignes-Mullol J, Sagues F, Moran C, Perez L, Clapes P, Pinazo A. *Langmuir*. 2003;19:10878.
29. Henon S, Meunier J. *Thin Solid Films*. 1993;234:471.
30. Ahuja RC, Caruso PL, Mobius D. *Thin Solid Films*. 1994;242:195.
31. Thirumoorthy K, Nandi N, Vollhardt D. *J. Phys. Chem. B*. 2005;109:10820.
32. Vollhardt D, Nandi N, Banik SD. *Physical Chemistry Chemical Physics*. 2011;13:4812.

33. Brezesinski G, Stefaniu C, Nandi D, Dutta Banik S, Nandi N, Vollhardt D. *J. Phys. Chem. C*. 2010;114:15695–15702.
34. Rajesh K, Balaswamy B, Yamamoto K, Yamaki H, Kawamata J, Radhakrishnan TP. *Langmuir*. 2011;27:1064.
35. Klaus A, Fajolles C, Bauer M, Collot M, Mallet JM, Daillant J. *Langmuir*. 2011;27:7580.
36. Helm CA, Mohwald H, Kjaer K, Als-Nielsen J. *Europhys. Letters*. 1987;4:697–703.
37. Giner-Casares JJ, Perez-Morales M, Bolink HJ, Lardies N, Munoz E, de Miguel G, Martin-Romero MT, Camacho L. *J. Mater. Chem.* 2008;18:1681.
38. Giner-Casares JJ, Perez-Morales M, Bolink HJ, Munoz E, de Miguel G, Martin-Romero MT, Camacho L. *J. Colloid Interf. Sci.* 2007;315:278.
39. Giner-Casares JJ, Keller J, Rotger C, Costa A, Brezesinski G. *Chem Phys Chem*. doi: 10.1002/cphc.201100666.
40. de Mul MNG, Mann JA. *Langmuir*. 1998;14:2455.
41. Giner-Casares JJ, de Miguel G, Perez-Morales M, Martin-Romero MT, Camacho L, Munoz E. *J. Phys. Chem. C*. 2009;113:5711.
42. Gonzalez-Delgado AM, Rubia-Paya C, Roldan-Carmona C, Giner-Casares JJ, Perez-Morales M, Munoz E, Martin-Romero MT, Camacho L, Brezesinski G. *J. Phys. Chem. C*. 2010;114:16685.
43. Gonzalez-Delgado AM, Giner-Casares JJ, Rubia-Paya C, Perez-Morales M, Martin-Romero MT, Brezesinski G, Camacho L. *J. Phys. Chem. C*. 2011;115:9059.
44. Jiménez-Millán E, Giner-Casares JJ, Martin-Romero MT, Brezesinski G, Camacho L. *J. Am. Chem. Soc.* 2011;133:19028.

45. Hatta E, Fischer TM. *J. Phys. Chem. B.* 2003;107:6406.
46. Hatta E, Fischer TM. *J. Phys. Chem. B.* 2005;109:2801.
47. Ali NM, Tucker CE, Smith FA. *Thin Solid Films.* 1996;289:267.



## 3.2 UV-Vis reflection spectroscopy under variable angle incidence at the air–liquid interface

Roldán-Carmona, C.<sup>1</sup>; Rubia-Paya, C.<sup>1</sup>; Perez-Morales, M.<sup>1</sup>; Martin-Romero, M.T.<sup>1</sup>;  
Giner-Casares, J.J.<sup>1,2</sup> and Camacho, L.<sup>1</sup>

<sup>1</sup>*Department of Physical Chemistry and Applied Thermodynamics, University of Córdoba, C. Rabanales, Ed. C3, Córdoba, Spain E-14014.*

<sup>2</sup>*Bionanoplasmonics Laboratory, CIC biomaGUNE, Paseo de Miramón 182, 20009 Donostia – San Sebastián, Spain.*

The UV-Vis reflection spectroscopy (UV-Vis-RS) in situ at the air–liquid interface provides information about tilt and aggregation of chromophores in Langmuir monolayers. This information is particularly important given in most cases the chromophore is located at the polar region of the Langmuir monolayer. This region of the Langmuir monolayers has been hardly accessible by other experimental techniques. In spite of its enormous potential, the application of UV-Vis-RS has been limited mainly to reflection measurements under light normal incidence or at lower incidence angles than the Brewster angle. Remarkably, this technique is quite sensitive to the tilt of the chromophores at values of incidence angles close to or larger than the Brewster angle. Therefore, a novel method to obtain the order parameter of the chromophores at the air–liquid interface by using s- and p-polarized radiation at different incidence angles is proposed. This method allowed for the first time the experimental observation of the two components with different polarization properties of a single UV-Vis band at the air–liquid interface. The method of UV-Vis spectroscopy under variable angle incidence is presented as a new tool for obtaining rich detailed information on Langmuir monolayers.

Paper published in *Phys. Chem. Chem. Phys.*, 16, 4012-4022, 2014.

### 3.2.1 Introduction

UV-Vis reflection spectroscopy (UV-Vis-RS) at the air–liquid interface was developed by D. Mobius et al. in the mid-80s.<sup>1–3</sup> This technique is based on recording the variations of reflection of incident light at the air–liquid interface covered with a Langmuir monolayer containing chromophores with respect to the clean air– liquid interface ( $\Delta R$ ). This technique is an extremely useful tool in different cases of study, which concerns both the study of Gibbs<sup>4</sup> and Langmuir monolayers.<sup>5</sup> Thus, UV-Vis-RS has been used for studying the interactions of various soluble components in the aqueous subphase, such as drugs,<sup>6,7</sup> proteins<sup>8–10</sup> and polyelectrolytes,<sup>11–13</sup> with ordered lipid Langmuir monolayers. Additionally, the study of ionic interactions,<sup>14–18</sup> molecular recognition,<sup>19–22</sup> and inclusion complex formation,<sup>23</sup> and analysis of phenomena such as photochromic,<sup>24–26</sup> photoisomerization,<sup>27–33</sup> charge and energy transfer,<sup>34–39</sup> and photoinduced electron-transfer<sup>40–43</sup> at the air–liquid interface have greatly benefited from the use of UV-Vis-RS.

The measurement of  $\Delta R$  provides information on the tilt and aggregation of the chromophores at the air–liquid interface. A large number of studies have been published concerning this subject.<sup>44–64</sup> This information is particularly important given that in most of the cases the chromophore is located in the polar region of the Langmuir monolayer. This region is a hardly accessible region by experimental techniques such as GIXS or PM-IRRAS, which mainly provide information on the packing of the hydrophobic region. However, a nonlinear optical technique like second harmonic generation (SHG) and sum frequency generation (SFG) can probe specifically this interfacial polar region.<sup>65</sup> Moreover, surface potential measurements at the water–air interface represent a very simple but effective method to obtain information on the polar head group region.

The applications of the UV-Vis-RS have been limited to reflection measurements under light normal incidence (LNI) in spite of the enormous potential of this technique. This limitation is mainly due to two reasons.



First, a complete theory for the UV-Vis-RS under light variable incidence (LVI) angle at the air–liquid interface is not available in the existing literature. This lack of a theoretical background restricts the previous studies to angles lower than the Brewster angle.<sup>2,3,66</sup> A large percentage of the methodology already developed for infrared reflection spectroscopy,<sup>67</sup> or PM-IRRAS,<sup>68,69</sup> can be applied in this case. However, no specific analytical criteria have been established for this type of spectroscopy in the UV-Vis region.

Second, for quite low absorption values as obtained in Langmuir monolayers and using LNI, the reflection intensities are proportional to the absorption.<sup>1</sup> Under these circumstances,<sup>44,48</sup> the use of LNI allows obtaining information on the chromophores tilt without the need for using more complex methods. This possibility is based on the experimental evidence of change of tilting of the chromophore with compression of the monolayer. Additionally, the oscillator strength of the chromophore is assumed to be conserved in its different aggregation modes.<sup>70,71</sup> However, this method cannot be applied in all cases due to either bands overlapping with different transition dipoles orientations, or significant changes in the oscillator strength with compression of the Langmuir monolayer.

Herein, the UV-Vis-RS under LVI is described from a theoretical and experimental point of view. This technique is very sensitive to the chromophores tilt, provided p-polarized incident radiation and incidence angle values are close to or greater than the Brewster angle of the air–water interface, i.e., 53.15°. Note that the s-polarized radiation does not provide information about the chromophores tilt, being exclusively sensitive to the in-plane component of the transition dipole. The UV-Vis-RS under LVI technique is closely related to the Vis-spectroscopic ellipsometry.<sup>72,73</sup> Note that  $|R_p/R_s| = \tan(\psi) \cdot \exp(i\Delta)$ . In UV-Vis-RS the absolute reflections are experimentally measured, while in VIS-spectroscopic ellipsometry the  $\psi$  and  $\Delta$  angles are measured. The absolute reflection is a more convenient magnitude to obtain experimentally for very small thickness of the proved film, i.e., in Langmuir monolayers. Moreover, the UV-Vis-RS under LVI requires the absorption of the incoming radiation from the chromophores at the air–liquid interface. Therefore, the

physical interpretation of the experimental data in UV-Vis-RS under LVI is rather simple than in ellipsometry. These experimental data can be directly related to the absorption of incoming radiation by the Langmuir monolayer, and the relative orientation of the chromophores.

Two experimental examples are studied. First, the Langmuir monolayer containing an amphiphilic derivative of the Rhodamine dye where the LNI method could be applied. The results are compared with those obtained using polarized radiation with a variable incidence angle. In the second example, an amphiphilic derivative of the hemicyanine dye is studied, where the splitting of the absorption band is observed. In the latter case, this absorption band has two components with different polarization properties. Therefore, the LVI method has to be applied to determine both components of the tilting of the hemicyanine moiety.

### **3.2.2. Experimental**

#### **Materials**

Rhodamine B octadecyl ester perchlorate (RhB), hemicyanine dye, 4-[4-(dimethylamino)styryl]-1-docosylpyridinium bromide (SP) and stearic acid (SA) were purchased from Sigma-Aldrich and used as received. The pure solvents chloroform and methanol were purchased from Aldrich (Germany) and used without further purification.

A mixture of chloroform:methanol, ratio 3 : 1 (v/v), was used as spreading solvent for solving both components. The standard solvent used for spreading Langmuir monolayers is chloroform. However, we found in our experiments that chloroform itself might lead to problems with reproducibility and not complete dissolution of the surfactants. By adding the specified fraction of methanol, reproducibility and total homogeneity of the stock solutions were ensured. The pure solvents were obtained without purification from Aldrich (Germany). Ultrapure water,

produced by a Millipore Milli-Q unit, pretreated by a Millipore reverse osmosis system (resistivity > 18.2 MO cm), was used as a subphase. The subphase pH was 5.7. The temperature was  $T = 21\text{ }^{\circ}\text{C}$ , controlled by a water thermostat.

## Methods

A NIMA 611D Langmuir trough (Nima Technology, Coventry, England), provided with a Wilhelmy type dynamometric system using a strip of filter paper, with one moving barrier for the measurement of the reflection spectra was used. The Langmuir monolayers were compressed at a speed of  $\sim 0.1\text{ nm nm}^2\text{ min}^{-1}\text{ molecule}^{-1}$ .

UV-visible reflection spectra under normal and variable angle incidence were obtained using Nanofilm Surface Analysis Spectrometers; Ref SPEC<sup>2</sup> for normal incidence and RefSpec2VA for variable angle incidence (supplied by Accurion GmbH, Göttingen, Germany).

UV-visible electronic absorption spectra of the films were recorded locating the substrate directly in the light path on a Cary 100 Bio UV-visible spectrophotometer.

Theoretical reflection calculus and numerical fitting were made using Mathcad program.

### 3.2.3 Theory

#### Reflection at the air-liquid interface under light normal incidence

Under LNI, the absorption by a film located on the surface of a given interface increases the total reflection of radiation at this interface. In case the absorption is small, i.e., less than 0.05 percent of the incident radiation, as usually found in Langmuir monolayers:<sup>1</sup>

$$\Delta R_n = R_{D,S} - R_S \approx \sqrt{R_S} \cdot A_s \quad (3.12)$$

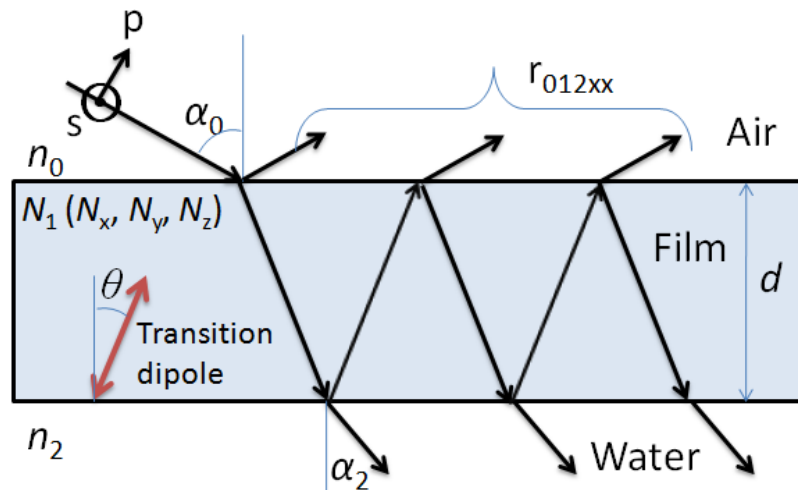
where  $\Delta R_n$  is the increase of reflection under normal incidence.  $R_S$  and  $R_{D,S}$  are the intensities of reflection of incoming radiation in the absence and presence of a Langmuir monolayer, respectively.  $A_s$  is defined as the absorption of incident radiation from the Langmuir monolayer. The above relationship can also be expressed by:<sup>44,48</sup>

$$\Delta R_n \approx 2.303 \times 10^3 f_o \varepsilon \sqrt{R_S} \Gamma \quad (3.13)$$

where  $\varepsilon$  is the molar absorptivity with units  $M^{-1} \cdot cm^{-1}$ ,  $\Gamma$  is the surface concentration in  $mol \cdot cm^{-2}$ , and  $f_o$  is the orientation factor. The orientation factor compares the average orientation of the dipole transition at the air–liquid interface with respect to the orientation in bulk solution. For an uniaxial chromophore the orientation factor is given by:<sup>48</sup>

$$f_o = \frac{3}{2} \langle \sin^2(\theta) \rangle = \frac{3}{2} P(\theta) \quad (3.14)$$

where  $\theta$  is the angle between the normal to the air–liquid interface and the direction of the transition dipole of the absorption band, see Scheme 3.1. The brackets indicate average values.  $P(\theta)$  is also called the order parameter.



**Scheme 3.1** Schematic illustration of reflection at a three-layer system in which layer 0 is air, layer 1 the thin film, and layer 2 is the subphase (water). Black arrows represent the light incidence and the red arrow represents the transition dipole direction.

The influence of surface concentration on the reflection spectrum can be eliminated by normalizing that given spectrum by the surface area:<sup>48</sup>

$$\Delta R_n^N = A \times \Delta R_n = \frac{2.303 \times 10^{17} f_0 \varepsilon}{N_A} \sqrt{R_S} = 5.41 \times 10^{-8} f_0 \varepsilon \quad (3.15)$$

where  $A$  is the area occupied per chromophore molecule and  $N_A$  is Avogadro's number.  $R_S = 0.02$  has been used as the reflection value for the bare air–liquid interface.  $\Delta R_n^N$  is expressed in  $\text{nm}^2 \cdot \text{molecule}^{-1}$ .

Eqn (3.15) provides a method to detect the presence of chromophores at the air–liquid interface using measurements of the increase of reflection of incoming radiation in a Langmuir monolayer-covered air–liquid interface with respect to the bare air–liquid interface. The amount of chromophore can be effectively quantified. Moreover, information about the orientation of the chromophore can be obtained. Typically,  $\Delta R_n$  values are about  $10^{-3}$ , so they are usually expressed in % ( $\Delta R_n \times 100$ ). For example, if  $\varepsilon = 10^5 \text{ M}^{-1} \cdot \text{cm}^{-1}$ , and  $A = 1 \text{ nm}^2$  ( $\Gamma = 1.67 \times 10^{-10} \text{ mol/cm}^2$ ), a value of  $\Delta R_n(\%) = 0.54$  is obtained. In fact, the described method is quite sensitive for chromophores with high  $\varepsilon$  values. On the other hand, values of reflection increase of  $\Delta R(\%) \geq 0.005$  could be detected as a function of the incidence angle with an adequate signal-to-noise ratio, see Fig. 3.19b. The limit of detection is below this value, and might depend on the physicochemical features of the Langmuir monolayer and the subphase. The minimum value of the extinction coefficient that can be detected using the present instrumentation mainly depends on: (a) the surface area and (b) the reflection of radiation from the monolayer even in the absence of absorption. In most of the cases, this minimum value of the extinction coefficient is estimated to be in the range of  $10^3$ - $10^2 \text{ M}^{-1} \text{ cm}^{-1}$ .

Eqn (3.13) ultimately aims to compare the reflection and bulk spectra. This comparison can be quantitatively expressed as the order parameter,  $P(\theta)$ .

Unfortunately, the order parameter,  $P(\theta)$ , cannot be obtained straightforwardly, given the molecular aggregation of the chromophores at the air–liquid interface, which

in turn result in significant variations of  $\varepsilon(\lambda)$ . The effect of these variations in  $\varepsilon(\lambda)$  can be assessed by relating the values of the oscillator strength in both media, *i.e.*, the air–liquid interface and bulk solution. The intensity of an electronic absorption band is usually represented in terms of the so-called oscillator strength,  $f$ .<sup>74</sup>

$$f = \frac{4\varepsilon_0 2.303 m_e c_0}{N_A e^2} \int_{\text{band}} \varepsilon \cdot d\nu = 1.44 \times 10^{-19} \int_{\text{band}} \varepsilon \cdot d\nu \quad (3.16)$$

Where  $\varepsilon_0$  is the vacuum permittivity,  $m_e$  and  $e$  are the electron mass and charge, respectively, and  $c_0$  is the speed of light in vacuum. The numerical factor  $1.44 \times 10^{-19}$  has units of  $\text{mol L}^{-1} \cdot \text{cm} \cdot \text{s}$ . A method for calculating the apparent oscillator strength through the integration of the normalized reflection band can be obtained by combining eqn (3.15) and (3.16),

$$f_{ap} = f \times f_0 = \frac{3}{2} f \times P(\theta) = 2.66 \times 10^{-12} \int_{\text{band}} \Delta R_n^N d\nu \quad (3.17)$$

where the factor  $2.66 \times 10^{-12}$  has units of  $\text{nm}^{-2} \cdot \text{s}$ . Note that in the above definition,  $f$  is the oscillator strength in solution, *i.e.*, isotropic conditions. According to the Davidov model corresponding to excited states of weakly interacting molecules, oscillator strength is preserved in different aggregation states.<sup>70,71</sup> In such a case, the variations of  $f_{ap}$  provide a direct measurement of the parameter order of the chromophores at the air–liquid interface. Eqn (3.17) has been applied to a number of different Langmuir monolayers, allowing a correct estimate of the average orientation of the transition dipoles at the air–water interface.<sup>48–50,52–57,63</sup> This method is referred to as LNI.

The LNI method cannot be applied in certain cases, such as bands overlapping with different transition dipoles orientations, or oscillator strength not preserved with compression of the Langmuir monolayer. These limitations have been usually overcome by transferring the Langmuir monolayers to a solid support, and subsequently analyzing the transmission spectra with incident s- and p-polarized radiation at different incidence angles.<sup>64,75</sup> However, the transference of the Langmuir monolayer to a solid support can result in significant variations of the molecular

arrangement within the monolayer. A method allowing the determination of the order parameter in situ at the air–liquid interface is therefore most desirable.

### Reflection at the air–liquid interface under inclined radiation incidence

The Fresnel expressions for the reflection of s- and p-polarized radiation at different incidence angles ( $\alpha_0$ ) originated for an anisotropic biaxial film between two isotropic media, e.g., air and water, are provided in the Appendix. The complex refractive indices of anisotropic materials are given by  $N_q = n_q - ik_q$ , where,  $q \equiv x, y, z$ ,  $n_q$  is the real part of the refractive index and  $k_q$  is the absorption constant along each axes. This theoretical model can be simplified as shown below, to reduce the number of unknown parameters. The variations in reflection are assumed to be caused mainly by absorption, and  $n_x = n_y = n_z = n_1$  can be assumed. In the region of spectral absorption, the dispersion of the real part of the refractive index can reach large values, as determined via the Kramers–Kronig relation.<sup>76</sup> However, this dispersion is zero at the wavelength of absorption maxima. Therefore, exclusively the increase of reflection at the wavelengths corresponding to the absorption maxima has been considered.

Furthermore, the examples discussed below correspond to uniaxial materials, and the film is assumed to be isotropic in the interface plane (x–y plane), so we can write

$$\begin{aligned} k_x = k_y &= \frac{3}{2} k_{\text{iso}} \langle \sin(\theta)^2 \rangle = \frac{3}{2} k_{\text{iso}} P(\theta) \\ k_z &= 3k_{\text{iso}} \langle \cos(\theta)^2 \rangle = 3k_{\text{iso}} \left[ 1 - \langle \sin(\theta)^2 \rangle \right] = 3k_{\text{iso}} [1 - P(\theta)] \end{aligned} \quad (3.18)$$

where  $k_{\text{iso}}$  is the absorption constant in an isotropic media. Using this model the reflection of the film at a given incidence angle,  $\alpha_0$ , and wavelength,  $\lambda$ , depends of four experimental parameters; film thickness ( $d$ ), refractive index,  $n_1$ , and the  $k_{\text{iso}}$  and  $P(\theta)$ . Under these conditions and under LNI, absorption and the in-plane component of the absorption constant,  $k_x$  are related by:<sup>77</sup>

$$As = \frac{4\pi \cdot d}{\lambda} \cdot 2k_x \quad (3.19)$$

Eqn (3.11) and (3.19) can be combined to obtain  $\Delta R_n$  as a function of the the absorption constant  $k_x$ . A molecule with  $\varepsilon = 10^5 \text{ M}^{-1} \cdot \text{cm}^{-1}$ , which occupies at the air–liquid interface an area,  $A = 1.0 \text{ nm}^2$ , with  $d = 2 \text{ nm}$  and  $\lambda = 500$ , displays a value of  $k_{\text{iso}} \approx 0.38$ .

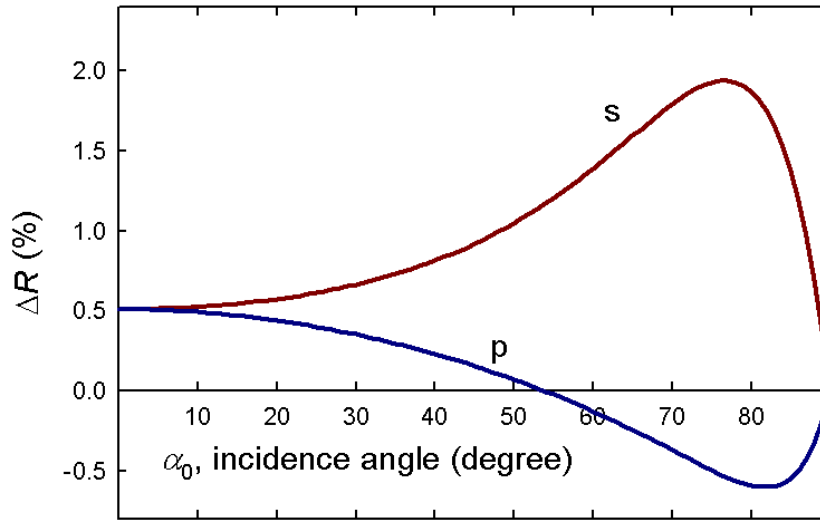


**Fig. 3.10.** Plot of  $\Delta R_s$  (red) and  $\Delta R_p$  (blue) vs  $\alpha_0$ , being  $d = 2 \text{ nm}$ ,  $n_1 = 1.55$ ,  $k_{\text{iso}} = 0.5$ ,  $P(\theta) = 0.8$ , and  $\lambda = 500 \text{ nm}$ .

The plot of  $\Delta R$  vs  $\alpha_0$  for  $d = 2 \text{ nm}$ ,  $n_1 = 1.55$ ,  $k_{\text{iso}} = 0.5$ ,  $P(\theta) = 0.8$  and  $\lambda = 500 \text{ nm}$  is shown in Fig. 3.10.  $\Delta R$  ( $\Delta R_s$ ,  $\Delta R_p$  or  $\Delta R_n$ ) represents the difference between the reflection of incoming radiation from the bare air–liquid interface and the Langmuir monolayer-covered air–liquid interface, see Fig. 3.10. Note that reflection is expressed in percentage (%). Using these parameters and under normal incidence reflection,  $\Delta R_n$  (%) = 0.509 is obtained.

$\Delta R_s$  (red solid line, Fig. 3.10) is always positive for the considered set of parameters.  $\Delta R_s$  is higher than  $\Delta R_n$  except for angles close to  $90^\circ$ .  $\Delta R_p$  (blue dashed line, Fig. 3.10) is lower than  $\Delta R_n$ , not being always the case as discussed below.  $\Delta R_p$  can be either positive or negative. The existence of negative bands, as in IR reflection-



absorption spectroscopy,<sup>67,68</sup> takes place exclusively for p-polarized light with very thin films and for incidence angles near or higher than the Brewster angle, i.e., 53.15° for the air–liquid interface. In these cases and depending on the experimental conditions, the reflection of incident light from the Langmuir monolayer-covered air–liquid coated interface might be lower than the bare air–liquid interface. This phenomenon is quite sensitive to the optical properties of the Langmuir monolayer.

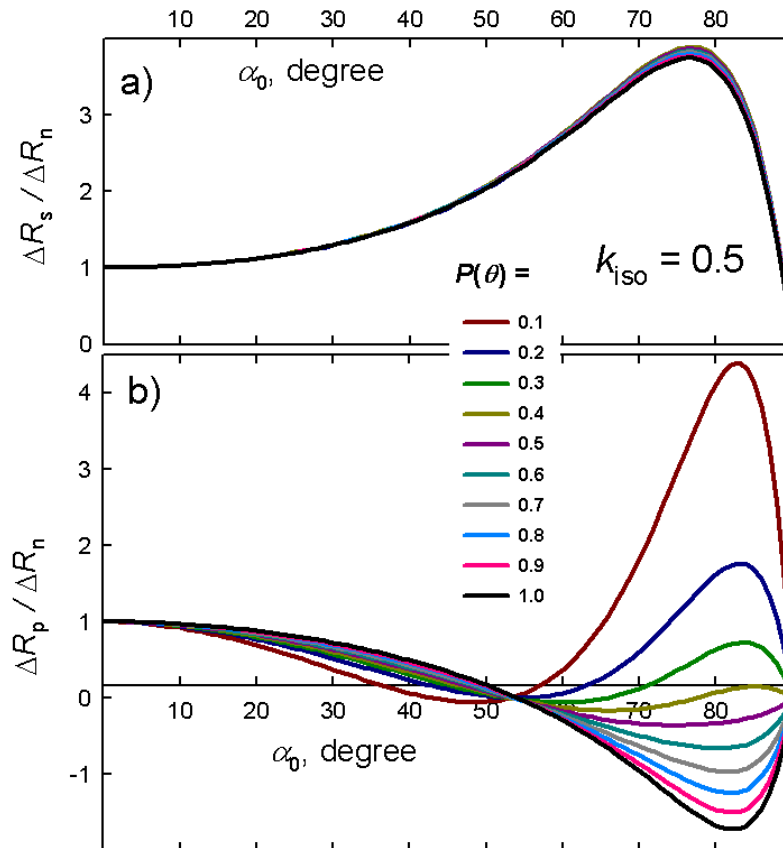


**Fig. 3.11.** a) Plot of  $\Delta R_s/\Delta R_n$  and b)  $\Delta R_p/\Delta R_n$  vs  $\alpha_0$ , being  $d = 2$  nm,  $n_1 = 1.55$ ,  $k_{\text{iso}} = 0.5$  and  $\lambda = 500$  nm. The different  $P(\theta)$  values are indicated in the figure.

Both  $\Delta R_s$  and  $\Delta R_n$  show dependence on  $k_x = k_y$ , i.e. the component on the x–y plane of the absorption constant, see eqn (3.18). Note that  $\Delta R_s$  and  $\Delta R_n$  do not depend on  $k_{\text{iso}}$  and  $P(\theta)$  separately. Therefore,  $P(\theta)$  cannot be obtained through  $\Delta R_s$  and  $\Delta R_n$ , see Appendix. Fig. 3.11a shows the representation of  $\Delta R_s/\Delta R_n$  versus  $\alpha_0$  for  $\lambda = 500$  nm,  $d = 2$  nm,  $n_1 = 1.55$ ,  $k_{\text{iso}} = 0.5$ , and different  $P(\theta)$  values. The plot of  $\Delta R_s/\Delta R_n$  has been used to allow the direct comparison of the different plots. The plot of  $\Delta R_s/\Delta R_n$  is

practically independent of the  $P(\theta)$  value, see Fig. 3.11a, indicating that the curves do not offer information about the dipole orientation, but only about the in-plane component of the dipole.

The variation of  $\Delta R_p/\Delta R_n$  vs  $\alpha_0$  assuming the same conditions as above is shown in Fig. 3.11b. The trend in this variation reaches larger values mainly for angles greater than the Brewster angle. This variation depends both in  $k_{\text{iso}}$  and  $P(\theta)$ , therefore allowing the calculation of  $P(\theta)$ . Fig. 3.11 clearly shows the enormous potential of the UV-Vis-RS under LVI, given that either positive or negative bands are obtained based solely on the transition dipole tilt of the chromophores at the air–liquid interface. Note that this feature requires incidence angles greater than or close to the Brewster angle, and incident p-polarized radiation.

The variation of  $\Delta R_p/\Delta R_n$  vs  $\alpha_0$  shown in Fig. 3.11 depends on the absolute value of  $k_{\text{iso}}$ ,  $d$ , and  $n_1$ . Therefore, although the curves show the qualitative trend,  $P(\theta)$  cannot be assessed in a general manner. A reliable criterion to estimate an approximate  $P(\theta)$  value without requiring the numerical fitting of experimental data is highly desirable. The dichroic relationship  $\Delta R_p/\Delta R_s$  can be used to this end. Fig. 3.12 shows the representation  $\Delta R_p/\Delta R_s$  vs.  $P(\theta)$  for  $k_{\text{iso}} = 0.5$  at different incidence angles.

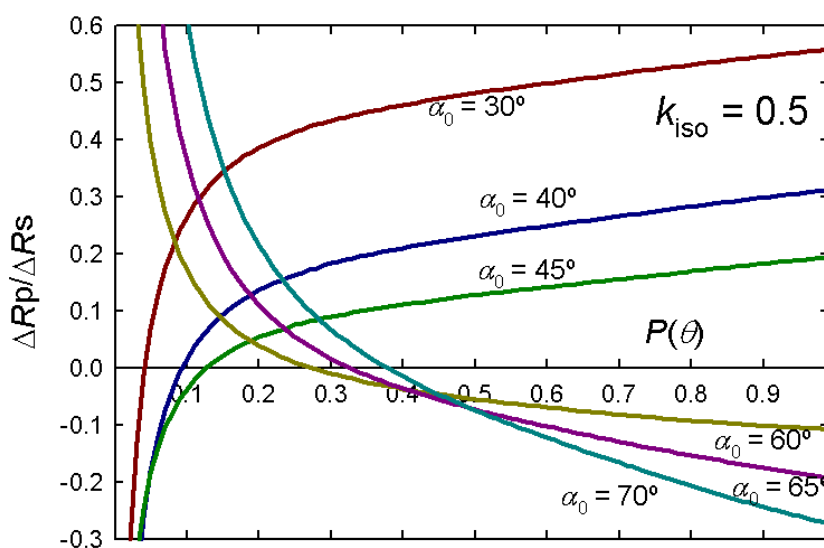


**Fig. 3.12.** Plot of  $\Delta R_p/\Delta R_s$  vs  $P(\theta)$ , being  $d = 2$  nm,  $n_1 = 1.55$ ,  $k_{\text{iso}} = 0.5$  and  $\lambda = 500$  nm. The different incidence angles values,  $\alpha_0$ , are indicated in the figure.

The curves shown in Fig. 3.11 and 3.12 cannot be used in a general manner, as discussed above. However, the relationship  $\Delta R_p/\Delta R_s$  is approximately coincident with those shown in Fig. 3.12, under the conditions:  $d \leq 3$  nm and  $1.75 \geq n_1 \geq 1.45$ , and leads to errors in the estimation of  $P(\theta)$  which are at most 10% when used for  $k_{iso}$  values in the range of  $1.5 \geq k_{iso} \geq 0.05$ . These values are typical in Langmuir monolayers. As commented, the curves shown in Fig. 3.11 and 3.12 exclusively offer an approximate value of  $P(\theta)$ . More accurate values require the numerical fit of the experimental values.

From a purely theoretical perspective, a wide range of experimental measurements of  $\Delta R_p$  and  $\Delta R_s$  as a function of  $\alpha_0$  would allow the determination of the four parameters of the described model, i. e.,  $k_{iso}$ ,  $P(\theta)$ ,  $d$  and  $n_1$  by numerical fitting. However, this information cannot be accessed using this wide range of measurements due to experimental limitations. In the case of the experimental setup used herein, measurements for  $\alpha_0 > 70^\circ$  and  $\alpha_0 < 20^\circ$  are not available. Moreover, the reflection of radiation under incident angles  $\alpha_0 > 70^\circ$  using p-polarized radiation is greatly sensitive to the optical properties of the film, see Fig. 3.11. The incidence angle of  $83^\circ$  appears as the optimum angle at which the greater variation of reflection is obtained.

These limitations can be overcome by separately measuring  $n_1$  and  $d$ , for example, by using ellipsometry at a wavelength without absorption. Alternatively, an estimation of these parameters prior to the experimental measurements might be performed. A value,  $n_1 = 1.55$  has been used in the examples discussed below, provided that values of  $n_1 = 1.5-1.6$  are quite common for thin films of organic matter.<sup>50,77,78</sup> This  $n_1$  value should be understood as an average refractive index arising from the refractive indices of the hydrophobic region, formed by the alkyl chains, and the polar region, formed in our case by bulky chromophores groups. Additional numerical fittings have been made in the experimental examples shown above, considering  $n_1 = 1.45$  and  $n_1 = 1.65$ , resulting in no differences in the obtained values of  $P(\theta)$ . The film thickness was estimated before fitting from CPK models, taking into account the molecular area given by the compression state of each Langmuir

monolayer. Concerning the tolerance of the obtained order parameters to variations in the film thickness, variations up to ca. 25% in the estimated thickness do not modify the obtained value of  $P(\theta)$ .

The characteristic features of the Langmuir monolayers, i.e., quite small thickness,  $d \ll \lambda$ , result in that the exact values of  $n_1$  and  $d$  are not required to determine the order parameter,  $P(\theta)$ . The value of  $k_{\text{iso}}$  depends on the considered values of  $n_1$  and  $d$  in the numerical fitting. On the other hand,  $P(\theta)$  does not depend on these values of  $n_1$  and  $d$  under these conditions of quite small thickness and values of  $k_{\text{iso}}$  in the range of 1.5 - 0.05.

Two experimental examples are considered herein to obtain  $P(\theta)$ , illustrating the described theoretical procedures. First, the method described in Section 3.1 has been applied, i.e., unpolarized LNI. The results have been compared with the method described in Section 3.2, i.e., s- and p-polarized LVI. Second, a case in which the LNI method cannot be applied has been considered.

## 3.2.4 Experimental results

### Rhodamine-containing Langmuir monolayers

The surface pressure–molecular area isotherm for the surface active derivative of Rhodamine C<sub>18</sub>RhB is shown in Fig. 3.13.<sup>79</sup> The overshoot of the surface pressure takes place at  $A = 1.7 \text{ nm}^2$ . The collapse takes place at approximately  $A = 0.63 \text{ nm}^2$  and  $\pi = 32 \text{ mN m}^{-1}$ .

The reflection under light normal incidence from the Langmuir monolayer at different surface areas is shown in Fig. 3.14a. The spectrum in bulk solution using chloroform:methanol = 3 : 1 as a solvent has been included for comparison, see Fig. 3.14a, dashed line. The absorption spectrum of C<sub>18</sub>RhB shows a band at 550 nm and a vibronic shoulder at 520 nm for highly diluted samples and no aggregation.

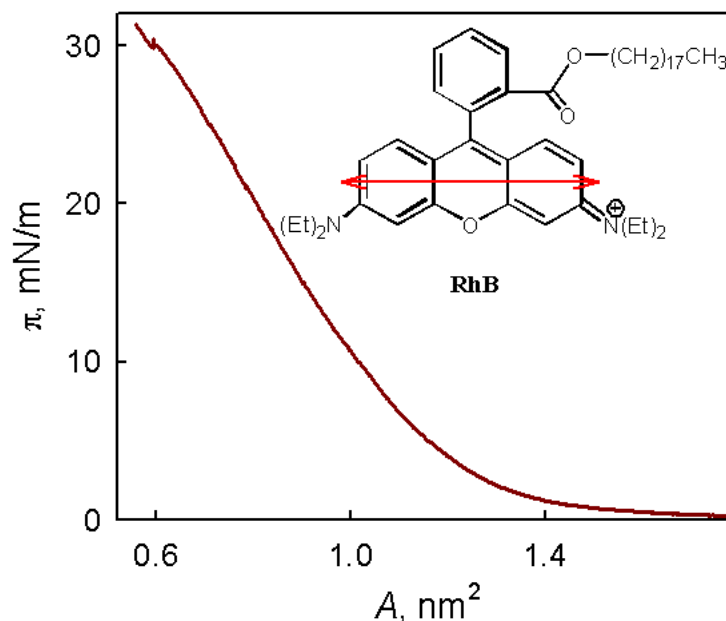


**Fig. 3.13.** Surface pressure - area ( $\pi - A$ ) isotherm of  $C_{18}RhB$ . The molecular structure of  $C_{18}RhB$  is shown in the inside. The transition dipole moment is indicated by the red arrow.

This vibronic shoulder at 520 nm coincides with the same wavelength as the H-aggregation band found at large concentration values of  $C_{18}RhB$ .<sup>80,81</sup>  $\Delta R_n$  increases with the decrease of the surface area, indicating that the surface density of the chromophore increases upon compression of the Langmuir monolayer. Additionally, the main absorption band is shifted from 568 nm to 580 nm as the monolayer is compressed. This shift might be related to the formation of J-aggregates of the Rhodamine moiety at the air-liquid interface.

The reflection spectra shown in Fig. 3.14 have been normalized by the molecular area of  $C_{18}RhB$ , eqn (3.15). The apparent oscillator strength of each reflection spectra has been obtained, according to eqn (3.17). The oscillator strength of the  $C_{18}RhB$  molecule in bulk solution has been also obtained, with  $f = 0.631$ . This value of oscillator strength is close to those observed for other Rhodamine derivatives.<sup>82</sup> Taking the mentioned data into account,  $P(\theta)$  is obtained from eqn (3.17). The obtained values of  $P(\theta)$  vs. the molecular area of  $C_{18}RhB$  are shown in Fig. 3.14b. The  $P(\theta)$  values range from  $P(\theta) \approx 0.8$  at  $\pi \leq 3$  mN/m, to  $P(\theta) \approx 0.58$  at  $\pi = 30$  mN/m.

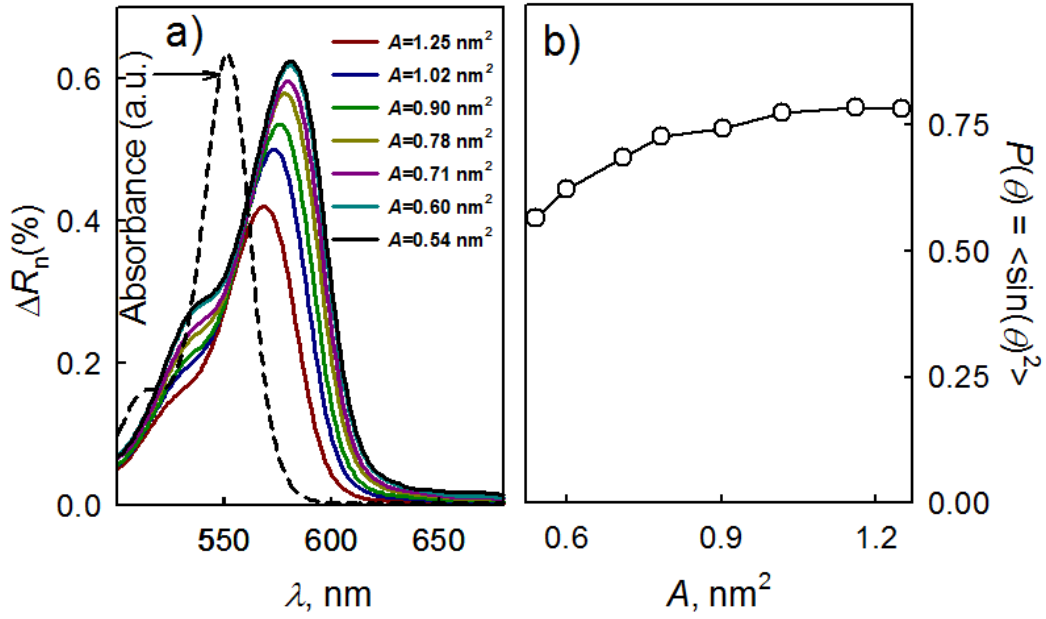


**Fig. 3.14.** a) Reflection spectra,  $\Delta R_n(\%)$ , of the RhB monolayer at different surface areas. b) Order parameter - area plot ( $P(\theta) - A$ ), obtained from spectra using equation (6), assuming a value of  $f=0.631$ .

The reflection spectra using s- and p-polarized light at variable incidence angle are shown in Fig. 3.15, at surface pressures of 3 and 30 mN/m, see Fig. 3.15. The reflection spectrum obtained at normal incidence is displayed as black lines. For an incidence angle of  $\alpha_0 = 70^\circ$ , we obtain  $\Delta R_p/\Delta R_s = -0.24$  and  $\Delta R_p/\Delta R_s = -0.14$  at  $\pi = 3$  and 30 mN/m, respectively. According to Fig. 3.12, these values of  $\Delta R_p/\Delta R_s$  ratios yield  $P(\theta) \approx 0.88$  and  $P(\theta) \approx 0.6$  at  $\pi = 3$  and 30 mN/m, respectively. These estimated  $P(\theta)$  values are in good agreement with the values shown in Fig. 3.14b.

A more accurate calculation of  $P(\theta)$  requires numerical fitting of the experimental data, as commented above. Assuming  $n_1 = 1.55$  as commented above, the estimated values of thickness were  $d \approx 1.2$  and  $d \approx 2$  nm, for  $\pi = 3$  and  $\pi = 30$  mN/m, respectively. Using these values, the numerical fitting of  $k_{\text{iso}}$  and  $P(\theta)$  can be performed by the minimized leastsquares fitting method.

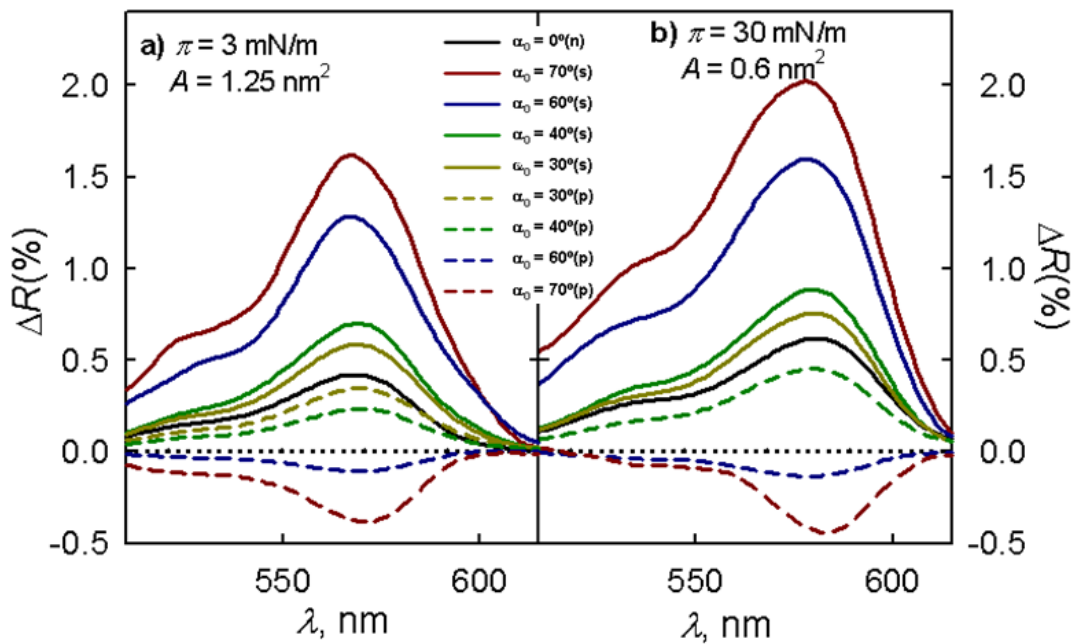


**Fig. 3.15.** Reflection spectra,  $\Delta R_n$  (black lines),  $\Delta R_s$  (solid line), and  $\Delta R_p$  (dashed line) of the  $C_{18}RhB$  Langmuir monolayer at different incidence angles, for a)  $\pi = 3$  mN/m, and b)  $\pi = 30$  mN/m. The incidence angle and the s- or p- polarization are indicated in the figure.

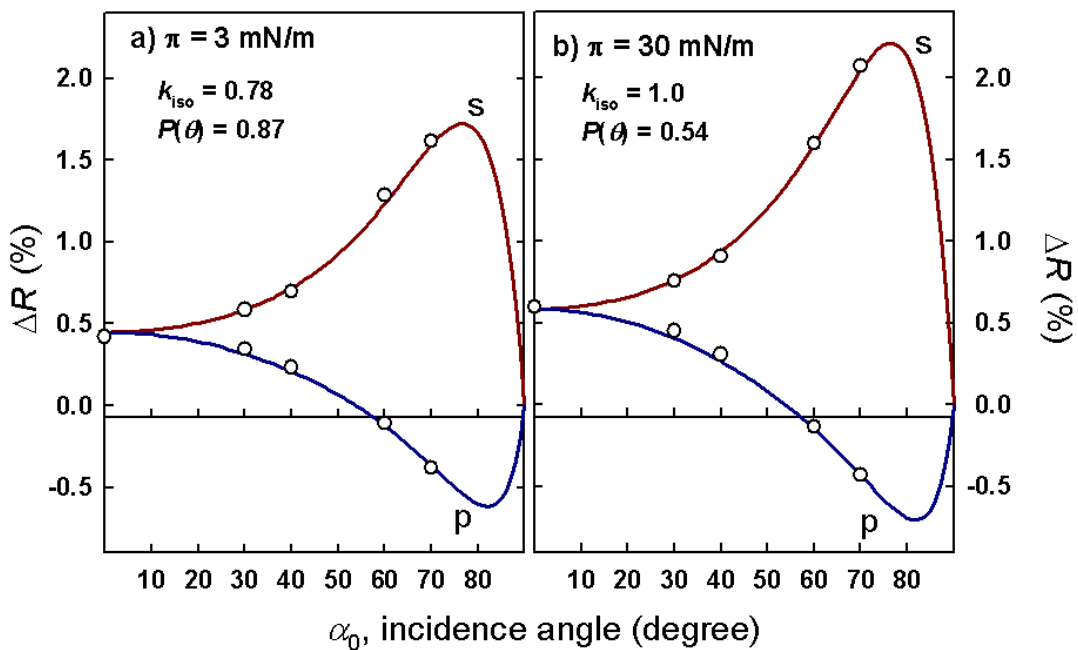


**Fig. 3.16.** Circles: Experimental  $\Delta R_s$  and  $\Delta R_p$  of the RhB monolayer, correspond at the wavelengths of the absorption maxima, (a)  $\lambda = 568$  nm for  $\pi = 3$  mN/m (b) and  $\lambda = 580$  nm for  $\pi = 28$  mN/m. The solid lines correspond to the theoretical variation of  $\Delta R_s$  (red) and  $\Delta R_p$  (blue) vs  $\alpha_0$  for: (a)  $n_1 = 1.6$ ,  $d = 1.2$  nm,  $k_x = 0.99$  and  $k^{\max} = 1.3$ . (b)  $n_1 = 1.6$ ,  $d = 2$  nm,  $k_x = 0.74$  and  $k^{\max} = 1.2$ .

The experimental  $\Delta R_s$  and  $\Delta R_p$  values at the absorption maxima,  $\lambda = 568$  and  $\lambda = 580$  nm at  $\pi = 3$  and 30 mN/m, respectively, are shown in Fig. 3.16 (circles). The calculated variation of  $\Delta R_s$  (red solid line) and  $\Delta R_p$  (blue dashed line) vs. the incidence angle, using the values of the parameters obtained in the numerical fitting, is shown in Fig. 3.16 as solid lines.  $k_{\text{iso}} = 0.78 \pm 0.07$  and  $P(\theta) = 0.88 \pm 0.08$  were obtained for  $\pi = 3$  mN/m.  $k_{\text{iso}} = 1.0 \pm 0.1$  and  $P(\theta) = 0.54 \pm 0.06$  were obtained for  $\pi = 30$  mN/m, in good agreement with the results obtained previously by the normal incidence method, see Fig. 3.14.

### **Mixed monolayers of a hemicyanine dye and stearic acid**

The mixed Langmuir monolayer of the hemicyanine dye, 4-[4-(dimethylamino)styryl]-1-docosylpyridinium bromide (SP) and stearic acid (SA) in the molar ratio 1 : 1 has been described in a previous report.<sup>64</sup> The surface pressure–molecular area isotherm of this mixed Langmuir monolayer is shown in Fig. 3.17 along with the chemical structures of SP and SA molecules.

The reflection spectrum under normal incidence of light is shown in Fig. 3.18. The reflection spectra show a low-energy band at 475 nm, corresponding to the  $\pi$ - $\pi^*$  transition of the chromophore in trans-configuration at low surface pressures.<sup>46,83</sup> With the compression of the mixed Langmuir monolayer, i.e., the increase of the surface pressure, the maximum wavelength in the reflection spectra was shifted to shorter wavelengths, from 475 nm to 410 nm. The band is additionally clearly deformed, displaying a shoulder at ca. 500 nm.

The shape of the absorption band of the hemicyanine is due to splitting of the band.<sup>64</sup> The band splitting has been related to the existence of non-equivalent molecules per unit cell in the aggregate. According to Davidov's exciton theory, a given molecular energy level may be split into as many components as there are nonequivalent molecules per unit cell.<sup>70,84</sup> For the mixed SP:SA Langmuir monolayer



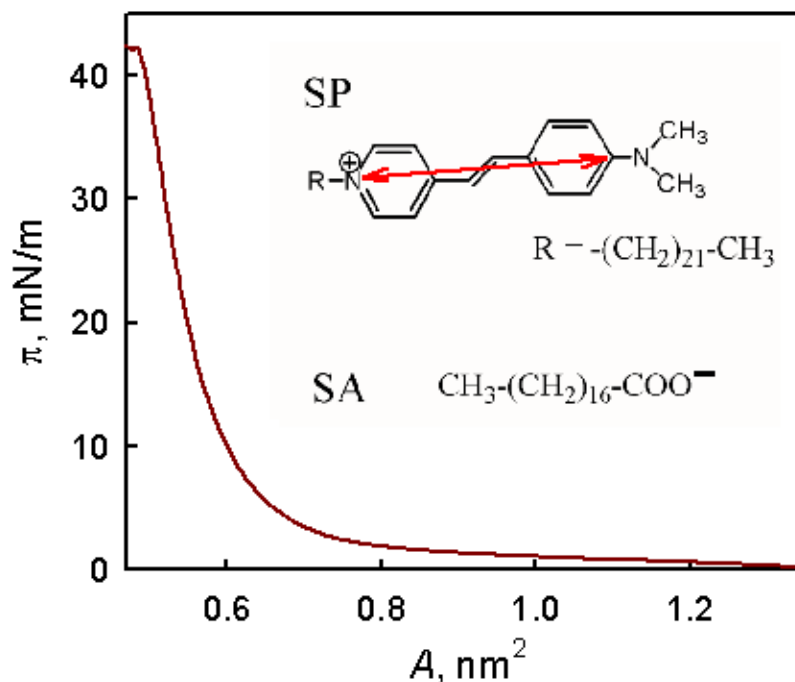


**Fig. 3.17.** Surface pressure - area ( $\pi - A$ ) isotherm of SP:SA = 1:1 mixed monolayer, and molecular structures. Red arrow indicates the transition dipole moment direction.

the absorption band has two components with different polarization properties, as observed by polarized UV-Vis transmission spectroscopy of the LS films.<sup>64</sup>

The close proximity between hemicyanine groups in the Langmuir monolayer leads to a strong repulsion between their dipole moments, despite the compensation of the positive charge of hemicyanine with the negative charge of stearic acid. The partial rotation of the hemicyanine groups in opposite directions might occur to reduce this repulsion energy, see Fig. 3.18b. For clarity, the two SP molecules are displayed in different colors. In this configuration, the transition dipoles are not parallel. The addition of the transition dipoles leads to two optically active components: one almost perpendicular to the support, with the maximum absorption at  $\sim 410$  nm (H component), and another almost parallel to the support, at  $\sim 500$  nm (J component), see Fig. 3.18b. In this scenario, the method described in Section 3.1 cannot be used to determine the order parameter,  $P(\theta)$ .<sup>64</sup>

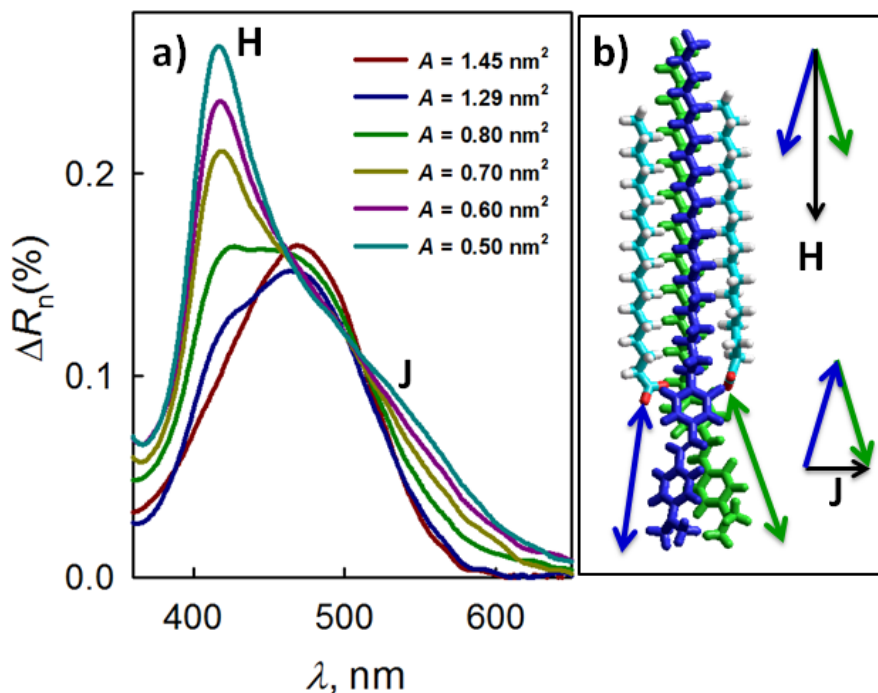


**Fig.3.18.** (a) Reflection spectra,  $\Delta R_n(\%)$ , of the SP:SA = 1:1 mixed Langmuir monolayer at different values of surface area. (b) A) Schematic representation of the hemicyanine aggregation model. Blue and green arrows indicate the transition dipole of each molecule. Black arrows indicated the two optically active components of the transition dipole addition.

The reflection spectra using light polarized under variable angle incidence are shown in Fig. 3.19. The reflection spectrum obtained under light normal incidence is shown as the black line in Fig. 3.19 for comparison. All reflection spectra were recorded at a surface pressure of  $\pi = 35$  mN/m. The spectra obtained with s-polarized radiation, Fig. 3.19a, display a similar shape as those obtained at normal incidence. As previously commented, the s-component of the spectra exclusively depends on  $k_x$ , not offering information on the orientation of the transition dipoles. Therefore, these reflection spectra are expected not to exhibit any change in shape, i.e., splitting of the band.

The reflection spectra using p-polarized radiation are shown in Fig. 3.19b. The spectrum obtained under normal incidence is shown for reference, see the black line in Fig. 3.19. The analysis of these reflection spectra clearly shows how the two components of the absorption band can be solved. For  $\alpha_0 = 50^\circ$  (blue line),  $\Delta R_p \approx 0$  is

obtained at  $\lambda = 410$  nm, whereas  $\Delta R_p > 0$  is obtained at 500 nm. On the other hand, for  $\alpha_0 > 54^\circ$ ,  $\Delta R_p > 0$  is obtained at  $\lambda = 410$  nm, whereas  $\Delta R_p < 0$  is obtained at 500 nm. The excellent resolution obtained for resolving the two components of the spectra cannot be achieved by transmission spectroscopy. Therefore, the great potential of the UV-Vis reflection spectroscopy is demonstrated by the results in Fig. 3.19.

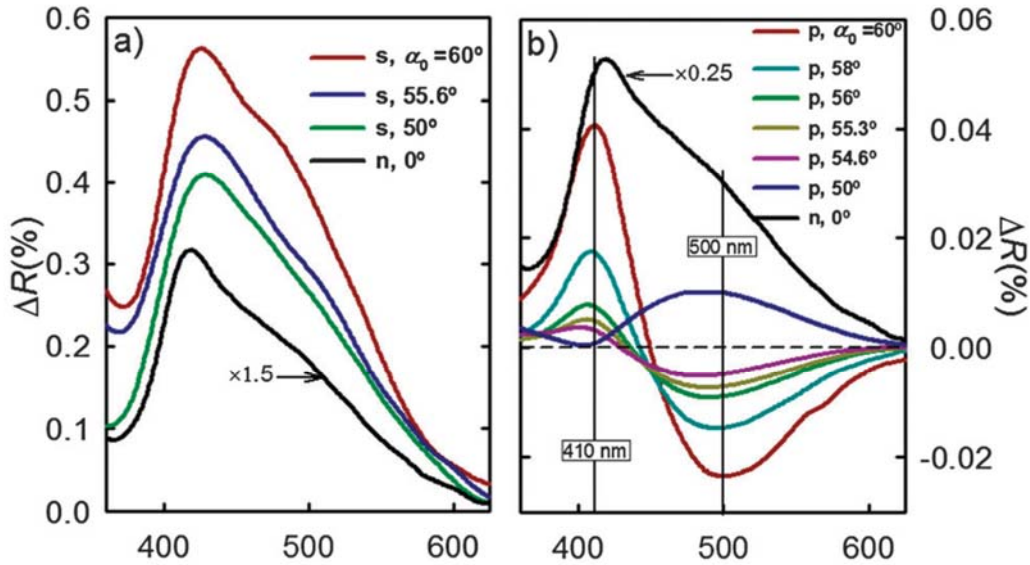


**Fig. 3.19.** Reflection spectra of the SP:SA = 1:1 mixed Langmuir monolayer at  $\pi = 35$  mN/m, (a)  $R_s$  and (b)  $\Delta R_p$ . The incidence angles are indicated in the Figure.  $\Delta R_n$  (black lines) is shown as a reference.

The experimental values for  $\Delta R_s$  and  $\Delta R_p$  vs  $\alpha_0$ , for  $\lambda = 410$  and 500 nm, i.e., the wavelength corresponding to the absorption maxima of each component, are shown as circles in Fig. 3.20, circles. In a first approximation, the relations used in Fig. 3.12 have been applied to estimate the value of  $P(\theta)$ . Thus, for  $\lambda = 410$  nm, and  $\alpha_0 = 65^\circ$ ,  $\Delta R_p/\Delta R_s = +0.2$  is obtained. On the other hand, for  $\lambda = 500$  nm,  $\Delta R_p/\Delta R_s = -0.14$  is obtained. According to Fig. 3, these  $\Delta R_p/\Delta R_s$  ratios correspond to  $P(\theta) \approx 0.15$  and  $P(\theta) \approx 0.7$  at  $\lambda = 410$  and 500 nm, respectively

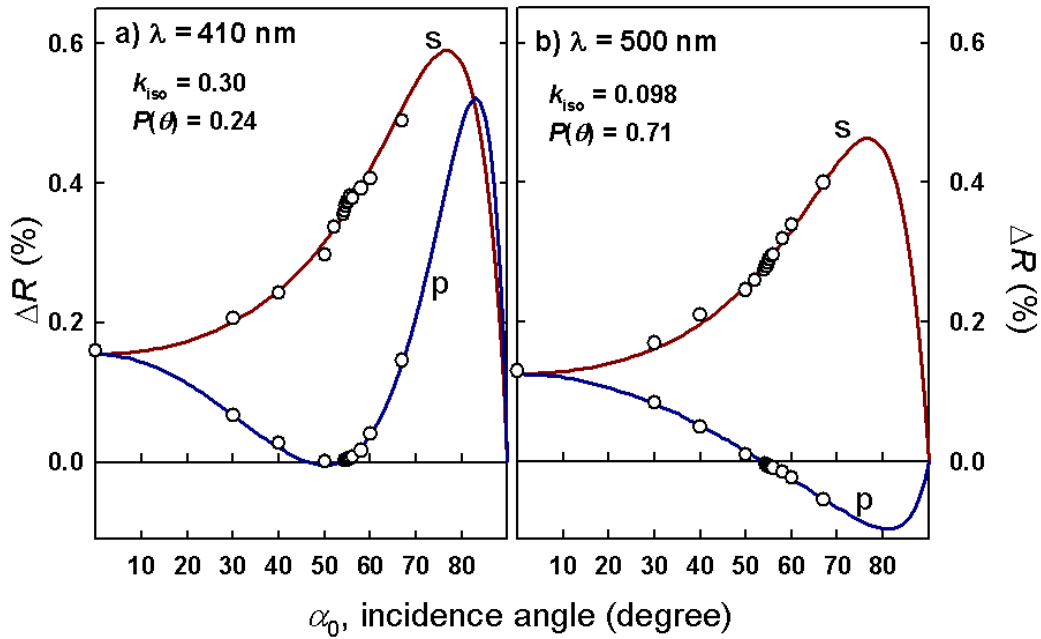


**Fig. 3.20.** Circles: Experimental  $\Delta R_s$  and  $\Delta R_p$  of the SP:SA = 1:1 mixed Langmuir monolayer for  $\pi = 35$  mN/m, corresponding to the wavelengths (a)  $\lambda = 410$  nm (b) and  $\lambda = 580$  nm. The solid lines correspond to the theoretical variation of  $\Delta R_s$  (red) and  $\Delta R_p$  (blue) vs  $\alpha_0$  for: (a)  $n_1 = 1.6$ ,  $d = 2.5$  nm,  $k_x = 0.11$  and  $k^{\max} = 1.1$ . (b)  $n_1 = 1.6$ ,  $d = 2.5$  nm,  $k_x = 0.07$  and  $k^{\max} = 0.11$ .

More accurate values of  $P(\theta)$  can be obtained through numerical fitting. Assuming, as in the previous cases, a value of  $n_1 = 1.55$ , the estimated thickness of the Langmuir monolayer at  $\pi = 35$  mN/m has been  $d \approx 2.5$  nm. The solid red (s) and blue (p) lines in Fig. 20 correspond to the theoretical predictions for the values of the parameters obtained after the numerical fitting. Thus, we obtain  $k_{\text{iso}} = 0.30 \pm 0.02$  and  $P(\theta) = 0.24 \pm 0.02$ , for  $\lambda = 410$  nm, while  $k_{\text{iso}} = 0.098 \pm 0.006$  and  $P(\theta) = 0.71 \pm 0.04$  for  $\lambda = 500$  nm are obtained. The  $P(\theta)$  obtained values are in good agreement with those obtained previously for Langmuir–Blodgett films of the mixed Langmuir monolayer,<sup>64</sup>  $P(\theta) = 0.28$  for  $\lambda = 405$  nm, and  $P(\theta) = 0.69$  for  $\lambda = 510$  nm, by using transmission spectroscopy of s- and p-polarized radiation at different incidence angles.

A hemicyanine dye closed to SP has been studied at the air– water interface by using second harmonic generation.<sup>85</sup> In this study and at higher compression the aggregation and tilt of the hemicyanine is confirmed although the average values of tilt of the chromophore is not provided.

### 3.2.5 Conclusions

The UV-Vis reflection spectroscopy provides highly valuable information on tilt and aggregation of chromophores at the air–liquid interface. Owing to a lack of theoretical background, the use of UV-Vis Reflection Spectroscopy has been restricted to normal incidence.

Herein, a method to obtain the order parameter  $P(\theta)$ , from  $\Delta R$  measurement by using s- and p-polarized radiation at different incidence angles has been presented. This method can be applied for any anisotropic thin film between two isotropic media, i.e., air and liquid in this case. Therefore, the UV-Vis reflection spectroscopy is highly sensitive to the tilt of the chromophores in the incidence angle regions close to or greater than the Brewster angle of the air–liquid interface using p-polarized radiation.

Two experimental examples illustrate the use of the method. First, a Rhodamine amphiphilic derivative. Second, a mixed Langmuir monolayer containing a hemicyanine derivative. In the first case,  $P(\theta)$  at two values of surface pressure is successfully obtained. In the second case, the two components with different polarization properties have been completely solved by using p-polarized light and incidence angles next to or greater than the Brewster angle.

Therefore, the standard usage of UV-Vis reflection spectroscopy has been presented, along with a new method for further advancing the use of this experimental technique. The theoretical background of this method has been thoroughly described; moreover two experimental examples have been included to illustrate its practical application. We expect the present work to inspire novel experiments in which privileged and richly detailed information on Langmuir monolayers can be achieved. A most appealing possibility would be to extend this spectroscopy to 2D mapping, allowing the imaging of the Langmuir monolayer. The different phases in the case of domains could be studied separately, and given enough lateral resolution, even the different sections within the domains.

## Appendix

The anisotropic thin film is assumed to be material with the complex refractive indices of  $N_x, N_y, N_z$ . As shown in Scheme 3.1, the reflection incidence angle  $\alpha_0$  and transmission angle  $\alpha_2$  of multiply reflected waves are constants and are related by  $n_0 \sin(\alpha_0) = n_2 \sin(\alpha_2)$ , where  $n_0 = 1$  (air) and  $n_2 = 1.333$  (water) show the real refractive indices of the ambient and the substrate, respectively.

In this case, the light reflection at the ambient/film interface can be expressed as follows:<sup>76</sup>

$$r_{01pp} = \frac{N_x N_z \cos(\alpha_0) - n_0 \left( N_z^2 - n_0^2 \sin(\alpha_0)^2 \right)^{1/2}}{N_x N_z \cos(\alpha_0) + n_0 \left( N_z^2 - n_0^2 \sin(\alpha_0)^2 \right)^{1/2}} \quad (3.20)$$

$$r_{12pp} = \frac{n_2 \left( N_z^2 - n_2^2 \sin(\alpha_2)^2 \right)^{1/2} - N_x N_z \cos(\alpha_2)}{n_2 \left( N_z^2 - n_2^2 \sin(\alpha_2)^2 \right)^{1/2} + N_x N_z \cos(\alpha_2)} \quad (3.21)$$

$$r_{01ss} = \frac{n_0 \cos(\alpha_0) - \left( N_y^2 - n_0^2 \sin(\alpha_0)^2 \right)^{1/2}}{n_0 \cos(\alpha_0) + \left( N_y^2 - n_0^2 \sin(\alpha_0)^2 \right)^{1/2}} \quad (3.22)$$

$$r_{12ss} = \frac{\left( N_y^2 - n_2^2 \sin(\alpha_2)^2 \right)^{1/2} - n_2 \cos(\alpha_2)}{\left( N_y^2 - n_2^2 \sin(\alpha_2)^2 \right)^{1/2} + n_2 \cos(\alpha_2)} \quad (3.23)$$

The total reflection coefficients

$$r_{012xx} = \frac{r_{01xx} + r_{12xx} \exp(-2 \cdot i \cdot \beta_x)}{1 + r_{01xx} r_{12xx} \exp(-2 \cdot i \beta_x)} \quad (3.24)$$

where  $x = s$  or  $p$  and

$$\beta_p = \frac{2\pi d}{\lambda} \frac{N_x}{N_z} \left( N_z^2 - n_0^2 \sin(\alpha_0)^2 \right)^{1/2} \quad (3.25)$$

$$\beta_s = \frac{2\pi d}{\lambda} \left( N_y^2 - n_0^2 \sin(\alpha_0)^2 \right)^{1/2} \quad (3.26)$$

where  $\lambda$  is the wavelength, and  $d$  is the thickness of the thin film. We obtain the reflectances for x = s or p-polarized waves as follows:

$$R_x = |r_{012xx}|^2 \quad (3.27)$$

The complex refractive indices of anisotropic materials along the x, y, and z axes are given by  $N_x = n_x - ik_x$ ,  $N_y = n_y - ik_y$ , and  $N_z = n_z - ik_z$ , respectively.

## Acknowledgements

The authors thank the Spanish CICYT for financial support of this research in the Framework of Project CTQ2010-17481 (FEDER A), and also thank Junta de Andalucía (Consejería de Economía, Innovación, Ciencia y Empleo) for special financial support (P08-FQM-and P10-FQM-6703). C.R-C. acknowledges the MECD (Spanish Ministry of Education, Culture, and Sport) for an FPU grant. Dr A. M. González-Delgado and Dr Dirk Hönig from Accurion ([www.nanofilm.de](http://www.nanofilm.de)) are acknowledged for their outstanding contribution.

## References

1. H. Gruniger, D. Mobius and H. Meyer, *J. Chem. Phys.*, 1983, 79, 3701.
2. D. Mobius, M. Orrit, H. Gruniger and H. Meyer, *Thin Solid Films*, 1985, 132, 41.
3. M. Orrit, D. Mobius, U. Lehmann and H. Meyer, *J. Chem. Phys.*, 1986, 85, 4966.
4. Y. Moriya, T. Hasegawa, T. Okada, N. Ogawa, E. Kawai, K. Abe, M. Ogasawara, S. Kato and S. Nakata, *Anal. Chem.*, 2006, 78, 7850.
5. D. Mobius and H. Mohwald, *Adv. Mater.*, 1991, 3, 19. 6 Z. Kozarac, A. Dhathathreyan and D. Mobius, *Colloids Surf.*, 1988, 33, 11.
7. M. Pinheiro, M. Lucio, S. Reis, J. L. F. C. Lima, J. M. Caio, C. Moiteiro, M. T. Martin-Romero, L. Camacho and J. J. Giner-Casares, *J. Phys. Chem. B*, 2012, 116, 11635.
8. M. Ahlers, R. Blankenburg, H. Haas, D. Mobius, H. Mohwald, W. Muller, H. Ringsdorf and H. U. Siegmund, *Adv. Mater.*, 1991, 3, 39.
9. M. Ohnishi, C. Ishimoto and J. Seto, *Bull. Chem. Soc. Jpn.*, 1995, 68, 230.
10. A. M. G. da Silva, R. S. Romao and S. M. B. Costa, *Chem. Phys. Lipids*, 2004, 127, 77.
11. K. Asano, K. Miyano, H. Ui, M. Shimomura and Y. Ohta, *Langmuir*, 1993, 9, 3587.
12. J. Engelking, M. Wittemann, M. Rehahn and H. Menzel, *Langmuir*, 2000, 16, 3407.
13. P. J. N. Kett, M. T. L. Casford, A. Y. Yang, T. J. Lane, M. S. Johal and P. B. Davies, *J. Phys. Chem. B*, 2009, 113, 1559.
14. R. C. Ahuja, P. L. Caruso, D. Mobius, G. Wildburg, H. Ringsdorf, D. Philp, J. A. Preece and J. F. Stoddart, *Langmuir*, 1993, 9, 1534.



15. W. Budach, R. C. Ahuja and D. Mobius, *Langmuir*, 1993, 9, 3093.
16. H. Huesmann, C. A. Bignozzi, M. T. Indelli, L. Pavanin, M. A. Rampi and D. Mobius, *Thin Solid Films*, 1996, 284, 62.
17. J. J. Giner-Casares, G. de Miguel, M. Perez-Morales, M. T. Martin-Romero, L. Camacho and E. Munoz, *J. Phys. Chem. C*, 2009, 113, 5711.
18. S. L. Selektor, O. A. Raitman, D. A. Silant'eva, N. V. Ivanova, G. Yonusauskas, E. V. Lukovskaya, P. Batat and V. V. Arslanov, *Prot. Met. Phys. Chem. Surf.*, 2011, 47, 484.
19. F. Porteu, S. Palacin, A. Ruaudelteixier and A. Barraud, *J. Phys. Chem.*, 1991, 95, 7438.
20. R. Ahuja, P. L. Caruso, D. Mobius, W. Paulus, H. Ringsdorf and G. Wildburg, *Angew. Chem., Int. Ed. Engl.*, 1993, 32, 1033.
21. T. M. Bohanon, P. L. Caruso, S. Denzinger, R. Fink, D. Mobius, W. Paulus, J. A. Preece, H. Ringsdorf and D. Schollmeyer, *Langmuir*, 1999, 15, 174.
22. O. Haruta, Y. Matsuo, Y. Hashimoto, K. Niikura and K. Ijiro, *Langmuir*, 2008, 24, 2618.
23. A. M. Gonzalez-Delgado, J. J. Giner-Casares, G. Brezesinski, J.-B. Regnouf-de-Vains and L. Camacho, *Langmuir*, 2012, 28, 12114.
24. Y. Tomioka, N. Tanaka and S. Imazeki, *J. Chem. Phys.*, 1989, 91, 5694.
25. E. Ando, K. Moriyama, K. Arita and K. Morimoto, *Langmuir*, 1990, 6, 1451.
26. G. Pace, V. Ferri, C. Grave, M. Elbing, C. von Haenisch, M. Zharnikov, M. Mayor, M. A. Rampi and P. Samori, *Proc. Natl. Acad. Sci. U. S. A.*, 2007, 104, 9937.
27. J. Freimanis, E. Markava, G. Matisova, L. Gerca, I. Muzikante, M. Rutkis and E. Silinsh, *Langmuir*, 1994, 10, 3311.

28. R. C. Ahuja, J. Maack and H. Tachibana, *J. Phys. Chem.*, 1995, 99, 9221.
29. H. Huesmann, J. Maack, D. Mobius and J. F. Biernat, *Sens. Actuators, B*, 1995, 29, 148.
30. J. Maack, R. C. Ahuja and H. Tachibana, *J. Phys. Chem.*, 1995, 99, 9210.
31. T. Kawai, R. Hane, F. Ishizaka and K. Kon-No, *Chem. Lett.*, 1999, 375.
32. I. Kim, J. F. Rabolt and P. Stroeve, *Colloids Surf., A*, 2000, 171, 167.
33. N. J. Dunn, W. H. Humphries, A. R. Offenbacher, T. L. King and J. A. Gray, *J. Phys. Chem. A*, 2009, 113, 13144.
34. R. C. Ahuja, D. Mobius and M. Matsumoto, *Thin Solid Films*, 1992, 210, 60.
35. W. Budach, R. C. Ahuja, D. Mobius and W. Schrepp, *Thin Solid Films*, 1992, 210, 434.
36. B. J. Dringenberg, R. C. Ahuja and D. Mobius, *Thin Solid Films*, 1994, 243, 569.
37. A. Gil, I. Aristegui, A. Suarez, I. Sandez and D. Mobius, *Langmuir*, 2002, 18, 8527.
38. S. Martin, M. Haro, M. C. Lopez, F. M. Royo and P. Cea, *Surf. Sci.*, 2006, 600, 3045.
39. C. Roldan-Carmona, A. M. Gonzalez-Delgado, A. Guerrero- Martinez, L. De Cola, J. J. Giner-Casares, M. Perez-Morales, M. T. Martin-Romero and L. Camacho, *Phys. Chem. Chem. Phys.*, 2011, 13, 2834.
40. G. Caminati, R. C. Ahuja and D. Mobius, *Thin Solid Films*, 1992, 210, 335.
41. P. L. Caruso, R. C. Ahuja, D. Mobius, G. Wildburg and H. Ringsdorf, *Thin Solid Films*, 1994, 243, 564.

42. I. Sandez-Macho, J. Gonzalez-Lopez, A. Suarez-Varela and A. Mobius, *J. Phys. Chem. B*, 2005, 109, 22386.
43. G. Gabrielli, G. Caminati and M. Puggelli, *Adv. Colloid Interface Sci.*, 2000, 87, 75.
44. M. T. Martin, I. Prieto, L. Camacho and D. Mobius, *Langmuir*, 1996, 12, 6554.
45. A. M. G. da Silva, M. I. Viseu, A. Malathi, P. Antunes and S. M. B. Costa, *Langmuir*, 2000, 16, 1196.
46. A. L. Lusk and P. W. Bohn, *J. Phys. Chem. B*, 2001, 105, 462. 47 A. M. G. da Silva, M. I. Viseu, R. I. S. Romao and S. M. B. Costa, *Phys. Chem. Chem. Phys.*, 2002, 4, 4754.
48. J. M. Pedrosa, M. T. M. Romero, L. Camacho and D. Mo"bius, *J. Phys. Chem. B*, 2002, 106, 2583.
49. A. Gil, D. Mobius, I. Sandez and A. Suarez, *Langmuir*, 2003, 19, 6430.
50. M. Perez-Morales, J. M. Pedrosa, M. T. Martin-Romero, D. Mobius and L. Camacho, *J. Phys. Chem. B*, 2004, 108, 4457.
51. S. G. Youm, K. Paeng, Y. W. Choi, S. Park, D. Sohn, Y. S. Seo, S. K. Satija, B. G. Kim, S. Kim and S. Y. Park, *Langmuir*, 2005, 21, 5647.
52. P. Cea, S. Martin, A. Villares, D. Mobius and M. C. Lopez, *J. Phys. Chem. B*, 2006, 110, 963.
53. A. A. Turshatov, D. Mobius, M. L. Bossi, S. W. Hell, A. I. Vedernikov, N. A. Lobova, S. P. Gromov, M. V. Alfimov and S. Y. Zaitsev, *Langmuir*, 2006, 22, 1571.
54. S. Martin, P. Cea, G. Pera, M. Haro and M. C. Lopez, *J. Colloid Interface Sci.*, 2007, 308, 239.

55. G. Pera, A. Villares, M. C. Lopez, P. Cea, D. P. Lydon and P. J. Low, *Chem. Mater.*, 2007, 19, 857.
56. J. J. Giner-Casares, M. Perez-Morales, H. J. Bolink, N. Lardies, E. Munoz, G. de Miguel, M. T. Martin-Romero and L. Camacho, *J. Mater. Chem.*, 2008, 18, 1681.
57. M. Haro, J. del Barrio, A. Villares, L. Oriol, P. Cea and M. C. Lopez, *Langmuir*, 2008, 24, 10196.
58. M. Lakshmanan, S. S. Raman and A. Dhathathreyan, *Appl. Surf. Sci.*, 2008, 255, 3381.
59. I. Giner, I. Gascon, R. Gimenez, P. Cea, M. Carmen Lopez and C. Lafuente, *J. Phys. Chem. C*, 2009, 113, 18827.
60. K. Ingot, T. Martynski and D. Bauman, *Opto-Electron. Rev.*, 2009, 17, 120.
61. C. Ingrosso, M. L. Curri, P. Fini, G. Giancane, A. Agostiano and L. Valli, *Langmuir*, 2009, 25, 10305.
62. H. Liu, H. Zheng, W. Miao and X. Du, *Langmuir*, 2009, 25, 2941.
63. A. M. Gonzalez-Delgado, C. Rubia-Paya, C. Roldan-Carmona, J. J. Giner-Casares, M. Perez-Morales, E. Munoz, M. T. Martin-Romero, L. Camacho and G. Brezesinski, *J. Phys. Chem. C*, 2010, 114, 16685.
64. A. M. Gonzalez-Delgado, J. J. Giner-Casares, C. Rubia-Paya, M. Perez-Morales, M. T. Martin-Romero, G. Brezesinski and L. Camacho, *J. Phys. Chem. C*, 2011, 115, 9059.
65. K. B. Eisenthal, *Chem. Rev.*, 1996, 96, 1343.
66. A. Tronin, J. Strzalka, V. Krishnan, I. Kuzmenko, H. C. Fry, M. Therien and J. K. Blasie, *Rev. Sci. Instrum.*, 2009, 80, 033102.
67. A. Gericke, A. V. Michailov and H. Huhnerfuss, *Vib. Spectrosc.*, 1993, 4, 335.

68. D. Blaudez, T. Buffeteau, J. C. Cornut, B. Desbat, N. Escafre, M. Pezolet and J. M. Turllet, *Appl. Spectrosc.*, 1993, 47, 869.
69. D. Blaudez, J. M. Turllet, J. Dufourcq, D. Bard, T. Buffeteau and B. Desbat, *J. Chem. Soc., Faraday Trans.*, 1996, 92, 525.
70. M. Pope and C. E. Swenberg, *Electronic Processes in Organic Crystals and Polymers*, Oxford Science Publ., New York, 1999.
71. T. Kobayashi, *J-Aggregates*, World Scientific, Singapore, 1996.
72. A. Carretero-Genevri, C. Boissiere, L. Nicole and D. Grosso, *J. Am. Chem. Soc.*, 2012, 134, 10761.
73. S. Rauch, P. Uhlmann and K. J. Eichhorn, *Anal. Bioanal. Chem.*, 2013, 405, 9061.
74. H. Kuhn and H. D. Försterling, *Principles of Physical Chemistry*, John Wiley and Sons, New York, 2000.
75. M. Vandevyver, A. Barraud, A. Raudelteixier, P. Maillard and C. Gianotti, *J. Colloid Interface Sci.*, 1982, 85, 571.
76. R. M. A. Azzam and N. M. Bashara, *Ellipsometry and Polarized Light*, Elsevier Science B. V., Amsterdam, 1999.



### 3.3 Molecular organization and effective energy transfer in iridium metallosurfactant–porphyrin assemblies embedded in Langmuir–Schaefer films

Roldán-Carmona, C.<sup>1</sup>; Gonzalez-Delgado, A.M.<sup>1</sup>; Guerrero-Martinez, A.<sup>2</sup>; De Cola, L.<sup>3</sup>;  
Giner-Casares, J.J.<sup>4</sup>; Perez-Morales, M.<sup>1</sup>; Martin-Romero, M.T.<sup>1</sup>. and Camacho, L.<sup>1</sup>

<sup>1</sup>*Depart. of Physical Chemistry, University of Cordoba, C. Rabanales, Ed. C3, Cordoba, E-14014, Spain.*

<sup>2</sup>*Depart. of Physical Chemistry, University of Vigo, C. Univ., Vigo, E-36310, Spain*

<sup>3</sup>*Physikalisches Institut, Westfälische Wilhelms Univ. Münster, Mendelstrasse 7, D-48149, Germany*

<sup>4</sup>*Max Planck Institute of Colloids and Interfaces, Int. Depart., Sci. Park Golm, D-14476, Germany*

Mixed Langmuir monolayers and Langmuir–Schaefer (LS) films containing the cationic metallosurfactant bis(2-phenylpyridine)(4,40-diheptadecyl-2,20-bipyridine)-iridium(III) chloride (Ir-complex) and the anionic tetrakis(4-sulfonatophenyl)porphyrin (TSPP) in 4 : 1 molar ratio have been successfully prepared by the co-spreading method at the air–water interface. The presence of both luminescent species at the interface, as well as the organization of the TSPP underneath the Ir-complex matrix in Langmuir and LS films, is inferred by surface techniques such as  $\pi$ - $A$  isotherms, reflection spectroscopy, Brewster angle microscopy (BAM) and UV–visible absorption spectroscopy. A red-shift in the absorption band of the porphyrin under the compression of the mixed monolayer suggests the J-aggregation of the TSPP under the Ir-complex matrix. To date, this is the first report of Langmuir and/or LS films containing these two types of species together. Furthermore, the intermolecular energy transfer between Ir-complex and TSPP molecules in solution and in transferred mixed films is investigated through steady-state fluorescence and lifetime measurements. These results indicate that effective intermolecular energy transfer occurs from the Ir-complex to the TSPP molecules in LS films. The influence of the spatial proximity of donor and acceptor molecules has been studied by the insertion of lipid interlayers among them.

Paper published in *Phys. Chem. Chem. Phys.* 13, 2834–2841, 2011.

### 3.3.1 Introduction

Several methods to build well-ordered molecular assemblies are being developed as a current objective of the Supramolecular Chemistry.<sup>1,2</sup> For these purposes, the air–water interface is an ideal model, as it allows for the assembly of organized ultrathin films containing different molecules with various functions and well-defined architectures (composition, structure, and thickness), by using the Langmuir trough technique. Furthermore, Langmuir monolayers can be transferred onto solid substrates by vertical deposition (Langmuir–Blodgett film, LB) or horizontal touching (Langmuir–Schaefer film, LS). Among the different available deposition methods, these techniques offer the possibility of arranging molecules and preparing highly-ordered ultrathin multilayers with precisely controlled thickness at the molecular level. Therefore, LB and LS techniques are interesting not only in a fundamental way, but they are also powerful tools for studying distance dependent energy and electron transfer processes.<sup>3</sup>

In this work, we report on the formation of a mixed monolayer at the air–water interface and transferred by the LS method onto a solid substrate, containing two luminescent molecules: an amphiphilic monocationic Ir(III) metallocosurfactant, Ir-complex, and a tetraanionic water-soluble porphyrin, TSPP (see Scheme 3.2). The Ir-complex used here belongs to the family of organometallic triplet emitters, which are receiving great attention not only because of their use in electroluminescent devices,<sup>4–7</sup> and gas sensing,<sup>8–10</sup> but also in biomedical applications.<sup>11,12</sup> Water-soluble porphyrins may be regarded as models of native porphyrin derivatives in the physiological state, as their structural simplicity, in comparison to the native analogues, facilitates the understanding of structure–biological activity relations. Moreover, porphyrin aggregates have attracted much attention as potential candidates for applications in non linear optics, nanometre-sized photoconductors, light-harvesting systems or optical sensors.<sup>13–17</sup>

The literature concerning organized molecular films of cyclometalated iridium-(III) complexes is limited, and has been focused on the preparation of pure films of



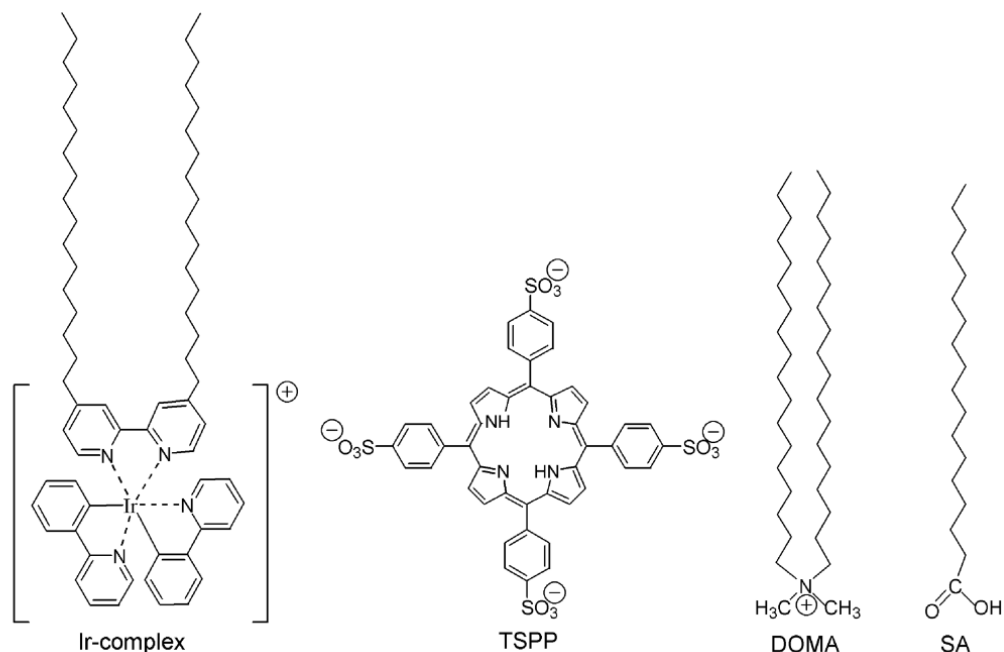
amphiphilic Ir(III) derivatives,<sup>10,18</sup> or mixed films containing water-insoluble complexes organized underneath a lipid matrix.<sup>19,20</sup> Valli et al. achieved densely packed LS films of an amphiphilic Ru(II) complex,<sup>21</sup> and more recently two reports have shown the deposition of LB films of amphiphilic iridium(III) complexes, mixed with polyoxometalates and alternated with an amphiphilic ruthenium complex for OLEDs application.<sup>22,23</sup> To date the preparation of organized thin films of porphyrin derivatives has been studied by several research groups and a large number of works concerning water-soluble porphyrins have been published.<sup>24–32</sup> Among these works, the research carried out by Valli's group is of special interest,<sup>31,32</sup> who obtained bichromophoric LS films containing water-soluble porphyrins with other cationic surfactants. However, the fabrication of an iridium metallosurfactant–porphyrin film is reported, for the first time to our knowledge, in this work. In this way, the Langmuir technique has allowed us to assemble these two luminescent species together, which may behave as energy donor and acceptor units in an energy transfer process. Moreover, the influence of the spatial proximity of the Ir-complex and the porphyrin ring has been studied by the insertion of interlayers among them, allowing a control of the two emissions.

### 3.3.2 Experimental

#### Materials

The iridium metallosurfactant bis(2-phenylpyridine)(4,40-diheptadecyl-2,20-bipyridine)-iridium(III) chloride (Ir-complex) was synthesized following the procedure published elsewhere.<sup>33</sup> Tetrakis(4-sulfonatophenyl)porphyrin (TSPP), dioctadecyldimethylammonium bromide (DOMA), and stearic acid (SA) were purchased from Fluka, Sigma and Aldrich, respectively, and used without purification. Their molecular structures are depicted in Scheme 3.2. Pure organic solvents were obtained without purification from Aldrich (Germany). A mixture of chloroform/methanol, ratio 3 : 1 (v/v), was used as a spreading solvent for the Ir-complex. A mixture of dichloromethane, methanol and water, ratio 15 : 9 : 2 (v/v/v),

was used as a spreading solvent for solving DOMA and TSPP. Ultrapure water, produced by a Millipore Milli-Q unit, pre-treated by a Millipore reverse osmosis system (>18.2MO cm), was used as a subphase. The subphase temperature was 21 °C with pH 5.7.



**Scheme 3.2** Molecular structures of amphiphilic iridium complex (Ir-complex), tetrakis(4-sulfonatophenyl)porphyrin (TSPP), dioctadecyldimethylammonium bromide (DOMA) and stearic acid (SA).

## Methods

Two different models of Nima troughs (Nima Technology, Coventry, England) were used in this work, both provided with a Wilhelmy type dynamometric system using a strip of filter paper: a NIMA 611D with one moving barrier for the measurement of the reflection spectra, and a NIMA 601, equipped with two symmetrical barriers to record BAM images.

UV–visible reflection spectra at normal incidence as the difference in reflectivity ( $\Delta R$ ) of the dye film-covered water surface and the bare surface<sup>34</sup> were obtained with a Nanofilm Surface Analysis Spectrometer (Ref SPEC2, supplied by

Accurion GmbH, Göttingen, Germany). The reflection spectra were normalized to the same surface density of Ir-complex by multiplying  $\Delta R$  by the surface area, i.e.,  $\Delta R_{\text{norm}} = \Delta R A$ , where  $A$  ( $\text{nm}^2/\text{Ir-complex molecule}$ ) is taken from the surface pressure–area ( $\pi$ – $A$ ) isotherms.

Images of the film morphology were obtained by Brewster angle microscopy (BAM) with a I-Elli2000 (Accurion GmbH) using a Nd:YAG diode laser with a wavelength of 532 nm and 50 mW, which can be recorded with a lateral resolution of 2  $\mu\text{m}$ . The image processing procedure included a geometrical correction of the image, as well as a filtering operation to reduce interference fringes and noise. The microscope and the film balance were located on a table with vibration isolation (antivibration system MOD-2 S, Accurion GmbH) in a large class 100 clean room.

The monolayers were transferred onto quartz substrates, cleaned in successive steps with an alkaline detergent, isopropanol, and ethanol and then rinsed with ultrapure water. The monolayers were transferred at a constant surface pressure by the Langmuir–Schaefer technique, i.e., by horizontal touching of the substrate and the interface covered with the mixed film. The multilayers were assembled by sequential monolayer transfer. The ratio of the transfer process to the solid substrates,  $\tau$ , was close to unity in all cases.

UV–visible electronic absorption spectra of the LS films were recorded locating the support directly in the light path on a Cary 100 Bio UV–visible spectrophotometer.

The steady state fluorescence and excitation spectra were measured using a FS920 Steady State Fluorimeter (Edinburgh Instrument, Livingston, UK). The emission lifetimes were measured by a FL920 Fluorescence Lifetime Spectrometer (Edinburgh Instrument), based on the TCSPC (Time-Correlated Single Photon Counting) technique<sup>35</sup> and using different picosecond pulsed diode lasers (372 and 406 nm). The luminescence decay curve analysis was performed by a deconvolution technique, where the experimental data were compared with a model decay function. The decay parameters were determined by least-squares fitting routine, the goodness of the fit was assessed by the reduced  $\chi^2$  values obtained (range 1–1.2). All

measurements were carried out at room temperature and solutions in the air-equilibrated solvent (dichloromethane/ methanol/water, ratio 15 : 9 : 2 v/v/v), using a 1.0 cm path length quartz cuvette.

### 3.3.3 Results and discussion

#### Surface pressure–area isotherms

The studied Ir-complex is amphiphilic and forms Langmuir monolayers on pure water. As this metallosurfactant is positively charged, mixed monolayers of Ir-complex and the anionic water-soluble porphyrin TSPP, in molar ratio 4 : 1, have been prepared by the co-spreading method<sup>36</sup> at the air–water interface.

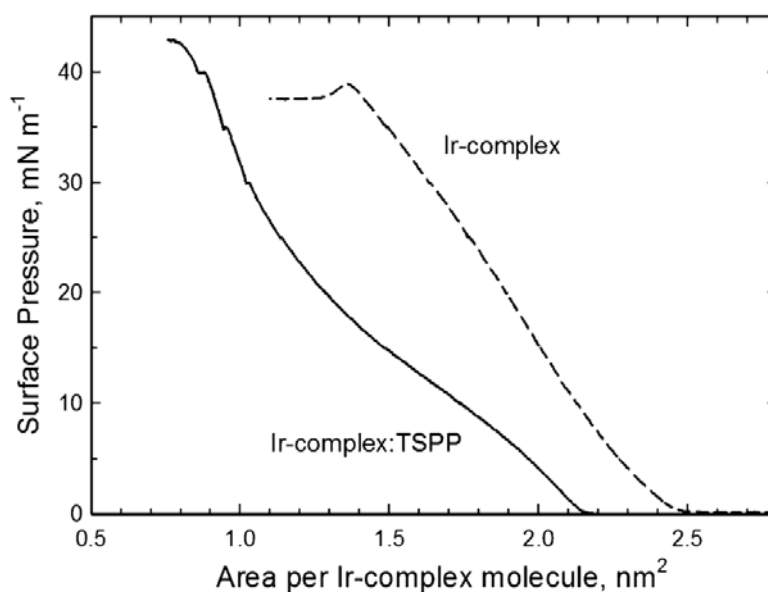


**Fig. 3.21** Surface pressure–area ( $\pi$ – $A$ ) isotherms of the Ir-complex monolayer and the Ir-complex : TSPP mixed monolayer in a molar ratio 4 : 1 ( $T = 21$  °C).

This mixing ratio corresponds to the stoichiometry to form neutral monolayers and thus we expect that all the porphyrin molecules remain bound to the complex matrix by electrostatic interactions, which was tested further on. The surface pressure–

area ( $\pi$ - $A$ ) isotherms of the pure Ir-complex and the mixture Ir-complex : TSPP (4 : 1) are shown in Fig. 3.21, and are expressed per Ir-complex molecule. In both cases, the collapse occurred around 40 mN m<sup>-1</sup>.

In previous works,<sup>28,37</sup> a mixed monolayer containing TSPP and the lipid dioctadecyldimethylammonium bromide (DOMA) in a 1 : 4 molar ratio was studied at the air-water interface. In such a system,<sup>28</sup> the isotherm of the mixed film was expanded compared to that of the pure DOMA. Any expansion with respect to the pure lipid isotherm is clear evidence of the presence of the porphyrin molecules at the interface. In fact, this effect is normally observed in mixed films composed by a lipid matrix. However, the opposite phenomenon was observed for the Ir-complex : TSPP (4 : 1) mixed film, as the isotherm was shifted to smaller effective molecular areas compared with the pure complex, for all surface pressure. Then, the presence of the TSPP dye at the interface, together with the Ir-complex molecules, will be demonstrated by reflection spectroscopy.

The morphology of the Ir-complex and mixed Ir-complex : TSPP (4 : 1) films was directly visualized by BAM, simultaneously to the  $\pi$ - $A$  isotherm register. In the case of the pure Ir-complex, small bright domains appeared from 5 mN m<sup>-1</sup>, increasing in number and covering the whole surface at high surface pressure (images not shown). However, for the mixed film, a homogeneous monolayer was observed during the compression process, and the reflectivity of the interface increased gradually as the monolayer was compressed (images not shown). This fact may indicate that the TSPP molecules are homogeneously distributed over the whole surface underneath the Ir-complex matrix. Then, the use of porphyrin molecules as counterions in the mixed film helps to homogenize and distribute the Ir-complex molecules along the air-water interface.

## Reflection measurements

Reflection spectroscopy allows the direct detection of the presence of chromophore molecules located at the air–water interface,<sup>34</sup> and gives us valuable information on their organization, density, and orientation.

In Fig. 3.22, a series of reflection spectra at different surface pressures ( $\pi$ ) recorded during the compression of the Ir-complex monolayer are shown (solid lines). For comparison, the spectrum of Ir-complex in chloroform/methanol (3 : 1 v/v) solution is also included (dashed line). The bands between 240 and 320 nm can be assigned to ligand-centered  $\pi$ – $\pi^*$  transitions involving the phenylpyridines at higher energy and the bipyridines at lower energy.<sup>38</sup>

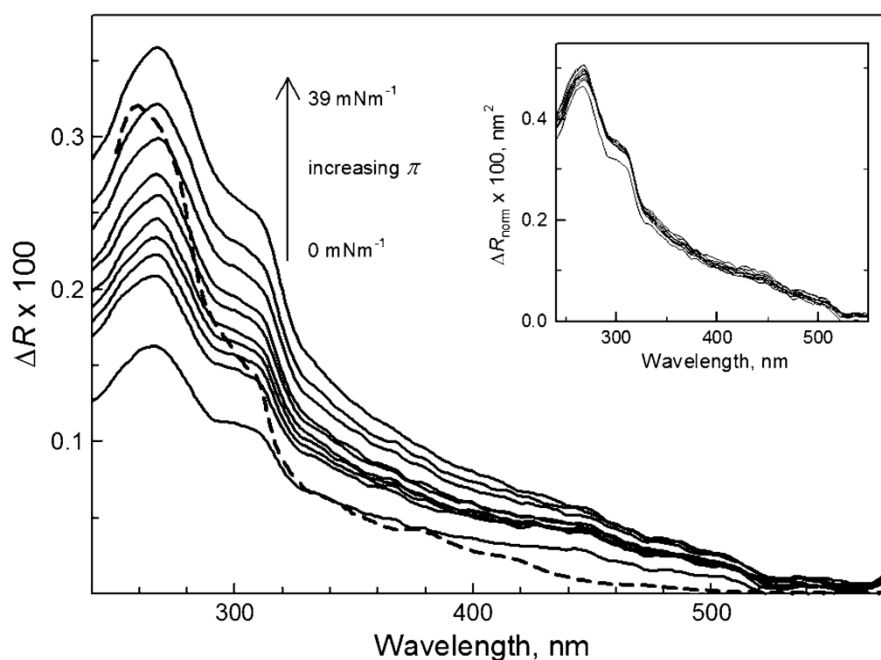


**Fig. 3.22** Reflection spectra  $\Delta R$  of the Ir-complex monolayer, from  $\pi = 0 \text{ mN m}^{-1}$  to  $39 \text{ mN m}^{-1}$ . Inset: normalized reflection spectra of the Ir-complex monolayer,  $\Delta R_{\text{norm}} = \Delta R \times A_{\text{Ir-complex}}$ .

As can be observed,  $\Delta R$  increased with the applied surface pressure, indicating that the surface concentration of the Ir-complex increased under compression of the film. Furthermore, it should be mentioned that reflection spectra were measured

during several compression and expansion cycles (data not shown), being these spectra identical during these processes and during several cycles.

Inset in Fig. 3.22 shows the normalized reflection spectra of the Ir-complex film,  $\Delta R_{\text{norm}}$ , being  $\Delta R_{\text{norm}} = \Delta R \times A_{\text{Ir-complex}}$ , where  $A_{\text{Ir-complex}}$  ( $\text{nm}^2$  per molecule) is taken from the isotherm. As can be observed, the normalized spectra did not experience any significant change in terms of intensity, shape and position of the bands as a function of the surface pressure. This result indicated the absence of changes of orientation and association of the metallosurfactant during the compression of the film.

The Ir-complex molecules present at the air–water interface can be quantified. For low values of absorption (e.g.,  $0.01$ ), the reflection  $\Delta R$  is given in a reasonable approximation by<sup>24,34,39,40</sup>

$$\Delta R = 2.303 \times 10^3 \Gamma f_{\text{orient}} \varepsilon \sqrt{R_s} \quad (3.28)$$

where  $R_s = 0.02$ <sup>41</sup> is the reflectivity of the air–water interface at normal incidence,  $\varepsilon$  is the extinction coefficient given as  $\text{L mol}^{-1} \text{cm}^{-1}$ ,  $f_{\text{orient}}$  is a numerical factor that takes into account the different average orientation of the chromophore in solution as compared to the monolayer at the air–water interface and  $\Gamma$  is the surface concentration in  $\text{mol cm}^{-2}$ . Additionally, surface concentration can be expressed as  $\Gamma = 10^{14}/N_A A$ , being  $N_A$  the Avogadro number and  $A$  the area per molecule in  $\text{nm}^2$ . Then, the normalized reflection can be expressed as:

$$\Delta R_{\text{norm}} \times 100 = 5.4 \times 10^{-6} f_{\text{orient}} \varepsilon \quad (3.29)$$

For the Ir-complex,  $\Delta R_{\text{norm}}$  can be calculated from eqn (2). The orientation factor can be considered equal to unity for the Ir-complex,<sup>42</sup> and assuming  $\varepsilon = \varepsilon_{\text{solution}}$  at  $\lambda_{\text{max}}$  ( $\varepsilon_{\text{sol},260} = 8 \times 10^4 \text{ L mol}^{-1} \text{cm}^{-1}$ ), we obtained  $\Delta R_{\text{norm}} \times 100 \approx 0.43 \text{ nm}^2$ . This value is in very good agreement with those obtained at any surface pressure (see inset in Fig.

3.22). This fact indicated that all the Ir-complex molecules initially spread remain at the air–water interface.

Fig. 3.23 shows the reflection spectra (a) and the normalized reflection spectra (b), obtained at different surface pressures for the Ir-complex : TSPP (4 : 1) monolayer. Together with the absorption bands due to the Ir-complex, all spectra showed the intense Soret band typical of porphyrins at  $\lambda_{\text{max}} = 422$  nm, which was clear evidence of the presence of TSPP molecules in the mixed monolayer. The wavelength of the peak at 422 nm corresponds to the position of the Soret band in solution, and therefore this peak must be related with non-aggregated porphyrin. As the film was compressed, the reflection intensity of both chromophores increased, which indicated that their surface densities in the monolayer also increased. Reflection spectra have also been measured during several cycles (data not shown) and identical spectra have been obtained, i.e., there was no loss of TSPP molecules toward the subphase.

At low surface pressure, TSPP molecules can be quantified by eqn (2). In this case,  $\epsilon_{\text{sol},420} = 4.5 \times 10^5 \text{ L mol}^{-1} \text{ cm}^{-1}$ . At this pressure, TSPP molecules are supposed to be flat oriented, which means  $f_{\text{orient}} = 1.5$  (see further comments). Then, the reflection was calculated to be  $\Delta R_{\text{norm}} \times 100 \approx 0.91 \text{ nm}^2$ . This value agreed well with that measured at 0 mN m<sup>-1</sup> ( $\Delta R_{\text{norm}} \times 100 \approx 0.88 \text{ nm}^2$ , see Fig. 3.23). Therefore, the former assumption of flat orientation and no loss of porphyrin TSPP molecules toward the aqueous subphase is correct.

Differently from the Ir-complex reflection bands, the porphyrin Soret band shifted to longer wavelengths upon compression. Inset in Fig. 3.23a plots the maximum absorption wavelength against the area per TSPP molecule. In previous work,<sup>28</sup> a blue-shift by ~12 nm with respect to the maximum wavelength at low surface pressure was observed for the DOMA : TSPP (4 : 1) system. In this case,<sup>28</sup> the wavelength shift was due to the appearance of a new band, related to the formation of TSPP dimers, i.e., only two maxima were detected along the compression.<sup>28</sup> However, for the Ir-complex : TSPP (4 : 1) mixed monolayer, the maximum wavelength red-



shifted continuously from  $\lambda_{\max} = 422$  nm until it reached a constant value  $\lambda_{\max} = 427$  nm, as shown in Fig. 3.23a (inset).

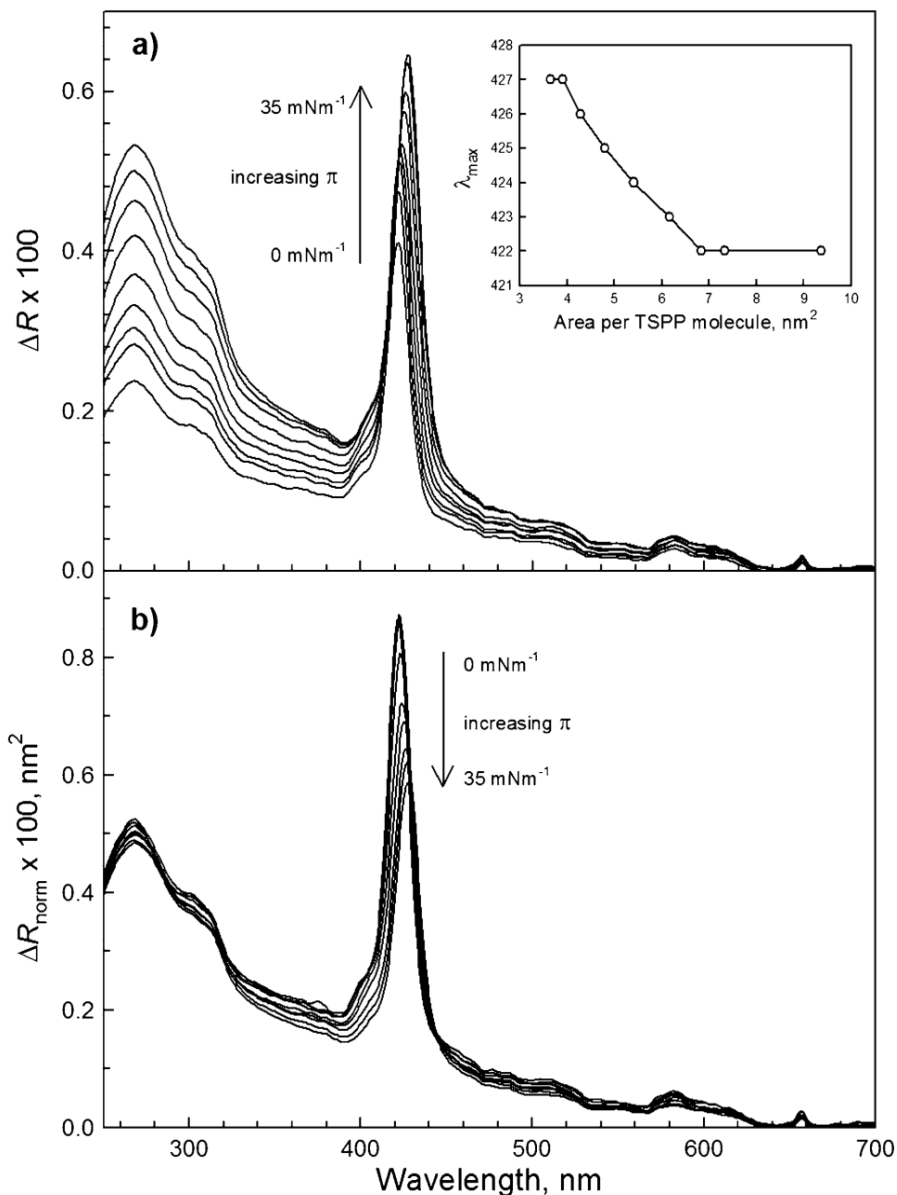


**Fig. 3.23** (a) Reflection spectra  $\Delta R$  of the Ir-complex : TSPP (4 : 1) monolayer, from  $\pi = 0$   $\text{mNm}^{-1}$  to  $35$   $\text{mNm}^{-1}$ . Inset: wavelength of maximum absorption of TSPP versus area per TSPP molecule; (b) normalized reflection spectra of the mixed monolayer,  $\Delta R_{\text{norm}} = \Delta R \times A_{\text{Ir-complex}}$ .

The reflection spectra have been normalized by the area per Ir-complex molecule (Fig. 3.23b),  $\Delta R_{\text{norm}} = \Delta R \times A_{\text{Ir-complex}}$ , where  $A_{\text{Ir-complex}}$  is taken from the isotherm of the mixed film. As can be clearly observed, the Soret band intensity of the

normalized spectra decreased under compression. Provided that all molecules of TSPP remain at the interface during the compression of the mixed film, the normalized reflection spectra show changes of orientation and/or association of the TSPP dye. In fact, J-aggregates are characterized by a shift of the spectral absorption band to longer wavelengths with respect to the non-aggregate state. In this mixed film, the red-shift may be due to interactions among the transition dipole moments of TSPP–TSPP or TSPP–Ir-complex neighboring molecules during the compression process.

In the case of porphyrins, i.e., molecules with two components of the transition dipole  $\neq 0$ , the orientation factor is given by

$$f_{orient} = \frac{3}{4}[1 + \langle \sin^2 \theta \rangle] \quad (3.30)$$

with  $\theta$  being the angle between the plane of the transition moments and the normal to the air–water interface (angle brackets denote average values), i.e.,  $\theta = 0^\circ$  and  $90^\circ$  for perpendicular and parallel orientation of the porphyrin ring with respect to the interface, respectively.<sup>43</sup> As the Ir-complex chromophore absorbs at  $\lambda_{max} = 422$  nm (Soret band of TSPP), the contribution of the Ir-complex reflection to each spectra has to be considered and subtracted. To infer the possible change in orientation of the TSPP molecules along the compression process, a further analysis has to be done as follows.

The oscillator strength is defined as<sup>44</sup>

$$f = \frac{4\varepsilon_0 2.303 m_e c_0}{N_A e^2} \int_{band} \varepsilon dv = 1.44 \times 10^{-19} \int_{band} \varepsilon dv \quad (3.31)$$

where  $\varepsilon_0$  is the permittivity of vacuum,  $m_e$  the electron mass,  $e$  the elementary charge,  $c_0$  the speed of light in a vacuum and  $N_A$  the Avogadro constant. In eqn (3.31), the numerical factor  $1.44 \times 10^{-19}$  is expressed in mol L<sup>-1</sup> cm s. From eqn (1) and (4) it is possible to define an apparent oscillator strength determined from the measured reflection spectra as<sup>40</sup>

$$f_{app} = f \times f_{orient} = \frac{1.44 \times 10^{-19}}{2.303 \times 10^3 \Gamma \sqrt{R_s}} \int_{band} \Delta R dv \quad (3.32)$$

If we take into account the relationship between the surface concentration,  $\Gamma$ , in mol cm<sup>-2</sup>, and the area per molecule,  $A$ , in nm<sup>2</sup> ( $\Gamma = 10^{14}/AN_A$ ) and we introduce the value  $R_s = 0.02$ ,<sup>41</sup> we obtain

$$\begin{aligned} f_{app} &= f \times f_{orient} = 2.6 \times 10^{-12} \int_{band} A \Delta R dv \\ &= 2.6 \times 10^{-12} \int_{band} \Delta R_{norm} dv \end{aligned} \quad (3.33)$$

where  $f$  is the oscillator strength in solution,  $A$  is the area per molecule of TSPP,  $\nu$  is the frequency, and the numeric factor  $2.6 \times 10^{-12}$  is expressed in nm<sup>-2</sup> s. Thus,  $f_{app}$  can be obtained by the integration of the reflection band in the range between 385 and 450 nm, for each surface pressure. Then, from the ratio between this apparent oscillator strength,  $f_{app}$ , and the oscillator strength obtained from the solution spectrum,  $f = 2.08$ , the orientation factor  $f_{orient}$  can be calculated for any surface pressure (eqn (6)). At low surface pressure (0 mN m<sup>-1</sup>),  $f_{orient} = 1.5$  was obtained, which is the maximum value that can be obtained only if there is no loss of the porphyrin molecules into the aqueous subphase and if those molecules lie parallel to the interface,  $\theta = 90^\circ$ . As the Ir-complex:TSPP mixed film was compressed, the orientation factor diminished up to 1.03, together with the tilt angle, approx. 40°. This evidenced the reorientation of the porphyrin molecules under compression, changing from a flat orientation at low surface pressure to the porphyrin rings inclined by approx. 40° with respect to the normal. These considerations have been made assuming the presence of all porphyrin molecules cospread at the interface, i.e., there was no loss of molecules toward the aqueous subphase.

## Absorption spectroscopy of Langmuir–Schaefer films

The Ir-complex : TSPP (4 : 1) mixed monolayer was transferred at  $35 \text{ mN m}^{-1}$  from the air–water interface onto quartz substrates, by the vertical dipping Langmuir–Blodgett (LB) and horizontal touching Langmuir–Schaefer (LS) techniques. In spite of LB films being poorly transferred, the LS method led to the successful deposition of monolayers and multilayers, with transfer ratios close to 1. In these LS films, the alkyl chains of the Ir-complex in the film were directly bound to the support surface. Fig. 3.24 shows the UV–visible absorption spectra of different number of Ir-complex : TSPP (4 : 1) LS layers.

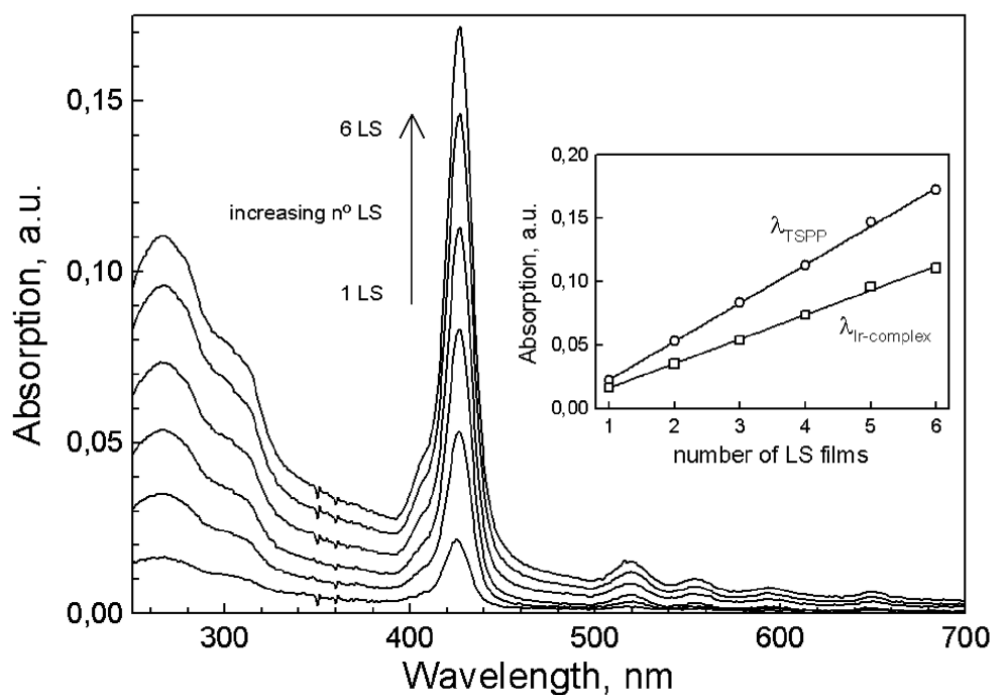


**Fig. 3.24** Absorption spectra of 1, 2, . . . 6 Ir-complex : TSPP (4 : 1) LS multilayers. Inset: maximum absorption of Ir-complex ( $\lambda_{\text{Ir-complex}} = 268 \text{ nm}$ ) and TSPP ( $\lambda_{\text{TSPP}} = 427 \text{ nm}$ ) bands vs. number of LS layers.

Both the Ir-complex and TSPP absorption bands were present, which indicated that the mixed films were successfully transferred in sequent depositions. Also, the wavelengths of the absorption peaks remained unchanged, indicating that aggregates were not formed between layers. The plot of the maximum absorption of the

chromophores of each spectrum vs. the number of consecutive LS transfers revealed a linear relationship (inset in Fig. 3.24), indicating that the TSPP molecules, attached to the Ir-complex matrix, could be regularly deposited layer by layer.

Although the ratio of the transfer onto the solid support was next to unit, additional information is required to prove that the porphyrin molecules attached to the Ir-complex matrix are correctly transferred to the substrate. For an ideal transfer process, where all Ir-complex molecules present at the air–water interface are transferred preserving their molecular orientation, the ratio between reflection and absorption is expected to be  $Abs/\Delta R = 3.64$ .<sup>34,45</sup> The experimental ratio has been calculated at  $\lambda = 268$  nm for the Ir-complex : TSPP (4 : 1) mixed monolayer at  $35\text{mN m}^{-1}$ , obtaining  $Abs/\Delta R=3.45$ , which was in agreement with that predicted for a complete dye transfer.<sup>34,45</sup> In any case, a change of the orientation of the porphyrin molecules during the transfer process may occur.

## **Emission spectra and lifetime measurements of Langmuir–Schaefer films**

Fig. 3.25a shows the room temperature emission spectra of the Ir-complex  $1.2 \times 10^{-5}$  M, TSPP  $3 \times 10^{-6}$  M, and the mixture Ir-complex : TSPP (4 : 1) (same concentrations) in aerated organic solutions (dichloromethane/methanol/water, ratio 15 : 9 : 2 v/v/v), under excitation at 260 nm.

As observed, the Ir-complex spectrum exhibited a broad structureless band with maximum emission at  $\sim 577$  nm that resulted from the characteristic mixing of the  $^3\text{MLCT}$  (triplet spin-forbidden metal-to-ligand charge transfer transition) and  $^3\text{LC}$  (triplet spin-forbidden ligand centered transition) excited states of iridium complexes,<sup>46</sup> while the TSPP spectrum showed the two emission bands typical of porphyrins,  $Q(0,0)$  and  $Q(0,1)$ , at  $\sim 651$  and  $\sim 715$  nm, respectively. In the case of the Ir-complex : TSPP mixture, the emission spectrum matched well with the sum of the spectra of Ir-complex and TSPP solutions. In Fig. 3.25b, the emission spectra of LS

films of Ir-complex and Ir-complex : TSPP (4 : 1) upon excitation at 260 nm are shown. The spectral shape of the Ir-complex LS film fitted well with that observed in solution. In contrast, the excitation of the Ir-complex : TSPP (4 : 1) LS film led to the total quenching of the Ir-complex emission, also accompanied by a concomitant enhancement of the TSPP emission.

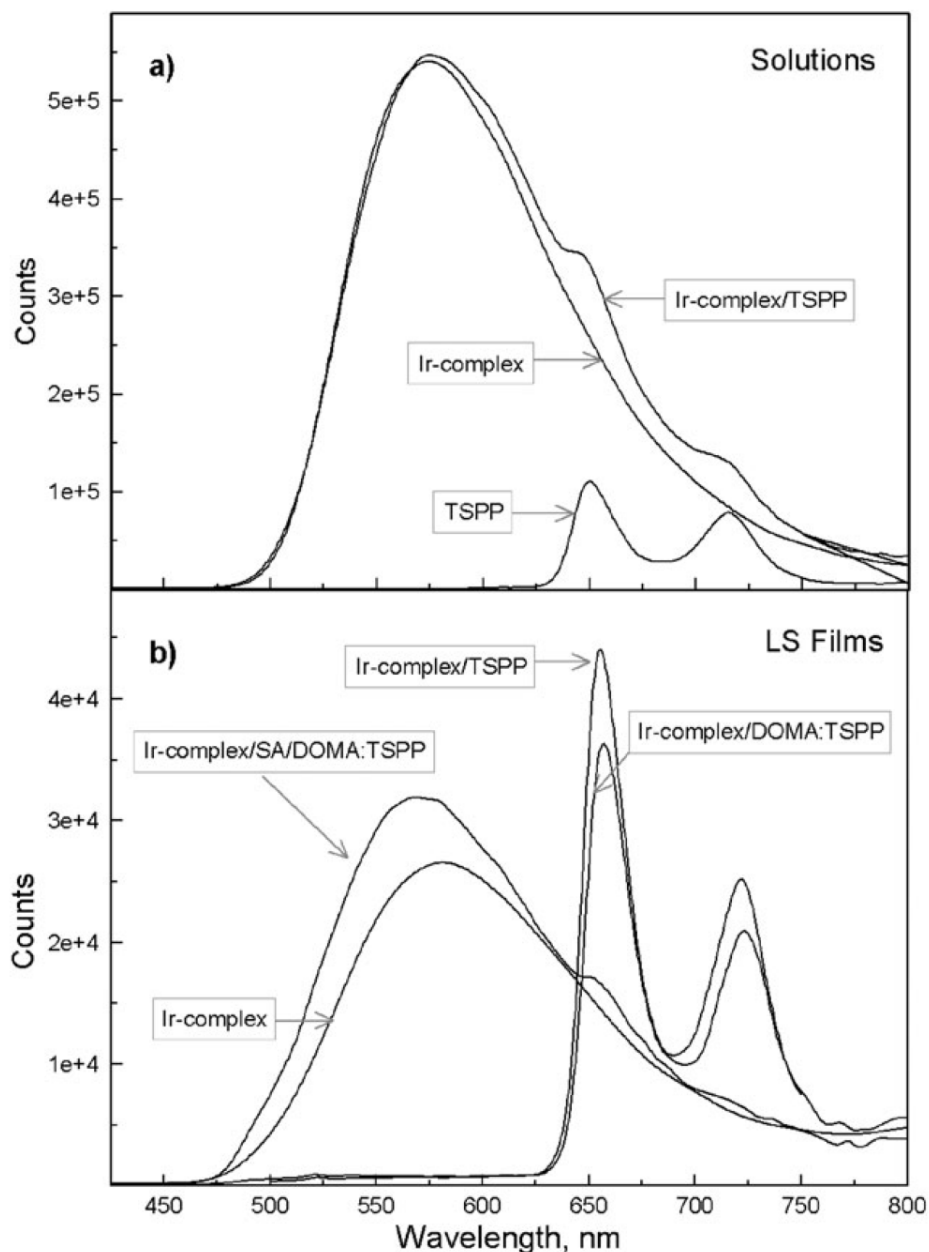


**Fig. 3.25** Luminescence spectra of: (a) solutions of Ir-complex, TSPP and Ir-complex : TSPP (4 : 1) in  $\text{CH}_2\text{Cl}_2/\text{CH}_3\text{OH}/\text{H}_2\text{O}$  (ratio 15 : 9 : 2 v/v/v), and (b) LS films of Ir-complex, Ir-complex : TSPP (4 : 1), Ir-complex/ DOMA : TSPP and Ir-complex/SA/DOMA : TSPP. Selected excitation wavelength = 260 nm.

The transfer efficiency  $E$  can be calculated from the luminescence intensities of the donor determined in the presence and absence of the acceptor, and is given by  $E = 1 - F_{da} / F_d$ , where  $F_d$  is the donor (Ir-complex) emission intensity determined at a given wavelength in the absence of the acceptor (TSPP), and  $F_{da}$  is the corresponding emission determined in the presence of the acceptor. Therefore, we obtained  $E = 1$  for the Ir-complex : TSPP (4 : 1) LS film. In fact, the energy transfer from the Ir-complex molecules to the TSPP dyes is feasible since the emission of Ir-complex occurs in the range of the  $Q$  absorption bands of the porphyrin (Fig. 3.24). Moreover, the distance between the Ir-complex and TSPP molecules (donor and acceptor, respectively) is short since the TSPP molecules are electrostatically attached to the Ir-complex matrix, which favors the dipole–dipole interactions among these molecules.

To study the intermolecular energy transfer, the distance between the planes of the donor and acceptor was increased by the insertion of lipid interlayers. For such a purpose, a mixed DOMA : TSPP (4 : 1) LS film was transferred onto a substrate previously covered with an Ir-complex LS film, obtaining a Ir-complex/DOMA : TSPP multilayer. The DOMA : TSPP (4 : 1) mixed monolayer has been previously investigated,<sup>28</sup> finding that both monomers and dimers of TSPP were present at high surface pressures. Furthermore, only TSPP monomers show the usual  $Q$  emission bands of porphyrins in the 625–775 nm range, while dimers have been found to exhibit Soret emission at ~500 nm.<sup>47</sup> To avoid the presence of TSPP aggregates, the mixed film has been transferred onto the Ir-complex covered substrate at 20 mN m<sup>-1</sup>, where the TSPP molecules arrange uniquely in the monomer form, and the porphyrin ring lying parallel to the surface.<sup>28</sup> In the fabricated film, the Ir-complex and the TSPP molecules were separated by a DOMA layer. The luminescence spectrum of this film (Fig. 3.25b) demonstrated that the emission of the Ir-complex was totally quenched, meaning that energy transfer to the TSPP molecules still occurred.

Finally, the donor–acceptor separation was further increased by the insertion of a fatty acid monolayer (stearic acid, SA). The film fabricated, Ir-complex/SA/DOMA : TSPP, led to the emission of the Ir-complex and the porphyrin together, indicating that the observed effective energy transfer did not take place (see Fig. 3.25b).

The kinetic decays were performed at room temperature, monitored at 575 or 650 nm (maximum emission of Ir-complex and TSPP, respectively), under excitation at 372 and/or 406 nm. All organic solutions (dichloromethane/methanol/ water, ratio 15 : 9 : 2 v/v/v) were air-equilibrated. Table 3.2 shows the decay parameters of the luminescence of different solutions and film structures; the excitation and the luminescence emission wavelength are also indicated.

	$\lambda_{\text{exc}}$ (nm)	$\lambda_{\text{em}}$ (nm)	$\tau_1$ (ns)	$\tau_2$ (ns)	$\chi^2$
Ir-complex (solution)	372.6	575	159	---	1.159
	406.4	650	160	---	1.153
TSPP (solution)	372.6/406.4	650	9.3	---	1.125
Ir-complex/TSPP (solution)	372.6/406.4	575	166.4	---	1.121
	372.6	650	9.9 (38%)	182 (62%)	1.153
	406.4	650	8.7 (81%)	126 (19%)	1.02
Ir-complex/TSPP (1 LS)	406.4	575	4.7	---	1.208
	406.4	650	4.5	---	1.231
Ir-complex/SA/DOMA-TSPP (1 LS)	406.4	575	134	---	1.068
	406.4	650	5.1 (79%)	139 (21%)	1.010

**Table 3.2** Decay parameters, excitation wavelength and monitoring wavelength of the luminescence of Ir-complex and TSPP in different solutions and film structures.

The Ir-complex in organic solution showed a mono-exponential decay in the order of 160 ns, independent of the selected excitation and emission wavelengths. The emission of TSPP solution followed a similar behavior, with  $t = 9.3$  ns. Regarding the mixture in solution, the luminescence decay monitored at 575 nm corresponded to the Ir-complex emission with  $\tau = 166$  ns, while the decay curves measured at 650 nm have been fitted to a bi-exponential decay function, with a fast ( $\tau_1$ ) and a slow ( $\tau_2$ ) decay component (Table 3.2). From the spectroscopic data of the isolated systems at diluted conditions in solution (optical density < 0.1), the short lifetime  $\tau_1$  is regarded as the excited state lifetime of the TSPP, while the long lifetime  $\tau_2$  comes from the Ir-complex luminescence. The small differences observed in lifetimes with respect to the



Ir-complex in solution could be associated to some non radiative processes such as decays due to vibrational modes and most likely also the oxygen quenching.<sup>48</sup>

Regarding the Ir-complex : TSPP (4 : 1) LS film, a monoexponential fit to the decay profile was found to be highly satisfactory, independently of the detection wavelength, and no improvement of the  $\chi^2$  value could be obtained when the data were fitted to a bi-exponential decay function. The calculated lifetime,  $\tau = 4.6$  ns, clearly corresponded to the TSPP emission in the film structure. This was clear evidence of the energy transfer from the Ir-complex to the TSPP in the film. When the Ir-complex and TSPP molecules were distanced by the DOMA and SA interlayers (Ir-complex/SA/DOMA : TSPP), the emission decay curve was bi-exponential. On analyzing the decay of the emission at 650 nm, we calculated  $\tau_1 = 5.1$  ns and  $\tau_2 = 139$  ns, which confirmed the emission of two components of the film, i.e., TSPP and Ir-complex. The slightly shorter lifetime (139 ns) observed for the iridium metallosurfactant in the presence of SA interlayers with respect to the Ir-complex in solution (160 ns) could be mainly associated to triplet–triplet annihilation processes between molecules of Ir-complex that were close in distance within the monolayer.<sup>33</sup> Additionally, the effect of oxygen on the reduction of the lifetime could not be excluded.<sup>48</sup>

### 3.3.4 Conclusions

In this work, the formation of a well-organized Ir-complex : TSPP (4 : 1) monolayer at the air–water interface has been reported. In this system, the TSPP molecules were electrostatically attached underneath the amphiphilic Ir-complex matrix, forming a homogeneous monolayer from low to high surface pressures. Under compression, TSPP and Ir-complex molecules formed J-aggregates, and the porphyrin rings changed their orientation until reaching, at high surface pressure, a tilt angle  $\sim 40^\circ$  with respect to the normal surface. Similarly, Langmuir monolayers and LS films containing the pure Ir-complex have been prepared for comparison.

A different number of Ir-complex : TSPP (4 : 1) monolayers have been successfully transferred onto quartz substrates by the Langmuir–Schaefer method (LS films). The linear increase of the absorbance indicated regular deposition of the films.

The energy transfer between the Ir-complex with the TSPP in solution, in a mixed film containing both dyes, and in adjacent layers of LS has been investigated. The results obtained by steady-state fluorescence and decay measurements indicated that effective intermolecular energy transfer took place in the Ir-complex : TSPP (4 : 1) LS film. In spite of the distance between donor and acceptor dyes has been increased by the insertion of a lipid monolayer, DOMA, the complete energy transfer between the Ir-complex and TSPP occurred. A longer separation, achieved by a stearic acid interlayer, led to the absence of energy transfer process.

## **Acknowledgements**

The authors thank the Spanish CICYT for financial support of this research in the framework of Project CTQ2007-64474/BQU (FEDER A), and also thank the Junta de Andalucía (Consejería de Innovación, Ciencia y Empresa) for special financial support P06-FQM-01698 and P08-FQM-4011. C. Roldán-Carmona, A. González-Delgado and A. Guerrero-Martínez thank the Ministerio de Ciencia e Innovación for the pre-doctoral grants (FPU and FPI) and for a Juan de la Cierva contract, respectively. J.J. Giner-Casares thanks the Alexander von Humboldt Foundation for a postdoctoral fellowship.

## References

1. J.-M. Lehn, *Angew. Chem., Int. Ed. Engl.*, 1990, 29, 1304.
2. D. Vollhardt, F. Liu and R. Rudert, *J. Phys. Chem. B*, 2005, 109, 17635.
3. H. Kuhn, *Pure Appl. Chem.*, 1981, 53, 2105.
4. M. A. Baldo, D. F. O'Brien, Y. You, A. Shoustikov, S. Silvey, M. E. Thompson and S. R. Forrest, *Nature*, 1998, 395, 151.
5. E. Holder, B. M. W. Langeveld and U. S. Schubert, *Adv. Mater.*, 2005, 17, 1109.
6. H. J. Bolink, L. Cappelli, E. Coronado, M. Grätzel, E. Ortí, R. Costa, P. Viruela and M. K. Nazeeruddin, *J. Am. Chem. Soc.*, 2006, 128, 14786.
7. H. J. Bolink, E. Coronado, S. G. Santamaria, M. Sessolo, N. Evans, C. Klein, E. Baranoff, K. Kalyanasundaram, M. Graetzel and M. K. Nazeeruddin, *Chem. Commun.*, 2007, 3276.
8. M. C. DeRosa, D. J. Hodgson, G. D. Enright, B. Dawson, C. E. B. Evans and R. J. Crutchley, *J. Am. Chem. Soc.*, 2004, 126, 7619.
9. M. S. Lowry and S. Bernhard, *Chem.–Eur. J.*, 2006, 12, 7970.
10. H. Sato, K. Tamura, M. Taniguchi and A. Yamagishi, *New J. Chem.*, 2010, 34, 617.
11. K. K. W. Lo, C. K. Chung, T. K. M. Lee, L. H. Lui, K. H. K. Tsang and N. Y. Zhu, *Inorg. Chem.*, 2003, 42, 6886.
12. E. C. Constable, H. Eriksson, C. E. Housecroft, B. M. Kariuki, E. Nordlander and J. Olsson, *Inorg. Chem. Commun.*, 2001, 4, 749.
13. K. M. Coakley and M. D. McGehee, *Chem. Mater.*, 2004, 16, 4533.

14. H. Imahori, Y. Sekiguchi, Y. Kashiwagi, T. Sato, Y. Araki, O. Ito, H. Yamada and S. Fukuzumi, *Chem.–Eur. J.*, 2004, 10, 3184.
15. N. Kobayashi, P. Janda and A. B. P. Lever, *Inorg. Chem.*, 1992, 31, 5172.
16. A. L. Briseno, S. C. B. Mannsfeld, M. M. Ling, S. Liu, R. J. Tseng, C. Reese, M. E. Roberts, Y. Yang, F. Wudl and Z. Bao, *Nature*, 2006, 444, 913.
17. A. Shi, S. Hu, J. Luo, T. D. Kim, N. M. Tucker, J. W. Ka, H. Sun, A. Pyajt, L. Dalton, A. Chen and A. K. Y. Jen, *Adv. Funct. Mater.*, 2007, 17, 2557.
18. H. A. Samha, T. J. Martinez, K. K. De Armond, F. O. Garces and R. J. Watts, *Inorg. Chem.*, 1993, 32, 2583.
19. J. J. Giner-Casares, M. Pe´rez-Morales, H. J. Bolink, E. Mu˜noz, G. de Miguel, M. T. Martin-Romero and L. Camacho, *J. Colloid Interface Sci.*, 2007, 315, 278.
20. J. J. Giner-Casares, M. Pe´rez-Morales, H. J. Bolink, N. Lardiés, E. Mu˜noz, G. de Miguel, M. T. Martı´n-Romero and L. Camacho, *J. Mater. Chem.*, 2008, 18, 1681.
21. S. Di Bella, S. Sortino, S. Conoci, S. Petralia, S. Casilli and L. Valli, *Inorg. Chem.*, 2004, 43, 5368.
22. M. Clemente-Le´on, E. Coronado, A. L´opez-Mu˜noz, D. Repetto, T. Ito, T. Konya, T. Yamase, E. C. Constable, C. E. Housecroft, K. Doyle and S. Graber, *Langmuir*, 2010, 26, 1316.
23. H. J. Bolink, E. Baranoff, M. Clemente-Le´on, E. Coronado, N. Lardiés, A. L´opez-Mu˜noz, D. Repetto and M. K. Nazeeruddin, *Langmuir*, 2010, 26, 11461.
24. M. T. Martı´n, I. Prieto, L. Camacho and D. Mobius, *Langmuir*, 1996, 12, 6554.
25. Z. Zhang, K. Nakashima, A. L. Verma, M. Yoneyama, K. Iriyama and Y. Ozaki, *Langmuir*, 1998, 14, 1177–1182.

26. M. I. Viseu, A. M. G. da Silva, P. Antunes and S. M. B. Costa, *Langmuir*, 2002, 18, 5772.
27. V. Sgobba, G. Giancane, S. Conoci, S. Casilli, G. Ricciardi, D. M. Guldi, M. Prato and L. Valli, *J. Am. Chem. Soc.*, 2007, 129, 3148.
28. M. Pérez-Morales, J. M. Pedrosa, M. T. Martín-Romero, D. Möbius and L. Camacho, *J. Phys. Chem. B*, 2004, 108, 4457.
29. G. de Miguel, M. T. Martín-Romero, M. Pérez-Morales, E. Muñoz and L. Camacho, *J. Porphyrins Phthalocyanines*, 2009, 13, 597.
30. J. L. Ruggles, K. M. Baldwin, S. A. Holt, G. J. Foran and I. R. Gentle, *J. Phys. Chem. B*, 2007, 111, 5651.
31. L. Valli, G. Giancane, A. Mazzaglia, L. Monsu` Scolaro, S. Conoci and S. Sortino, *J. Mater. Chem.*, 2007, 17, 1660.
32. G. Giancane, L. Valli and S. Sortino, *ChemPhysChem*, 2009, 10, 3077.
33. A. Guerrero-Martinez, Y. Vida, D. Dominguez-Gutierrez, R. Q. Albuquerque and L. De Cola, *Inorg. Chem.*, 2008, 47, 9131.
34. H. Gruber, D. Möbius and H. Meyer, *J. Chem. Phys.*, 1983, 79, 3701.
35. J. R. Lakowicz, *Principles of Fluorescence Spectroscopy*, Kluwer Academic, New York, 1999.
36. H. Hada, R. Hanawa, A. Haraguchi and Y. Jonezawa, *J. Phys. Chem.*, 1985, 89, 560.
37. A. M. González-Delgado, M. Pérez-Morales, J. J. Giner-Casares, E. Muñoz, M. T. Martín-Romero and L. Camacho, *J. Phys. Chem. B*, 2009, 113, 13249.
38. M. G. Colombo, A. Hauser and H. U. Güdel, *Inorg. Chem.*, 1993, 32, 3088.
39. M. Orrit, D. Möbius, U. Lehmann and H. Meyer, *J. Chem. Phys.*, 1986, 85, 4966.

40. J. M. Pedrosa, M. T. Martín-Romero, L. Camacho and D. Möbius, *J. Phys. Chem. B*, 2002, 106, 2583.
41. H. Grüniger, D. Möbius, U. Lehmann and H. Meyer, *J. Chem. Phys.*, 1986, 85, 4966.
42. H. Huesmann, C. A. Bignozzi, M. T. Indelli, L. Pavanin, M. A. Rampi and D. Möbius, *Thin Solid Films*, 1996, 284–285, 62.
43. J. M. Pedrosa, C. M. Dooling, T. H. Richardson, R. K. Hyde, C. A. Hunter, M. T. Martín and L. Camacho, *Langmuir*, 2002, 18, 7594.
44. H. Kuhn and H. D. Försterling, *Principles of Physical Chemistry*, John Wiley & Sons, New York, 1999.
45. G. de Miguel, M. T. Martín-Romero, J. M. Pedrosa, E. Muñoz, M. Pérez-Morales, T. H. Richardson and L. Camacho, *Phys. Chem. Chem. Phys.*, 2008, 10, 1569.
46. J. O. Barcina, N. Herrero-Garcia, F. Cucinotta, L. De Cola, P. Contreras-Carballada, R.M. Williams and A. Guerrero-Martinez, *Chem.–Eur. J.*, 2010, 16, 6033.
47. M. Pérez-Morales, G. de Miguel, H. J. Bolink, M. T. Martín-Romero and L. Camacho, *J. Mater. Chem.*, 2009, 19, 4255.
48. M. C. DeRosa, D. J. Hodgson, G. D. Enright, B. Dawson, C. E. B. Evans and R. J. Crutchley, *J. Am. Chem. Soc.*, 2004, 126, 10493.

**Chapter 4**

**Thin films in LECs**

**Dynamic and static interlayer**





## 4.1 Engineering charge injection interfaces in hybrid light-emitting electrochemical cells

Cristina Roldán-Carmona,<sup>a,b</sup> Takeo Akatsuka,<sup>a,c</sup> Michele Sessolo,<sup>a</sup> Scott Watson<sup>d</sup> and Henk J. Bolinka,<sup>a</sup>

<sup>a</sup> *Instituto de Ciencia Molecular, Univ. de Valencia, Catedrático J. Beltrán 2, 46980 Paterna, Spain.*

<sup>b</sup> *Depart. of Physical Chemistry and Applied Thermodynamics, Univ. of Cordoba, C. Rabanales, Ed. Marie Curie, 14014 Córdoba, Spain*

<sup>c</sup> *Nippon Shokubai Co., Ltd. 5-8 Nishi Otabi-cho, Suita 564-8512 Osaka, Japan*

<sup>d</sup> *Materials Science and Engineering and Computational Informatics, CSIRO, Private Bag 33, Clayton South, Victoria 3169, Australia*

In their simplest form, light-emitting electrochemical cells (LECs) consists in a thin films of an ionic organic semiconductor sandwiched between two electrodes. Due to the large density of ions in the active layer, the applied potential initially drops at the electrode/active layer interfaces enhancing charge injection. For this reason, LECs are often reported to perform independently on the work function of the electrodes used. In this letter, we use metal oxide thin films as charge injection layers placed between the electrodes and the active layer. We demonstrate that, while electroluminescence is observed independently of the electrodes used, the device performances are strongly dependent on the choice of the materials at the interfaces. Such hybrid device architecture is of particular interest for real lighting applications, because it meets at the same time the requirement of speed, brightness and efficiency. Moreover, relying on metal oxide charge injection layers, hybrid LECs could pave the way for new environmentally stable, low-cost lighting sources.

Paper submitted to *ACS Applied Materials & Interfaces*.

The stage of development of organic light-emitting diodes (OLEDs) is so advanced that these devices are now competing with established technologies in the display market. On the other side, the successful introduction of OLEDs into the lighting market will depend essentially on a reduction in the associated production costs. For this reason, novel materials as well as different device architectures are continuously being investigated. Light-emitting electrochemical cells (LECs) are much simpler types of electroluminescent devices, relying on a single ionic solution processed light-emitting layer sandwiched in between two electrodes.<sup>1</sup> Two types of emitters have been explored so far, i) conjugated polymers blended with salt or ionic liquids<sup>2</sup> and ii) ionic transition metal complexes (iTMCs).<sup>3</sup> The latter have been the subject of intense research due to the intrinsic higher photoluminescence quantum yield (PLQY) associated with phosphorescent emitters, resulting in higher power conversion efficiency (PCE).<sup>4-5</sup>

The key features of LECs is the high concentration of ionic species in the emitting layer, which redistribute after application of an external bias forming interfacial electric double layers (EDLs).<sup>6-7</sup> EDLs generate strong fields able to assist the injection of holes and electrons at the anode and cathode, respectively. For this reason, LECs are often reported to perform independently on the work function of the electrodes used.<sup>8</sup> This statement is only partially true, as we will demonstrate later in our discussion. As higher voltages are applied, increasing charges are injected into the active material leading to its oxidation and reduction, in a similar fashion to what is obtained by chemical p- and n-doping in state of the art OLEDs.<sup>9-10</sup> Hence, the applied potential drops in-between the doped zones over the low-conductive intrinsic region, where the light emission occurs.<sup>11</sup> Within this perspective, the maximum PCE would be obtained when the carrier recombination zone (intrinsic region) is located near the center of the active layer, where exciton quenching at the electrodes is minimized. Assuming a balanced ambipolar mobility of the semiconductor, the position of the recombination zone will depend mainly on the equilibrium between the processes of hole and electron injection.<sup>11</sup> In this letter, we correlate the brightness, efficiency and

turn-on time ( $t_{on}$ ) of efficient and stable LECs with the work function and the properties of the charge injection materials used.

Despite of the wide range of commercially available charge injecting, transporting, and blocking molecular materials,<sup>12</sup> we focused on architectures employing metal oxides thin films. Metal oxides charge injection layers have been chosen because of their unique properties of high carrier mobility, high transparency and the intrinsic stability towards moisture and oxygen.<sup>13-14</sup> Thanks to these unique features, metal oxides have been widely employed in a variety of efficient organic optoelectronic devices.<sup>15-18</sup> In particular, we used zinc oxide (ZnO) and molybdenum trioxide (MoO<sub>3</sub>) as the electron and hole injection materials, respectively (EIL and HIL). ZnO is a n-type semiconductor with a conduction band edge ( $E_c$ ) close in energy to the lowest unoccupied molecular orbital (LUMO) of the iTMC used in this work (Fig. 4.1).<sup>19</sup> On the other side, the Fermi level ( $E_F$ ) of MoO<sub>3</sub> is so large that the use of thin films of MoO<sub>3</sub> as hole injection layers leads to ohmic contacts with most organic semiconductors.<sup>20-21</sup> We demonstrate that, while electroluminescence generation in LECs is rather independent from the type of charge injection material or electrode used, their work function and exciton blocking property, on the other hand, strongly influence the device performances.

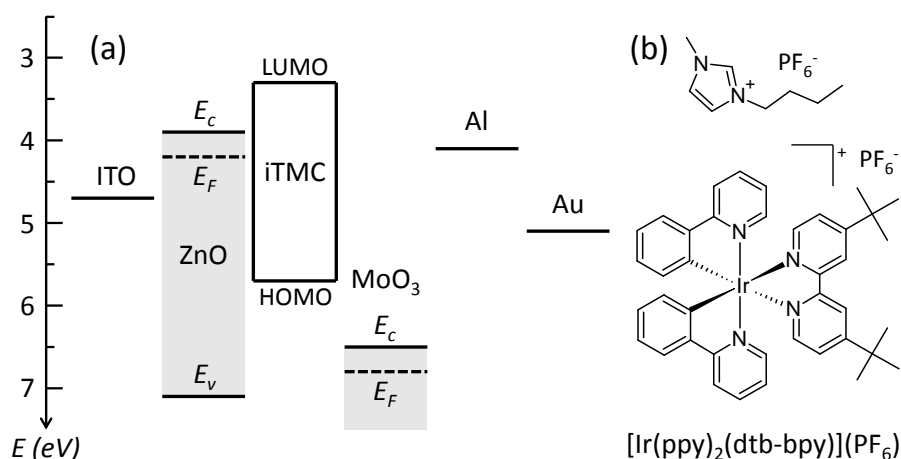


**Fig. 4.1.** (a) Energy-levels for the materials employed in this work and (b) chemical structure of the ionic liquid and the iTMC constituting the light-emitting layer. Energy levels for the inorganic materials are taken from literature, while the iTMC bands have been determined experimentally from photoelectron spectroscopy in air (PESA) and UV-Vis absorption spectra (Supporting Information).

The iTMC used as the light-emitting material is the  $[\text{Ir}(\text{ppy})_2(\text{dtb-bpy})](\text{PF}_6)$  (Fig. 4.1b), where ppy is 2-phenylpyridinato and dtb-bpy is 4,4'-di(tert-butyl)-2,2'-bipyridine), synthesized according to previously described methods.<sup>22</sup> LECs were prepared on pre-patterned indium tin oxide (ITO) coated glass plates, which were thoroughly cleaned by subsequent sonication in aqueous detergent, water, and 2-propanol baths, and activated by exposure to an UV-ozone lamp. ZnO thin films were prepared by spin coating a solution of zinc acetate dihydrate ( $10 \text{ mg ml}^{-1}$  in ethanol: water: acetic acid, volume ratio 50:2:1) on the ITO-coated substrates, and by annealing them on a hot plate at  $450 \text{ }^\circ\text{C}$  for 2 hours. Thin films (100 nm) of the iTMC were obtained by spin-coating a solution in acetonitrile. To improve the ionic conductivity of the layer,<sup>23</sup> the ionic liquid (IL) 1-butyl-3-methylimidazolium hexafluorophosphate ( $[\text{BMIM}](\text{PF}_6)$ , Fig. 4.1b) was added to the iTMC solution resulting in a molar ratio iTMC:IL of 4:1. Metals (Al, Au) and  $\text{MoO}_3$  thin films were deposited through a shadow mask with a thermal vacuum-evaporation system integrated in an inert atmosphere glove box. The active area of the devices was  $6.5 \text{ mm}^2$ . The LECs were not encapsulated and characterized inside the glove box by applying pulsed current ( $J = 200 \text{ A m}^{-2}$ , 1 kHz, 50% duty cycle) and monitoring the voltage and luminance with a True Colour Sensor MAZeT (MTCSiCT Sensor) using a Botest OLT OLED Lifetime-Test System.

We first describe the properties of hole injection into the iTMC layer by using bare and  $\text{MoO}_3$  coated ITO as the anode and Al or Au as the cathode. Devices were driven with pulsed current with a maximum current density  $J_{\text{max}} = 200 \text{ A m}^{-2}$  and a duty cycle of 50 %, resulting in an average current density  $J_{\text{avg}} = 100 \text{ A m}^{-2}$ . Performances over time as well as the key parameters for this set of devices are reported in Fig. 4.2 and Table 4.1, respectively. The device with bare ITO anode and structure ITO/iTMC/Al (1) shows a slow rise of the electroluminescence with a turn-on time  $t_{\text{on}}$  (here defined as the time needed to reach a luminance of  $100 \text{ cd m}^{-2}$ ) of 41 s. Luminance steadily increased until reaching a maximum  $L_{\text{max}} = 1059 \text{ cd m}^{-2}$  at 100 minutes, corresponding to a maximum  $\text{PCE}_{\text{max}} = 6 \text{ lm W}^{-1}$ . This behavior indicates an injection limited regime dominated by the dynamics of ions accumulations at the

interfaces (formation of EDLs). In this regime, the current flowing through the device recombines at/close to one interface and is dissipated through direct charge recombination and exciton quenching. Once EDLs build up, p- and n-doping of the iTMC take place, moving the recombination zone towards the center of the active layer with a substantial increase of photon generation. Insertion of a thin (10 nm) film of MoO<sub>3</sub> in between the ITO anode and the iTMC results in a substantial change of the device performances (device 2). First of all, electroluminescence is instantaneous and intense with an initial luminance  $L_0 = 269 \text{ cd m}^{-2}$ , meaning that the barrier for hole injection no longer exists upon coating of the ITO with MoO<sub>3</sub>. This hypothesis is also supported by a reduction of about 2 V in the average voltage measured at time  $t = 0$  ( $t_0$ ) after inserting the MoO<sub>3</sub>. Both luminance and PCE increase fast at the beginning of measurements (note the log scale of the time domain), reaching  $L_{\text{max}} = 888 \text{ cd m}^{-2}$  and  $\text{PCE}_{\text{max}} = 5 \text{ lm W}^{-1}$  only 1 minute after biasing the device. These values are somewhat lower compared to what obtained for device (1), most likely due to the proximity of the exciton recombination zone to the Al cathode, consequence of the ohmic hole injection. As an extreme case we also fabricated a device with MoO<sub>3</sub> HIL but using a Au cathode instead. As expected, this LEC (3) shows a large turn-on time of 158 s, consequence of the wide electron injection barrier, and the maximum luminance and efficiency are only achieved after about 100 minutes of device operations. Interestingly, the device still reaches high luminance and PCE ( $L_{\text{max}} = 893 \text{ cd m}^{-2}$  and  $\text{PCE}_{\text{max}} = 4.8 \text{ lm W}^{-1}$ ), indicating that LECs can indeed efficiently generate electroluminescence independently of the electrodes work function, but at the cost of viable switching speeds.

A common feature of the first set of LECs is the presence of a rather high electron injection barrier at the iTMC/Al interface (Fig. 4.1a), evident also from the measured average voltage  $V_{\text{avg}}$  reported in Fig. 4.2b. All LECs show a relatively high voltage at the beginning of the measurements which, due to the generation of doped zones, steadily decreases for converging to the value  $V_{\text{avg}} = 2.7 \text{ V}$ , corresponding to the band gap of the iTMC ( $\sim 2.7 \text{ eV}$ ). This is true also in the case of the device with

the ohmic ITO/MoO<sub>3</sub>/iTMC contact, which shows an initial  $V_{\text{avg}} = 5.4$  V, confirming the presence of the electron injection barrier.

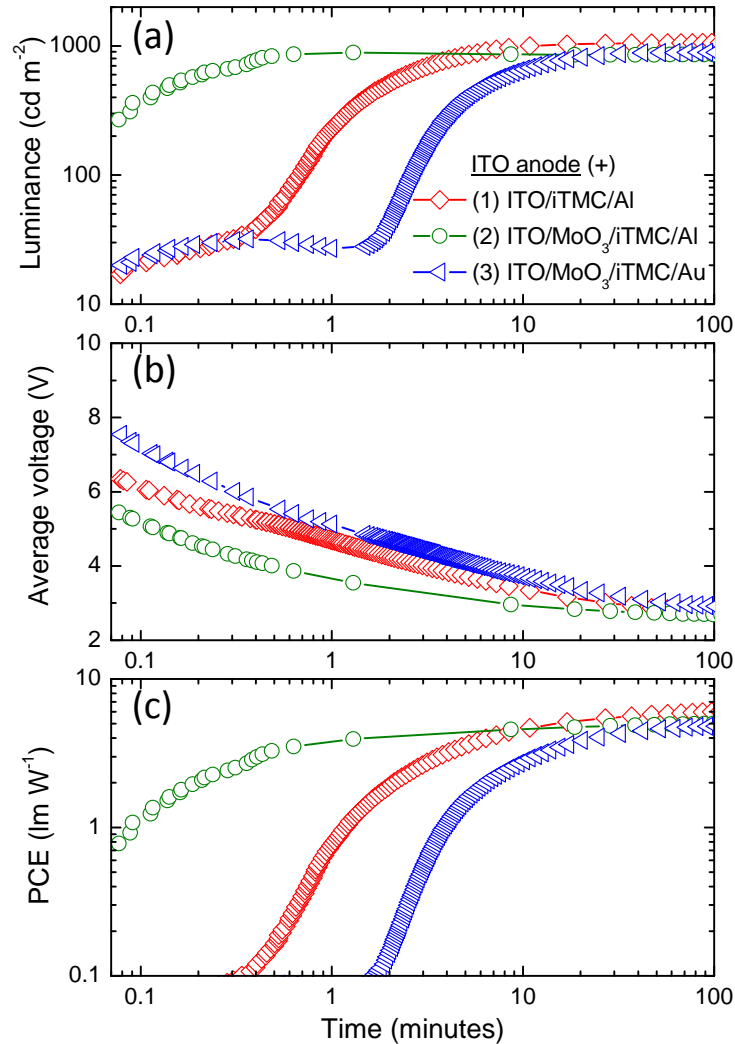


**Fig. 4.2.** (a) Luminance, (b) average measured voltage and (c) PCE characteristics versus time for a series of devices where the ITO is used as the anode (positively biased).

**Table 4.1.** Key performance parameters for a series of LECs where ITO is used as the anode

	$L_0$ ( $\text{cd m}^{-2}$ )	$t_{\text{on}}$ (s)	$L_{\text{max}}$ ( $\text{cd m}^{-2}$ )	$t_{\text{max}}$ (min)	$\text{PCE}_{\text{max}}$ ( $\text{lm W}^{-1}$ )
(1) ITO/iTMC/Al	17	41	1059	100	6.0
(2) ITO/MoO <sub>3</sub> /iTMC/Al	269	-	888	1	5.0
(3) ITO/MoO <sub>3</sub> /iTMC/Au	20	158	893	100	4.8

The use of low work function metal electrodes such as Ba or Ca has been shown to lead to ohmic electron injection into iTMC,<sup>12</sup> but their high reactivity towards oxygen and moisture would require a rigorous encapsulation of the device, undermining the intrinsic simplicity of LECs. Hence, the electron injection interface was modified by the insertion of solution processed ZnO thin films. For this purpose, we adopted the inverted configuration where the ITO is used as the cathode,<sup>24</sup> since ZnO cannot be processed from solution on top of the iTMC layer. Performances over time as well as the key parameters for this series of inverted devices are reported in Fig. 4.3 and Table 4.2, respectively. A LEC with bare ITO cathode and Au anode is used as the reference (device 4). As expected from the energy difference between the ITO work function and the iTMC LUMO (1.6 eV), the device is strongly injection limited with an initial  $V_{\text{avg}}$  as large as 9 V and poor luminance  $L_0 = 4 \text{ cd m}^{-2}$ . As the EDLs form and the doped regions start growing, electroluminescence slowly rises with a  $t_{\text{on}} = 48 \text{ s}$ , stabilizing around  $L_{\text{max}} = 300 \text{ cd m}^{-2}$  after 2.5 minutes driving. The PCE, however, remains quite low due to the unbalanced charge injection causing the recombination zone to be close to the ITO cathode. The insertion of a ZnO EIL (device 5) strongly improves the device characteristics. Immediately after biasing the LEC, the measured electroluminescence is  $L_0 = 51 \text{ cd m}^{-2}$  and  $V_{\text{avg}}$  is reduced to 5.7 V. The luminance increases fast ( $t_{\text{on}} = 18 \text{ s}$ ) reaching  $800 \text{ cd m}^{-2}$  after 2 minutes and  $L_{\text{max}} = 955 \text{ cd m}^{-2}$ . The PCE is comparable to what measured for the first series of devices (Fig. 4.2), with  $\text{PCE}_{\text{max}} = 5.5 \text{ lm W}^{-1}$ . Despite of the favorable performances, device 5 still suffers from a limited injection since the measured voltage takes about 10 minutes to converge to the value of the band gap of the iTMC. A balanced charge injection can be achieved through the contemporary use of a ZnO EIL and a MoO<sub>3</sub> HIL (device 6). This device architecture leads to a large improvement in the device performances, with instantaneous and intense electroluminescence ( $L_0 = 154 \text{ cd m}^{-2}$ ) and an initial measured voltage as low as 3.3 V, indicating a very efficient charge injection into the iTMC, even without the assistance of EDLs at the interfaces.

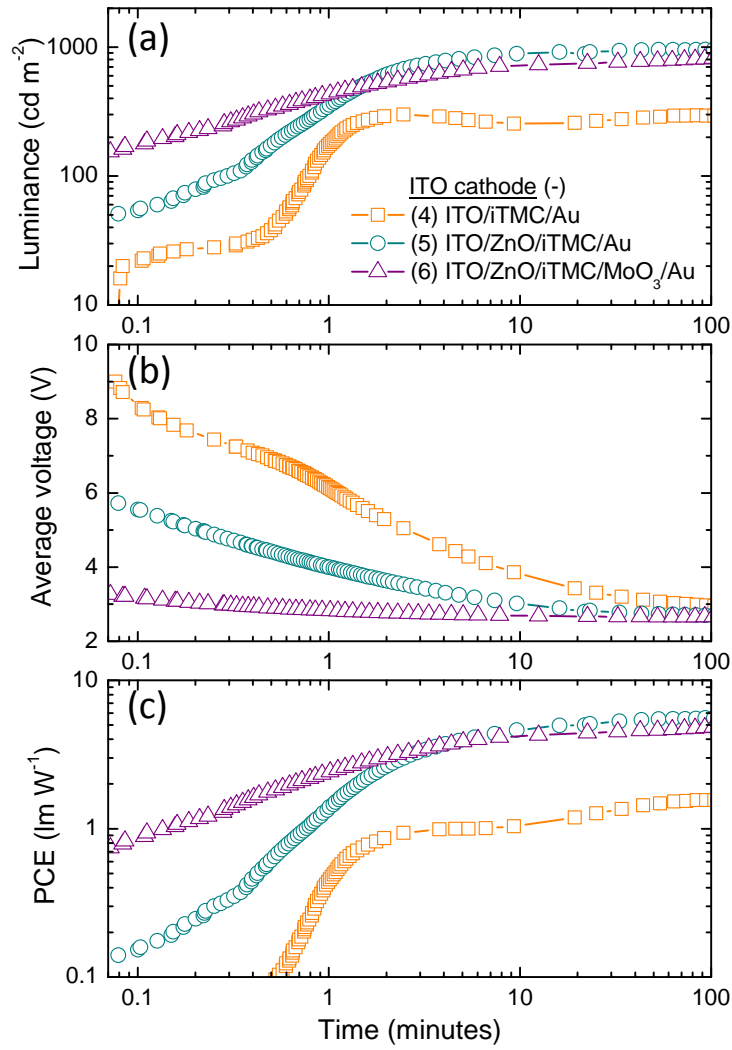


**Fig. 4.3.** (a) Luminance, (b) average measured voltage and (c) PCE characteristics versus time for a series of devices where the ITO is used as the cathode (negatively biased).

**Table 4.2.** Key performance parameters for a series of LECs where ITO is used as the cathode

	$L_0$ ( $\text{cd m}^{-2}$ )	$t_{on}$ (s)	$L_{max}$ ( $\text{cd m}^{-2}$ )	$t_{max}$ (min)	$\text{PCE}_{max}$ ( $\text{lm W}^{-1}$ )
(1) ITO/iTMC/Au	4	48	300	2.46	1.6
(2) ITO/ZnO/iTMC/Au	51	18	955	93	5.5
(3) ITO/ZnO/iTMC/MoO <sub>3</sub> /A	154	-	820	92	4.8

On the other hand,  $\text{PCE}_{max}$  is limited to  $4.8 \text{ lm W}^{-1}$ , suggesting that non-radiative recombination processes take place. Since the process of hole injection can



be considered ohmic, the exciton recombination zone is likely to extend close to the ZnO/iTMC interface, where a small electron injection barrier still exists. While the energetics of this interface allows to exclude the direct hole recombination at the cathode, excitons formed in its proximity could be separated via charge transfer with a mechanism analogous to that of dye-sensitized solar cells. The use of metal oxides, however, remains very advantageous due to their ability to confine carriers in the active layer and to reduce the exciton quenching observed at metallic interfaces. Last but not least, these materials are intrinsically more stable compared to low work function electrodes or traditional organic electronics materials, and their application is of special interest for simple low-cost optoelectronics devices.

In conclusion, we have demonstrated efficient hybrid LECs employing metal oxides as charge injecting materials. While electroluminescence from the iTMC is observed independently of the electrodes used, their performances are strongly dependent on the choice of the materials at the interfaces. Maximum device efficiency and luminance, for example, are mainly determined from the equilibrium between the processes of hole and electron injection. As a matter of fact, even in injection limited devices, the formation of EDLs at the interfaces and the subsequent propagation of highly conductive doped regions can lead to bright and efficient electroluminescence. On the other side, fast device switching requires the minimization of the barrier for hole and electron injection, which can be easily achieved by using charge selective contact such as ZnO and MoO<sub>3</sub>, respectively. Such hybrid device architecture is of particular interest for real lighting applications, because it meets at the same time the requirement of speed, brightness and efficiency. Moreover, relying on metal oxide charge injection layers, hybrid LECs could pave the way for new environmentally stable, low-cost lighting sources.

## Supporting Information

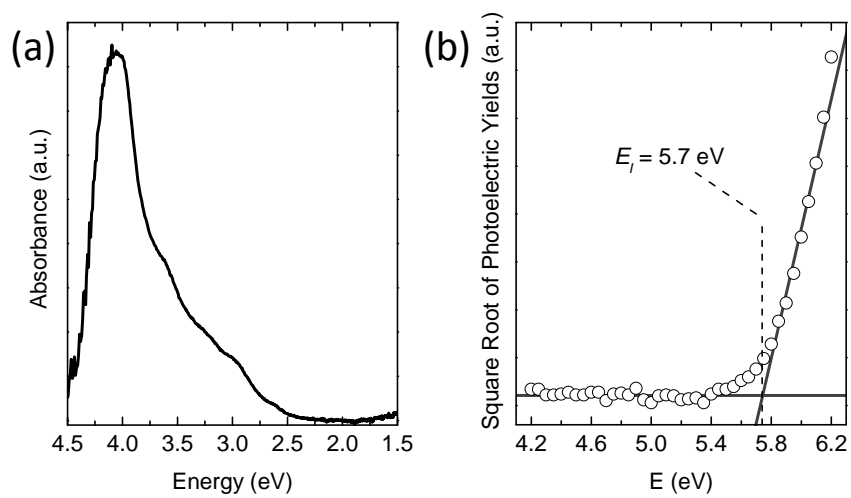


**Fig. S4.1** (a) UV-Vis absorption and (b) photoelectron spectroscopy in air (PESA) spectra of a pure thin film of the  $[\text{Ir}(\text{ppy})_2(\text{dtb-bpy})](\text{PF}_6)$  complex.

## References

1. Meier, S. B.; Tordera, D.; Pertegás, A.; Roldán-Carmona, C.; Ortí, E.; Bolink, H. J., *Materials Today* 2014, 17 (5), 217-223.
2. Pei, Q. B.; Yu, G.; Zhang, C.; Yang, Y.; Heeger, A. J. *Science* 1995, 269 (5227), 1086-1088.
3. Lee, J. K.; Yoo, D. S.; Handy, E. S.; Rubner, M. F. *Applied Physics Letters* 1996, 69 (12), 1686-1688.
4. Slinker, J. D.; Rivnay, J.; Moskowitz, J. S.; Parker, J. B.; Bernhard, S.; Abruna, H. D.; Malliaras, G. G., *J Mater Chem* 2007, 17 (29), 2976-2988.
5. Costa, R. D.; Ortí, E.; Bolink, H. J.; Monti, F.; Accorsi, G.; Armaroli, N. *Angew Chem Int Edit* 2012, 51 (33), 8178-8211.
6. DeMello, J. C.; Tessler, N.; Graham, S. C.; Friend, R. H., *Physical Review B - Condensed Matter and Materials Physics* 1998, 57 (20), 12951-12963.
7. Slinker, J. D.; DeFranco, J. A.; Jaquith, M. J.; Silveira, W. R.; Zhong, Y. W.; Moran-Mirabal, J. M.; Craighead, H. G.; Abruna, H. D.; Marohn, J. A.; Malliaras, G. G., *Nat Mater* 2007, 6 (11), 894-899.
8. Gorodetsky, A. A.; Parker, S.; Slinker, J. D.; Bernards, D. A.; Wong, M. H.; Malliaras, G. G.; Flores-Torres, S.; Abruña, H. D., *Applied Physics Letters* 2004, 84 (5), 807-809.
9. Matyba, P.; Maturova, K.; Kemerink, M.; Robinson, N. D.; Edman, L., *Nat Mater* 2009, 8 (8), 672-676.
10. Lenes, M.; Garcia-Belmonte, G.; Tordera, D.; Pertegás, A.; Bisquert, J.; Bolink, H. J. *Adv Funct Mater* 2011, 21 (9), 1581-1586.
11. Van Reenen, S.; Matyba, P.; Dzwilewski, A.; Janssen, R. A. J.; Edman, L.; Kemerink, M., *J Am Chem Soc* 2010, 132 (39), 13776-13781.

12. Liao, C. T.; Chen, H. F.; Su, H. C.; Wong, K. T., *Phys Chem Chem Phys* 2012, 14 (27), 9774-9784.
13. Greiner, M. T.; Lu, Z. H., *NPG Asia Materials* 2013, 5 (7).
14. Meyer, J.; Hamwi, S.; Kröger, M.; Kowalsky, W.; Riedl, T.; Kahn, A., *Advanced Materials* 2012, 24 (40), 5408-5427.
15. Morii, K.; Ishida, M.; Takashima, T.; Shimoda, T.; Wang, Q.; Nazeeruddin, M. K.; Gratzel, M., *Applied Physics Letters* 2006, 89 (18), 183510.
16. Sessolo, M.; Bolink, H. J., *Advanced Materials* 2011, 23 (16), 1829-1845.
17. Cai, W.; Gong, X.; Cao, Y., *Solar Energy Materials and Solar Cells* 2010, 94 (2), 114-127.
18. Li, G.; Zhu, R.; Yang, Y., *Nature Photonics* 2012, 6 (3), 153-161.
19. Li, H.; Schirra, L. K.; Shim, J.; Cheun, H.; Kippelen, B.; Monti, O. L. A.; Bredas, J. L., *Chemistry of Materials* 2012, 24 (15), 3044-3055.
20. Matsushima, T.; Kinoshita, Y.; Murata, H., *Applied Physics Letters* 2007, 91 (25).
21. Kröger, M.; Hamwi, S.; Meyer, J.; Riedl, T.; Kowalsky, W.; Kahn, A., *Organic Electronics: physics, materials, applications* 2009, 10 (5), 932-938.
22. Slinker, J. D.; Gorodetsky, A. A.; Lowry, M. S.; Wang, J.; Parker, S.; Rohl, R.; Bernhard, S.; Malliaras, G. G., *J Am Chem Soc* 2004, 126 (9), 2763-2767.
23. Parker, S. T.; Slinker, J. D.; Lowry, M. S.; Cox, M. P.; Bernhard, S.; Malliaras, G. G., *Chemistry of Materials* 2005, 17 (12), 3187-3190.
24. Bolink, H. J.; Coronado, E.; Repetto, D.; Sessolo, M., *Applied Physics Letters* 2007, 91 (22).

## 4.2 Dynamically Doped White Light Emitting Tandem Devices

Akatsuka, T.<sup>1,2</sup>; Roldán-Carmona, C.<sup>1,3</sup>; Ortí, E.<sup>1</sup> and Bolink, H. J.<sup>1</sup>

<sup>1</sup> *Instituto de Ciencia Molecular, Univ. de Valencia, Catedrático J. Beltrán 2, 46980, Paterna, Spain*

<sup>2</sup> *Nippon Shokubai Co., Ltd. 5-8 Nishi Otabi-cho, Suita, 564-8512, Osaka, Japan*

<sup>3</sup> *Depart. of Physical Chemistry, Univ. of Cordoba, C. Rabanales, Ed. C3, 14014, Córdoba, Spain.*

Solution-processed, salt-containing, blue and orange light-emitting layers lead to efficient white light-emitting devices when arranged in a tandem configuration separated by a thin metal layer.

Lighting accounts for about 10% of the world global energy consumption. There is therefore a strong incentive for new, low consumption lighting solutions to reduce global energy demand. In this context, organic light-emitting diodes (OLEDs) have considerable advantages compared to other solid-state lighting technologies, which are based on inorganic semiconductors.<sup>1</sup> Currently, best-performing white OLEDs are based on a tandem approach, in which two or more sub-devices are stacked on top of each other.<sup>2</sup> In tandem OLEDs the middle electrode needs to inject electrons and holes in the adjacent sub-devices, which is an energetically unfavorable process when air-stable metals are used as the middle contact.<sup>3</sup> For this reason, doped layers are used adjacent to or as the middle contact to facilitate electron and hole injection into the sub-devices.<sup>4</sup> As it is very difficult to prepare doped injection layers using solution-based processes, almost all tandem OLEDs are prepared using high vacuum sublimation of the active materials. Only one example of a solution-processed tandem OLED has been reported, in which a Cs<sub>2</sub>CO<sub>3</sub> /ZnO n-doped electron injection layer was processed from solution by blending it with poly(4-vinylpyridine).<sup>5</sup>

The infrastructure investment for multiple vacuum sublimation tools, especially for large areas, is elevated, making the production of low-cost OLEDs only possible if very high production volumes are reached. Solution-based processing requires lower investments and is compatible with high throughput; hence this technique is more suitable for low-cost device production. Another type of electroluminescent device, referred to as light-emitting electrochemical cell (LEC), contains salts in the light-emitting layer and has a much simpler architecture.<sup>6</sup> Contrary to OLEDs,<sup>4a</sup> LECs do not rely on air-sensitive injection layers and metals used for electron injection.<sup>6a,7</sup> This facilitates solution processing and reduces the encapsulation requirements.<sup>8</sup> LECs are based on either a conjugated light-emitting polymer mixed with a salt<sup>7c</sup> or an ionic transition-metal complex (iTMC).<sup>7d</sup> Recently, it was shown that both types of LECs operate according the same mechanism governed principally by the ionic conductivity of the salts in the thin film.<sup>9</sup>

The operating mechanism of LECs involves the dissociation of the salt in the active layer and, subsequently, the migration of the constituent ions towards the electrode interfaces leading to the formation of doped zones (Fig. 4.4, panel a and b).<sup>10</sup>

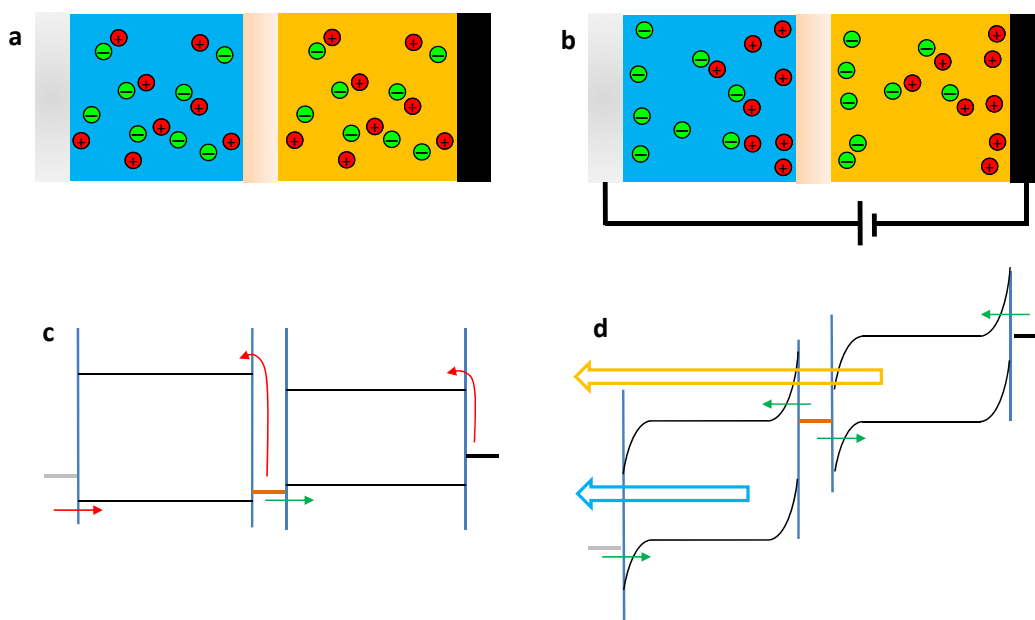


**Fig. 4.4.** Operational mechanism of LECs and its application to a tandem configuration. (a) Schematic of a tandem LEC in which both the blue and orange light-emitting layers have ions. (b) Same tandem LEC as in panel (a) showing schematically the ion displacement when an external potential is applied. (c) Energy level diagram of the tandem LEC without external potential and (d) with external potential applied. The Fermi levels of the metals and the HOMO and LUMO levels of the blue and orange light-emitting materials are shown. The red solid arrows indicate large injection barriers for electron and holes, the green arrows indicate efficient electron and hole injection. The hollow arrows indicate the emission of light.

In a tandem LEC, such dynamically doped layers will be generated on both sides of the middle electrode removing the injection barriers for electrons and holes and allowing for efficient electroluminescence (Fig. 4.4, panel c and d). Therefore, no intentionally doped layers are required adjacent to the middle electrode, which facilitates the solution processing of tandem light-emitting devices. A first hint that it should be possible to prepare tandem LECs in this way was obtained from the report of cascaded LECs, in which the electrodes are used simultaneously as anode and cathode for laterally connected cells.<sup>11</sup> White LECs based on both polymer- and iTMC-emitting materials have been reported using different methods such as blending two or three emitters,<sup>12</sup> profiting from dual emission from a single polymer,<sup>13</sup> and

employing a color conversion layer.<sup>14</sup> However, these devices only work efficiently at low luminance values. The main reason for the poor performance of white LECs is the lack of a good blue light-emitting device. In blue light-emitting iTMC-based LECs, efficiencies up to 18.3 cd A<sup>-1</sup> have been reported, but only at low current densities and, consequently, at low luminances (14.5 cd m<sup>-2</sup>).<sup>12b</sup> In tandem devices both sub-devices operate with the same current density. Therefore, if the before-mentioned blue LECs are used to prepare tandem LECs, their maximum luminance would be severely limited. Hence, to confirm that indeed LECs are ideally suited for solution-processed tandem devices, a better blue LEC is required that can function as the blue-emitting sub-device.

Orange LECs with high luminance and efficiency, on the contrary, are quite abundant. Here we report white light-emitting LECs, based on a tandem structure and employing an air stable middle electrode, that exhibit a current efficiency of 8.5 cd A<sup>-1</sup> at a luminance of 845 cd m<sup>-2</sup>. The tandem LEC consists of a novel polymer composite as the bottom blue light-emitting layer and an ionic iridium complex as the top orange light-emitting layer, both prepared using solution processing.

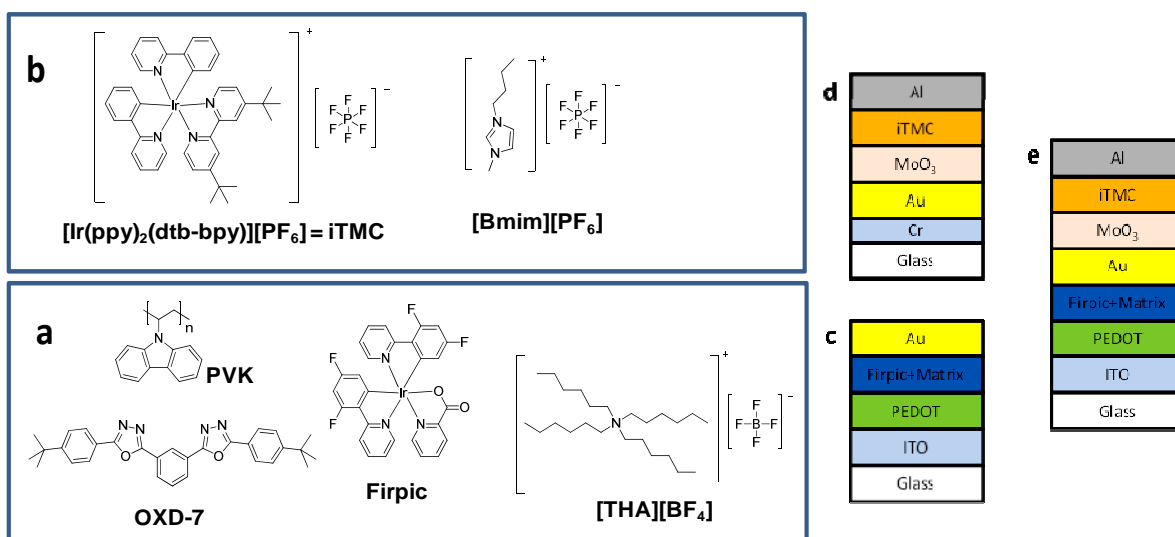


**Fig. 4.5** Structure of chemical compounds used and schematic of the device layouts. a) Chemical structures of the compounds used for the bottom LEC. (b) Chemical structures of the compounds used for the top LEC. (c) Scheme of the bottom-LEC layout. (d) Scheme of the top-LEC layout. (e) Scheme of the tandem-LEC layout.



In view of the limited luminance and efficiency of iTMC based blue LECs, we developed an alternative based on a well-known blue light-emitting OLED configuration. In this configuration, the neutral hole transporting host poly(N-vinylcarbazol) (PVK), the neutral electron transporter 1,3-bis[2-(4-*tert*-butylphenyl)-1,3,4-oxadiazol-5-yl]benzene (OXD-7), and the blue emitter bis[2-(4',6'-difluorophenyl)pyridinato-N,C2'] iridium(III)-picolinate (FIrPic) were mixed with a small amount of the ionic liquid (IL) tetrahexylammonium tetrafluoroborate [THA][BF<sub>4</sub>] (Fig. 4.5 panel a). A similar approach for red LECs was reported by Shin et al.<sup>15</sup> The device had the following configuration: ITO/PEDOT:PSS/PVK:OXD-7:FIrPic:IL = 10:10:2:1 (mass ratio)/Au (Fig. 4.5, panel a and c) and reached a maximum luminance of 160 cd m<sup>-2</sup> at a constant current of 100 A m<sup>-2</sup> (see Fig. 4.6, panel a). When an aluminum cathode was used, the performance of this blue LEC improved to a luminance of 400 cd m<sup>-2</sup> (4 cd A<sup>-1</sup>) (Fig. S4.2 in the Supporting Information).

To identify a complementary broad-band orange light-emitter, the electroluminescence spectrum of the FIrPic-based bottom LEC (Fig. 4.6, panel b) was compared with that of many different orange LECs. This was done screening the literature as well as our own database. From this comparison, a rather good match was found for the orange LEC using the iTMC [Ir(ppy)<sub>2</sub>(dtb-bpy)][PF<sub>6</sub>], where Hppy stands for 2-phenylpyridine and dtb-bpy for 4,4'-di-*ter*-butyl-2,2'-bipyridine, as the emitter (Fig. 4.6, panel b).<sup>16</sup> Hence, the top LEC was prepared using this emitter, mixed with the IL 1-butyl-3-methylimidazolium hexafluorophosphate [BMIm][PF<sub>6</sub>], and Au as the semi-transparent anode (Fig. 4.5, panel b). A thin layer of Cr was used to ensure good adhesion of the semitransparent gold electrode on the glass substrate. To maintain a good transparency, the bottom electrode was built up using 2 nm of Cr, 5 nm of Au and 5 nm of MoO<sub>3</sub> (the reason for the MoO<sub>3</sub> layer is commented upon in the next paragraph) deposited by sequential thermal vacuum evaporation on top of a flat glass substrate (Fig. 4.5, panel d). The maximum luminance of the Cr/Au/MoO<sub>3</sub>/iTMC:[BMIm][PF<sub>6</sub>] = 4:1 (molar ratio)/Al top LEC reaches 727 cd m<sup>-2</sup> at a constant current of 100 A m<sup>-2</sup> (see Fig. 4.6, panel a). In addition to the charge generation function, the middle electrode has the role of protecting the bottom device during the

processing of the top device. In this work Au layers of 0, 5, 10, and 40 nm were evaluated as the semitransparent middle electrode.

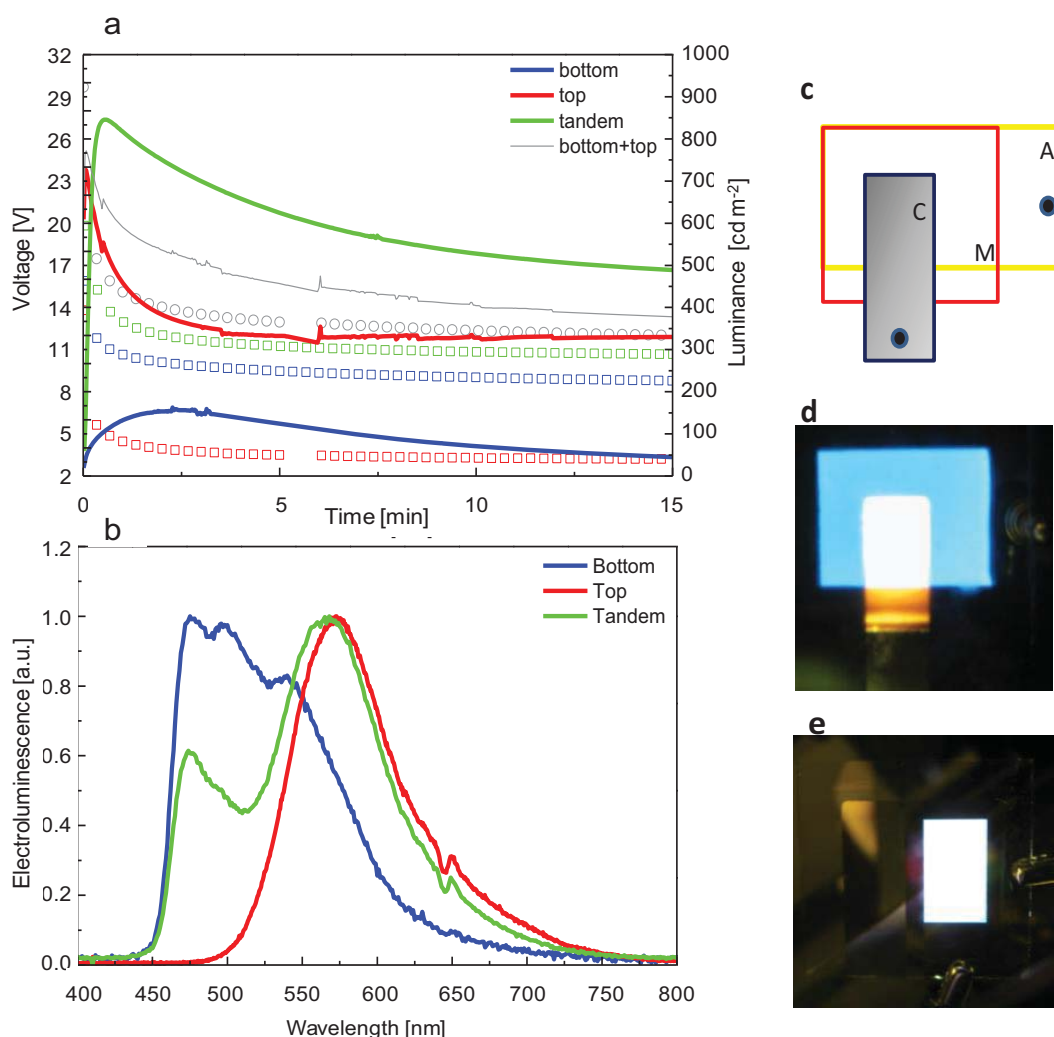


**Fig. 4.6** Performance of bottom, top, and tandem LECs. (a) Voltage (symbols) and luminance (lines) versus operation time for the bottom (blue), top (red), and tandem LECs (green) when operated at a constant current density of  $100 \text{ A m}^{-2}$ . (b) Electroluminescence spectra of the bottom (blue), top (red), and tandem LECs (green) when operated at a constant current density of  $100 \text{ A m}^{-2}$ . (c) Scheme depicting the position and size of the ITO bottom (A), Au middle (M), and Al top (C) electrodes, black dots indicate the position where the anode and cathode are contacted. (d) Photograph of a tandem LEC driven at  $100 \text{ A m}^{-2}$  with a 10 nm thick Au middle electrode. (e) Photograph of a tandem LEC driven at  $100 \text{ A m}^{-2}$  with a 5 nm thick Au middle electrode.

With thin Au layers, the bottom device was partially removed during the solution processing of the top light-emitting layer. Hence, an additional layer is required to prevent damaging of the bottom device. In tandem OLEDs using doped

electron injection layers, MoO<sub>3</sub> has been used as the interlayer.<sup>2e</sup> Therefore, a thin layer of MoO<sub>3</sub> was thermally evaporated on top of the Au electrode in the tandem LECs. A MoO<sub>3</sub> layer as thin as 5 nm on top of the Au electrode is sufficient to protect the bottom layer during processing of the top device.

To verify the effect of the different Au thicknesses, the electrodes used in the tandem device had a different area, 78, 72, and 36 mm<sup>2</sup> for the ITO bottom-, the Au middle-, and the Al top-electrode, respectively (Fig. 4.6, panel c). The tandem LEC without Au did emit but the light was orange indicating it came from the top device only. Hence, in contrast to what was observed in a tandem OLED, no electron injection into the bottom device is occurring from the MoO<sub>3</sub> layer. This suggests that the dynamic doping levels in LECs are lower than what is achieved by intentionally doping. The tandem device with a very thick Au layer (40 nm) had a very poor transparency and, although both sub-devices emit light, only very weak orange light is detected from the top device. The tandem LEC with 10 nm Au emits from both top and bottom devices leading to white light emission (Fig. 4.6, panel d). Additionally, blue light emission is obtained over the area where the Au electrode overlaps with the ITO anode. Hence, electrons are injected into the bottom device over the whole area of the Au middle electrode, implying that its lateral conductivity is higher than required. At the area at which there is no overlap between the Al cathode and the ITO anode but with the Au interlayer present, only orange light from the top device is observed (Fig. 4.6, panel d).

This demonstrates nicely the tandem device concept showing simultaneously light-emission from bottom, top, and tandem devices. The best tandem LEC was obtained with an Au layer of 5 nm. In this tandem device, light emission (white) is only observed from the area at which the Al cathode overlaps with the ITO anode (Fig. 4.6, panel e). Now, the lateral conductivity of the thin Au layer is insufficient to allow for the injection of electrons outside the area defined by the top contact. For this reason, no light-emission can be observed for the bottom and top cell separately.

	$\text{Lum}_{\max}$ [cd m <sup>-2</sup> ]	$\text{Efficacy}_{\max}$ [cd A <sup>-1</sup> ]	$\text{Lum}_{\text{st}}^{[a]}$ [cd m <sup>-2</sup> ]	$\text{U}_{\text{st}}^{[a]}$ (V)
Bottom	156	1.6	110	9.3
Top	728	7.3	328	3.5
Tandem	845	8.4	604	11.1

[a]  $\text{Lum}_{\text{st}}$  and  $\text{U}_{\text{st}}$  refers to the luminance and driving voltage at quasi steady-state conditions (here taken at 6 minutes after turn-on).

**Table 4.3.** Performance of bottom, top, and tandem LECs when operated at a constant current density of 100 A m<sup>-2</sup>.

The typical performance of the optimized tandem LEC is depicted in Fig. 4.6 (panels a and b). The electroluminescence of the tandem LEC clearly contains contributions from bottom and top devices (Fig. 4.6, panel b). The CIE coordinates of the white light emitted are  $x = 0.38$  and  $y = 0.47$ , which is slightly above the black-body radiation curve. The driving voltage of the tandem LEC drops rapidly after turning-on the current (Fig. 4.6, panel a). The drop is caused by the migration of ions to the electrode interfaces and the build-up of electrical double layers and, eventually, the formation of the dynamically doped zones, which rapidly reduces the injection barriers for electrons and holes (Fig. 4.4). As such, the voltage needed to sustain a current density of 100 A m<sup>-2</sup> continuously decreases until it reaches a quasi-steady state, which is related to the charge transport of the carriers in the light-emitting layers. The luminescence of the white tandem LEC reaches a maximum of 845 cd m<sup>-2</sup> at a constant current of 100 A m<sup>-2</sup>. At this luminance the current efficiency is 8.5 cd A<sup>-1</sup> (Table 4.3). Although device performance was not the main goal of this work, these values are significantly above those reported previously for white LECs.<sup>12-14</sup> The luminance of the tandem LEC decreases quite rapidly with time mainly due to the poor stability of the bottom blue LEC.

For a tandem configuration with two devices in series, the luminance and the driving voltage are expected to be the sum of the two individual devices. Interestingly, the tandem LEC here described shows a higher luminance and a lower driving voltage than what is obtained from the sum of luminance and driving voltage performance

values for the bottom and top LEC separately (Fig. 4.6, panel a). This observation implies that the individual cells in the tandem configuration outperform the stand alone bottom and top LECs. Moreover, there appears to be no charge balancing issue with this tandem device. That is expected as the formation of the dynamic doped zones is a self-regulating mechanism causing the current density to be equal in both top and bottom devices without potential losses at the junction.

In summary, salt-containing organic semiconducting materials are ideally suited for the preparation of tandem devices. Upon applying an external bias, the presence of the ions lead to the generation of dynamically doped regions adjacent to the external and internal electrodes. This self-regulates the potential drop, leads to ideal junction formation, and removes the need to use permanently doped charge injection layers. This was demonstrated by preparing a partially solution-processed white tandem LEC exhibiting a current efficiency of  $8.5 \text{ cd A}^{-1}$  at a luminance of  $845 \text{ cd m}^{-2}$ . To achieve this, a novel high luminance blue LEC was developed by adding an ionic liquid to a composite frequently employed in OLEDs.

## Experimental Section

### *Materials:*

Aqueous dispersions of poly(3,4-ethylenedioxythiophene) doped with poly(styrenesulfonate) (PEDOT:PSS, CLEVIOS P VP Al 4083) were obtained from Heraeus Holding GmbH and used as received. The ionic transition-metal complex (iTMC) 4,4'-di(*tert*-butyl)-2,2'-bipyridine bis(2-phenylpyridinato) iridium(III) hexafluorophosphate  $[\text{Ir}(\text{ppy})_2(\text{dtb-bpy})][\text{PF}_6]$  was synthesized following a previously published procedure.<sup>16</sup> The ionic liquids (ILs) 1-butyl-3-methyl-imidazolium hexafluorophosphate  $[\text{BMIm}][\text{PF}_6]$  and tetrahexylammonium tetrafluoroborate  $[\text{THA}][\text{BF}_4]$  were purchased from Aldrich and Fluka, respectively. The host-polymer poly(N-vinylcarbazol) (PVK) was purchased from Aldrich and 1,3-bis[2-(4-*ter*-

butylphenyl)-1,3,4-oxadiazole-5-yl]benzene (OXD-7) was purchased from Luminescence Technology Corp. The phosphorescent guest bis(2-(4',6'-difluoro)phenylpyridinato) iridium(III) picolinate (FIrPic) was also purchased from Luminescence Technology Corp. All commercially available materials were used as received. The chemical structure of the iTMC, the ILs, and the phosphorescent host-guest materials are displayed in Fig. 4.5.

#### *Device Preparation:*

The tandem LECs were made as follows. Indium tin oxide ITO-coated glass plates were patterned by conventional photolithography (purchased from Naranjo substrates). The substrates were subsequently cleaned ultrasonically in water-soap, water, and 2-propanol baths. After drying, the substrates were placed in a UV-ozone cleaner (Jelight 42-220) for 20 min. An 80 nm layer of PEDOT:PSS was spin-coated on the ITO glass substrate. A first emitting layer of FIrPic in a composite matrix, comprising 10 mg of PVK, 10 mg of OXD-7, 2 mg of FIrPic, and 1 mg of [THA][BF<sub>4</sub>] in 10 mL chlorobenzene, was spin-coated at 1500 rpm for 40 s on top of the PEDOT:PSS layer. Then the gold and the molybdenum oxide (5 nm) were thermally evaporated as the middle electrode using a shadow mask. After that, a second light-emitting layer consisting of the iTMC and [BMIm][PF<sub>6</sub>] at a molar ratio of 4 to 1 was spin-coated from an acetonitrile solution (solid content 40 mg mL<sup>-1</sup>) at 1500 rpm for 40 s on top of the middle electrode layer. Finally the top Al electrode (70 nm) was thermally evaporated. Spin-coating was done in ambient atmosphere; the base pressure during the thermal evaporation was  $1 \times 10^{-6}$  mbar.

#### *Device Characterization:*

The thickness of the films was determined with an Ambios XP-1 profilometer. Thin film photoluminescence spectra and quantum yields were measured with a Hamamatsu C9920-02 Absolute PL Quantum Yield Measurement System. The voltage versus time ( $J - t$ ) and electroluminescence versus time ( $Lum - t$ )

characteristics were collected using a Keithley Model 2400 source measurement unit and a Si-photodiode coupled to a Keithley Model 6485 picoamperometer, respectively. The photocurrent was calibrated using a Minolta Model LS100 luminance meter. Electroluminescence spectra were recorded using an Avantis fiberoptics photospectrometer. The devices were not encapsulated and were characterized inside the glovebox.

## Supporting Information

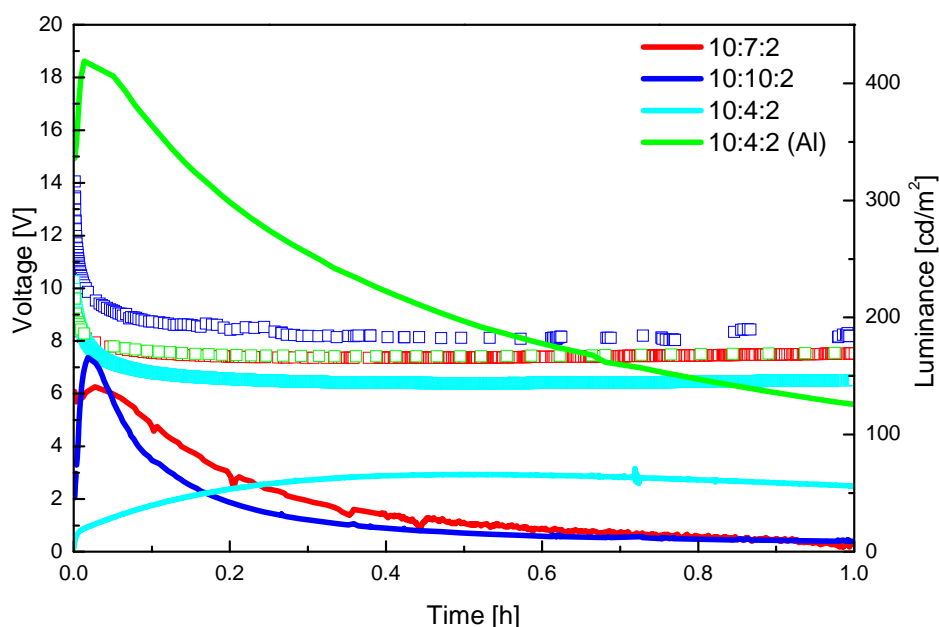


Fig. S4.2. Optimization of the blue LECs. (a) Voltage (symbols) and luminance (lines) versus operation time for the different compositions of PVK:OXD-7:FIrPic in the active layer when operated at a constant current density of  $100 \text{ A m}^{-2}$ . The device configurations used were: ITO/PEDOT:PSS/(PVK:OXD-7:FIrPic):IL=22:1 (mass ratio)/Au (red, blue and cyan) or Al (green) curve. The ratio's PVK:OXD-7:FIrPic are depicted in the legend.

## References

1. a) J. H. Burroughes, D. D. C. Bradley, A. R. Brown, R. N. Marks, K. Mackay, R. H. Friend, P. L. Burns, A. B. Holmes, *Nature* **1990**, 347, 539 – 541; b) C. W. Tang, S. A. VanSlyke, *Appl. Phys. Lett.* **1987**, 51, 913 – 915.
2. a) J. Kido, M. Kimura, K. Nagai, *Science* **1995**, 267, 1332– 1334 ; b) T. Chiba, Y.-J. Pu, R. Miyazaki, K.-I. Nakayama, H. Sasabe, J. Kido, *Org. Electron.* **2011**, 12, 710 – 715; c) M. C. Gather, A. Köhnen, K. Meerholz, *Adv. Mater.* **2011**, 23, 233 – 248 ; d) T. Matsumoto, T. Nakada, J. Endo, K. Mori, N. Kawamura, A. Yokoi, J. Kido, *Dig. Tech. Pap. – Soc. Inf. Disp. Int. Symp.* **2003**, 34 , 979; e) H. Kanno, R. J. Holmes, Y. Sun, S. Kena-Cohen, S. R. Forrest, *Adv. Mater.* **2006**, 18, 339 – 342 .
3. a) S. Hamwi, J. Meyer, M. Kröger, T. Winkler, M. Witte, T. Riedl, A. Kahn, W. Kowalsky, *Adv. Funct. Mater.* **2010**, 20, 1762 – 1766; b) Q.-Y. Bao, J.-P. Yang, J.-X. Tang, Y. Li , C.-S. Lee, S.-T. Lee, *Org. Electron.* **2010**, 11, 1578 – 1583.
4. a) K. Walzer, B. Maennig, M. Pfeiffer, K. Leo, *Chem. Rev.* **2007**, 107, 1233 – 1271 ; b) Y. Chen, D. Ma, *J. Mater. Chem.* **2012**, 22, 18718 – 18734 .
5. T. Chiba, Y.-J. Pu, H. Sasabe, J. Kido, Y. Yang, *J. Mater. Chem.* **2012**, 22 , 22769 – 22773.
6. a) Q. B. Pei, G. Yu, C. Zhang, Y. Yang, A. J. Heeger, *Science* **1995**, 269, 1086 – 1088; b) J.-K. Lee, D. S. Yoo, E. S. Handy, M. F. Rubner, *Appl. Phys. Lett.* **1996**, 69, 1686 – 1688.
7. a) K. M. Maness, R. H. Terrill, T. J. Meyer, R. W. Murray, R. M. Wightman, *J. Am. Chem. Soc.* **1996**, 118, 10609 – 10616 ; b) J. D. Slinker, J. Rivnay, J. S. Moskowitz, J. B. Parker, S. Bernhard, H. D. Abruna, G. G. Malliaras, *J. Mater. Chem.* **2007**, 17 , 2976 – 2988; c) Q. J. Sun, Y. F. Li, Q. B. Pei, *J. Display Technol.* **2007**, 3, 211 – 224; d) R. D. Costa, E. Ortí, H. J. Bolink, F. Monti, G. Accorsi, N. Armaroli, *Angew. Chem. Int. Ed.* **2012**, 51, 8178 – 8211; e) T. Hu, L. He, L. Duan, Y. Qiu, *J. Mater. Chem.* **2012**, 22, 4206 – 4215.



8. A. Sandström, H. F. Dam, F. C. Krebs, L. Edman, *Nat. Commun.* **2012**, *3*, 1002.
9. S. van Reenen, T. Akatsuka, D. Tordera, M. Kemerink, H. J. Bolink, *J. Am. Chem. Soc.* **2013**, *135*, 886 – 891.
10. a) P. Matyba, K. Maturova, M. Kemerink, N. D. Robinson, L. Edman, *Nature Mater.* **2009**, *8*, 672 – 676; b) S. van Reenen, P. Matyba, A. Dzwilewski, R. A. J. Janssen, L. Edman, M. Kemerink, *J. Am. Chem. Soc.* **2010**, *132*, 13776 – 13781; c) M. Lenes, G. García-Belmonte, D. Tordera, A. Pertegás, J. Bisquert, H. J. Bolink, *Adv. Funct. Mater.* **2011**, *21*, 1581 – 1586.
11. a) C. Tracy, J. Gao, *Appl. Phys. Lett.* **2005**, *87*, 143502; b) Bernards, D. A.; Slinker, J. D.; Malliaras, G. G; Flores-Torres, S.; Abruna, H. D. *Applied Physics Letters* **2004**, *84*, 4980.
12. a) L. He, J. Qiao, L. Duan, G. F. Dong, D. Q. Zhang, L. D. Wang, Y. Qiu, *Adv. Funct. Mater.* **2009**, *19*, 2950 – 2960; b) L. He, L. A. Duan, J. A. Qiao, G. F. Dong, L. D. Wang, Y. Qiu, *Chem. Mater.* **2010**, *22*, 3535 – 3542; c) H. C. Su, H. F. Chen, Y. C. Shen, C. T. Liao, K. T. Wong, *J. Mater. Chem.* **2011**, *21*, 9653 – 9660.
13. S. Tang; Y. Pan; H. A. Buchholz; L. Edman *J. Am. Chem. Soc.* **2013**, *135*, 3647-3652.
14. H. B. Wu, H. F. Chen, C. T. Liao, H. C. Su, K. T. Wong, *Org. Electron.* **2012**, *13*, 483 – 490.
15. I.-S. Shin, H.-C. Lim, J.-W. Oh, J.-K. Lee, T. H. Kim, H. Kim, *Electrochemistry Communications* **2011**, *13*, 64 – 67.
16. J. D. Slinker, A. A. Gorodetsky, M. S. Lowry, J. J. Wang, S. Parker, R. Rohl, S. Bernhard, G. G. Malliaras, *J. Am. Chem. Soc.* **2004**, *126*, 2763 – 2767.



## **Chapter 5**

# **Thin film high efficient solar cells**



## **5.1 CH<sub>3</sub>NH<sub>3</sub>PbI<sub>3</sub> and organic blocking layers: a versatile solar cell configuration**

The hybrid organic-inorganic perovskite semiconductors have been highlighted as one of the major scientific breakthroughs of 2013, representing for the first time a real alternative to the established inorganic based solar cell technology. Thin perovskite films can be easily solution processed from a wide variety of techniques, allowing their fabrication in a fast, simple and easy way.

Such a simple and accessible fabrication process has favored these materials to be accessible for the majority of the PV research groups. As a consequence, perovskite have been synthesized in very different ambient conditions, by using different techniques, precursors and processes. Although it is not understood yet the influence of the perovskite morphology on the performance and photocurrent behavior of the PSC, different methods of synthesis can lead to different perovskite behavior, mainly when the crystalline film is fabricated directly from a solution-deposition process. Additionally, some of the most efficient cells have shown hysteresis when they are forward or reversed bias, impeding to obtain reliable fundamental studies. In such situation, the control and certification of PSC performances is an actual necessity as well as the development of controllable sintering processes to achieve reproducible results and reliable conclusions.

According to the above mentioned demands, we attempted to synthesize the perovskite material through an alternative approach, by using a dual source evaporating process, in a similar way than reported previously.<sup>1-3</sup> This process consisted on evaporating both precursors, CH<sub>3</sub>NH<sub>3</sub>I and PbI<sub>2</sub>, at the same time inside a high vacuum evaporator.

By adjusting the stoichiometry of precursors, pure perovskite layers with an accurate control on the layer thickness and composition were obtained. This allowed the preparation of very reproducible samples which makes possible an in

depth study of these materials. A schematic picture of the evaporation process is shown in Fig. 5.1.

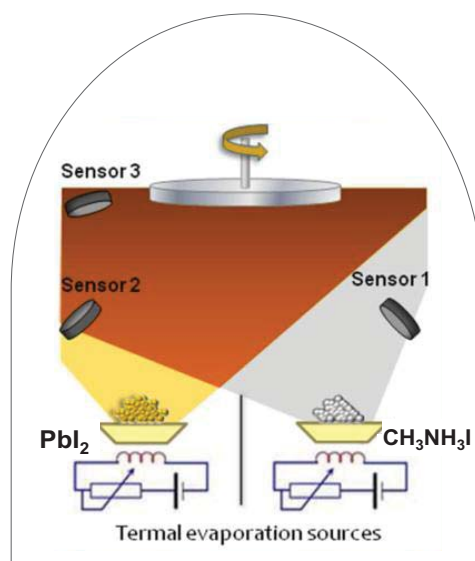


**Fig. 5.1** Schedule of the thermal evaporator used in the dual source evaporation process.

Both starting materials were heated simultaneously to their corresponding sublimation temperatures forming a perovskite layer at the height of the substrate, as it is shown in the above figure. Since the perovskite is formed by a specific stoichiometry it is fundamental to know the evaporation rate for each material, what implies the calibration of each sensor. Nevertheless, the calibration for  $\text{CH}_3\text{NH}_3\text{I}$  resulted very difficult as the films were very soft and not homogeneous. As an alternative, we fixed the temperature of evaporation for this material and modified the rate for  $\text{PbI}_2$  until the right stoichiometry was achieved. The obtained films were analyzed and characterized by grazing incidence X-ray diffraction (GIXRD), atomic force microscopy (AFM) and scanning electron microscopy (SEM), which confirmed the typical tetragonal structure for  $\text{CH}_3\text{NH}_3\text{MX}_3$  hybrid perovskites ( $\text{M} = \text{Pb}^{+2}, \text{Sn}^{+2}$ ;  $\text{X} = \text{Cl}^-, \text{Br}^-, \text{I}^-$ ), together with a very compact and smooth surface, with a root mean square (rms) roughness of 5.5 nm, as it is shown in Fig. 5.2.

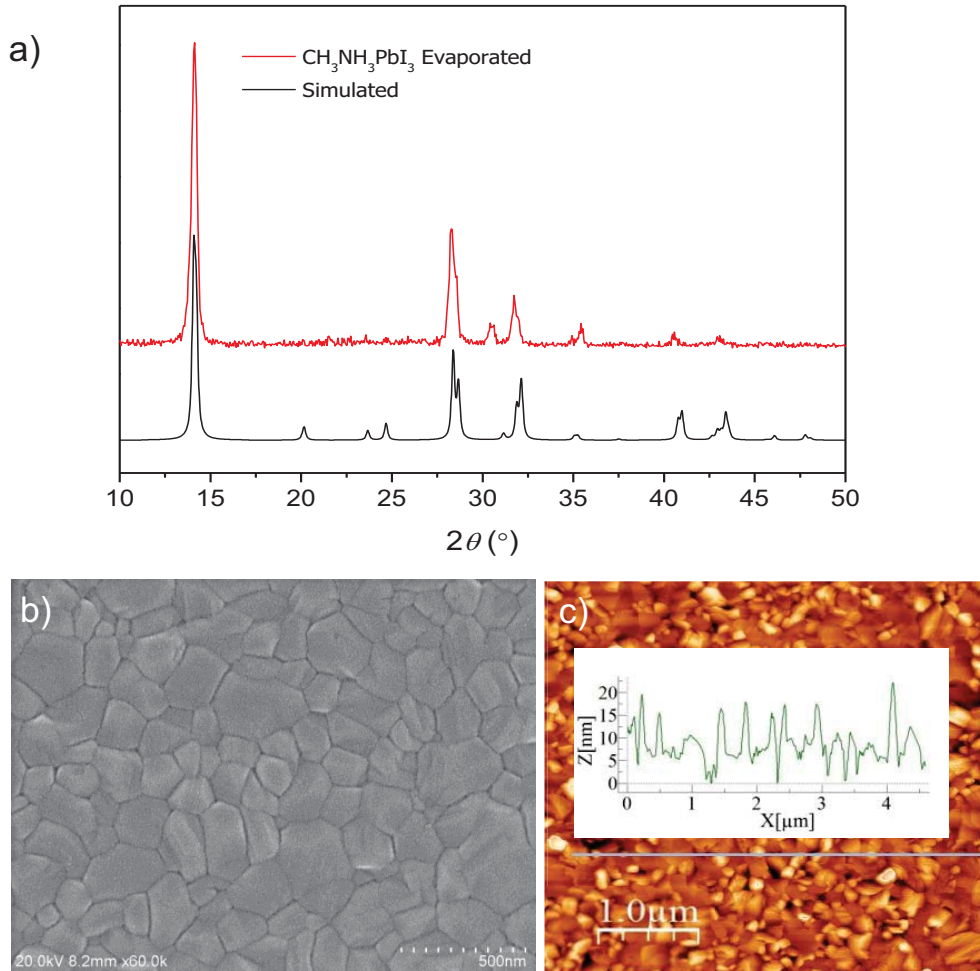


**Fig. 5.2** Surface characterization of an evaporated methylammonium lead iodide perovskite film with a thickness of  $\sim 250$  nm, a) GIXRD diffractogram of the prepared sample (red) compared with the simulated X-ray powder pattern for CH<sub>3</sub>NH<sub>3</sub>PbI<sub>3</sub> with preferred orientation along the (100), (010) and (001) directions (black); b) SEM picture and c) AFM image and profile of the thin perovskite film.

Most high efficiency perovskite solar cells reported in literature are based on the use of metal oxides such as Al<sub>2</sub>O<sub>3</sub>, TiO<sub>2</sub> or ZrO<sub>2</sub>, which require a high temperature sintering process and possess limited flexibility that may compromise their performance on alternative applications such as flexible devices. To exploit the potential of perovskites, new configurations with compatible materials are needed. In contrast, organic materials can be processed very easily at low

temperatures and are compatible with solution based roll-to-roll printing, which is one of the lowest cost and highest throughput method of fabrication.<sup>4</sup>

For that purpose, the evaporated perovskite thin film was sandwiched between two organic electron and hole transporting materials, which could also act as charge blocking layers, facilitating the injection / extraction of charges from the active material. As electron blocking layer, a thin film of poly(4-butylphenyl-diphenyl-amine) (polyTPD) was used. This material presents a very low conductivity ( $<2 \times 10^{-8} \text{ S cm}^{-1}$ ). However, it presents a HOMO energy very similar to that of the  $\text{VB}_{\text{perovsk}}$ , allowing an efficient hole extraction from the active material by using very thin layers ( $\sim 20 \text{ nm}$ ). On the contrary, its LUMO energy is high enough to avoid any electron diffusion from the  $\text{CB}_{\text{perovs}}$  to the anode, behaving as an electron blocking material. Due to the low thickness of the polyTPD film, another layer of  $\sim 70 \text{ nm}$  PEDOT:PSS was deposited between the ITO and the thin blocking layer, to soft the high roughness of this electrode surface at the same time that facilitates the extraction of holes by lowering the energy barrier.

On the other hand, as electron transport material, a 20 nm film of [6,6]-phenyl-C61-butyric acid methyl ester ( $\text{PCBM}_{60}$ ) was used, which presents a LUMO that is almost aligned to the perovskite  $\text{CB}_{\text{perovs}}$ . In a similar way as polyTPD, this material presents a deep HOMO energy, making more difficult the extraction of holes through the perovskite/ $\text{PCBM}$  interface. Finally, to complete the cell a 70 nm layer of Au was used as metallic cathode. Fig. 5.3 shows the device configuration and energy level diagrams of the PSC used in this Thesis.



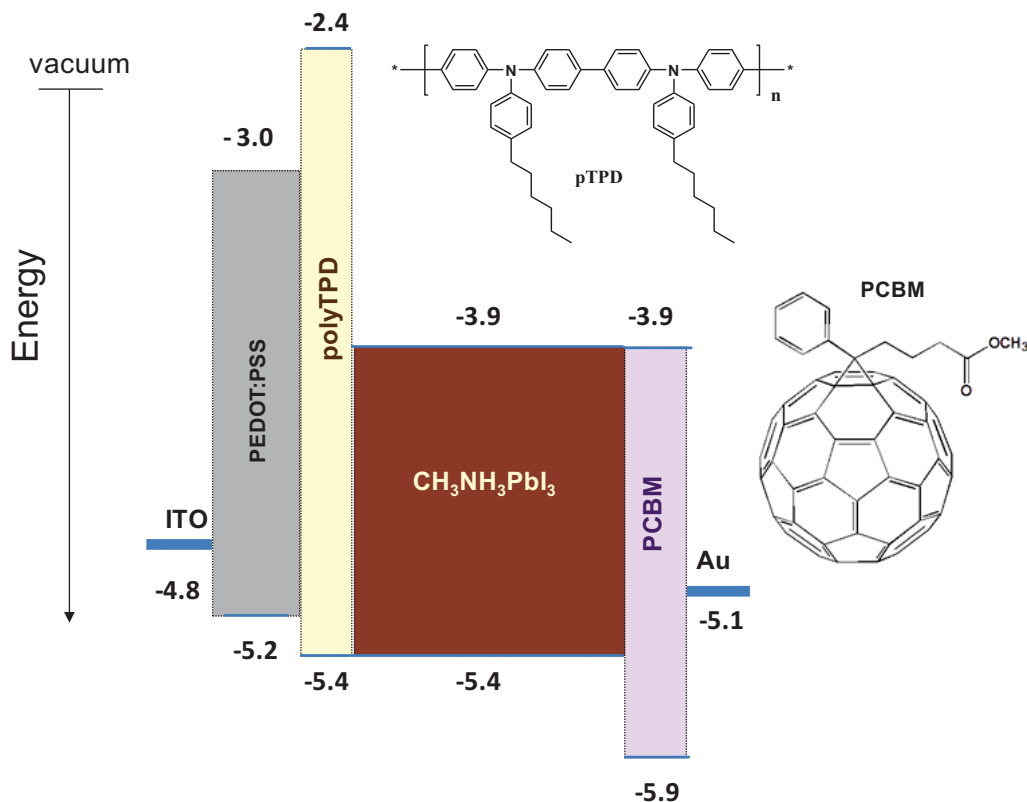


**Fig. 5.3** Approximate energy band diagram of the fabricated solar cell structure. Energy levels are taken from references 5-11.

One surprising characteristic of this configuration is the use of two electrodes with a very similar work function, what implies that there is no apparent built-in potential provoked by them ( $\Delta V \sim 0.3$  eV). Thus, in the absence of charge blocking materials, this configuration does not show any photoactive response.<sup>12</sup> Nevertheless, thanks to the charge blocking effect, the photo-generated electrons in the perovskite material are blocked and unable to reach the ITO/PEDOT:PSS anode, diffusing to the opposite electrode. On the contrary, the holes that are photo-generated in the perovskite can reach the ITO electrode easily, but not the Au electrode as there is a high potential barrier between the  $V_{B_{\text{perovs}}}$  and the  $HOMO_{\text{PCBM}}$ . As a consequence, a photo-generated current flows from the cell, leading to very good performances. Table 5.1 summarizes the most relevant results.

**Table 5.1** Most important results achieved with the metal-oxide free PSC, in the presence of the presence and absence of the electron blocking layer. The absence of any CBL leads to large ohmic conductivities.

CH <sub>3</sub> NH <sub>3</sub> PbI <sub>3</sub> 300 [nm]	$J_{sc}$ [mA cm <sup>-2</sup> ]	$V_{oc}$ [V]	FF [%]	PCE [%]
<i>PolyTPD</i>	12.4	0.6	58	4.6
PCBM <sub>60</sub> , <i>PolyTPD</i>	18.2	1.09	75	14.8

The evaporated perovskite, sandwiched in an organic-based configuration lead to power converted efficiencies close to 15 %. This configuration combines a very reproducible, controllable perovskite sintering process, with a robust layout, which is compatible with solution and low temperature processes by adapting the processing of the perovskite film, resulting a very versatile configuration. Thanks to these characteristics, the cells could be adapted to other interesting solar cells configurations allowing the preparation of high efficient flexible solar cells or high efficient semitransparent single junction cells, as will be shown in the next sections. Moreover, by this method no hysteresis is observed when bias the PSC in reversed or forward mode, suggesting its suitability for carrying deeper studies.

## References

1. Liu, M.; Johnston, M. B.; Snaith, H. J. *Nature* 2013, 501, 395.
2. Era, M.; Hattori, T.; Taira, T.; Tsutsui, T. *Chem. Mater.* 1997, 9, 8.
3. Mitzi, D. B. *Chem. Mater.* 2001, 13, 3283.
4. Krebs, F. C.; Tromholt, T. and Jorgensen, M. *Nanoscale* 2006, 2, 873.
5. Sun, Q. ; Wang, Y. A.; Li, L. S.; Wang, D.; Zhu, T.; Xu, J.; Yang, C.; Li, Y. *Nat. Photonics* 2007 , 1 , 717
6. Sun, S.; Salim, T.; Mathews, N.; Duchamp, M.; Boothroyd, C.; Xing, G.; Sum, T. C.; Lam, Y.-M. *Energy Environ. Sci.* 2014 , 7 , 399
7. Kim, H.-S.; Lee, C.-R.; Im, J.-H.; Lee, K.-B.; Moehl, T.; Marchioro, A.; Moon, S.-J.; Humphry-Baker, R.; Yum, J.-H.; Moser, J. E.; Gratzel, M.; Park, N.-G. *Sci. Rep.* 2012 , 2 , 591.
8. Heo, J. H.; Im, S. H.; Noh, J. H.; Mandal, T. N.; Lim, C.-S.; Chang, J. A.; Lee, Y. H.; Kim, H.-j.; Sarkar, A.; Nazeeruddin, M.K.; Gratzel, M.; Seok, S. I. *Nat. Photonics* 2013 , 7 , 486.
9. A. R. Kandada , G. Grancini , A. Petrozza , S. Perissinotto , D. Fazzi , S. S. Raavi , G. Lanzani , *Sci. Rep.* 2013 , 3 , 2073
10. C.-W. Chu , V. Shrotriya , G. Li , Y. Yang , *Appl. Phys. Lett.* 2006 , 88 , 153504
11. S. Sun , T. Salim , N. Mathews , M. Duchamp , C. Boothroyd , G. Xing , T. C. Sum , Y. M. Lam , *Energy Environ. Sci.* 2014 , 7 , 399.]
12. Malinkiewicz, O; Roldán-Carmona, C.; Soriano, A.; Bandiello, E.; Camacho, L.; Nazeeruddin, M.K. and Bolink, H.J. *Adv. Energy Mater.* 2014, 1400345.



## 5.2 Flexible high efficiency perovskite solar cells

Roldán-Carmona, C.<sup>1,2</sup>; Malinkiewicz, O.<sup>1</sup>; Soriano, A.<sup>1</sup>; Espallargas, G.M.<sup>1</sup>; Garcia, A.<sup>3</sup>; Reinecke, P.<sup>3,4</sup>; Kroyer, T.<sup>3</sup>; Dar, M.I.; Nazeeruddin, M.K.<sup>4</sup> and Bolink, H.J.<sup>1</sup>

<sup>1</sup>*Instituto de Ciencia Molecular, Univ. de Valencia, Catedrático J. Beltrán 2, 46980 Paterna, Spain.*

<sup>2</sup>*Depart. of Physical Chemistry, Univ. of Cordoba, C. Rabanales, Ed. C3, 14014, Spain*

<sup>3</sup>*Fraunhofer Institute for Solar Energy Systems ISE, Heidenhofstrasse 2, 79110 Freiburg, Germany*

<sup>4</sup>*Freiburg Materials Research Center (FMF), Stefan-Meier-Strasse 21, 79104 Freiburg, Germany*

<sup>5</sup>*Laboratory of Photonics and Interfaces, Swiss Federal Institute of Technology (EPFL), Station 6, Lausanne, CH 1015, Switzerland*

Thin film photovoltaics represent the ultimate goal in the quest for clean renewable energy. Recently, methylammonium lead halide perovskites have been identified as promising absorbers for solar cells. Over the past three years, the performance of perovskite-based solar cells has rapidly improved reaching efficiencies as high as 15%. The perovskite absorbers are prepared from low-cost and abundantly available components allowing for the preparation of low cost photovoltaic devices and modules. However, to achieve very low cost devices they should be prepared using roll to roll (R2R) processes on large area flexible substrates. This requires a device architecture that does not need high temperature steps and that can be prepared using large area coating or printing methods.

Here we show that methylammonium lead iodide perovskite layers when sandwiched in between two thin organic charge-transporting layers and processed on a polymer based conductive substrate using large area compatible coating techniques lead to flexible solar cells with high power conversion efficiencies as high as 7%. Moreover, extended bending of these devices does not deteriorate their performance demonstrating the suitability of perovskite based solar cells for roll to roll processing.

Paper published in *Energy & Environmental Science* 7, 994, 2014.

Thin film photovoltaic devices hold great promise to reduce the dependencies on fossil energy.<sup>1</sup> After the seminal work of Miyasaka et al.,<sup>2</sup> tremendous progress in the performance of methylammonium lead iodide perovskite based solar cells has been made.<sup>3–12</sup> The hybrid organic–inorganic methylammonium lead iodide perovskites, pioneered by Mitzi, have been recognized for their excellent semiconducting properties.<sup>13,14</sup> The ease with which these organic–inorganic hybrid perovskite materials can be prepared and processed from solution has made them attractive for photovoltaic applications.<sup>15</sup> All high efficiency perovskite solar cells reported until now use (mesoscopic) metal oxides such as Al<sub>2</sub>O<sub>3</sub>, TiO<sub>2</sub> or ZrO<sub>2</sub> requiring a high temperature sintering process. Ball et al. showed that a thick layer (350 nm) of the mixed halide methylammonium lead perovskite (CH<sub>3</sub>NH<sub>3</sub>PbI<sub>3-x</sub>Cl<sub>x</sub>) leads to efficient solar cells (12%).<sup>9</sup> They argued that the perovskite functions as the absorber and as the electron and hole transporter. Additionally, it was suggested that the excitons predominantly dissociate in the bulk and not at a donor–acceptor interface. Hence, no bulk heterojunction between donor and acceptor is required to achieve efficient cells. This was confirmed by Liu et al., who showed that the mesostructure of the metal oxide is not required to prepare efficient (15.4%) perovskite based solar cells.<sup>12</sup> Recent results indicate that at least part of the excitons dissociate at the interface of the perovskite layer and the hole and electron transporting layer.<sup>16,17</sup> An inverted layout, similar to that employed in small molecular weight and polymeric solar cells, has also been described.<sup>18,19</sup> In these devices, the holes are extracted via the transparent conductor poly(3,4-ethylenedioxythiophene): poly(styrenesulfonic acid) (PEDOT:PSS).

Recently, we have improved the performance of such inverted devices by sandwiching an evaporated CH<sub>3</sub>NH<sub>3</sub>PbI<sub>3</sub> perovskite in between organic electron and hole blocking layers, reaching an average PCE of 12%.<sup>20</sup> In view of the above mentioned results the perovskite based solar cells are very well suited for roll to roll

(R2R) processing on flexible substrates. It is not clear, however, how the perovskite active layer will behave on a flexible substrate especially when it is bent. The perovskite is a crystalline material; hence, cracks or other imperfection may occur upon bending it.

Here, we present a flexible thin film solar cell based on a sublimated methylammonium lead iodide perovskite layer that is sandwiched in between two very thin electron and hole blocking layers consisting of organic molecules. A flexible transparent conductor based on a stack of thin layers of aluminium doped ZnO (AZO), silver and AZO was used (Fig. 5.4). Power conversion efficiencies (PCEs) as high as 7% were obtained and maintained when the solar cell was bent over a roll with a diameter of 5.5 cm for 50 times. No significant deterioration of the key performance parameters of the solar cell was observed indicating that the perovskite is compatible with roll to roll processing.

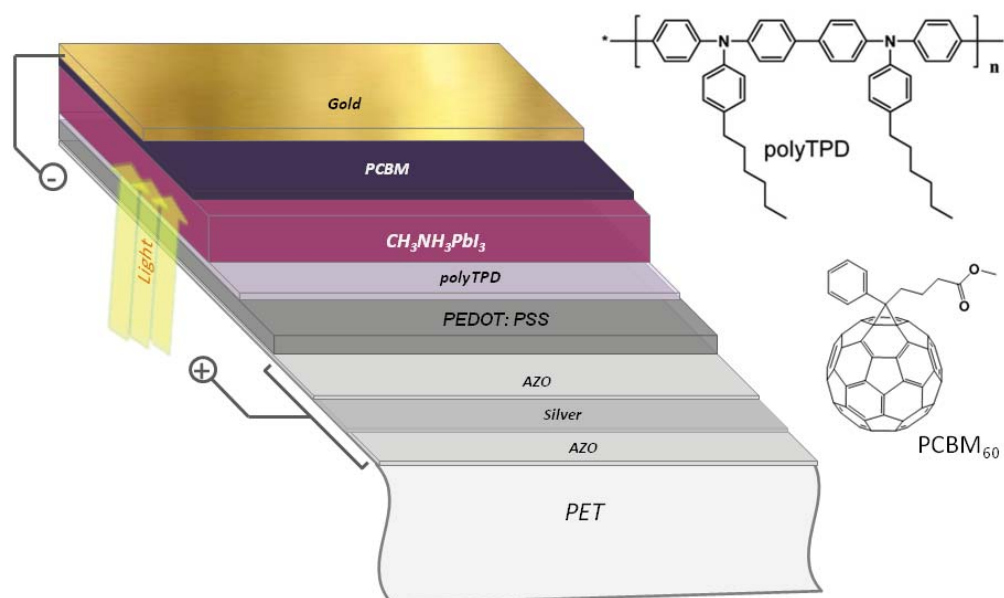


**Fig. 5.4** Schematic layout of the flexible perovskite solar cell and chemical structure of the materials used as the electron and hole blocking layer.

The flexible solar cell was prepared on 50 micron thick PET foil coated with a transparent silver electrode. The electrodes were produced by depositing a multilayer

stack composed of AZO 30 nm/Ag 9 nm/AZO 30 nm, where AZO designates Al doped ZnO with 2 wt% Al. The coating was applied by DC magnetron sputtering in a batch coater. For the AZO planar ceramic targets were used. The process pressure was about  $5 \times 10^{-3}$  mbar. In the visual range, the electrode transparency was 81%, with a sheet resistance of 7.5 Ohm. The coating process can be easily transferred to large scale roll to roll coating.<sup>21,22</sup> After cleaning the foils by rinsing them with ultrapure water and isopropanol a 70 nm poly(3,4-ethylenedioxythiophene):poly(styrenesulfonic acid) (PEDOT:PSS) layer was deposited using spin coating and it was annealed for 15 minutes at 90 °C. Following the PEDOT:PSS layer a thin layer (20 nm) of poly[N,N0-bis(4-butylphenyl)-N,N0-bis(phenyl)benzidine] (polyTPD) was deposited by spin coating (Fig. 5.4), as the electron blocking layer. On top of this the  $\text{CH}_3\text{NH}_3\text{PbI}_3$  was thermally evaporated to a thickness of 260 nm followed by a thin layer (30 nm) of [6,6]-phenyl C61-butyric acid methylester (PCBM) as the hole blocking layer.<sup>23</sup> The device was completed by the evaporation of an Au top electrode (70 nm). The PCBM layer was deposited using a meniscus coating process to ensure a high quality film.<sup>24</sup>

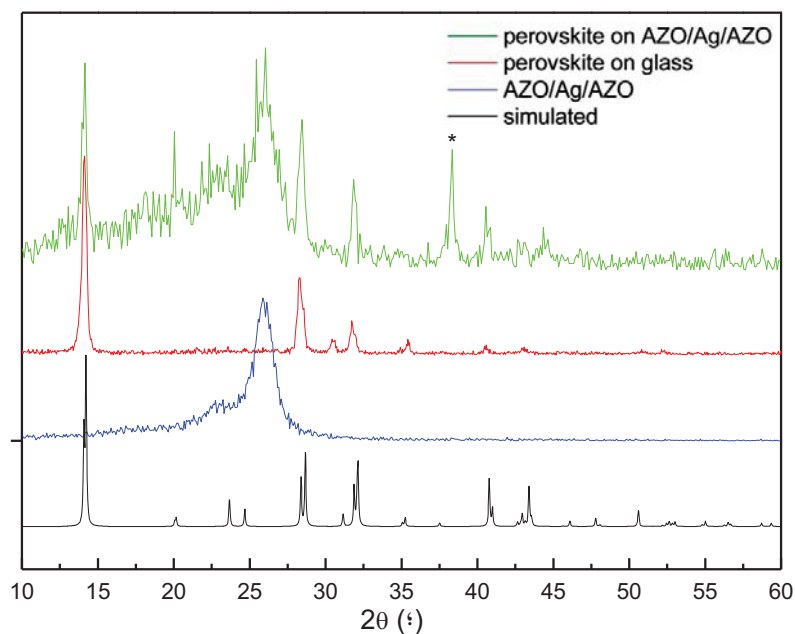


**Fig. 5.5** Grazing incidence X-ray diffraction (GIXRD) pattern with  $\text{K}\alpha_1$  radiation ( $\lambda = 1.54056$  °Å) of the sublimed thin film on AZO/Ag/AZO (green) compared with a film sublimed on glass (red),<sup>20</sup> the AZO/Ag/ AZO substrate (blue) and the calculated one for  $\text{CH}_3\text{NH}_3\text{PbI}_3$  (black). The star on the green diffractogram indicates a reflection of the gold used in the device.



The thickness of the layers was established using absorbance measurements. Full details of the device fabrication and characterization are provided in the ESI.† The  $\text{CH}_3\text{NH}_3\text{PbI}_3$  films grown on the AZO/Ag/AZO substrates were characterized using grazing incidence X-ray diffraction (GIXRD). Fig. 5.5 shows the X-ray powder pattern of a  $\text{CH}_3\text{NH}_3\text{PbI}_3$  film evaporated on an AZO/Ag/AZO substrate, revealing the formation of a crystalline layer. The sharp diffraction peaks of the perovskite can readily be identified.

Interestingly, upon comparison with a perovskite film evaporated on glass it can be noted that no preferential orientation is observed on the flexible AZO/Ag/AZO substrates, in contrast to what happens in the case of glass.

Due to the small sample size the application of the hole blocking layer using meniscus coating is difficult. In particular, the thickness of this layer was not easy to control. Due to this we used a PCBM layer of approximately 30 nm which is thicker than needed. A scanning electron microscope (SEM) cross-section of the thin film device is shown in Fig. 5.6 The resolution of the image is limited by the charging of the sample at higher magnification.

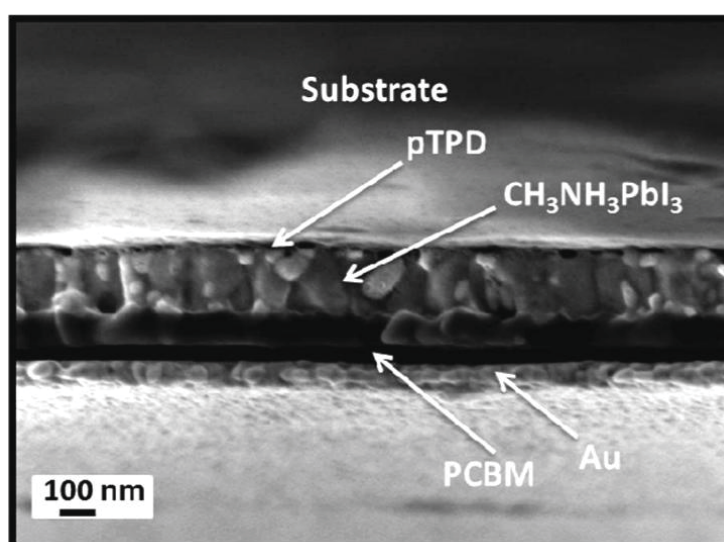


**Fig. 5.6** SEM cross-section of the perovskite device on the PET foil. A thin graphite layer was deposited on top to prevent excessive charging during measurement.

Fig. 5.7a shows the current–voltage ( $J$ – $V$ ) characteristics of a typical small area ( $0.12 \text{ cm}^2$ ) flexible perovskite solar cell measured under light intensities of  $100 \text{ mW cm}^{-2}$ . The reproducibility from device to device was within 10%. The short-circuit current density ( $J_{\text{SC}}$ ), open-circuit voltage ( $V_{\text{OC}}$ ) and fill factor (FF) for a typical device, respectively, are  $14.3 \text{ mA cm}^{-2}$ ,  $1.04 \text{ V}$  and  $0.47$ , leading to a power conversion efficiency of 7%.

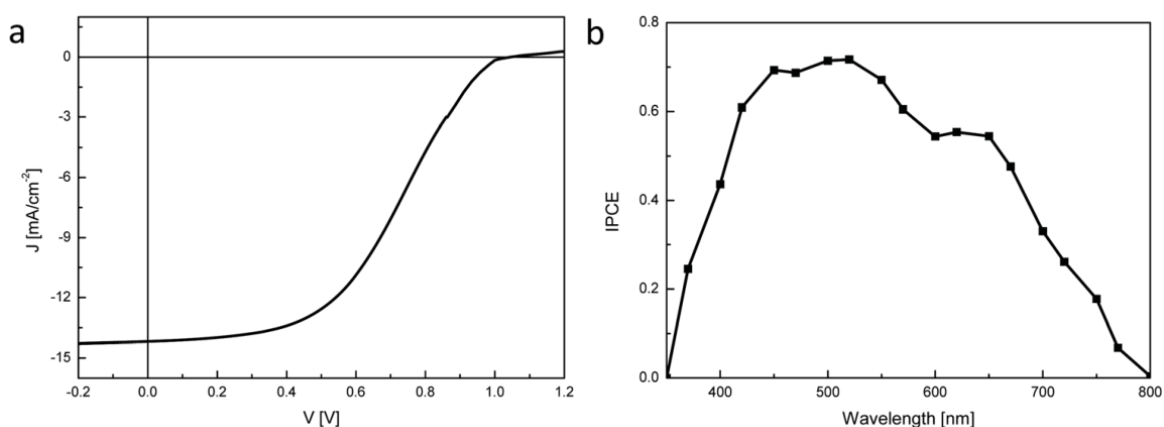


**Fig. 5.7** Characterization of a typical solar cell. (a) Photocurrent density versus voltage at  $100 \text{ mW cm}^{-2}$ . (b) IPCE spectrum

Previously, on glass substrates  $J_{\text{SC}}$ ,  $V_{\text{OC}}$  and FF of  $16.1 \text{ mA cm}^{-2}$ ,  $1.05 \text{ V}$  and  $0.67$ , respectively, have been obtained leading to a PCE of 12%.<sup>20</sup> Hence, the main difference between the devices on the glass substrates and on the foils is the lower FF which causes the strong reduction in the PCE. The main reason for this decrease in FF and PCE is due to the thicker hole and electron blocking layers in the flexible cells. The increased thickness of these layers is caused by more difficult handling of the small area flexible substrates. This can be solved when a larger substrate is used in either a batch or roll-to-roll (R2R) process employing slot-die coaters. The incident photon-to-current conversion efficiency (IPCE) spectra exhibit 74% (Fig. 5.7b) where the generation of photocurrent started at  $790 \text{ nm}$  in agreement with the band gap of the  $\text{CH}_3\text{NH}_3\text{PbI}_3$ . In spite of the before mentioned shortcomings the PCE obtained is among the highest reported for flexible solar cells using organic molecules.<sup>25–27</sup> Yet, more important than the actual value of the PCE is the effect that repeated bending of

the substrate has on it. To investigate this, the flexible solar cells were bent over a roll with a diameter of 5.5 cm. The performance was evaluated up to 50 bending cycles and no reduction of the key performance indicators was observed.  $J_{SC}$  and  $V_{OC}$  remained identical throughout the test and the fill factor decreased slightly from 0.474 to 0.464 after 50 bending cycles, which lead to a decrease in the PCE of 0.1% (Fig. 5.8b).

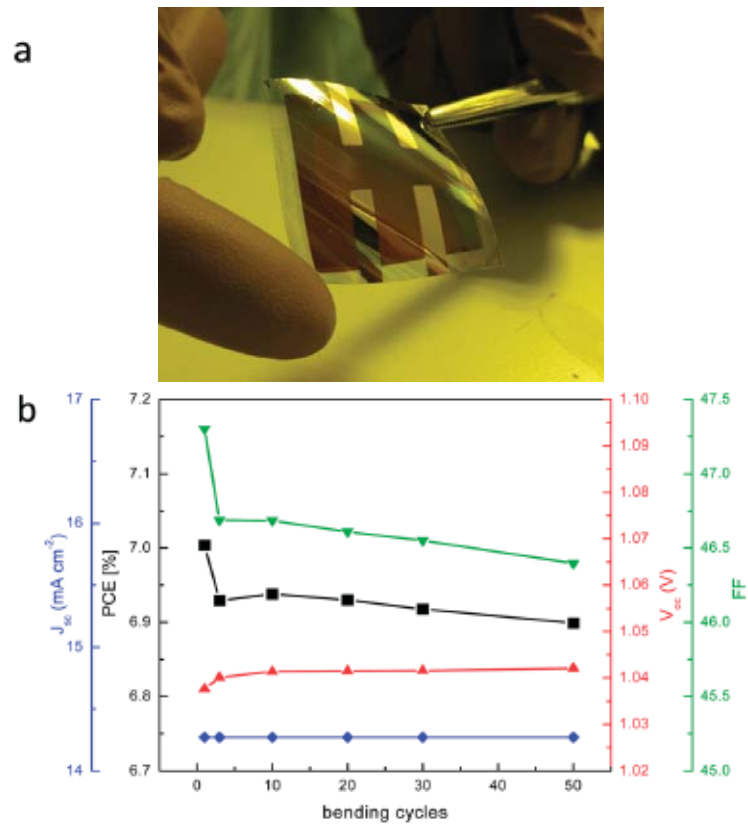


**Fig. 5.8** Bending test of the flexible solar cells. (a) Photograph of the flexible solar cell. (b) PCE, FF,  $J_{SC}$  and  $V_{OC}$  as a function of bending cycles.

## Conclusions

In summary, flexible solar cells based on the  $\text{CH}_3\text{NH}_3\text{PbI}_3$  perovskite absorber have been prepared. The device layout is very compatible with flexible substrates because all the processes are performed at room temperature. The exception is the annealing at 90 °C of the polymeric conductor (PEDOT:PSS) which is well below the critical temperature of most polymers. An AZO/Ag/AZO coated PET foil was used as the flexible substrate. In spite of some difficulties in controlling the thickness of the essential electron and hole blocking layers power conversion efficiencies as high as 7% were obtained. More importantly, this solar cell layout is very robust leading to a decline of the power conversion efficiency of only 0.1% after 50 bending cycles. This demonstrates that the perovskite solar cells are very suitable for roll to roll production.

## Supporting Information

### Methods

#### Materials

Aqueous dispersions of poly(3,4-ethylenedioxythiophene) doped with poly(styrenesulfonate) (PEDOT:PSS, CLEVIOS P VP Al 4083) were obtained from Heraeus Holding GmbH and used as received. poly[N,N'-bis(4-butylphenyl)-N,N'-bis(phenyl)benzidine] (poly-TPD) was purchased from ADS Dyesource.  $\text{PbI}_2$  was purchased from Aldrich and used as is,  $\text{CH}_3\text{NH}_3\text{I}$  was prepared similar to a previously published method<sup>28</sup>, in brief:  $\text{CH}_3\text{NH}_3\text{I}$ , was synthesized by reacting 21.6 ml methylamine (40%wt in water, Aldrich) and 30 ml hydroiodic acid (57 wt% in water, Aldrich) in a 250 ml round-bottomed flask at 0 °C for 2 h with stirring. The white precipitate was recovered by evaporation at 50 °C for 1 h. The product, methylammonium iodide ( $\text{CH}_3\text{NH}_3\text{I}$ ), was dissolved in ethanol, filtered and recrystallized from diethyl ether, and dried at 60 °C in a vacuum oven for 24 h.

## Device preparation

Devices were prepared on cleaned AZO/Ag/AZO on PET substrates, by spincoating a thin layer of PEDOT:PSS from the commercial aqueous dispersion (1200rpm 30sec and a short annealing at 150 °C result in 70 nm thickness). On top of this layer a thin film of polyTPD was deposited from a chlorobenzene solution (10 mg ml<sup>-1</sup>) using spincoating. Then the substrates were transferred to a vacuum chamber integrated into an inert glovebox (MBraun, <0.1 ppm O<sub>2</sub> and <0.1 ppm H<sub>2</sub>O) and evacuated to a pressure of  $1 \times 10^{-6}$  mbar. The sublimation of the perovskite was performed using a vacuum chamber of MBraun integrated in an inert glovebox (MBraun).

Temperature controlled evaporation sources from Creaphys fitted with ceramic crucibles were employed to sublime the CH<sub>3</sub>NH<sub>3</sub>I and the PbI<sub>2</sub>. The sources are directed upwards with an angle of approximately 90 ° with respect to the bottom of the evaporator. The substrates were placed at a distance of 20 cm from the top of the evaporation sources. Shutters are present at the evaporation sources and below the substrate holder. Three quartz microbalance sensors are present in the chamber, two monitoring the rate of each evaporation source and a third one at the height of the substrate holder. After the ceramic crucibles were loaded with the CH<sub>3</sub>NH<sub>3</sub>I and the PbI<sub>2</sub> the chamber was evacuated to a base pressure of  $1 \cdot 10^{-6}$  mbar. Fresh CH<sub>3</sub>NH<sub>3</sub>I was used for each evaporation. After the base pressure was reached, the CH<sub>3</sub>NH<sub>3</sub>I crucible was heated to 70 °C. At this temperature, all three quartz sensors gave a signal.

We were, however, unable to calibrate the sensor by measuring the thickness of a deposited CH<sub>3</sub>NH<sub>3</sub>I film. Therefore, an alternative process was used. Upon stabilization of the sensor reading the crucible containing the PbI<sub>2</sub> was heated. Only at PbI<sub>2</sub> evaporation temperatures in excess of 200 °C were dark brown films obtained. The film thickness of the perovskite film was monitored using quartz sensor nr 3 (at the height of the substrate holder).

Perovskite films were prepared at different PbI<sub>2</sub> evaporation temperatures, increasing with 10 degrees from the predetermined 200 °C. In this way the optimum

films were obtained at an evaporation temperature of the PbI<sub>2</sub> crucible of 250 °C. The PCBM layer was deposited using a chlorobenzene solution of 10 mg ml<sup>-1</sup> in ambient conditions using a meniscus coater and a coating speed of 10 mm/ second. The device was completed by the thermal evaporation of the top metal electrode under a base pressure of  $2 \times 10^{-6}$  mbar to a thickness of 100nm. The solar cells (active area of 0.12 cm<sup>2</sup>) were characterized inside the inert glovebox.

### Film Characterization

GIXRD data were collected at room temperature in the  $2\theta$  range 5–50 ° on an Empyrean PANalytical powder diffractometer, using Cu K $\alpha$ 1 radiation. Typically four repeated measurements were collected and merged into a single diffractogram. Pawley refinements<sup>29</sup>, were performed using the TOPAS computer program<sup>30</sup> and revealed an excellent fit to a one-phase model with a tetragonal cell ( $a = 8.80(2)$ ,  $c = 12.57(2)$  Å) and space group  $I4/mcm$ . Additional peaks corresponding to the ITO substrate were also observed.

Film thickness was investigated using a high-resolution scanning electron microscope (MERLIN, Zeiss) and micrographs were acquired using an in-lens secondary electron detector. Prior to analysis, the sample was coated with 12 nm carbon to minimize the charging effect.

### Device characterization

Solar cells were illuminated by a white light halogen lamp in combination with interference filters for the EQE and  $J-V$  measurements (MiniSun simulator by ECN the Netherlands). A black mask was used to limit the active area of the device. Before each measurement, the exact light intensity was determined using a calibrated Si reference diode. An estimation of the short-circuit current density ( $J_{SC}$ ) under standard test conditions was calculated by convolving the EQE spectrum with the AM1.5G reference spectrum, using the premise of a linear dependence of  $J_{SC}$  on light intensity. Current-voltage ( $J-V$ ) characteristics were measured using a Keithley 2400 source

measure unit. All characterization was done in a nitrogen filled glove box ( $<0.1$  ppm  $O_2$  and  $<0.1$  ppm  $H_2O$ ) without exposure to ambient atmosphere.

## **Acknowledgements**

This work has been supported by the European Community's Seventh Framework Programme (TREASORES, grant 314068), (FP7/2007–2013, ENERGY.2012.10.2.1; NANOMATCELL, grant agreement no. 308997), the Spanish Ministry of Economy and Competitiveness (MINECO) (MAT2011-24594) and the Generalitat Valenciana (Prometeo/2012/053). C.R.-C. would like to thank the MINECO for the financial support of this research in the framework of project CTQ2010-17481, the Junta de Andalucía (CICyE) for special financial support (P08-FQM-4011 and P10-FQM-6703) and the MECD (Spanish Ministry of Education, Culture, and Sport) for an FPU grant.

## References

1. Darling, S. B and You, F. *RSC Adv.*, **2013**, 3, 17633–17648.
2. Kojima, A.; Teshima, K.; Shirai, Y. and Miyasaka, T. *JACS*, **2009**, 131, 6050–6051.
3. Im, J.-H.; Lee, C.-R.; Lee, J.-W; Park, S.-W. and Park, N.-G. *Nanoscale*, **2011**, 3, 4088–4093.
4. Chung, I.; Lee, B.; He, J.; Chang, R. P. H. and Kanatzidis, M. G. *Nature*, **2012**, 485, 486–489.
5. Etgar, L. ; Gao, P.; Xue, Z.; Peng, Q.; Chandiran, A. K.; Liu, B.; Nazeeruddin, M. K. and Grätzel, M. *JACS*, **2012**, 134, 17396– 17399.
6. Kim, H.-S.; Lee, C.-R.; Im, J.-H.; Lee, K.-B.; Moehl, T.; Marchioro, A.; Moon, S.-J.; Humphry-Baker, R.; Yum, J.-H.; Moser, J. E.; Gratzel, M. and Park, N.-G. *Sci. Rep.*, **2012**, 2, 591.
7. Lee, M. M.; Teuscher, J.; Miyasaka, T.; Murakami, T. N. and Snaith, H. J. *Science*, **2012**, 338, 643–647.
8. Abrusci, A.; Stranks, S. D.; Docampo, P.; Yip, H.-L.; Jen, A. K. and Snaith, H. J. *Nano Lett.*, **2013**, 13, 3124–3128.
9. Ball, J. M.; Lee, M. M.; Hey, A. and Snaith, H. J. *Energy Environ. Sci.*, **2013**, 6, 1739.
10. Burschka, J.; Pellet, N.; Moon, S.-J.; Humphry-Baker, R.; Gao, P.; Nazeeruddin, M. K. and Gratzel, M. *Nature*, **2013**, 499, 316– 319.
11. Heo, J. H.; Im, S. H.; Noh, J. H.; Mandal, T. N.; Lim, C.-S.; Chang, J. A.; Lee, Y. H.; Kim, H.-j.; Sarkar, A.; NazeeruddinMd, K.; Gratzel, M. and Seok, S. I. *Nat. Photonics*, **2013**, 7, 486–491.
12. Liu, M.; Johnston, M. B. and Snaith, H. J. *Nature*, **2013**, 501, 395–398.



13. Kagan, C. R.; Mitzi, D. B. and Dimitrakopoulos, C. D. *Science*, **1999**, 286, 945–947.
14. Mitzi, D. B. *J. Mater. Chem.*, **2004**, 14, 2355–2365.
15. Snaith, H. J. *J. Phys. Chem. Lett.*, **2013**, 3623–3630.
16. Stranks, S. D.; Eperon, G. E.; Grancini, G.; Menelaou, C.; Alcocer, M. J. P.; Leijtens, T.; Herz, L. M.; Petrozza, A. and Snaith, H. J. *Science*, **2013**, 342, 341–344.
17. Xing, G.; Mathews, N.; Sun, S.; Lim, S. S.; Lam, Y. M.; Grätzel, M.; Mhaisalkar, S. and Sum, T. C. *Science*, **2013**, 342, 344–347.
18. Jeng, J.-Y.; Chiang, Y.-F.; Lee, M.-H.; Peng, S.-R.; Guo, T.-F.; Chen, P. and Wen, T.-C. *Adv. Mater.* **2013**, 25, 3727–3732.
19. Sun, S.; Salim, T.; Mathews, N.; Duchamp, M.; Boothroyd, C.; Xing, G.; Sum, T. C. and Lam, Y.-M. *Energy Environ. Sci.*, **2014**, 7, 399–407.
20. Malinkiewicz, O. ; Aswani, Y.; Lee, Y. H.; Minguez Espallargas, M.; Graetzel, M.; Nazeeruddin, M. K. and Bolink, H. J. *Nat. Photonics*, **2013**, DOI: 10.1038/nphoton.2013.341.
21. Kroyer, T.; Georg, A.; Regnat, M.; Zimmermann, B.; Wuerfel, U. and Graf, W. Proceedings of the Large-area, *Organic and Printed electronics Convention*, **2010**.
22. Kohlstädt, M.; Grein, M.; Reinecke, P.; Kroyer, T.; Zimmermann, B. and Würfel, U. *Sol. Energy Mater. Sol. Cells*, **2013**, 117, 98–102.
23. Yu, G.; Gao, J.; Hummelen, J. C.; Wudl, F. and Heeger, A. J. *Science*, **1995**, 270, 1789–1791.
24. Malinkiewicz, O.; Lenes, M.; Brine, H. and Bolink, H. J. *Rsc. Adv.*, **2012**, 2, 3335–3339.

25. Kaltenbrunner, M.; White, M. S.; Głowacki, E. D.; Sekitani, T.; Someya, T.; Sariciftci, N. S. and Bauer, S. *Nat. Commun.*, **2012**, 3, 770.
26. da Silva, W. J.; Kim, H. P.; Rashid, A.; Yusoff, B. M. and Jang, J. *Nanoscale*, **2013**, 5, 9324–9329.
27. Heliatek reported 9% efficiency tandem OPV on foil (<http://www.heliatek.com>).
28. Etgar, L.; Gao, P.; Xue, Z.; Peng, Q.; Chandiran, A. K.; Liu, B.; Nazeeruddin, M. K. and Grätzel, M. *Journal of the American Chemical Society*, **2012**, 134, 17396-17399.
29. Pawley, G. S. *J. Appl. Cryst.*, 1981, 14, 357-361.
30. Coelho, A. A. TOPAS-Academic, Version 4.1, **2007**, see: [http:// www.topas-academic.net](http://www.topas-academic.net).

## 5.3 High efficiency single-junction semitransparent perovskite solar cells

Roldán-Carmona, C.<sup>1,2</sup>; Malinkiewicz, O.<sup>1</sup>; Betancur, R.<sup>3</sup>; Longo, G.<sup>1</sup>; Momblona, C.<sup>1</sup>; Jaramillo, F.<sup>3</sup>; Camacho, L.<sup>2</sup> and Bolink, H.J.<sup>1</sup>

<sup>1</sup> Instituto de Ciencia Molecular, Univ. de Valencia, Catedrático J. Beltrán 2, 46980 Paterna, Spain.

<sup>2</sup> Depart. of Physical Chemistry, Univ. of Cordoba, C. Rabanales, Ed. C3, 14014, Spain

<sup>3</sup> Centro de investigación, innovación y desarrollo de materiales, Univ. de Antioquia, 70, 52-21, Medellín, Colombia

Hybrid organic–inorganic lead halide perovskites have excellent semiconductor properties leading to solar cells with efficiencies surpassing 17%. These perovskite based photovoltaic devices are structurally very similar to organic photovoltaic (OPV) devices enabling the preparation of light weight, thin and color tunable solar devices that can be deposited on a wide variety of substrates. One of the unique applications of the perovskite solar cells is their use in building integrated applications, in particular as facade and window elements, as this would greatly contribute to self-sustaining buildings at low cost. However, this application requires the preparation of efficient semi-transparent perovskite solar cells. Here we present a solar cell employing very smooth thin perovskite layers in combination with thin organic blocking layers reaching average visible transmittances (AVT) as high as 44%. When a semitransparent gold top electrode capped with a dielectric is employed to complete the solar cell, an efficiency of 6.4% and an AVT of 29% are obtained. Even with this non-optimal semi-transparent top electrode, this result demonstrates the potential of perovskite based solar cells for building integrated applications.

Paper published in *Energy & Environmental Science* (DOI: 10.1039/c4ee01389a)

Thin film photovoltaics have attracted much attention as a promising source of renewable energy to reduce the dependencies on fossil and nuclear industries.<sup>1</sup> In the past years, a lot of effort has been devoted to the development of organic photovoltaics (OPV), including new materials and device structures, to provide an alternative to Si-based solar cells. The advantages of OPV include their potential low cost manufacturing, light weight, flexibility and the availability of different materials allowing for colour tuning of the devices.<sup>2-4</sup> In addition, they can be made semitransparent, which allows for specific building integrated elements that could lead to totally self-sustaining buildings at low cost. Even though some breakthroughs in device efficiency have been recently reported, the efficiency of single-junction OPV devices is generally below 10%.<sup>5-8</sup> In the case of semitransparent (ST) solar cells, the use of absorbers with a lower bandgap, in order to shift the absorption spectra to the infrared region, the absence of the light reflecting electrode and the implementation of thin active layers compromise even more the power conversion efficiency (PCE).<sup>9-12</sup>

In order to enhance the performance of ST solar cells, in terms of their average visible transparency (AVT) and PCE, several strategies have been implemented including extensive studies about semitransparent electrodes, tandem devices and recently the implementation of more efficient materials. In the case of transparent electrodes, the most explored material has been thin silver,<sup>8,13,14</sup> also in combination with different capping layers<sup>15-17</sup> or in configurations like Ag grids<sup>18,19</sup> or Ag NWs.<sup>12,20</sup> PEDOT has also been explored as a transparent electrode.<sup>21,22</sup> Finally, other materials like thin Al,<sup>23,24</sup> thin Au,<sup>25,26</sup> ITO,<sup>27,28</sup> graphene<sup>29,30</sup> and CNTs<sup>31-33</sup> have also been tested with more discrete results. Among these studies, considering just single-junction devices with AVT higher than 20%, the top performance was set by Chen et al.<sup>8</sup> who reported 6.2% PCE – 21.2% AVT using a thin silver layer, followed by a study that reported 5.6% PCE – 30% AVT<sup>11</sup> using thin silver and including an external photonic structure for trapping the UV and NIR sunlight, and finally by another study that reported 4.0% PCE – 50% AVT<sup>12</sup> using ITO nanoparticles and Ag NW mixed electrode. A way to increase the performance of these kinds of devices has been the

development of tandem OPVs, for example, Chen et al. obtained a 7% PCE – 30% AVT.<sup>34</sup> However, the complexity of tandem devices impedes their facile integration in low cost applications which is easier to achieve with single-junction devices with improved performances.

An alternative approach to increase the performance of semitransparent photovoltaic devices is to use more efficient materials. Methylammonium lead halide perovskites are an interesting class of materials that have excellent semiconductor properties and have led to very efficient solar cells.<sup>35,36</sup> From the first report by Miyasaka et al.,<sup>37</sup> tremendous progress in the performance of methylammonium lead iodide perovskite based solar cells has been achieved.<sup>38-43</sup> Power conversion efficiencies in excess of 15% have been obtained.<sup>38-40</sup> Most of the highly efficient perovskite solar cells reported until now sandwich the perovskite between a metal oxide layer, such as Al<sub>2</sub>O<sub>3</sub>, TiO<sub>2</sub> or ZrO<sub>2</sub>, and an organic hole transport material. In most cases the organic hole-transporting material (frequently spiro-OMeTAD) is applied on top of the perovskite as a rather thick layer and partially oxidized. The presence of the several hundred nanometer thick partially oxidized hole transport layer leads to parasitic absorption losses, reducing the transparency of the active stack. As a consequence, this would ultimately limit the achievable transparency of semi-transparent devices. Based on this approach, ST perovskite solar cells achieved 3.5% PCE – 30% AVT.<sup>44</sup> Their strategy relied on the dewetting of the perovskite film to create ‘perovskite islands’ achieving a high transmittance due to the voids in the film.

Recently, an alternative device layout where the thickness of continuous perovskite layers can be precisely controlled by thermal evaporation while avoiding the use of materials that induce parasitic absorption was developed.<sup>45</sup> In this layout, the conductive polymer poly(3,4-ethylenedioxythiophene): poly(styrenesulfonic acid) (PEDOT:PSS) is deposited on top of the transparent conductive substrate. PEDOT:PSS has been designed for its transparency in the visible part of the spectrum and with layer thicknesses around 100 nm it has a transmittance of above 90%. In the first examples the perovskite layer was deposited on top of the PEDOT:PSS and capped with a hole blocking/electron transporting layer ([6,6]-phenyl C61- butyric

acid methylester, PCBM<sub>60</sub>) leading to PCEs of 7.4%. Recently, You et al., improved the performance of this configuration reaching a maximum PCE of 11.5%.<sup>46</sup> When besides the hole blocking layer also a thin electron blocking layer is used in between the PEDOT:PSS and the perovskite layer, the device performance is further improved to reach a PCE of 14.8%.<sup>45,47</sup> Hence, the transmittance of this type of solar cell is almost completely determined by the perovskite layer and the two electrodes. An additional advantage of this layout is the absence of metal oxides which facilitates the manufacturing of the cells and makes them compatible with flexible applications and roll to roll (R2R) processing.<sup>46,48</sup>

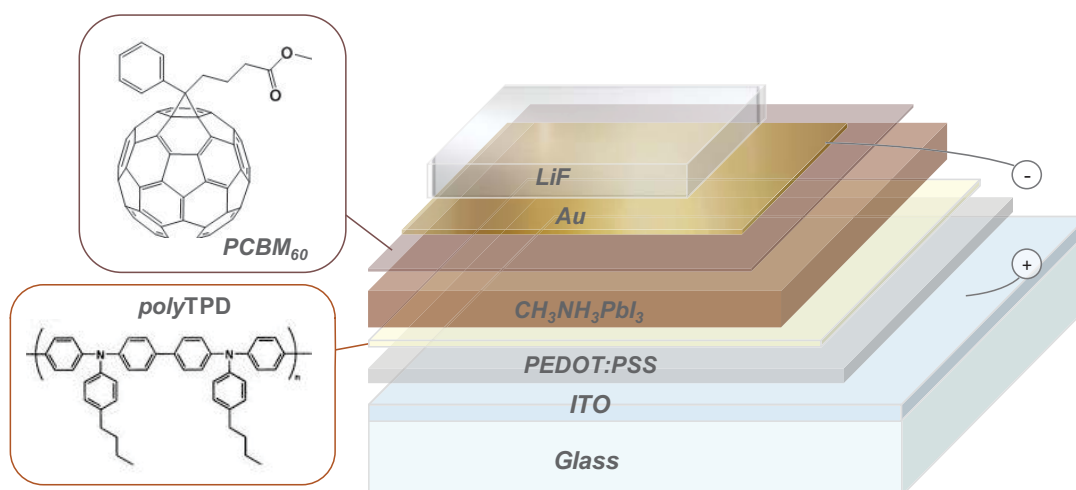


**Fig. 5.9** Schematic layout of the semitransparent solar cell and chemical structures of the organic hole and electron blocking materials

Here we present the development of perovskite semitransparent solar cells reaching 6.4% PCE – 29% AVT and 7.3% PCE – 22% AVT. This successful implementation is based on the robustness of the perovskite evaporation process enabling deposition of continuous layers as thin as 40 nm. The strategy included the implementation of the device layout described above with minimized parasitic absorption and the development of an ultra-thin gold electrode capped with a LiF layer. Such a capping layer was intended to protect the gold layer while

simultaneously reducing the energy lost, by device specular reflection, which resulted in an enhanced device transparency. These results are the best reported to date for semitransparent single-junction solar cells, demonstrating their capability for building integrated photovoltaics and other industrial semitransparent applications.

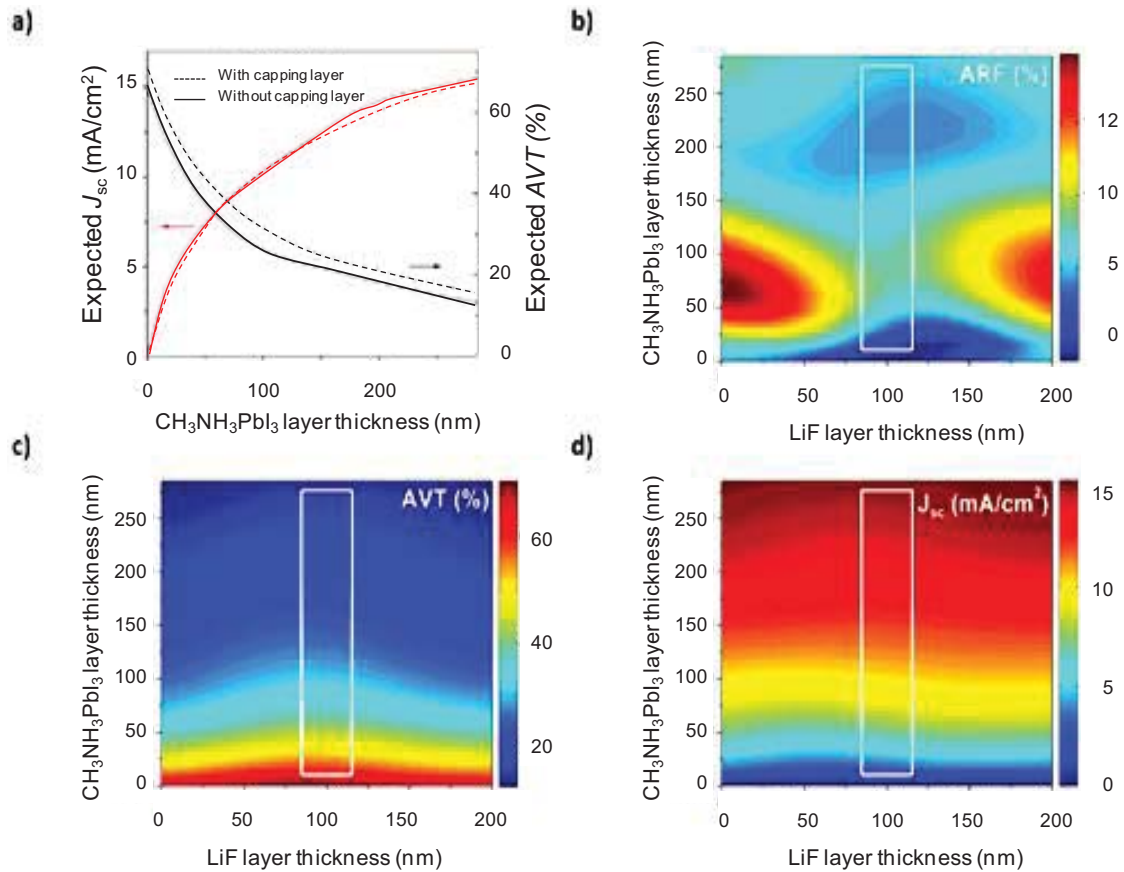


**Fig. 5.10** Optical modelling of the semitransparent perovskite solar cells. (a) Negative-related  $J_{sc}$  (red lines) and AVT (black lines) for a 6 nm thick gold device. The effect of including a 100 nm LiF capping layer is illustrated (dashed lines). In general, such a capping layer modifies the field distribution inside the device, which has an effect on the (b) average reflected sunlight (ARF, 400–800 nm), (c) average visible transmission (AVT, 400–800 nm) and (d) short-circuit current density. The white square encloses the combinations of  $\text{CH}_3\text{NH}_3\text{PbI}_3$  and LiF thicknesses that simultaneously reduce the ARF, enhance the AVT and keep a high  $J_{sc}$ .

The architecture for the semitransparent perovskite device explored in this work is presented in Fig. 5.9. In order to achieve a semitransparent device, the top gold

electrode was designed to be only 6 nm thick. This structure was computationally modelled by employing the transfer matrix formalism,<sup>49,50</sup> where the optical properties of the materials were obtained from the literature or estimated using the method reported by Manificier et al.<sup>51</sup> Fig. 5.10a shows the dependence of  $J_{sc}$  and AVT on the perovskite thickness with and without a protective LiF layer. Clearly, a higher  $J_{sc}$  is theoretically expected for thicker perovskite layers but imply a strongly reduced AVT. Therefore, a trade-off needs to be achieved between the perovskite's inversely related efficiency and sunlight transmission, which implies the sacrificing of either efficiency or transparency as seen in recent related publications.<sup>44</sup> This negative relationship can be partially overcome by exploring optical interference effects inherent to the coherent interaction of sunlight with thin film photovoltaic devices.<sup>52</sup> In particular, the LiF transparent capping layer besides providing protection for the underlying gold layer can be used to modify the electric field distribution inside the device. The optical properties of the different device layers determine that the average sunlight reflected out of the device (ARF) is minimized for the combinations of perovskite and LiF thicknesses enclosed in the white square shown in Fig. 5.10b. Equivalent maps were developed for the expected AVT and  $J_{sc}$  (Fig. 5.10c and d, respectively). From these graphs it is concluded that, for any given thickness of the perovskite layer, a LiF layer around 100 nm thick is optimal for reducing the energy lost by the specular reflection of the device while enabling more transparency and keeping a high  $J_{sc}$  as shown in Fig. 5.10a (dashed lines).

The semitransparent solar cells were prepared by sandwiching the methylammonium lead iodide perovskite between two very thin electron and hole-blocking layers consisting of organic molecules (see Fig. 5.9). First, a 75 nm of poly(3,4-ethylenedioxythiophene): poly(styrenesulfonic acid) (PEDOT:PSS) CLEVIOS P VP Al 4083 from Hereaus was spin-coated on an ITO covered glass substrate. After annealing for 15 minutes at 150 °C, a thin layer of the electron-blocking material poly[N,N'-bis(4-butylphenyl)-N,N'-bis(phenyl)benzidine] (*polyTPD*) from ADSdyesource was deposited (20 nm) from a chlorobenzene solution (7 mg ml<sup>-1</sup>) and then annealed at 180 °C for 30 minutes. This annealing step was required in order to



fix the *poly*TPD and prevent its removal when the hole-blocking layer is deposited on the rather thin perovskite layers from the same solvent. To ensure high purity and high control of the thickness, the  $\text{CH}_3\text{NH}_3\text{PbI}_3$  layers were prepared by the co-evaporation of the two starting materials  $\text{PbI}_2$  and  $\text{CH}_3\text{NH}_3\text{I}$  in a high vacuum chamber as described previously.<sup>45,48</sup> Four different thicknesses (40 nm, 100 nm, 180 nm and 280 nm) were evaluated. Subsequently, a thin layer (20 nm) of the hole-blocking material [6,6]-phenyl C61- butyric acid methylester ( $\text{PCBM}_{60}$ ) Solenne BV was deposited from a chlorobenzene solution,  $10 \text{ mg ml}^{-1}$ , using meniscus coating.<sup>53</sup> The thickness of the layers was verified using both profilometer and absorbance measurements. For non-transparent devices the described stack was covered by a 70 nm gold layer deposited using vacuum evaporation. In the case of semitransparent devices, an alternative top electrode is required that is conductive and has high transparency. In addition, the top electrode and its deposition method should be compatible with the device stack. Therefore, only top electrodes prepared by evaporation of metals and dielectrics were considered (Fig. S5.1†). The optimum gold layer had a thickness of 6 nm, as it showed good homogeneity and acceptable conductivity and transparency values. This gold layer is considerably thinner than previously reported semitransparent gold layers in ST perovskite devices,<sup>44</sup> which leads to a reduction in the parasitic absorption induced by metallic layers. As predicted by the optical model, this ultra-thin layer of Au (6 nm) was capped by a 100 nm layer of lithium fluoride (LiF) to enhance the device optically. This LiF layer also protected the cell allowing for easier handling. More details of the device fabrication and characterization are provided in the ESI.†

The robustness of thermal evaporation to grow perovskite layers in a wide range of thicknesses is crucial to the development of these semitransparent perovskite solar cells. Indeed, the resulting  $\text{CH}_3\text{NH}_3\text{PbI}_3$  layers showed very high crystallinity and uniformity as evidenced by grazing incidence X-ray diffraction (GIXRD) and scanning electron microscopy. As shown in Fig. 5.11a, despite their thicknesses, all the deposited perovskite layers showed high crystallinity reaching an excellent fit to a one-phase model with a tetragonal cell ( $a = 8.80(2)$ ,  $c = 12.57(2) \text{ \AA}$ ) and space group

14/cm. Additionally, high film uniformity is apparent from the SEM pictures presented in Fig. 5.11b.

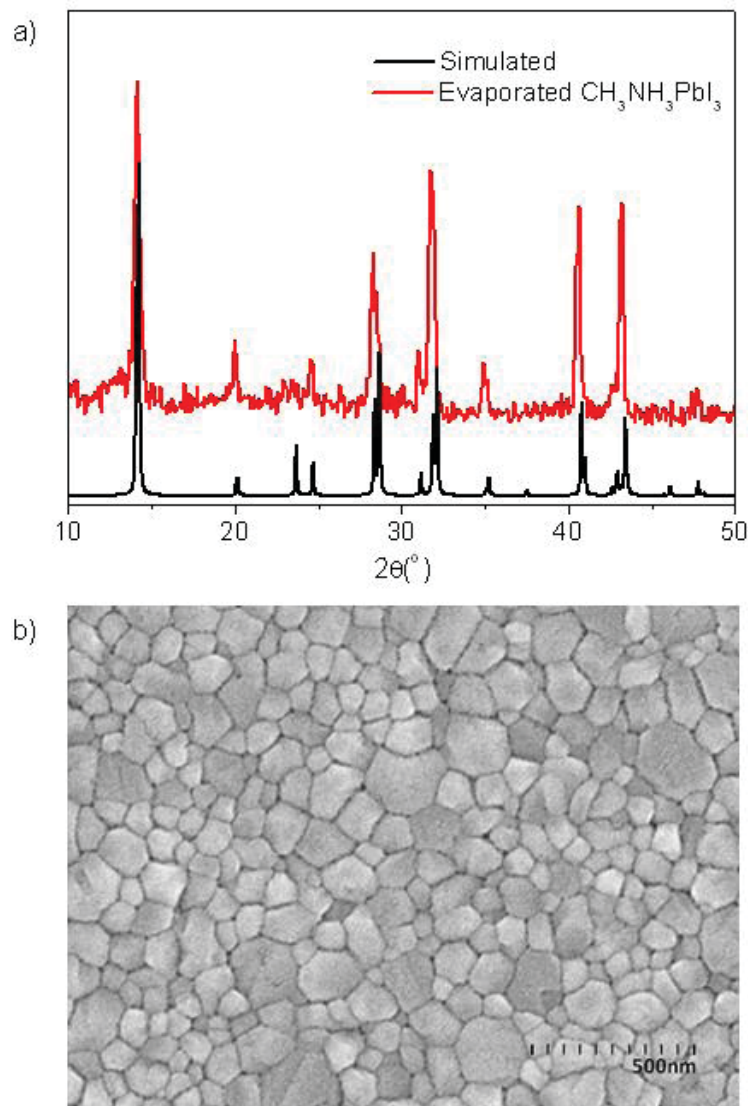


**Fig. 5.11** (a) Grazing incidence X-ray diffraction (GIXRD) pattern of a typical evaporated  $\text{CH}_3\text{NH}_3\text{PbI}_3$  film. As a reference, the simulated perovskite pattern with preferred orientation along the (100) and (001) directions is also presented. (b) SEM picture of a typical evaporated perovskite layer of 200 nm.

The transmittance of the layers including the glass substrate (device without top electrode), the ST top contact and the completed ST device are depicted in Fig. S5.2† for a perovskite thickness of 100 nm. Clearly, the ST top electrode reduces significantly the transmittance of the complete device. The transmittance spectra for

the completed ST device employing different perovskite layer thicknesses are shown in Fig. 5.12a.

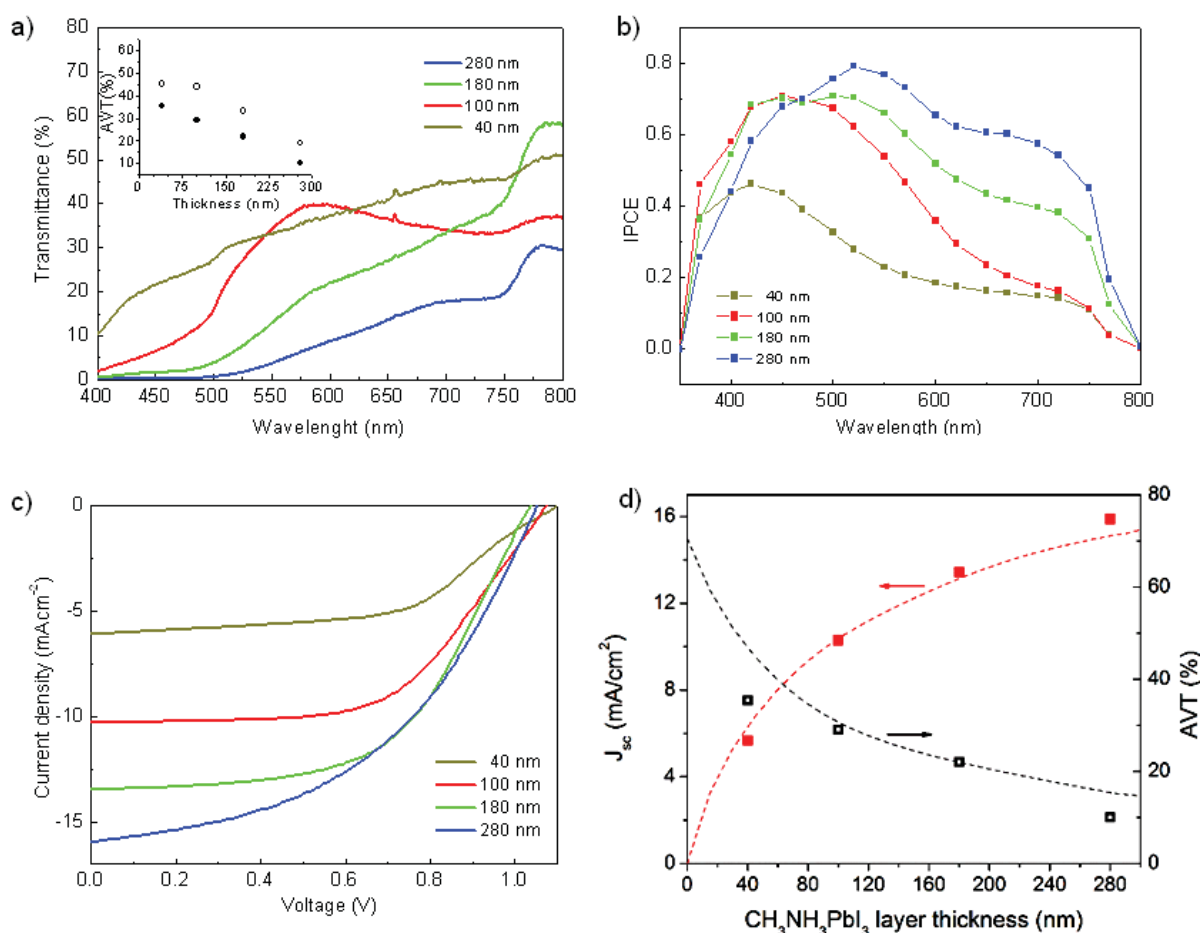


**Fig. 5.12** (a) Transmittance spectra through the complete device for different perovskite layer thicknesses. The inset shows the AVT values for the devices with (filled circle) and without (open circles) the ST electrode. (b) IPCE spectrum. (c) J–V characteristics of the best semitransparent devices comprising the Au/LiF electrode for different perovskite thicknesses. (d) Comparison between the experimentally obtained AVT (black open squares) and  $J_{sc}$  (red full squares) with the optical modelling (dashed lines).

As expected the transmission increases with reducing perovskite layer thickness, although not completely linearly in function of the film thickness probably due to slight changes in the perovskite optical properties depending on its particular evaporation process. To highlight the effect of the different perovskite thicknesses on the transparency of the device, the values for the AVT of the device stacks with and without the ST top electrode are given (inset Fig. 5.12a). Such AVT is taken as the

average of the transmittance in the visible region of the spectra between 400 and 800 nm. The stack layout (without top electrode) leads to good transmittance when the thickness is below 200 nm, showing an AVT of 44% for a perovskite thickness of 100 nm. Thicker perovskite films lead to an important decrease in transmittance, reducing the AVT value to 19% for films with a thickness of 280 nm. The completed device with a perovskite layer thickness of 100 nm has an AVT close to 30%, which is high enough for many applications. Fig.5.12c shows the current density versus voltage ( $J-V$ ) characteristics for the described cells with  $0.12 \text{ cm}^2$  active area under light intensities of  $100 \text{ mW cm}^{-2}$ . It is important to mention that the curves are the same under forward and reverse scan directions and as such do not display hysteresis.

The results show a decrease in the current density when the active layer thickness decreases. This is expected as less light is absorbed and as a consequence fewer charges can be photogenerated. This trend is also seen in the IPCE graph (Fig. 5.12b) where the most notable decrease is observed in the red region of the spectra. The key performance parameters deduced from Fig. 5.12 for the different devices are depicted in Table 5.2. Additionally, an informative table including average values and standard deviation for the most important parameters can be found in the ESI, Table S5.2.†

Finally, Fig. 5.12d presents a comparison between the experimentally obtained parameters and the optically modelled ones. A reasonably good fitting was achieved. Only small discrepancies appeared for AVT in the case of the 40 and 280 nm thick perovskite devices, which could be due to slight changes in their thicknesses or due to the above mentioned small variations in the optical properties of the deposited perovskite layers. All the devices exhibited a yellowish/brown tonality with considerably good agreement with optical modelling (Fig. S5.3†). The 40 nm thick perovskite device displayed the most neutral color (0.36; 0.37), and future studies could be addressed to develop optical strategies to tune such tonalities.

In the optical computer simulation, the IPCE was modeled as  $\text{IPCE} = \Phi \eta_{\text{abs}}(\lambda)$ ,<sup>50</sup> where  $\eta_{\text{abs}}(\lambda)$  is related to the efficiency in absorbing the sunlight and the wavelength-

independent parameter  $\Phi$  is associated with the exciton diffusion efficiency, charge separation efficiency, charge transport efficiency and final charge collection efficiency. The final fitting of this parameter, after matching the experimental and computer modelled  $J_{sc}$ , resulted to be 0.9, which indicates the excellent exciton and charge conductivity properties of the perovskite layers.

	$J_{sc}$ (mA cm <sup>-2</sup> )	$V_{oc}$ (V)	FF	PCE (%)	AVT <sup>a</sup> (%)	AVT <sup>b</sup> (%)
40 nm	5.66	1.037	57.7	3.39	35.4	45
100 nm	10.30	1.074	57.9	6.41	29	44
180 nm	13.43	1.037	52.5	7.31	22	33
280 nm	15.88	1.052	46.	7.73	10	19

**Table 5.2** Most important parameters for the best studied semitransparent solar cells. The symbol <sup>a</sup> indicates the average transmittance values through the whole device, while <sup>b</sup> are the average transmittance values without the top semitransparent electrode.

As a result, power conversion efficiencies as high as 6.4% for devices with an AVT of 30% were achieved. This is amongst the highest values reported for semitransparent single-junction cells. Most of the devices lead to quite high  $J_{sc}$  (10 to 16 mA cm<sup>-2</sup>). The  $V_{oc}$  is almost not affected by the thickness of the active layer and remains above 1 V in all the cells. The fill factor (FF) is good for the thin devices, reaching values of 60%, but with increasing perovskite layer thickness it decreases to around 45%. The reduction of the FF of the cells with thicker perovskite layers is likely caused by the limited conductivity of the ST top electrode. Comparison experiments were performed with the same perovskite layer but with a thicker (70 nm) top electrode, and these non-transparent devices had slightly higher current densities and FF around 60% (see Table S5.2† of the ESI†).

The obtained 100 nm or 180 nm perovskite cells present one of the best performances reported for semitransparent single-junction solar cells achieving power conversion efficiencies as high as 6.4% and 7.3%, respectively. A photograph of a typical semitransparent solar cell is shown in Fig. 5.13. Typical samples look yellowish/light brown depending on the perovskite thickness (see ESI, Fig. S5.3†).

More importantly, this work shows a clear route to develop high performance ST solar cells.



**Fig. 5.13** Photograph of the semitransparent solar cell having a 100 nm perovskite layer resulting in an AVT  $\sim$  30% and a PCE of 6.4%.

## Conclusions

We have successfully prepared highly efficient semitransparent solar cells based on methylammonium lead iodide perovskite layers sandwiched between two organic charge transport layers. A simple cell configuration, which does not require high temperature processes, leads to semitransparent cells with AVT close to 22% and 29% through the complete device, and high power conversion efficiencies of 7.3% and 6.4%, respectively. These results are among the best performances reported to date for single ST solar cells and are fundamentally based on the successful development of thin uniform perovskite layers by thermal evaporation. In addition, the implementation of an ultra-thin gold layer as electrode helped in minimizing its parasitic absorption, and the introduction of a LiF capping layer was crucial in reducing the energy lost through device specular reflection, thus enhancing device transparency without affecting the photon harvesting in the active layer. Furthermore, better performances are expected by implementing these ideas with even better semitransparent electrodes.

## Supporting information

### 1. Methods

#### Materials

Aqueous dispersions of poly(3,4-ethylenedioxythiophene) doped with poly(styrenesulfonate) (PEDOT:PSS, CLEVIOS P VP Al 4083) were obtained from Heraeus Holding GmbH and used as received. Poly[N,N'-bis(4-butylphenyl)-N,N'-bis(phenyl)benzidine] (poly-TPD) was purchased from ADS Dyesource. PbI<sub>2</sub> was purchased from Aldrich and used as is, CH<sub>3</sub>NH<sub>3</sub>I was prepared similar to a previously published method<sup>1</sup>, in brief: *CH<sub>3</sub>NH<sub>3</sub>I, was synthesized by reacting 21.6 ml methylamine (40%wt in water, Aldrich) and 30 ml hydroiodic acid (57 wt% in water, Aldrich) in a 250 ml round-bottomed flask at 0 °C for 2 h with stirring. The white precipitate was recovered by evaporation at 50 °C for 1 h. The product, methylammonium iodide (CH<sub>3</sub>NH<sub>3</sub>I), was dissolved in ethanol, filtered and recrystallized from diethyl ether, and dried at 60 °C in a vacuum oven for 24 h.*

#### Device preparation

Devices were prepared on a photolithographically patterned ITO on glass substrates, by spincoating a thin layer of PEDOT:PSS from the commercial aqueous dispersion (1000rpm 30sec and a short annealing at 150 °C result in 75 nm thickness). On top of this layer a thin film of polyTPD was deposited from a chlorobenzene solution (7 mg ml<sup>-1</sup>) using spincoating. Then the substrates were annealed at 180 °C during 30 minutes and transferred to a vacuum chamber integrated into an inert glovebox (MBraun, <0.1 ppm O<sub>2</sub> and <0.1 ppm H<sub>2</sub>O) and evacuated to a pressure of  $1 \times 10^{-6}$  mbar. The sublimation of the perovskite was performed using a vacuum chamber of MBraun integrated in an inert glovebox (MBraun) as previously reported<sup>45</sup>. The PCBM60 layer was deposited using a chlorobenzene solution of 10 mg ml<sup>-1</sup> in ambient conditions using a meniscus coater and a coating speed of 10 mm/second. The device was completed by the thermal evaporation of the top

semitransparent electrode under a base pressure of  $2 \times 10^{-6}$  mbar. The solar cells (active area of 0.12 cm<sup>2</sup>) were characterized inside the inert glovebox.

## Device characterization

Solar cells were illuminated by a white light halogen lamp in combination with interference filters for the EQE and  $J$ - $V$  measurements (MiniSun simulator by ECN the Netherlands). A black mask with openings matching the active cell area was used to limit the active area of the device. Before each measurement, the exact light intensity was determined using a calibrated Si reference diode. An estimation of the short-circuit current density ( $J_{sc}$ ) under standard test conditions was calculated by convolving the EQE spectrum with the AM1.5G reference spectrum, using the premise of a linear dependence of  $J_{sc}$  on light intensity. Current-voltage ( $J$ - $V$ ) characteristics were measured using a Keithley 2400 source measure unit. All characterization was done in a nitrogen filled glove box (<0.1 ppm O<sub>2</sub> and <0.1 ppm H<sub>2</sub>O) without exposure to ambient atmosphere.

## 2. Electrode transmittance measurements

Different cathodes were prepared in order to use the most appropriate to our cell configuration. All of them consisted on an evaporated mixture of metals, metals and oxides, as well as the lithium fluoride salt. Due to the better performance of our solar cells when using gold as the cathode, it was used as the seed layer in most of the cases. The transmittance of the studied cathodes is shown in Fig. S5.1.



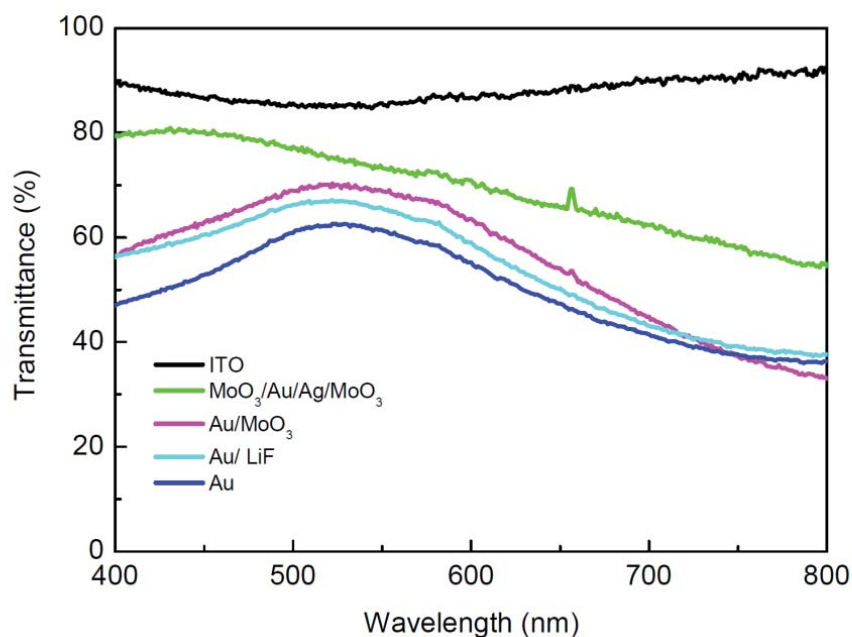


**Fig. S5.1.** Transmittance spectra for the different semitransparent electrodes. The presence of LiF and MoO<sub>3</sub> increases slightly the transmittance referred to the 6 nm gold. ITO electrode is also included as a reference.

**Table S5.1.** Most important parameters of non-optimized semitransparent solar cells with the following configuration: ITO/PEDOT:PSS/PolyTPD/Perovskite/PCBM60/ST electrode for an active layer thickness of 250nm.

ST electrode	$J_{sc}$ (mA cm <sup>-2</sup> )	$V_{oc}$ (V)	FF	PCE (%)	AVT <sup>1</sup> (%)
Au (6nm)	14.0	1.019	45.8	6.6	52
Au (6nm)/ LiF (100nm)	13.5	1.035	46.2	6.4	56
Au (6nm)/MoO <sub>3</sub> (15nm)	5.2	0.929	27.6	1.4	59
MoO <sub>3</sub> (3nm)/Au(1nm)/Ag(6nm)/MoO <sub>3</sub> (5nm) <sup>5</sup>	9.5	0.915	9.9	0.9	71

<sup>1</sup> Average transmittance for the electrode

### 3. Perovskite film characterization

#### Grazing incidence X-ray diffraction (GIXRD)

After the evaporation of the perovskite the films were characterized by using grazing incidence X-ray diffraction (GIXRD). The data were collected at room temperature in the  $2\theta$  range 5–50 ° on an Empyrean PANalytical powder

diffractometer, using Cu K $\alpha$ 1 radiation. In Fig. 5.10a a typical diffractogram for the thin perovskite layer is shown. Typically four repeated measurements were collected and merged into a single diffractogram. Pawley refinements<sup>55</sup>, were performed using the TOPAS computer program<sup>56</sup> and revealed an excellent fit to a one-phase model with a tetragonal cell ( $a = 8.80(2)$ ,  $c = 12.57(2)$  Å) and space group I4/ cm.

## Scanning Electron Microscopy

Perovskite film morphology was investigated using a high-resolution scanning electron microscope (MERLIN, Zeiss) and micrographs were acquired using an in-lens secondary electron detector (Fig. 5.10b).

## 4. Performance of perovskite solar cells with 70nm Au as cathode

Comparison experiments were performed with the same device structure and perovskite layer thicknesses but using a thicker (70 nm) top electrode. Table S5.2 summarizes the most important parameters of these cells including average values and standard deviation of more than 35 devices for both ST and standard devices.

**Table S5.2.** Key parameters of the perovskite solar cells with the ST and the thick gold electrodes as cathodes. Devices were prepared with the following configuration: ITO/PEDOT:PSS/PolyTPD/Perovskite/PCBM<sub>60</sub>/Cathode.

Perovskite thickness	$J_{sc}$ (mA cm <sup>-2</sup> )	$V_{oc}$ (mV)	FF	PCE (%)	AVT <sup>1</sup> (%)
<b>6nm Au/ 100nm LiF</b>					
40 nm	5.8 ± 0.2	1009 ± 27	57 ± 1	3.4 ± 0.1	45
100 nm	10.3 ± 0.2	1072 ± 2	57 ± 1	6.3 ± 0.2	44
180 nm	14.1 ± 0.6	1034 ± 3	47 ± 5	6.9 ± 0.5	33
280 nm	15.5 ± 0.6	1047 ± 7	44 ± 3	7.1 ± 0.7	19
<b>70 nm Au</b>					
100 nm	10.3 ± 0.2	1066 ± 2	58 ± 1	6.9 ± 0.3	44
180 nm	17.6 ± 0.7	1088 ± 4	61 ± 2	11.6 ± 0.5	33

<sup>1</sup> Average transmittance for the device without the metallic cathode

In the case of devices prepared using 70 nm Au the main difference when decreasing the perovskite thickness is the lower current density that the devices produce, as the FF and  $V_{OC}$  are almost not affected when using active layers thicknesses above 100 nm. Nevertheless, there is an important decrease for the 40 nm devices, which affects strongly the device performance. The best efficiencies are obtained for 180 nm and 250 nm perovskite films, leading to values of PCE close to 12%. Comparing these results with the obtained for the ST cells it is evident the limitation that the ST electrode may have in the current density during the device operation, lowering the resulting FF. Moreover, the device with 180 nm of active layer shows a high value for PCE and AVT of 33 % without the top electrode. These results suggest that really high efficiencies could be achieved with a proper semitransparent electrode.

## 5. Transmittance spectra for optimized device

The transmittance spectra through a typical semitransparent solar cell with the best semitransparent electrode (Au/LiF) and 100 nm of perovskite thickness is shown in Fig. S5.2.

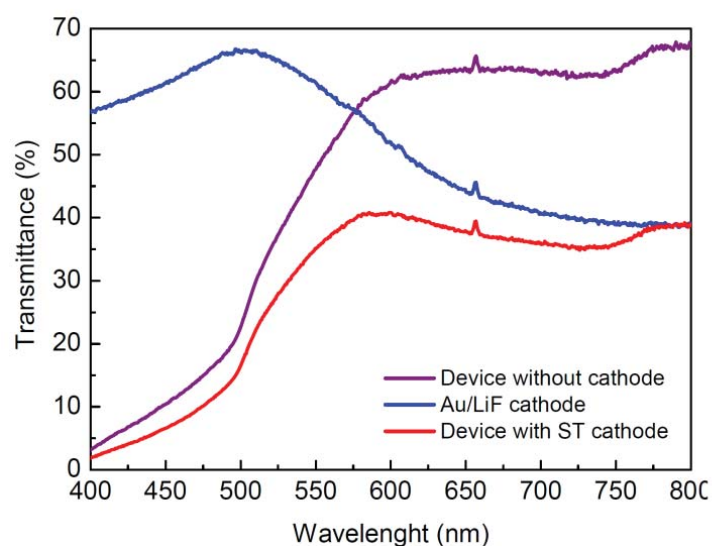


**Fig. S5.2.** Transmittance spectra for the device without top electrode, the semitransparent (ST) top contact and the completed device with ST top contact using a perovskite layer thickness of 100 nm.

## 6. Chromaticity coordinates for the semitransparent devices

The color calculation of both actual and simulated devices is based on the determination of the CIE 1931 chromaticity coordinates  $x$  and  $y$ . Given the devices transmittance  $T(\lambda)$  and taking as reference the daytime  $D65(\lambda)$  standard illuminant,<sup>57</sup> the  $X$ ,  $Y$  and  $Z$  tristimulus values are calculated as follows:<sup>58</sup>

$$\begin{aligned} X &= \frac{1}{N} \int_{\lambda} \bar{x}(\lambda) T(\lambda) I(\lambda) d\lambda \\ Y &= \frac{1}{N} \int_{\lambda} \bar{y}(\lambda) T(\lambda) I(\lambda) d\lambda \\ Z &= \frac{1}{N} \int_{\lambda} \bar{z}(\lambda) T(\lambda) I(\lambda) d\lambda \end{aligned}$$

Where  $\bar{x}(\lambda)$ ,  $\bar{y}(\lambda)$  and  $\bar{z}(\lambda)$  are the CIE standard observers functions. Finally, the chromaticity coordinates are directly calculated as:

$$\begin{aligned} x &= \frac{X}{X + Y + Z} \\ y &= \frac{Y}{X + Y + Z} \end{aligned}$$

Fig. S5.3 shows the CIE( $x,y$ ) calculated for the semitransparent devices using both the transmission spectra of the experimental devices and the predicted ones in the optical modeling.

All devices exhibited a yellowish/brown tonality with considerably good agreement with the optical modeling. The 40 nm thick perovskite device displays the most neutral color (0.36; 0.37) and future works could be addressed to develop optical strategies to tune such tonalities.

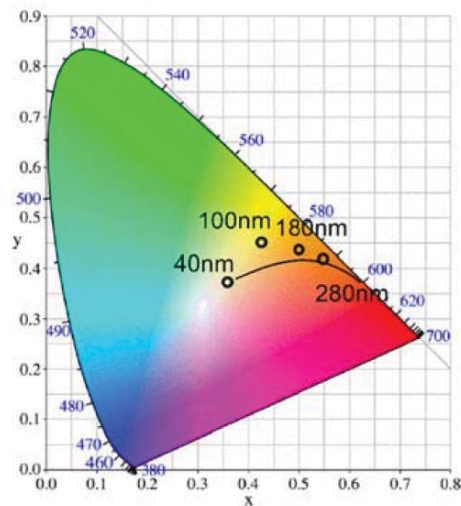


**Fig. S5.3.** b) CIE 1931 color coordinates calculated using the transmission spectra of the experimental devices (black circles), and the transmission spectra predicted in the optical modeling (solid line).

## Acknowledgements

We are grateful to Jorge Ferrando and Alejandra Soriano for technical assistance. This work has been supported by the Spanish Ministry of Economy and Competitiveness (MINECO) (MAT2011-24594), the Generalitat Valenciana (Prometeo/2012/ 053). C.R.-C. would like to thank the MINECO for the financial support of this research in the framework of project CTQ2010- 17481, the Junta de Andalucía (CICyE) for special financial support (P10-FQM-6703) and the MECED (Spanish Ministry of Education, Culture, and Sport) for a FPU grant. F.J. and R.B. thank the program “Estrategia de Sostenibilidad 2013–2014 de la Universidad de Antioquia” and Empresas Públicas de Medellín-EPM for funding the optical simulation of the project. Additionally, F.J. and R.B. thank Jordi Martorell for useful guidance in the development of the optical modeling of the photovoltaic devices.

## References

1. Darling, S. B. and You, F. *RSC Adv.* 2013, 3, 17633–17648.
2. Chung, I.; Lee, B.; He, J.; Chang, R. P. H. and Kanatzidis, M. G. *Nature*, 2012, 485, 486–489.
3. Li, G.; Zhu, R. and Yang, Y. *Nat. Photonics*, 2012, 6, 153–162.
4. You, J.; Dou, L.; Yoshimura, K.; Kato, T.; Ohya, K.; Moriarty, T.; Emery, K.; Chen, C.-C.; Gao, J.; Li, G. and Yang, Y. *Nat. Commun.*, 2013, 4, 1446.
5. He, Z.; Zhong, C.; Su, S.; Xu, M.; Wu, H. and Cao, Y. *Nat. Photonics*, 2012, 6, 591–595.
6. Zhang, D.-D.; Jiang, X.-C.; Wang, R.; Xie, H.-J.; Ma, G.-F.; Ou, Q.-D.; Chen, Y.-L.; Li, Y.-Q. and Tang, J.-X. *ACS Appl. Mater. Interfaces*, 2013, 5, 10185–10190.
7. Beiley, Z. M.; Christoforo, M. G.; Gratia, P.; Bowring, A. R.; Eberspacher, P.; Margulis, G. Y.; Cabanetos, C. ; Beaujuge, P. M.; Salleo, A. and McGehee, M. D. *Adv. Mater.*, 2013, 25, 7020–7026.
8. Chen, K.-S.; Salinas, J.-F.; Yip, H.-L.; Huo, L.; Hou, J. and Jen, A. K. Y. *Energy Environ. Sci.*, 2012, 5, 9551–9557.
9. Zhang, H.; Wicht, G.; Gretener, C.; Nage, M.; Nüesch, F.; Romanyuk, Y.; Tisserant, J.-N. and Hany, R. *Sol. Energy Mater. Sol. Cells*, 2013, 118, 157–164.
10. Kim, H. P. ; Lee, H. J. ; Bin, A. R. ; Yusoff, M. and Jang, J. *Sol. Energy Mater. Sol. Cells*, 2013, 108, 38–43.
11. Betancur, R.; Romero-Gomez, P.; Martinez-Otero, A.; Elias, X.; Maymo, M. and Martorell, J. *Nat. Photonics*, 2013, 7, 995– 1000.
12. Chen, C.-C.; Dou, L.; Zhu, R.; Chung, C.-H.; Song, T.-B.; Zheng, Y. B.; Hawks, S.; Li, G.; Weiss, P. S. and Yang, Y. *ACS Nano*, 2012, 6, 7185–7190.

13. Bailey-Salzman, R. F.; Rand, B. P. and Forrest, S. R. *Appl. Phys. Lett.*, 2006, 88, 233502.
14. Chen, C.-C.; Dou, L.; Zhu, R.; Chung, C.-H.; Song, T.-B.; Zheng, Y. B.; Hawks, S.; Li, G.; Weiss, P. S. and Yang, Y. *ACS Nano*, 2012, 6, 7185–7190.
15. Galagan, Y.; Debiije, M. G. and Blom, P. W. M. *Appl. Phys. Lett.*, 2011, 98, 043302.
16. Han, S.; Lim, S.; Kim, H.; Cho, H. and Yoo, S. *IEEE J. Sel. Top. Quantum Electron.*, 2010, 16, 1656–1664.
17. Meiss, J.; Holzmueller, F.; Gresser, R.; Leo, K. and Riede, M. *Appl. Phys. Lett.*, 2011, 99, 193307.
18. Ameri, T.; Dennler, G.; Waldauf, C.; Azimi, H.; Seemann, A.; Forberich, K.; Hauch, J.; Scharber, M.; Hingerl, K. and Brabec, C. J. *Adv. Funct. Mater.* 2010, 20, 1592–1598.
19. Seemann, A.; Egelhaaf, H. J.; Brabec, C. J. and Hauch, J. A. *Org. Electron.*, 2009, 10, 1424–1428.
20. Lee, J.-Y.; Connor, S. T.; Cui, Y. and Peumans, P. *Nano Lett.*, 2010, 10, 1276–1279.
21. Colsmann, A.; Reinhard, M.; Kwon, T.-H.; Kayser, C.; Nickel, F.; Czolk, J.; Lemmer, U.; Clark, N.; Jasieniak, J.; Holmes, A. B. and Jones, D. *Sol. Energy Mater. Sol. Cells*, 2012, 98, 118–123.
22. Czolk, J.; Puetz, A.; Kutsarov, D.; Reinhard, M.; Lemmer, U. and Colsmann, A. *Adv. Energy Mater.*, 2013, 3, 386–390.
23. Colsmann, A.; Puetz, A.; Bauer, A.; Hanisch, J.; Ahlswede, E. and Lemmer, U. *Adv. Energy Mater.*, 2011, 1, 599–603.

24. Bauer, A.; Wahl, T.; Hanisch, J. and Ahlswede, E. *Appl. Phys. Lett.*, 2012, 100, 073307.
25. Li, G.; Chu, C. W.; Shrotriya, V.; Huang, J. and Yang, Y. *Appl. Phys. Lett.*, 2006, 88, 253503.
26. Shrotriya, V.; Wu, E. H.-E.; Li, G.; Yao, Y. and Yang, Y. *Appl. Phys. Lett.*, 2006, 88, 064104.
27. Schmidt, H.; Flügge, H.; Winkler, T.; Bülow, T.; Riedl, T. and Kowalsky, W. *Appl. Phys. Lett.*, 2009, 94, 243302.
28. Huang, J.; Li, G. and Yang, Y. *Adv. Mater.*, 2008, 20, 415–419.
29. Liu, Z.; Li, J.; Sun, Z.-H.; Tai, G.; Lau, S.-P. and Yan, F. *ACS Nano*, 2011, 6, 810–818.
30. Lee, Y.-Y.; Tu, Yu, C.-C.; Li, S.-S.; Hwang, J.-Y.; Lin, C.-C.; Chen, K.-H.; Chen, L.-C.; Chen, H.-L. and Chen, C.-W. *ACS Nano*, 2011, 5, 6564–6570.
31. Tanaka, S.; Zakhidov, A. A.; Ovalle-Robles, R.; Yoshida, Y.; Hiromitsu, I.; Fujita, Y. and Yoshino, K. *Synth. Met.*, 2009, 159, 2326–2328.
32. Xia, X.; Wang, S.; Jia, Y.; Bian, Z.; Wu, D.; Zhang, L.; Cao, A. and Huang, C. *J. Mater. Chem.*, 2010, 20, 8478–8482.
33. Kim, Y. H.; Müller-Meskamp, L.; Zakhidov, A. A.; Sachse, C.; Meiss, J.; Bikova, J.; Cook, A.; Zakhidov, A. A. and Leo, K. *Sol. Energy Mater. Sol. Cells*, 2012, 96, 244–250.
34. Chen, C.-C.; Dou, L.; Gao, J.; Chang, W.-H.; Li, G. and Yang, Y. *Energy Environ. Sci.*, 2013, 6, 2714–2720.
35. Kagan, C. R.; Mitzi, D. B. and Dimitrakopoulos, C. D. *Science*, 1999, 286, 945–947.



36. Kaltenbrunner, M.; White, M. S.; Głowacki, E. D.; Sekitani, T.; Someya, T.; Sariciftci, N. S. and Bauer, S. *Nat. Commun.*, 2012, 3, 770.
37. Kojima, A.; Teshima, K.; Shirai, Y. and Miyasaka, T. *J. Am. Chem. Soc.*, 2009, 131, 6050–6051.
38. Wang, J. T.-W.; Ball, J. M.; Barea, E. M.; Abate, A.; Alexander-Webber, J. A.; Huang, J.; Saliba, M.; Mora-Sero, I.; Bisquert, J.; Snaith, H. J. and Nicholas, R. J. *Nano Lett.*, 2014, 14, 724–730.
39. Liu, D. and Kelly, T. L. *Nat. Photonics*, 2014, 8, 133–138.
40. Liu, M.; Johnston, M. B. and Snaith, H. J. *Nature*, 2013, 501, 395–398.
41. Burschka, J.; Pellet, N.; Moon, S.-J.; Humphry-Baker, R.; Gao, P.; Nazeeruddin, M. K. and Gratzel, M. *Nature*, 2013, 499, 316–319.
42. Ball, J. M.; Lee, M. M.; Hey, A. and Snaith, H. J. *Energy Environ. Sci.*, 2013, 6, 1739–1743.
43. Lee, M. M.; Teuscher, J.; Miyasaka, T.; Murakami, T. N. and Snaith, H. J. *Science*, 2012, 338, 643–647.
44. Eperon, G. E.; Burlakov, V. M.; Goriely, A. and Snaith, H. J. *ACS Nano*, 2014, 8, 591–598.
45. Malinkiewicz, O.; Aswani, Y.; Lee, Y. H.; Minguéz Espallargas, M.; Graetzel, M.; Nazeeruddin, M. K. and Bolink, H. J. *Nat. Photonics*, 2014, 8, 128.
46. You, J.; Hong, Z.; Yang, Y.; Chen, Q.; Cai, M.; Song, T.-B.; Chen, C.-C.; Lu, S.; Liu, Y.; Zhou, H. and Yang, Y. *ACS Nano*, 2014, 8(2), 1674–1680.
47. Malinkiewicz, O.; Roldán-Carmona, C.; Soriano, A.; Bandiello, E.; Camacho, L.; Nazeeruddin, M. K. and Bolink, H. J. *Adv. Energy Mater.*, 2014, DOI: 10.1002/aenm.201400345.

48. Roldan-Carmona, C.; Malinkiewicz, O.; Soriano, A.; Minguez Espallargas, G.; Garcia, A.; Reinecke, P.; Kroyer, T.; Dar, M. I.; Nazeeruddin, M. K. and Bolink, H. J. *Energy Environ. Sci.*, 2014, 7, 994.
49. Pettersson, L. A. A.; Roman, L. S. and Inganas, O. *J. Appl. Phys.*, 1999, 86, 487–496.
50. Betancur, R. Doctoral dissertation, 2013.
51. Manificier, J. C.; Gasiot, J. and Fillard, J. P. *J. Phys. E: Sci. Instrum.*, 1976, 9, 1002.
52. Niggemann, M.; Riede, M.; Gombert, A. and Leo, K. *Phys. Status Solidi A*, 2008, 205, 2862–2874.
53. Malinkiewicz, O.; Lenes, M.; Brine, H. and Bolink, H. J. *RSC Adv.*, 2012, 2, 3335–3339.
54. Etgar, L.; Gao, P.; Xue, Z.; Peng, Q.; Chandiran, A. K.; Liu, B.; Nazeeruddin, M. K. and Grätzel, M. *Journal of the American Chemical Society*, **2012**, 134, 17396–17399.
55. Pawley, G. S. *J. Appl. Cryst.*, **1981**, 14, 357–361.
56. Coelho, A. A. TOPAS-Academic, Version 4.1, **2007**, see: [http:// www.topas-academic.net](http://www.topas-academic.net)
57. Commission Internationale De L'eclairaige (2013).
58. Betancur, R. (2013). Photon control in nano structured organic photovoltaic materials (Doctoral dissertation, Universitat Politècnica de Catalunya Barcelona).

## **Chapter 6**

### **Overview of the main results**



## 6.1 Physical control of thin films at the air-water interface (Chapter 3)

In Chapter 3 two surface techniques have been analyzed and pointed out as very useful for the study of organized Langmuir monolayers containing absorbing polar head-groups. Additionally, mixed Langmuir and Langmuir-Schaefer monolayers with an amphiphilic Ir-complex and a water-soluble porphyrin derivative have been prepared, allowing the characterization and study of intermolecular energy transference between both units.

The firstly studied surface technique has been the Brewster Angle Microscopy (BAM) which is a powerful technique that allows the in situ visualization in situ of the Langmuir monolayer. Traditionally, the information provided by this technique has been related with the organization of the alkyl chains of the molecules, neglecting the influence that the polar head-group could have in the reflectivity. Nevertheless, in this work the influence of the molecular arrangement of the polar headgroup has been pointed out by analyzing the monolayer using a two layer model, where both the hydrophobic and the polar regions are considered. Four different scenarios have been analyzed as a function of the size and the absorption from the polar headgroup: small and nonabsorbent groups (Scenario I), large and nonabsorbent groups (Scenario II), small and absorbent groups (Scenario III) and large and absorbent groups (Scenario IV). By comparing the results obtained from the two layer model and the traditional model, the relative increase on reflection provoked by the polar headgroup was obtained ( $\Delta R_p/R$ ).

The results obtained showed that the traditional model is suitable for Scenario I, when simple amphiphilic molecules are used, such as long chain esters, alcohols or amines. In such a situation the relative increase on reflection was only  $\sim 24\%$ . However, when the polar headgroup was larger the same model led to very significant differences. In this case, the relative increase in reflection was  $\sim 85\%$  suggesting that

the reflection provoked by the alkyl chain in such situation was not so relevant as that of the polar headgroup.

Scenario	$n_{\text{chains}}$	$d_{\text{chains}}$ , nm	$n_{\text{polar}}$	$d_{\text{polar}}$ , nm	$k$	$R \times 10^5$	$\Delta R_p/R$ %
I			1.4	0.4	0	0.099	24.2
II	1.42	2	1.6	0.8	0	0.494	84.8
III			1.4	0.4	0.5	0.158	54.4
IV			1.6	0.8	0.5	1.304	94.3

**Table 6.1.** The most important optical parameters for the different scenarios considered in this study.  $n_i$  the refractive index,  $d_i$  is the thicknesses (expressed in nanometers),  $k$  is the absorption coefficient of the polar headgroup.  $R$  is the total reflection of the incident light from the Langmuir monolayer and  $\Delta R_p$  is the enhancement of reflection originated by the polar headgroup.

A qualitative example of these scenarios was shown by analyzing a mixed Ir-complex : DMPA (1:x ; x>1) monolayers, where the Ir-dye represented a big nonabsorbent polar headgroup while the DMPA a small nonabsorbent headgroup. In such situation, the equimolecular mixture Ir-dye: DMPA formed a uniform monolayer, while the excess of DMPA segregated, leading to small domains in the BAM picture (see Fig. 6.1 A, left). Often, the formation of a condense phase leads to increased reflection and the appearance of bright domains. Nevertheless such a monolayer behaved differently. At low surface pressure, the domains were bright. However they transformed to dark domains when  $\pi > 12.5 \text{ mN m}^{-1}$ . Such a situation could be explained by considering the influence of the polar headgroup. Thus, at low surface pressure the Ir-dye molecules were highly dispersed and strongly hydrated (Scenario I), presenting low reflectivity. However, as the monolayer was compressed, the density of the monolayer increased and the hydration of the Ir-dye reduced, resulting in higher reflectivity. As a consequence, an inversion in the BAM pictures was observed and the domains appeared dark. Such an inversion in the BAM picture could not be understood without considering the influence of the polar headgroup.

On the contrary, the situation changed when the headgroup absorbed the incident light (Scenarios III and IV). In the case of a small headgroup, the model

showed that both the alkyl and the polar group contributed significantly to the reflectivity, depending on the absorption coefficient value ( $k$ ). For an intermediate value  $k = 0.5$ , the increase in reflectivity was  $\sim 54\%$ . Nevertheless, large polar groups led to an important relative increase of reflectivity  $\sim 94\%$  for  $k = 0.5$ . In such a situation the total reflection of the monolayer could be analyzed without considering the alkyl chain. As in the previous example, a qualitative experiment representing Scenario IV was shown (see Fig. 6.1 A, right). It consisted on the study of a mixed monolayer of an amphiphilic derivative of Rhodamine ( $C_{18}RhB$ ) and an alkyl benzyl ester (molar ratio 1:2 respectively). At low surface pressure the monolayer appeared homogeneous. Nevertheless dark irregular domains appeared as compressing the monolayer, due to the formation of a condensed phase. Again, the dark domains were composed by the segregated nonabsorbent benzyl ester, and the bright environment was enriched with the high absorbent  $C_{18}RhB$ , leading to an impressive contrast.

Nevertheless, not only qualitative but also quantitative structural information could be obtained by simulating the textures observed in the domains using the Fresnel equations. When the alkyl chain did not contribute to the reflection (scenario IV), such inner textures were related to the ordered arrangement of the polar headgroup and its absorption. One example was shown by analyzing the mixed DMPA:SP monolayer in a molar ratio 1:1. Such system showed well defined circular 2D domains with particular inner textures, due to the organization of the polar SP group. These textures could be analyzed by ignoring the presence of the alkyl chains. For that, it was necessary to consider all the space parameters needed for representing the orientation of the transition dipole respect to the air-water interface in a circular domain. As a result, the total reflection  $R_p$  could be defined as a function of  $\gamma$ , the angle formed between the x axis (projection of the incident light to the air-water surface) and any radius of the circular domain. The resulting reflectivity was then expressed in terms of a relative grey level scale from 0 (black) to 255 (white), which could be transformed, by using polar coordinates, into a simulated circular domain, and compared with the real domain. By this approach the experimentally observed circular domains in the DMPA:SP monolayer were related to a concentric

configuration of the transition dipole of the SP polar headgroup with a tilt angle of  $\theta = 50^\circ$ , as it is shown in Fig. 6.1.B.

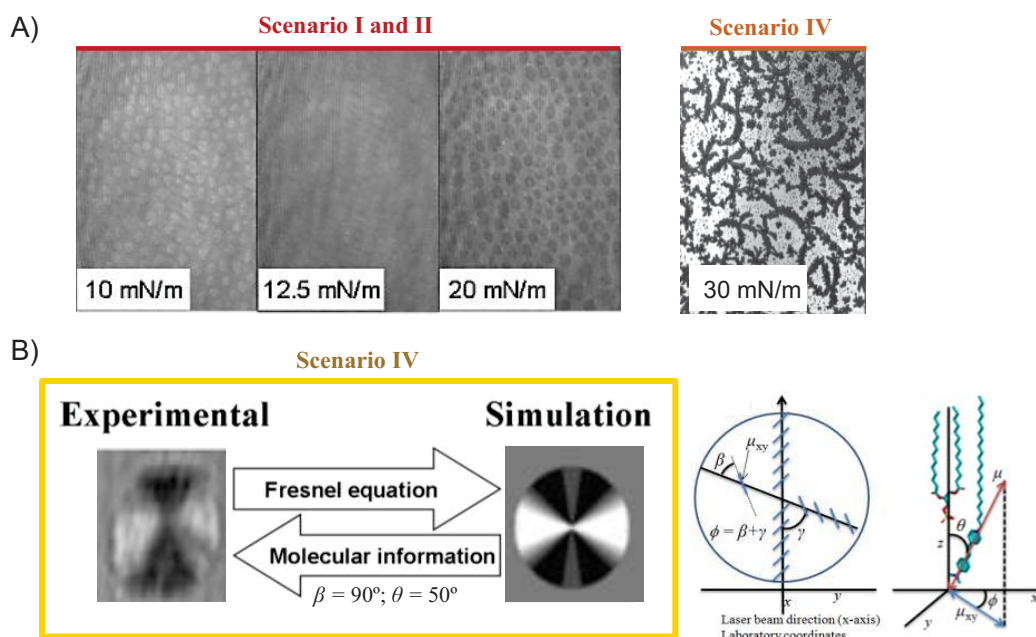


**Fig. 6.1.** A) Qualitative examples for Scenario I and II (left) where an inversion in the BAM picture is observed with compression of the monolayer; and for Scenario IV (right), where the absorbent  $C_{18}RhB$  leads to an impressive contrast in the picture. B) Quantitative analysis for an anisotropic film with circular domains such as DMPA:SP (1:1).

The presented model offers a simple tool for further research in the molecular arrangement of the polar headgroups in organized ultrathin films by using the BAM technique.

Another important technique which provides information about the tilt and aggregation of chromophores at the air-water interface is the UV-Vis Reflection Spectroscopy. This information results particularly important as the polar region is hardly accessible by other experimental techniques such as GIXS or PM-IRRAS. According to that, in the second Section of Chapter 3 a new Reflection Spectroscopy method has been proposed. Traditionally, the application of this technique has been limited to measurements under light normal incidence,  $\Delta R_n$  (LNI), due to the simple theoretical treatment needed for obtaining information. Nevertheless, the LNI method



cannot be applied in certain cases, such as bands overlapping with different transition dipole orientations or oscillator strength that change during compression of the monolayer. In this Section a new method of UV-Vis-RS under light variable incidence (LVI) was described from a theoretical and practical point of view, which solved the limitations of LNI.

The treatment consisted on considering the Fresnel expressions for the reflection of p- and s- polarized light at different incident angles ( $\alpha_0$ ) in an anisotropic biaxial film situated between two isotropic media, air and water. To simplify the model, the real part of the complex refractive index was assumed to be the same,  $n_x = n_y = n_z = n_1$ , which is correct for nonabsorbent wavelengths and at the maxima absorption wavelength ( $\lambda_{\max}$ ). As a result, we obtained an expression for the reflection at a given incidence angle ( $\alpha_0$ ) and wavelength ( $\lambda$ ) where reflectivity depended on four parameters: film thickness ( $d$ ), refractive index ( $n_1$ ), absorption constant in the isotropic media ( $k_{\text{iso}}$ ) and order parameter ( $P(\theta)$ ). By plotting  $\Delta R_s/\Delta R_n$  and  $\Delta R_p/\Delta R_n$  vs the incident angle, it was possible to analyze the influence of  $P(\theta)$  in the reflectivity intensities for s- and p- polarizations.

From these plots only  $\Delta R_p/\Delta R_n$  turned out to show a big dependence on  $P(\theta)$ , experimenting an inversion in the intensity for some incident angles, as it is summarized in Fig. 6.2.a. The dependence with  $P(\theta)$  resulted particularly important for angles greater than the Brewster angle, suggesting them as the best conditions for the calculation of  $P(\theta)$ . However, for such a treatment it was required the numerical fitting of the experimental parameters  $d$ ,  $n_1$  and  $k_{\text{iso}}$ , so the curve  $\Delta R_p/\Delta R_n$  could not be treated in a general fashion. In order to avoid this, the dichroic relation  $\Delta R_p/\Delta R_s$  was used. Such new data were approximately coincident for most of the typical values of  $d$ ,  $n_1$  and  $k_{\text{iso}}$  observed in Langmuir films ( $d \leq 3$  nm;  $1.75 \geq n_1 \geq 1.45$  and  $1.5 \geq k_{\text{iso}} \geq 0.05$ ), leading to an approximate value of  $P(\theta)$  with a maxima error on estimation of 10%. As a consequence, by using the proposed method it is possible to obtain a good approximation of the tilt angle of chromophores in ultrathin films by measuring  $\Delta R_s$  and  $\Delta R_p$ .

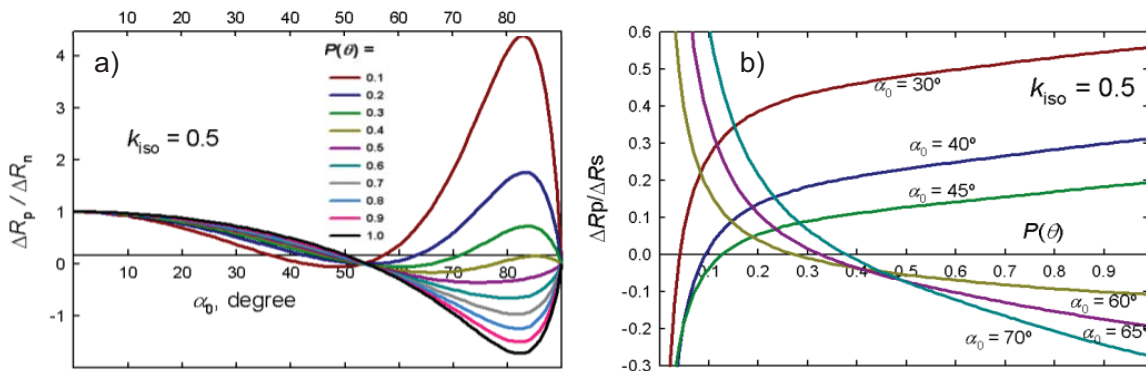


**Fig. 6.2** a)  $\Delta R_p/\Delta R_n$  vs  $\alpha_0$  for different  $P(\theta)$  values; b) Plot of  $\Delta R_p/\Delta R_s$  vs  $P(\theta)$ , for different incidence angles values,  $\alpha_0$ , being  $d = 2$  nm,  $n_1 = 1.55$ ,  $k_{iso} = 0.5$  and  $\lambda = 500$  nm.

Two experimental examples were considered to apply this model on the estimation of  $P(\theta)$ . In the first case, the new method was applied to a simple system to compare the results with the LNI method. The studied system consisted of a pure monolayer of the amphiphilic rhodamine derivative,  $C_{18}RhB$ . By analyzing the normalized  $\Delta R_n$  and the  $\Delta R_p/\Delta R_s$  ratios at  $\alpha_0 = 70^\circ$ , values of  $P(\theta)_{30mN/m} = 0.8$ ;  $P(\theta)_{30mN/m} = 0.58$  and  $P(\theta)_{30mN/m} = 0.88$ ;  $P(\theta)_{30mN/m} = 0.6$  were obtained respectively for each method, confirming a formidable agreement between them.

As a second example, an amphiphilic derivative of the hemicyanine dye was studied, in which a splitting of the absorption band takes place. The splitting of this band had been previously related with the existence of non-equivalent molecules per unit cell in the aggregate. As a consequence, the transition dipole moments were not parallel, which led to two optically active components in the same band: one with the maxima absorption at  $\sim 410$  nm ( $H$  component) and another with the maxima absorption at  $\sim 500$  nm ( $J$  component). As discussed above, these two components could not be analyzed by the LNI method, but was possible by the LVI method. For this purpose, different reflection spectra with s- and p- polarized light were taken under a surface pressure of  $35 \text{ mN m}^{-1}$ . As it was expected, the spectra obtained for s-polarized radiation did not show any change in their shape. Nevertheless, the spectra obtained with p- polarized radiation clearly showed 2 components on the reflection band for the chosen experimental conditions ( $35 \text{ mN m}^{-1}$ ;  $\alpha_0 > 50^\circ$ ): one positive band

centered at 410 nm and another negative band centered at 500 nm. By applying the proposed method good approximations on  $P(\theta)$  values for both bands were obtained. A more accurate calculation was also possible through numerical fitting, the results being obtained in good concordance with those obtained previously in LB films via transmission spectroscopy of s- and p- radiation.

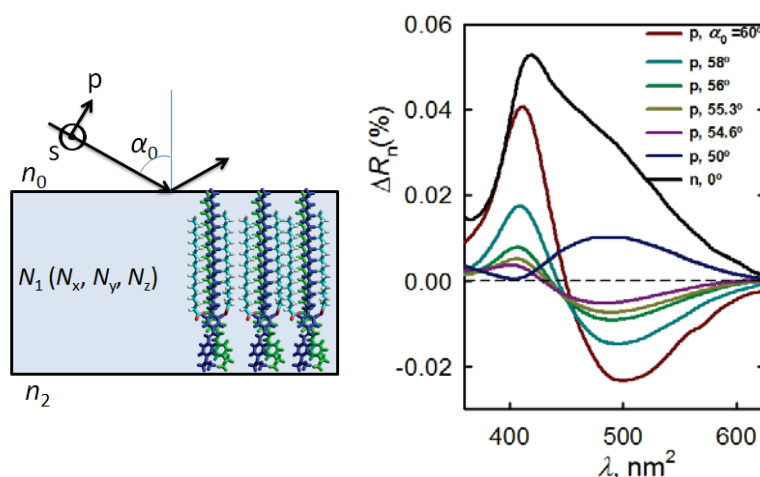


**Fig. 6.3** Reflection spectra of a hemicyanine monolayer with two overlapped bands associated to two different transition dipole components.

Therefore, the new method presented for using UV-Vis reflection spectroscopy represents an important tool for further advancing on the use of this experimental technique.

Finally, in the third part of the Chapter 3 the Langmuir technique have been used for assembling organized ultrathin films containing two luminescent molecules: an amphiphilic cationic Ir-complex and a water soluble anionic porphyrin (TSPP), with a molar ratio 4:1. This stoichiometry was chosen to ensure the neutrality of the monolayer, where molecules remained bounded by electrostatic interactions.

By using the Reflection Spectroscopy technique both mixed Ir-complex : TSPP monolayers and simple monolayer of Ir-complex were analyzed during the compression process. The results showed that, in the case of the Ir-complex monolayer, there was no significant change in terms of intensity, shape and position of the bands for the normalized spectra, which was associated to the absence of changes

in the orientation or aggregation between the Ir-molecules. However, the behavior was different in the presence of TSPP. At low surface pressure no loss of porphyrin towards the aqueous surface was detected, and the molecules oriented flat to the surface. Nevertheless, with compression the porphyrin Soret band shifted continuously to longer wavelengths, decreasing its intensity when normalizing the spectra. This behavior suggested changes in the orientation and/or association between TSPP–TSPP or TSPP–Ir-complex neighboring molecules.

To reveal the origin of this changes, a further analysis was developed, which required the subtraction of the Ir-complex contribution to the reflectivity at the Soret band of the TSPP. By integrating the experimental reflection Soret band, the apparent oscillator strength,  $f_{app}$ , could be obtained for each surface pressure. Thus, at low surface pressures  $f_{orient} = 1.5$  was obtained, which corresponded to a flat orientation of porphyrin molecules at the interface ( $\theta = 90^\circ$ ), but it decreased to  $f_{orient} = 1.03$  with compression, which corresponded to a tilt angle  $\theta = 40^\circ$ .

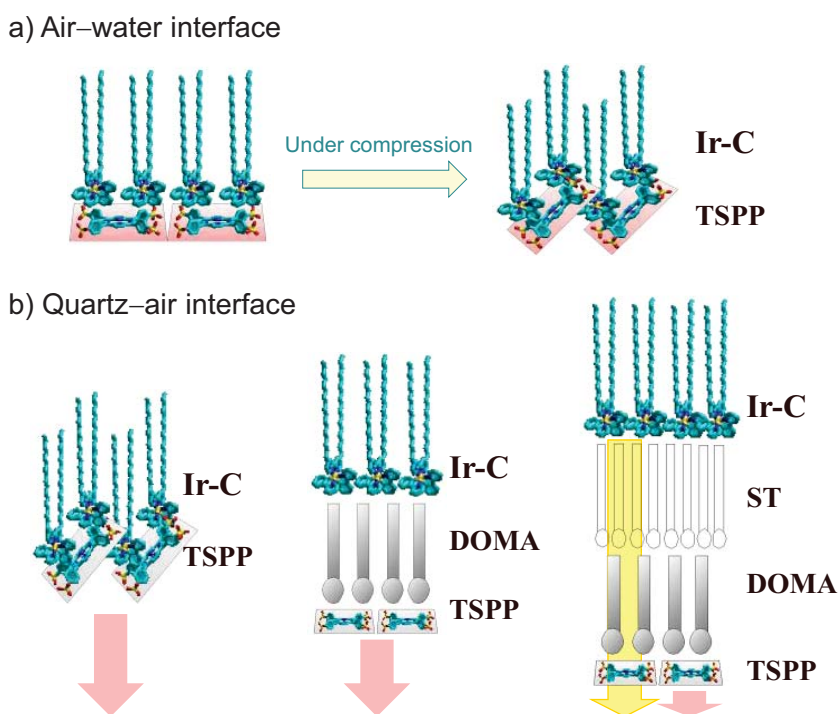


**Fig 6.4** Schedule of the molecular assemblies prepared by Langmuir and Langmuir-Schaefer techniques by introducing dioctadecyldimethylammonium bromide (DOMA) and stearic acid (SA) units between the donor (Ir-C) and the acceptor (TSPP) molecules.

The fabricated Langmuir monolayers were then successfully transferred to quartz substrates by the Langmuir-Schaefer technique and analyzed by fluorescence and time resolved spectroscopy. First results showed a total quenching of the Ir-complex emission due to the presence of the porphyrin. This quenching was attributed to an effective transfer of energy ( $E = 1$ ) from Ir-complex to the TSPP porphyrin, as its emission occurs in the range of the  $Q$  absorption bands of the porphyrin. In order to study the intermolecular energy transfer, the distance between planes of the donor and acceptor units were modified by inserting lipid interlayers of DOMA and SA. After trying different configurations, the energy transfer was avoided by inserting a monolayer of DOMA and a monolayer of ST between the donor–acceptor units, leading to the following film structure: Ir-complex/SA/DOMA/TSPP. Under such conditions, the emission of both the Ir-complex and TSPP were observed. Additionally, the kinetics decays of the studied ensembles were analyzed by time resolved spectroscopy. A monoexponential decay of the mixed Ir-complex:TSPP film was obtained for any excitation wavelength, which was related with the TSPP emission ( $\tau = 4.6$  ns). This behavior changed to a bi-exponential decay at the emission wavelength of 650 nm when inserting the interlayers, confirming the emission from the two molecules ( $\tau_1 = 5.1$  ns and  $\tau_2 = 139$  ns) and the inhibition of the energy transfer process.

## **6.2 Thin films in LECs. Dynamic and static interlayers (Chapter 4)**

In this Chapter the influence on the LEC performance and the dynamic of different thin inorganic interlayers have been studied as charge injection layers situated close to the electrode.

In the first part of the chapter, a qualitative study of the effect of the energy barrier at the electrode/iTMC interfaces on the LECs performance has been carried out by using different metals and metal oxides as charge injecting materials. We correlated the brightness, efficiency and turn-on time with the work function of the electrode materials, in the presence and absence of thin interlayers of ZnO and MoO<sub>3</sub>.

Firstly, the hole injection barrier was studied by preparing iTMC-LECs using a bare and MoO<sub>3</sub> coated ITO as anode, and Al or Au as cathode. In all cases, the active layer consisted on a mixture of [Ir(ppy)<sub>2</sub>(dtb-bpy)](PF<sub>6</sub>) and an ionic liquid in a molar ratio 4:1. Results showed that, while electroluminescence generation was rather independent on the charge injecting material or electrode used, their work function and exciton blocking properties strongly influenced the device performance. The device with bare ITO reached the highest  $L_{\max}$  ( $\sim 1000 \text{ cd m}^{-2}$ ) but the turn-on time and  $t_{\max}$  were also long, suggesting an injection limited regime related with the high energy barrier existing at the ITO/iTMC interface. By incorporating a thin layer of MoO<sub>3</sub>, values of  $t_{\text{on}} < 1 \text{ seg}$  were achieved, and the hole injection barrier no longer existed.

Such conclusion was also supported by a strong reduction on the average voltage of 2 V. Nevertheless,  $L_{\max}$  and PCE were slightly lower compared to the bare ITO electrode, which could be related with a partial exciton quenching due to the proximity of the recombination zone to the metallic cathode. The same configuration but replacing the aluminum by gold resulted in very long turn-on times, as the electron injection barrier was higher at the iTMC/Au interface. Nevertheless, very similar luminance and PCE values were achieved. Such results suggested that LECs can operate with a relative independency of the electrodes work function showing high luminances and efficiencies, but at the cost of a slower response.

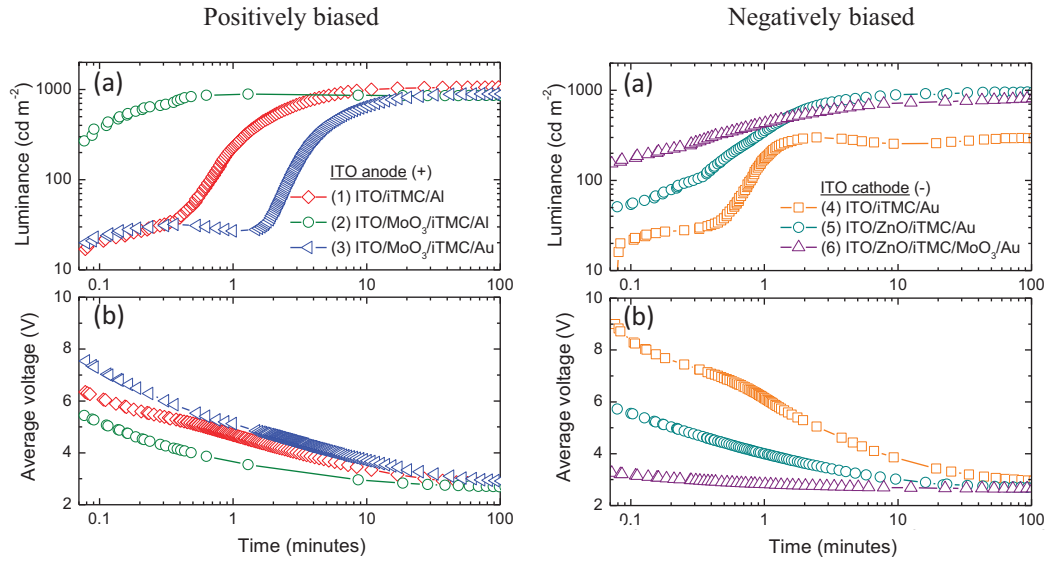


**Fig 6.5** (a) Luminance and (b) average measured voltage characteristics versus time for a series of devices where the ITO is used as the anode (positively biased) or as the cathode (negatively biased).

In a similar way than described above, the electron injecting barrier was studied by preparing iTMC-LECs using a bare and ZnO coated ITO as cathode, and a thin layer of Au or Au/MoO<sub>3</sub> as anode in an inverted configuration. In the case of using bare ITO and Au, the device was strongly injection limited, leading to a very poor luminance ( $L_{\max} = 300 \text{ cd m}^{-2}$ ) and very high averaged voltage (9 V). Nevertheless, by incorporating a thin layer of ZnO as EIL the average voltage decreased considerably and the luminance dramatically increased to  $L_{\max} = 955 \text{ cd m}^{-2}$ . However, the averaged voltages decreased slowly with time, needing 10 minutes to converge to the band gap value of the iTMC, suggesting that the injection was still limited. By combining both ZnO as EIL and MoO<sub>3</sub> as HIL instantaneous electroluminescence, low averaged voltage (3.3 V) and high luminances ( $L_{\max} \sim 900 \text{ cd m}^{-2}$ ) were achieved.

As a consequence, bright and efficient hybrid LECs employing metal oxides as charge injecting layer were prepared by using ZnO and MoO<sub>3</sub> interlayers. The results demonstrated that the performance of such LECs was strongly influenced by the electrode used, affecting the equilibrium between the hole and the electron injection, at the same time than the turn-on time of the device. Fast device switching required

the minimization of the energy barrier at the electrodes, which could be easily achieved by choosing selective contacts such as inorganic metal oxides forming hybrid-LECs, particularly interesting for real lighting applications.

In the second part of Chapter 4 a partial solution process white light-emitting LEC based on a tandem structure was reported for the first time, employing an air stable intermediate electrode composed by thin evaporated films of Au(5nm)/MoO<sub>3</sub>(5nm). The fabrication of the tandem structure required the combination of two individual units linked by such intermediate layer, which connected them physically and electrically. In our case, the strategy consisted on using one blue-bottom unit and one orange-top unit so that the combination of their electroluminescent spectra led to white color. Nevertheless the lack of high luminance blue LECs limited the performance of the white tandem LECs.

For this purpose, a blue light emitting device with reasonable good luminance was prepared by using a novel polymer composite as the blue emitting layer, composed by a typical OLED configuration where a hole transport material (PVK), an electron transport material (OXD-7) and an emitter Ir-complex (FIrPic) were mixed together with a small amount of ionic liquid. The device configuration was the following: ITO/PEDOT:PSS/PVK:OXD-7:FIrPic:[THA][BF<sub>4</sub>]/Al and showed reasonable efficiencies of 4 cd A<sup>-1</sup> for a luminance of 400 cd m<sup>-2</sup>. However, the performance of such device decreased to 160 cd m<sup>-2</sup> when an Au electrode was used instead of Al, in a similar situation as it had in the bottom cell. On the other hand, as top-tandem cell, an orange light-emitter iTMC [Ir(ppy)<sub>2</sub>(dtb-bpy)][PF<sub>6</sub>] mixed with another ionic liquid [BMIm][PF<sub>6</sub>] was sandwiched between a thin layer of Al as the cathode and a semitransparent layer of Au(5nm)/MoO<sub>3</sub>(5nm) as the anode. Such configuration exhibited an efficiency of 7.27 cd A<sup>-1</sup> with a luminance value of 721 cd m<sup>-2</sup>. By combining both structures in a unique tandem cell, a white tandem LEC was obtained (CIE<sub>x,y</sub> = 0.38 ; 0.47) which exhibited a peak efficiency of 8.45 cd A<sup>-1</sup> at a luminance 845 cd m<sup>-2</sup>.



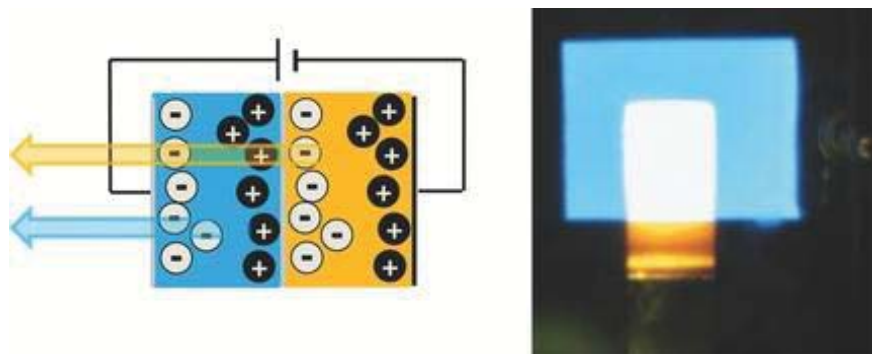


**Fig 6.6** White tandem-LEC composed by a stack of a blue p-LEC and an orange iTMC-LEC joined by a semitransparent interlayer of Au-MoO<sub>3</sub>.

As deduced from the above results, salt-containing organic materials are very suitable for the preparation of tandem structures. Under an applied bias, the accumulation of ions at the electrodes and the formation of dynamically doped zones close remove the injection barriers at the interface for electrons and holes, allowing the efficient injection of charges without the need of additional doped layers close to the intermediate electrode.

### 6.3 Thin films in high efficient solar cells (Chapter 5)

In this Chapter, high efficient solar cells have been prepared through the development of the synthesis process of an hybrid organic-inorganic perovskite, CH<sub>3</sub>NH<sub>3</sub>PbI<sub>3</sub>, together with the combination of a solution processed organic architecture based on the presence of very thin hole and electron blocking films, which resulted cheap, easy to fabricate and highly versatile. By adapting this architecture to flexible substrates, high efficient solar cells were prepared with high robustness to repeated bending. Additionally, by improving a suitable semitransparent electrode, high efficient semitransparent cells were also achieved.

The perovskite material was obtained by the development of the dual source evaporating process, where both reactants materials ( $\text{CH}_3\text{NH}_3\text{I}$  and  $\text{PbI}_2$ ) were heated and sublimated simultaneously in a high vacuum evaporator. By this evaporation process, the thickness as well as the composition of the perovskite could be modified in a controllable way, ensuring good qualities films.

Once the perovskite material was obtained and characterized, it was incorporated into an organic based architecture device, where the active layer was sandwiched between two electron and hole blocking materials, *poly*TPD and PCBM respectively. The high LUMO energy on the first and the low HOMO energy on the later avoided any transference of electrons or holes, respectively, from the perovskite material, while their HOMO and LUMO presented suitable energy levels to ensure a good extraction of charges to the desirable electrodes. A thin film of 70 nm gold was used as cathode, while a PEDOT:PSS covered ITO substrate was used for hole extraction. The final perovskite based solar cell architecture was ITO/PEDOT:PSS(75nm)/*poly*TPD(20nm)/ $\text{CH}_3\text{NH}_3\text{PbI}_3(\text{X})$ /PCBM(20nm)/Au(70nm).

This architecture was successfully adapted to flexible transparent conductor substrates based on a stack of thin layers of aluminum doped zinc oxide (AZO), silver and AZO deposited on a PET substrate. As a result, by using a perovskite thickness of 260 nm, a short circuit current density ( $J_{\text{sc}}$ ), open-circuit voltage ( $V_{\text{oc}}$ ) and field factor (FF) equal to  $14.3 \text{ mA cm}^{-2}$ , 1.04 V and 0.47 were obtained respectively, leading to power conversion efficiencies of 7%. Compared to results obtained in glass, the main difference was the value obtained for FF, which decreased from 0.67 to 0.47 in the PET cell. This considerable difference could be related with the quality of the organic films and the slight increase in their thickness experimented as a consequence of the difficult manipulation of such flexible and small devices. However, such performances are among the highest reported for flexible organic-based solar cells. Moreover, repeated bending of the cell through a roll with a diameter of 5.5 cm did not affect their performance, leading to a decrease in PCE lower than 0.1 %.

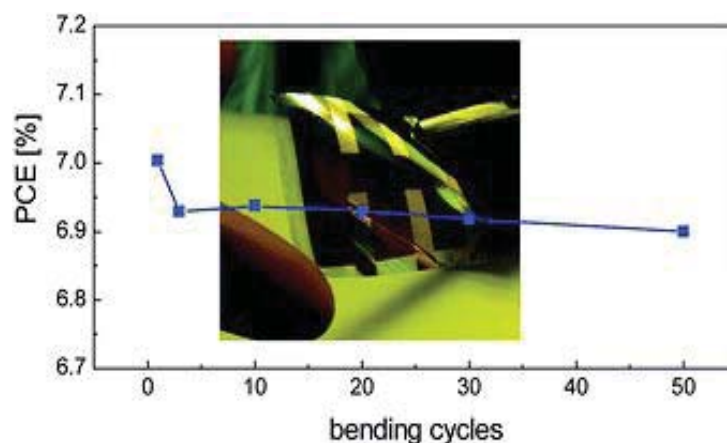


**Fig. 6.7** Power conversion efficiency of the flexible PSC after repeated bending through a role with a diameter of 5.5 cm.

Finally, a semitransparent high efficient single junction perovskite solar cell was also prepared by adapting the above configuration. The developed PSC architecture was composed by very thin organic layers which had a transmittance in the visible spectrum above 80%. Hence, in this type of solar cell, the transmittance was almost completely determined by the perovskite layer and the semitransparent electrode. As expected, higher perovskite thicknesses lead to higher  $J_{SC}$ , thus higher efficiency, but implying a strong reduction in the averaged transmittance of the device (AVT). This inconvenient was partially overcome by an optimized combination of Au (6 nm) and a capping layer of LiF (~ 100 nm), which provided protection for the thin gold electrode while also modified the electric field distribution inside the device, enabling more transparency.

The development of a controllable evaporation process allowed to evaluate different perovskite thicknesses from 40 to 280 nm. Grazing incidence X-ray diffraction (GIXRD) and Scanning Electron Microscopy (SEM) showed a very high crystallinity and uniformity for the ultrathin perovskite layers. Additionally, UV-Vis transmittance spectra were obtained for the device stacks with different perovskite thicknesses, showing an AVT > 44% for  $d_{\text{perovs}} < 100$  nm without the Au-LiF electrode, and AVT ~ 30% for the completed device.

The prepared cells were characterized by measuring the current density versus voltage response ( $J$ - $V$ ), leading to efficiencies ranging from 3.4 % to 7.7 % for the different semitransparent cells with AVT between 45 % to 19 % in the absence of ST electrode, and 35 % to 10 % for the completed devices respectively. The devices showed an expected reduced current density with lowering the perovskite thickness, which could be also seen in the IPCE graph. Nevertheless, high current densities from 10 to 16 mA cm<sup>-2</sup> were achieved, as well as high values of  $V_{oc}$  ~ 1V (almost constant for all thicknesses). However a reduction in the FF with increasing the perovskite thickness affected considerably the performance of such cells, mainly due to the limited conductivity of the ST electrode.

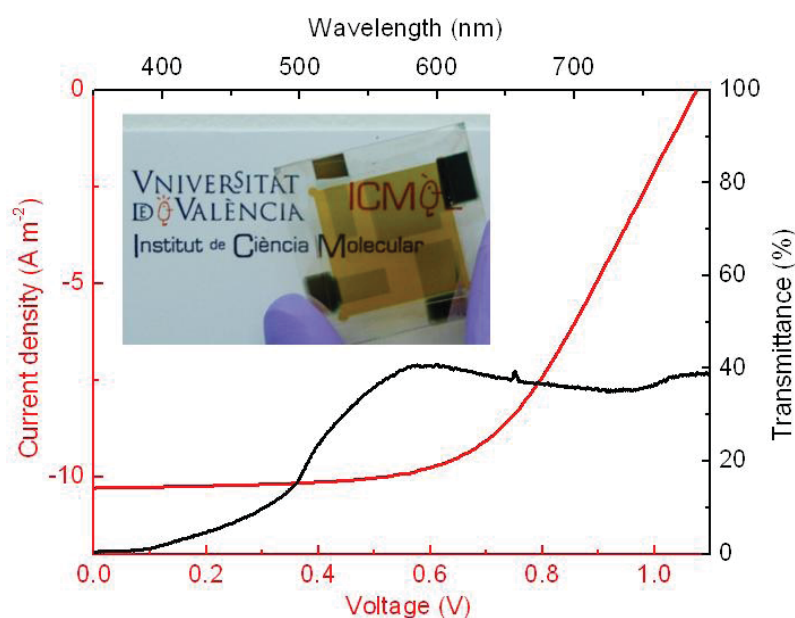


**Fig. 6.8**  $J$ – $V$  curve and transmittance spectra for the semitransparent perovskite solar cell with a perovskite film thickness of 100 nm and PCE 6.4 %.

The semitransparent solar cells that showed the best performance–AVT ratio were those fabricated with 100 and 180 nm of perovskite film thickness, achieving PCE as high as 6.4 % (29% AVT) and 7.3 % (22% AVT) respectively. These values were among the best reported for semitransparent single-junction solar cells.

# **Chapter 7**

## **Conclusions & Outlook**



## 7.1 Conclusions of this work

At the end of each section in Chapters 3, 4 and 5 the most important conclusions for each topic have been mentioned. In this chapter the main conclusions of this thesis are presented.

Organic thin films are acquiring more importance for both present and future technology. Of special interest is the control of their molecular arrangement, which can result in new or modified properties useful for many applications. One of the techniques which provide monolayer or multilayer structures with a high degree of order is the Langmuir technique, which has been widely used in the last decades. Nevertheless, most of the characterization techniques of Langmuir monolayers are directed to analyze the hydrophobic region, without considering the arrangement of the polar region in these systems. This implies a big limitation as many interesting properties of Langmuir monolayers are direct consequences of the molecular arrangement of the polar units located in such a region (for example, chromophore dyes, magnetic components or emissive molecules...). With this in mind, in Chapter 3 we studied and proposed two different techniques to provide useful information about the polar headgroup arrangement on Langmuir films. The first technique was the Brewster Angle Microscopy, which traditionally had considered exclusively the structure of the alkyl chain. We have shown that for bulky and absorbing polar headgroups the BAM pictures must be related with the reflectivity of such groups. Such influence has a special importance in the case of high degree ordered Langmuir monolayer, as quantitative structural information can be obtained. For such films, we have described a mathematical procedure to simulate the different textures of the domains in the BAM picture, which allows the extraction of quantitative information about the polar headgroup organization, being possible its application in many different Langmuir monolayers.

Additionally, we proposed a new method for obtaining the order parameter of the chromophores ( $P(\theta)$ ) by introducing a modified version of the traditional UV-Vis

Normal Reflection Spectroscopy technique, which provides useful information about the tilt angle ( $\theta$ ) and aggregation of such units. We described in detail the theoretical background of this method, resulting in a simple way for obtaining such information by measuring  $\Delta R$  for s- and p- polarized radiation at different incident angles. This procedure avoids the need of rigorous numerical fitting for intrinsic parameters such as the refractive index, the thickness or the exact value of the absorption constant of the film, assuming a range of values valid for typical Langmuir monolayers. Moreover, this method could be applied on systems where the traditional method is limited, representing a standard usage of UV-Vis Reflection Spectroscopy. We have also highlighted the potential of Langmuir monolayers on studying fundamental processes at molecular scale. With that purpose we have built multilayer architectures where an energy transfer process took place between a donor and an acceptor molecule. By building different architectures with controlled intermolecular distance, we have shown its suitability to analyze such intermolecular energy transfer process by using Steady State and Time resolved Fluorescence Spectroscopy.

Thin films have been also applied in optoelectronic devices, such as light emitting electrochemical cells and thin film solar cells. In Chapter 4 we have shown the influence of the energy barrier at the electrode/organic interface in the performance of LECs by incorporating ultrathin inorganic films of conductive metal oxides. Although the performance of LECs is according to some theories independent on the electrode used we showed that the performance of LECs depends strongly on the type of material located at the electrode interfaces. This dependence results from a shift in the location of the recombination zone and of the dynamically doped regions. However, even in injection limited devices, the formation of EDLs and doped regions at the interfaces lead to bright and efficient electroluminescence. By using charge selective contacts such as ZnO and MoO<sub>3</sub> we have demonstrated fast device turn-on for very bright and efficient devices. Additionally, we demonstrated that such metal oxide layers can be used as cheap and stable interlayers in tandem LECs. In this thesis we showed the first reported white tandem LEC with a thin Au-MoO<sub>3</sub> interlayer. Thanks to the dynamic working mechanism of LECs, efficient injection of charges can



be achieved through both external and internal electrodes. Such a self-regulating mechanism leads to an ideal junction formation which causes the current to be equal in both top and bottom devices without potential losses at the junction, and without the need of additional doped layers close to the intermediate electrode.

Finally, thin films have also been applied in high efficient hybrid methylammonium lead iodide perovskite solar cells. We showed the relevance of thin hole and electron blocking layers in the performance of such solar cells, as well as the potential of organic materials in achieving low cost and efficient photovoltaic systems. The development of a well controllable synthesis for the perovskite material has been crucial for adapting its deposition to several different substrates with a high control on the thickness and composition. Additionally, the absence of hysteresis when applying forward and reverse bias opens the possibilities for future reliable in depth studies on their mechanism. By sandwiching the evaporated layer between an organic hole transporting material and an electron transporting material that also function as charge selective layers we were able to prepare high efficient PSC. Moreover, the advantages of organic materials used in conjunction with a strongly absorbing hybrid organic-inorganic material allows for a wide range of architectures. For example, we have prepared high efficiency solar cells on flexible substrates suitable for roll-to-roll processes. Additionally, semitransparent device architectures were developed that are ideal for façades or building integrated windows, as well as high efficient tandem structures.

## 7.2 Outlook

We expect that the work developed during this Thesis can and will be used to inspire new research on the study of thin films in order to be applied in real-life technologies.

We have already shown in this work that the organization of ultrathin films can be determined by the polar region in highly ordered Langmuir systems, and proposed two different methods to obtain highly valuable information through the use of BAM and UV-Vis Reflection Spectroscopy techniques. However, it would be intriguing to perform BAM experiments with different lasers at different wavelengths, which could enhance the reflection of some regions at the expense of another regions within the domain, in the case of an absorbing polar headgroup, at the same time that could offer the chance to visualize either the polar headgroup or the alkyl chain in the same experiment. Moreover, we have proposed a standard usage of UV-Vis Reflection Spectroscopy which could inspire novel experiments in which privileged and richly detailed information could be achieved. This spectroscopy could be extended to 2D mapping, allowing the imaging of the Langmuir monolayer and the study of the different phases separately, or even different sections within the domain, leading to a new concept in the molecular description of Langmuir monolayers.

Thin films have also been studied as interlayers in optoelectronic devices, in particular in light-emitting and photovoltaic devices. Metal oxide interlayers have been pointed out as possible route to achieve stable, efficient and fast response light emitting electrochemical cells, allowing the fabrication of the first white tandem-LEC. These results are particularly promising as they confirm that no charge generation layer is needed in such devices. However, one of the key remaining issues that prevent LECs from being applied in general lighting is the lack of stable and efficient blue emitters. Currently, their stability is now much lower than the orange counterparts, compromising the final performance of the tandem system. In-depth studies in this direction could help to unravel the origin of such instabilities in wide band-gap

emitters and provide the keys to develop high performing emitters in the whole visible spectral range.

Finally, the development of high efficient perovskite solar cells has opened a way towards a low-cost and efficient alternative for electricity production. Such a technology can lead to electricity prices well below these of today making electricity available not only to a wide population of developed but also of less developed regions in the world. In this Thesis high efficient perovskite solar cells based on organic interlayers have been developed, which are suitable for applications in clothes, portable utensils or even semitransparent cells for windows integrated buildings or tandem structures by using semitransparent electrodes. However, this technology has only recently emerged which implies that there are some remaining unknowns, such as their long term stability. We have shown that it is possible to prepare cells which do not show significant hysteresis in their  $J - V$  curves which will facilitate this study. Another issue is the presence of lead in the perovskite material. Containment and recyclability needs to be developed or even better, alternative materials without lead with similar performances.



## Resumen en castellano

La evolución de la Tecnología implica la manipulación del medio que nos rodea para poder satisfacer las necesidades humanas, tales como alimento, salud, refugio y comunicación. A pesar de su evolución a lo largo de la historia de la humanidad, la tecnología ha experimentado toda una revolución en el último siglo, encontrándonos hoy en día rodeados de innumerables aparatos electrónicos. Sin embargo, la cada vez más creciente demanda energética de los países desarrollados y emergentes, junto con el impacto medioambiental de la mayoría de los procesos industriales, nos está llevando hacia un sistema claramente insostenible. A su vez, muchos de estos aparatos requieren el uso de limitadas y costosas fuentes primarias, condicionando su accesibilidad. Es urgente un cambio tanto en la manera de consumir de la sociedad como en la manera de producir energía, lo que sugiere la búsqueda de nuevas alternativas eficientes y respetuosas con el medio ambiente.

En este contexto, los materiales orgánicos representan una prometedora alternativa a alguno de los actuales y limitados materiales inorgánicos, puesto que son fáciles de fabricar, abundantes y relativamente baratos. Concretamente, las películas delgadas de semiconductores orgánicos poseen un gran potencial tecnológico debido a sus particulares propiedades ópticas, magnéticas y eléctricas, que han permitido el nacimiento de lo que actualmente se conoce como Electrónica Orgánica. Comparados con los semiconductores tradicionales como Si o GaAs, los semiconductores orgánicos son ligeros, flexibles, con propiedades fácilmente modificables y pueden ser procesados fácilmente, permitiendo la fabricación de un gran número de dispositivos electrónicos de bajo coste. En las últimas décadas se ha experimentado un enorme avance en el estudio y fabricación de este tipo de materiales, facilitando su incorporación en dispositivos orgánicos, tales como diodos emisores de luz, transistores de efecto de campo, fotodiodos o también células solares, algunos de cuyos prototipos están entrando actualmente en el mercado.

Las películas delgadas presentan un elevado potencial tecnológico debido a varios factores, uno de los cuales consiste en la influencia de la composición y morfología en sus propiedades, resultado de interacciones colectivas entre las moléculas que lo conforman. Como consecuencia, en los últimos años se ha realizado un enorme esfuerzo en la elaboración de nuevas estrategias, que permitan no sólo controlar la morfología de las películas delgadas, sino también trasladar estas propiedades a procesos de producción a gran escala.

Una de las técnicas más estudiadas que permite preparar sistemas monocapa y multicapa con un elevado control en su organización molecular es la técnica de Langmuir. Esta técnica permite la preparación de películas delgadas en la interfase aire-agua con una composición muy variada, en la que al menos un componente debe ser anfifílico. La mayoría de las técnicas de caracterización de monocapas Langmuir están centradas en el estudio y organización de las cadenas alquílicas que conforman el sistema, siendo más escasas aquellas que proporcionan información directa de la organización del grupo polar. Esta situación representa una gran limitación en este tipo de sistemas, puesto que muchas propiedades interesantes y con gran potencial tecnológico derivan precisamente de la organización de los grupos o moléculas presentes en la parte polar (actividad óptica, cambios de absorción-emisión, propiedades magnéticas...).

Por todo ello, la primera parte de la presente Tesis va dirigida al estudio y revisión de dos técnicas de caracterización ampliamente usadas en la interfase aire-agua, con el objetivo de obtener información útil acerca de la organización de las unidades moleculares que conforman la región polar, difícilmente accesible por otras técnicas. La primera técnica revisada fue la Microscopía de Angulo de Brewster (BAM), la cual se ha usado tradicionalmente atendiendo a la ordenación de la cadena alquílica, es decir a la parte hidrofóbica de la monocapa de estudio. Sin embargo, nuestros trabajos demuestran la importancia de incluir al grupo polar en el análisis de las imágenes BAM, particularmente cuando presenta un tamaño grande y/o absorbe la radiación incidente. A su vez proponemos un procedimiento matemático que permite

simular las diferentes texturas de los dominios observados en las imágenes BAM, permitiendo así conocer información estructural acerca de sus componentes, tal como inclinación y disposición de las moléculas.

La segunda técnica estudiada fue la Espectroscopía de Reflexión UV-Vis, cuyo uso ha estado limitado tradicionalmente a incidencia normal respecto a la interfase aire-agua, debido a la simplicidad del tratamiento teórico requerido. Esta técnica permite obtener información tanto del ángulo de inclinación del momento de transición del cromóforo, así como de la agregación existente entre moléculas. No obstante, requiere el uso de otras técnicas para obtener ciertos parámetros necesarios en el cálculo, y tiene una aplicación limitada. Ante estas circunstancias, en esta Tesis se ha propuesto un nuevo método de análisis basado en las expresiones de reflectividad ( $R$ ) obtenidas a partir de las ecuaciones de Fresnel. Gracias a este método, es posible conocer el valor del parámetro de orden (relacionado con el ángulo de inclinación del cromóforo) sencillamente midiendo experimentalmente  $\Delta R_p/\Delta R_s$  para un ángulo de incidencia dado, así como analizar aquellos sistemas que no pueden ser resueltos mediante el método tradicional de incidencia normal.

La técnica de Langmuir permite construir fácilmente ensamblados moleculares con un alto grado de control en su organización y composición, permitiendo así estudiar procesos físico-químicos que tengan lugar entre sus componentes, tales como procesos de transferencia de energía. Con este objetivo, se prepararon varios sistemas multicapa formados por dos moléculas emisoras comúnmente presentes en dispositivos ópticos, y se analizó la transferencia de energía entre ambas mediante Espectroscopía de Fluorescencia en estado estacionario y en tiempo resuelto. Mediante la inserción controlada de espaciadores moleculares entre donador y aceptor, fue posible abolir el proceso de transferencia y analizar la distancia crítica intermolecular para que se produzca.

Sin embargo, no sólo la morfología influye en las propiedades de este tipo de películas. Las películas delgadas pueden mostrar propiedades físicas muy diferentes a

las del material a escala macroscópica, especialmente si el espesor es muy pequeño. La elevada relación superficie/volumen hace que los procesos físico-químicos que tienen lugar en la interfase condicionen la mayoría de sus aplicaciones, adquiriendo propiedades electrónicas de gran interés para Electrónica Orgánica. Un ejemplo donde estas películas son usadas ampliamente como componentes activos son los dispositivos optoelectrónicos. En ellos frecuentemente una o varias películas de un semiconductor es depositada entre dos electrodos, generalmente inorgánicos. Mediante un ajuste adecuado de los niveles energéticos, es posible inyectar o extraer electrones y huecos a muy bajo voltaje, generando por ejemplo luz, en el caso de dispositivos emisores de luz, o corriente eléctrica, en el caso de células solares.

Existe aún una intensa investigación en este tipo de dispositivos hacia la obtención de sistemas eficientes, de bajo coste y accesibles para todo el mundo. En este sentido, las células electroquímicas emisoras de luz (LECs) constituyen una prometedora alternativa puesto que pueden operar con electrodos estables al aire, son fácilmente procesadas desde disolución y están compuestas por una sola capa orgánica, lo cual simplifica enormemente su fabricación. Su funcionamiento se basa en la presencia de iones en la capa activa que, bajo la aplicación de un voltaje externo, se acumulan en la interfase de los electrodos formando lo que se conoce como doble capa eléctrica (EDL). La elevada concentración de estos iones favorece procesos redox que provocan el dopado de las zonas próximas a éstos, permitiendo la inyección de carga, su transporte hacia el interior y la emisión de luz. Por tanto, los dispositivos LECs no precisan de electrodos inestables, y pueden ser procesados fácilmente como una sola capa activa. Existen dos tipos principales de LECs, los basados en materiales poliméricos mezclados con sales (p-LECs), o los basados en complejos de transición iónicos (iTMC-LECs), en los que se usan más ampliamente complejos de transición de Ir(III).

Este tipo de dispositivos han mejorado considerablemente en los últimos años, habiéndose conseguido mayor estabilidad, eficiencia de iluminación y un menor tiempo de respuesta, lo cual los convierten en serios candidatos para la producción de



sistemas de iluminación de bajo coste. Sin embargo, para ello es preciso obtener emisión de luz blanca, que junto con la estabilidad a largo plazo, constituyen los principales reto de este tipo de tecnología. Ante este contexto, en esta Tesis se ha analizado la influencia que diferentes materiales electródicos podían tener en el rendimiento de este tipo de dispositivos, fabricando LECs híbridos orgánicos-iorgánicos. Mediante el uso de óxidos metálicos conductores tipo ZnO o MoO<sub>3</sub>, cuyos niveles energéticos permiten usarlos como inyectores de electrones o huecos respectivamente, se ha demostrado que la luminancia, eficiencia y tiempo de respuesta de estos dispositivos está muy condicionada por el material usado. Este hecho se ha relacionado fundamentalmente con el desplazamiento de la zona de emisión, lo que puede favorecer otros procesos como quenching, si se encuentra muy cerca del electrodo.

En esta Tesis se han obtenido LECs híbridos de alta eficiencia y rápido tiempo de respuesta usando electrodos modificados con óxidos metálicos, lo que pone en evidencia su potencial como, por ejemplo, electrodos intermedios baratos y estables para fabricar tándem-LECs. Se ha demostrado por primera vez la posibilidad de fabricar tándem-LECs sin necesidad de usar inter-electrodos complejos, con adicionales capas dopadas inyectoras de huecos y electrones. Mediante el uso de una fina película de Au-MoO<sub>3</sub> ha sido posible fabricar tándem-LECs de emisión blanca y relativamente eficientes, demostrándose que la inyección de carga a ambas unidades del tándem puede realizarse fácilmente gracias a su característico mecanismo de autorregulación.

A su vez, también se han construido células solares orgánicas de capa fina, fabricadas con un nuevo material fotoactivo híbrido, CH<sub>3</sub>NH<sub>3</sub>PbI<sub>3</sub>, que combina la flexibilidad de los materiales orgánicos, con algunas propiedades de los materiales inorgánicos, alcanzando como resultado eficiencias realmente elevadas. Se ha desarrollado un proceso de síntesis de este material que permite controlar su composición y espesor de manera precisa, mediante la evaporación simultánea de los materiales precursores PbI<sub>2</sub> y CH<sub>3</sub>NH<sub>3</sub>I, permitiendo así una elevada calidad en las

películas formadas. Alternativamente, mediante el uso de películas orgánicas de semiconductores que actúan como bloqueadores de carga específicos, ha sido posible obtener células fotovoltaicas de capa fina de alta eficiencia y altamente flexibles, que a su vez son compatibles con procesamiento vía disolución. Además los dispositivos fotovoltaicos fabricados han demostrado gran resistencia mecánica, al no alterar su rendimiento tras someterse a continuo estrés mecánico. Por otro lado, modificando esta estructura mediante el uso de un electrodo semitransparente, se han obtenido células fotovoltaicas semitransparentes altamente eficientes, en las que se combina una alta conversión fotoeléctrica con una transparencia elevada, ideal para ser aplicadas en fachadas de edificios, como decoración o integradas como ventanas. Las eficiencias alcanzadas representan las más elevadas descritas para células simples hasta el momento, lo cual denota su tremendo potencial. Estas células representan por primera vez una alternativa de bajo coste, abundante y eficiente, a los costosos paneles solares basados en silicio que ocupan la mayoría del actual mercado fotovoltaico.

## Publications used for this Thesis

### CHAPTER 3:

- **Roldán-Carmona, C.**; Gonzalez-Delgado, A.M.; Guerrero-Martinez, A. ; De Cola, L.; Giner-Casares, J.J.; Perez-Morales, M.; Martin-Romero, M.T.; Camacho, L. “Molecular organization and effective energy transfer in iridium metallosurfactant-porphyrin assemblies embedded in Langmuir-Schaefer films”  
*Physical Chemistry Chemical Physics* 13, 2834-2841 (2011)

Journal Citation Reports (JCR):

Area: *Physical Chemistry*; IF= 3.573(2011)                      Ranking: 34/134

- **Roldán-Carmona, C.**; Giner-Casares, J.J.; Perez-Morales, M.; Martin-Romero, M.T. ;Camacho, L. “Revisiting the Brewster Angle Microscopy: The relevance of the polar headgroup”  
*Advances in Colloid and Interface Science* 173, 12-22 (2012)

Journal Citation Reports (JCR):

Area: *Physical Chemistry*; IF= 6.169 (2012)                      Ranking: 17/135

- **Roldán-Carmona, C.**; Rubia-Paya, C. ; Perez-Morales, M. ; Martin-Romero, M.T. ; Giner-Casares, J.J. ; Camacho, L. “UV-Vis reflection spectroscopy under variable angle incidence at the air-liquid interface”  
*Physical Chemistry Chemical Physics* 16, 4012-4022 (2014)

Journal Citation Reports (JCR):

Area: *Physical Chemistry*; IF= 4.19 (2013)                      Ranking: 33/136

### CHAPTER 4:

- **Roldán-Carmona, C.**; Akatsuka, T.; Sessolo, M.; Watson, S. and Bolink, H. J. “Engineering charge injection interfaces in hybrid light-emitting electrochemical cells”  
Submitted to *ACS Applied Materials & Interfaces* (September 2014).

Journal Citation Reports (JCR):

Area: *Material Science, Multidisciplinary*; IF= 5.9 (2013)                      Ranking: 26/251

- Akatsuka, T.; **Roldán-Carmona, C.**; Orti, E.; Bolink, H. J.  
“Dynamically doped white light emitting tandem devices”  
*Advanced materials* 26, 770-4 (2014) (Epub 2013 Oct 25)

Journal Citation Reports (JCR):

Area: *Materials Science, Multidisciplinary*; IF= 15.409 (2013) Ranking: 6/251

## CHAPTER 5:

- **Roldán-Carmona, C.**; Malinkiewicz, O.; Soriano, A.; Espallargas, G.M.; Garcia, A.; Reinecke, P.; Kroyer, T.; Dar, M.I.; Nazeeruddin, M.K.; Bolink, H.J.  
“Flexible high efficiency perovskite solar cells”  
*Energy & Environmental Science* 7, 994-997 (2014)

Journal Citation Reports (JCR):

Area: *Environmental Sciences*; IF= 15.49 (2013) Ranking: 1/215

- **Roldán-Carmona, C.**; Malinkiewicz, O.; Betancur, R.; Longo, G.; Momblona, C.; aramillo, J.; Camacho, L.; Bolink, H.J.  
“High efficiency single-junction semitransparent perovskite solar cells”  
*Energy & Environmental Science*. DOI: 10.1039/c4ee01389a

Journal Citation Reports (JCR):

Area: *Environmental Sciences*; IF= 15.49 (2013) Ranking: 1/215

## Other contributions derived from this Thesis

- Gonzalez-Delgado, A.M.; Rubia-Paya, C.; **Roldán-Carmona, C.**; Giner-Casares, J.J.; Perez-Morales, M.; Munoz, E.; Martin-Romero, M.T.; Camacho, L.; Brezesinski, G.  
“Control of the Lateral Organization in Langmuir Monolayers via Molecular Aggregation of Dyes “  
*Journal of Physical Chemistry C* 114, 16685-16695, (2010)

Journal Citation Reports (JCR):

Area: *Physical Chemistry*; IF= 4.52 (2010) Ranking: 27/127

- Shavaleev, N.M. ; Scopelliti, R; Gratzel, M.; Nazeeruddin, M.K. ; Pertegas, A.; **Roldán-Carmona, C.**; Tordera, D.; Bolink, H.J.  
“Pulsed-current versus constant-voltage light-emitting electrochemical cells with trifluoromethyl-substituted cationic iridium (III) complexes”  
*Journal of Materials Chemistry C* 1, 2241-2248 (2013)

Journal Citation Reports (JCR):

Area: *Physical Chemistry*; IF= 6.626 (2013) Ranking: 19/136

- Malinkiewicz, O.\*; **Roldán-Carmona, C.\***; Soriano, A.; Bandiello, E.; Camacho, L.; Nazeeruddin, M.K. and Bolink, H.J.  
“Metal oxide free methylamonium lead iodide perovskite based solar cells; influence of organic charge transport layers”  
*Advanced Energy Materials* 1400345 (2014)

*\*Both contributed equally to this work.*

Journal Citation Reports (JCR):

Area: *Materials Science, Multidisciplinary*; IF= 14.385 (2013) Ranking: 7/251

- Meier, S.B.; Tordera, D.; Pertegás, A.; **Roldán-Carmona, C.**; Ortí, E. and Bolink, H.J.  
“Light-emitting electrochemical cells: recent progress and future prospects”  
*Materials Today* 17, (2014) <http://dx.doi.org/10.1016/j.mattod.2014.04.029>

Journal Citation Reports (JCR):

Area: *Materials Science, Multidisciplinary*; IF= 10.85 (2013) Ranking: 11/251

- Momblona, C.; Malinkiewicz, O.; **Roldán-Carmona, C.**; Soriano, A.; Gil-Escrig, L.; Edri, E. and Bolink, H.J. “Methylammonium lead iodide perovskite thickness independent efficient solar cells”  
*APL Materials* 2, 081504 (2014)

E-ISSN: 2166-532X (new high impact journal, JCR are not available yet).

- Hasan, K.; **Roldán-Carmona, C.**; Bolink, H.; Zysman-Colman, E.  
“Incorporation of Methoxy Groups on the Cyclometallating Ligand as a Strategy for Tuning the Optoelectronic Properties of Cationic Iridium (III) Complexes Towards the Red: Predictions, Synthesis, Characterization and Light-Emitting Electrochemical Cells”  
*The Journal of Physical Chemistry* (submitted).
- Evariste, S.; Sandroni, M.; Rees, T.; **Roldán-Carmona, C.**; Gil-Escrig, L.; Bolink, H.; Baranoff, B. and Zysman-Colman, E.  
“Fluorine-free Blue-green Emitters for Light-Emitting Electrochemical Cells”  
*Journal of Material Chemistry C* 2, 5793-5804, (2014)

Journal Citation Reports (JCR):

Area: *Physical Chemistry*;

IF= 6.626 (2013)

Ranking: 19/136

## Congresses

- Authors: *Roldán-Carmona, Cristina; Giner-Casares, Juan José; Gálvez, Nuria; Domínguez-Vera, José Manuel; Watt, R. K.; Martín-Romero, María T.; Camacho, Luis.*  
Title: *Mixed monolayers of eicosylamine and a bacterial-ferritin prepared by adsorption technique at the air–water interface.*  
Contribution: *Poster*  
Congress: *III Reunión Ibérica de Coloides e Interfases (RICI). VIII Reunión del Grupo Especializado de Coloides e Interfases (GECI) de la Reales Sociedades Españolas de Física y Química*  
Publication: *Abstract Book*  
Place: *Granada (Spain)* Date: 2009

- Author: *C. Roldán-Carmona, J.J Giner-Casares, N. Gálvez, J. M. Domínguez Vera, Richard K. Watt, M. T. Martín-Romero and Luis Camacho.*  
 Title: *Preparación de monocapas en la interfase aire-agua: estudio de las propiedades de adsorción de una nueva bacterioferritina*  
 Contribution: *oral presentation*  
 Congress: *II Encuentro Nanouco: Encuentro Sobre Nanociencia Y Nanotecnología de Investigadores y Tecnólogos de la Universidad de Córdoba*  
 Publication: *Abstract Book*  
 Place: *Córdoba (Spain)* Date: *2010*
  
- Author: *C. Roldán-Carmona, J.J Giner-Casares, N. Gálvez, J. M. Domínguez Vera, Richard K. Watt, M. T. Martín-Romero and Luis Camacho.*  
 Title: *Mixed monolayers of eicosylamine and a bacterial-ferritin prepared by adsorption technique at the air–water interface.*  
 Contribution: *Póster*  
 Congress: *II Encuentro Nanouco: Encuentro Sobre Nanociencia Y Nanotecnología de Investigadores y Tecnólogos de la Universidad de Córdoba*  
 Publication: *Abstract Book*  
 Place: *Córdoba (Spain)* Date: *2010*
  
- Author: *Cristina Roldán-Carmona, Antonio M. González-Delgado, Andrés Guerrero-Martínez, Luisa De Cola, Juan J. Giner-Casares, Marta Pérez-Morales, María T. Martín-Romero and Luis Camacho.*  
 Title: *Molecular Organization and effective energy transfer in iridium metallosurfactant-porphyrin assemblies embedded in Langmuir-Schaefer films*  
 Contribution: *Poster*  
 Congress: *III Encuentro de Nanouco: Encuentro sobre Nanociencia y Nanotecnología de Investigadores y Tecnólogos Andaluces*  
 Publication: *Abstract book*  
 Place: *Córdoba (Spain)* Date: *2011*
  
- Author: *Cristina Roldán-Carmona, Marta Pérez-Morales, Henk Bolink, Andrés Guerrero-Martínez, Luisa De Cola, Juan J. Giner Casares, María T. Martín-Romero, Luis Camacho.*  
 Title: *Molecular organization of three different iridium-complex derivatives in mixed amphiphilic films*  
 Contribution: *Poster*  
 Congress: *European Conference on Organized Films (ECOF 12)*  
 Publication: *Abstract book*

- Place: *Sheffield (England)*      Date: 2011
- Author: *Cristina Roldán-Carmona, Juan J. Giner-Casares, Marta Pérez-Morales, María T. Martín-Romero, Luis Camacho*
  - Title: *The Significant Role of Polar Headgroup of the Amphiphiles in the Brewster Angle Microscopy*  
Contribution: *Poster*  
Congress: *IV Encuentro de Nanouco: Encuentro sobre Nanociencia y Nanotecnología de Investigadores y Tecnólogos Andaluces*  
Publication: *Abstract book*  
Place: *Córdoba (Spain)*      Date: 2013
  - Author: *Cristina Roldán-Carmona*  
Contribution: *no contribution, invited attendee by the Conference Chair.*  
Congress: *Gordon Research Congress: Electronic Processes in Organic Materials, Exploring the Fundamentals of Organic Electronics*  
Place: *Lucca (Barga), Italy*      Date: 2012
  - Author: *Cristina Roldán-Carmona, Nail M. Shavaleev, Rosario Scopelliti, Michael Grätzel, Mohammad K. Nazeeruddin, Antonio Pertegás, Daniel Tordera, Henk J. Bolink*  
Title: *"Light-emitting electrochemical cells with trifluoromethyl-substituted cationic iridium(III) complexes. The importance of driving conditions*  
Contribution: *Poster*  
Congress: *Nanostructured Hybrid Materials for Energy Devices: From experiment to modeling. ORION Summer School.*  
Publication: *Abstract book*  
Place: *Granada (Spain)*      Date: 2013
  - Authors: *Cristina Roldán-Carmona, Olga Malinkiewicz, Giulia Longo, Cristina Momblona and Henk Bolink.*  
Title: *Metal-oxide free perovskite solar cells: high efficient, flexible and semitransparent devices*  
Contribution: *Poster*  
Congress: *Hybrid and organic photovoltaics. NanoGe. HOPV14*  
Publication: *Abstract book*  
Place: *Lausanne (Switzerland)*      Date: 2014



## Stays at National and International Research Centers

- Center for Molecular and Nanoscale Electronics, University of Durham, United Kingdom (U.K.).  
Duration: From 28th June to 8th October      Date: 2010
- Instituto de Ciencia Molecular (ICMol), Universidad de Valencia, España.  
Duration: From 1st September to 15th December      Date: 2011
- SINCROTRÓN Hamburg (Germany)  
Duration: From 13 October to 17 October      Date: 2011
- SINCROTRÓN Hamburg (Germany)  
Duration: From 1st April to 4th April      Date: 2012
- Instituto de Ciencia Molecular (ICMol), Universidad de Valencia, España.  
Duration: From 1st April to 30th June      Date: 2013



